Spatial Control of Mechanical Factors: a New Design Rationale for Nerve Tissue Engineering

Celine Kayal

Mechanical Engineering

University College London

A thesis submitted for the degree of

Doctor of Philosophy

2019

I, Celine Kayal , confirm that the work presented in this thesis is my own. Where information has been derived from other sources, I confirm that this has been indicated in the work.

Abstract

Peripheral nerve injuries (PNI) result from traumatic injury, surgery or repetitive compression, and are reported in 3-5% of all trauma patients. The impact ranges from severe (major loss of sensory/motor function and/or intractable neuropathic pain) to mild (some sensory and/or motor deficits) and in both cases, is devastating for the patient. PNI affect ∼1M people in Europe and the US p.a. of whom 660,000 have surgery. PNI has high healthcare, unemployment, rehabilitation, societal costs and affects mostly young people. The current surgical practice for nerve gaps >3 cm is to bridge the site of injury with a graft taken from the patient. However, this involves additional time, cost and damage to a healthy nerve, limited supply, and unsatisfactory functional recovery (50% of the cases). For these reasons, research has focused on developing artificial nerve conduits to replace grafts, but to-date those available for clinical use do not match and/or exceed the functional performance of the autograft.

This project develops a rational basis for promoting neurite growth through tissue-engineered conduits for peripheral nerve repair, by exploiting the response of cells to spatial variations in mechanical properties of conduits to inform their design. This is achieved through an interdisciplinary approach, that combines in vitro experimentation with mathematical modelling. First of all, the mechanical and structural properties of RAFT-Stabilised collagen gels (RsC) are explored, physiologically coherent RsC stiffness gradients are fabricated and characterised as well as the neuronal response to them. Finally, a predictive framework to inform the design of nerve conduits is parameterised and tested using experimental results and literature.

The use of this multidisciplinary approach can help tissue engineers in the development of novel tissue repair solutions, as well as informing mathematical models of neurite behaviour which can contribute to the design process.

Statement of Originality

In Chapter 2, originality is claimed for the mechanical characterisation of sciatic rat nerve tissue under dynamic testing, not reported in the literature yet. The harvesting of sciatic rat nerve was carried out by Richard Bartlett. Mechanical testing and data analysis were done by myself.

In Chapter 3, originality is claimed for the mechanical characterisation of collagen gels made using RAFT-Stabilisation, a commercially-available method for fabricating gels for tissue engineering applications, developed in 2015. As protocols to define and compare the mechanical behavior of RAFT-stabilised collagen gels have not standardised across the field, this Chapter presents a thorough mechanical characterisation in the three dimensions under dynamic testing.

In Chapter 4, originality is claimed for the development, optimisation and characterisation of a new reproducible protocol to fabricate stiffness gradient of collagen type I gel. As it is challenging to control the rigidity of substrate, the development of a new method to fabricate defined-stiffness gradient profiles with hydrogels is necessary.

In Chapter 5, originality is claimed for the use of neural cells to study durotaxis. As for the peripheral nervous system, studies investigating mechanotaxis used substrates with spatially uniform stiffness only and for studies investigating durotaxis, other type of cells have been used. For the first time, the mechanosensitivity of neural cells on physiologically relevant stiffness gradients is explored.

In Chapter 6, originality is claimed for the development of a 2D discrete computational model based on a specific data set for durotaxis, through which it is possible to obtain neurite elongation influenced by the mechanical properties of a substrate. The predictions obtained in this Chapter informs the next experimental design and demonstrates the

importance of the use of the feedback theoretical-experimental loop to accelerate progress in the design of artificial nerve tissue replacements.

All Figures, unless stated otherwise in the respective caption, were created by myself. Standard two-dimensions plots were generated using Matlab (2018a The MathWorks, Inc., Natick, Massachusetts, US.) or PRISM (GraphPad Software, Inc.) The study in Chapter 3 has been submitted for publication and the work reported in Chapter 4-5 is also under submission.

Impact Statement

Peripheral nerve injury, leading to loss of sensory and motor function, occurs through traumatic and iatrogenic events and the use of a nerve graft is the current clinical solution. Peripheral nerve tissue engineering researchers have been exploring various strategies to develop autograft alternatives. The importance of mechanical and structural properties of the substrate environment on cell behavior has been highlighted. Cells are able to detect and respond to mechanical cues from their environment and tissue engineers are investigating new material strategies to support and influence cell behavior. Furthermore, the mechanical resistance of materials to surgical handling and their mechanical similarities to the host site are to be considered in tissue engineering to maximise their efficiency.
This thesis provides scope for the development of optimised nerve guidance conduits using stiffness gradients to control neuronal regeneration. In addition, it improves fundamental understanding of the mechanosensitivity of neural cells.

In this work, the mechanical properties of fresh rat nerve tissue were characterised, as well as a biomimetic material, RAFT-Stabilised collagen gel, with potential to be used as a nerve repair substrate. Quantifying the mechanical properties of the target tissue helped in the development of a new protocol to create physiologically coherent stiffness gradients to study cell durotaxis. The investigation of cell mechanoresponse to the defined-stiffness gradient profiles provides important insight into more fundamental behavior. The created gradients induced neural cell changes in behavior and the specific experimental data set obtained informed a computational model to explore various gradient architectures. The combination of experimental and computational models enables predictions for the development of the next generation of nerve guidance conduits.
Progress in this area using a multidisciplinary approach can help to refine our understanding of fundamental cell behavior, optimise nerve repair solutions and hopefully can be beneficial to accelerate clinical translation.

This thesis is dedicated to my parents, Matthieu,

... and Jamila.

Acknowledgements

Firstly, I would like to thank my supervisors Dr Rebecca Shipley and Dr James Phillips for their endless support, motivation and guidance throughout my years as part of their team. They have been true mentors for me, I could not have hoped for better supervision, and for this I will always be grateful.

I would like to thank funding support from the UCL Dean's Prize from UCL, Mechanical Engineering Department for supporting this work.

I am also grateful to the people in the office 509 who made this challenging journey amazing. They provided a perfect combination of an intellectual, fun, supportive and friendly environment, alongside the team in the lab at the Eastman Dental Institute and at the School of Pharmacy. I would like to thank all the staff and students I have worked with as they helped me discover various aspect of research. I would like to thank Dr Emad Moendaarbary and Richard Thorogate at the London Centre for Nanotechnology for their precious help and expertise regarding the AFM, including training, and trouble shooting.

Furthermore, I would like to thank especially some of my colleagues: Mat, Paul, Reza, Pierre, Simao, Antonio, Adam, Caitriona, Celia, Mariann, Rachael, Richard, Kulraj. I have been extremely lucky to have met them and they all, in different ways, shaped the way I do and approach research.

Last but not least, I would like to thank my friends and family. To my flatmates, my London family, Ilinca and Metal for making my life in London so perfect, and to my parents, Marie-Christine and Samer Kayal and my brother, Matthieu for their love and emotional support during this time.

Thank you everyone !

Contents

List of Figures

List of Tables

Chapter 1

General Introduction

Damage to the peripheral nervous system is common and highly debilitating for the patient (Sexton et al., 2012). It can cause limb dysfunction and unbearable neuropathic pain, disrupting professional and social life. These traumas can be acquired due to sport activities, automobile accidents or even during surgical procedures causing serious nerve damage (Houschyar et al., 2016; Dodla et al., 2019). Patients, mostly young males (Ciaramitaro et al., 2010), with severe peripheral nerve injuries usually undergo a surgical intervention to encourage nerve regeneration and to help improve functional outcomes.

The concept of the nerve was first described in the second century A.D, by Galen (Kaplan et al., 2009a; Griffin et al., 2013) but it was not until the 7^{th} century that Paulus of Aegina, a military surgeon, described the first attempt to repair severed peripheral nerves with wound closure (Griffin et al., 2013). This lead, in the 19^{th} century, to the first nerve graft reported by the surgeon Eduard Albert (Schmidt, 1993). Since then, nerve grafting has become the gold standard procedure, and uses either nerve harvested directly from the patient (autografts), or decellularised tissue from a donor (acellularised allografts) (Moore et al., 2011) for patients with inadequate autologous nerve donor tissue. However, this reference standard is often unsatisfactory (Sexton et al., 2012) in terms of functional recovery and comes with various limitations such as donor site morbidity, the need of a second incision site,

and the limited supply of tissue (Siemionow and Brzezicki, 2009; Muheremu and Ao, 2015). Therefore, there is interest in developing peripheral nerve repair strategies that match or exceed the performance of the graft (Muheremu and Ao, 2015) and can be translated to the clinic (Mobini et al., 2017).

This medical challenge attracts much attention and nerve conduits have been investigated as an alternative to the nerve autograft. Cells of the peripheral nervous system are mechanosensitive, i.e. the cells sense and adapt their behaviour as a function of mechanical stimuli, e.g. the stiffness of the substrate. At the moment, tissue engineering is an appealing research field for peripheral nerve repair, given the vast number of biomaterials available, and the growing technologies to control nerve conduit mechanical, structural and biochemical properties to guide neurite growth. Therefore mechanical properties of the cell environment are considered as a key control parameter for the development of artificial nerve tissue conduits. However, there is no overarching consensus on how to spatially combine and arrange physical and chemical cues within a conduit to achieve a distinct functional outcome (see Figure 1.1).

Trial-and-error experimental approaches provide a platform to gain a better understanding of fundamental mechanisms that underpin nerve repair, however they come with limitations due to the extensive number of experiments that would be required to test all options in the laboratory; this is prohibitive in terms of time and cost, and due to the requirement for extensive, ethically challenging animal experiments. Mathematical modelling provides a very useful and complementary tool with the opportunity to run a comparatively larger number of scenarios in order to direct and refine the experimental work. Combining experimental and computational approaches would contribute significant advantages to the optimisation of conduit design (Coy et al., 2017).

It is important to understand the anatomy and the mechanics of nerves to develop engineered solutions whose properties closely match the physiological environment

within a nerve in order to maximise the chance of peripheral nerve repair. First of all, this Chapter provides an overview of the peripheral nervous system, the types of injuries encountered and the biology of nerve regeneration.

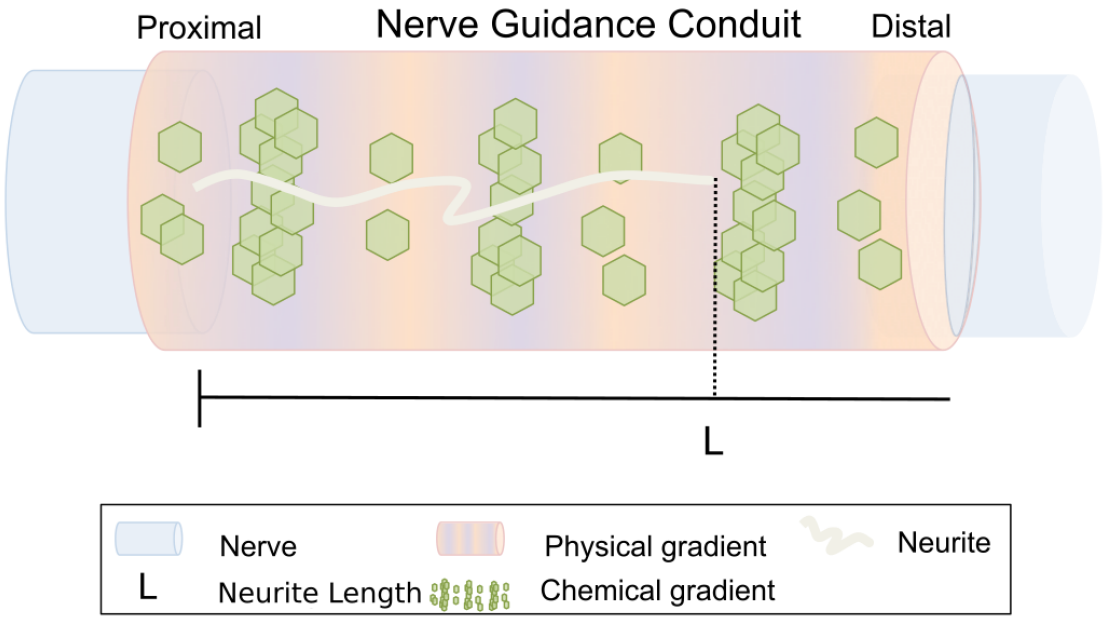

Figure 1.1: Schematic of a nerve guidance conduit combining overlapping growth factor and stiffness gradients in the conduit on nerve outgrowth, L.

1.1 Peripheral nervous system

The peripheral nervous system (PNS) is the part of the nervous system external to the brain and the spinal cord. It is divided into the somatic nervous system, the autonomic nervous system, and connects the central nervous system (CNS) to the organs, skin and limbs, and stimulates muscles to contract (Moskow et al., 2018). This important connective role is performed by the sensory neurons, stimulus receptors, and the motor neurons, which respond by causing an action. Both types of neurons are electrically excitable cells, processing and transmitting information through electrical and chemical signals (Davis, 1926).

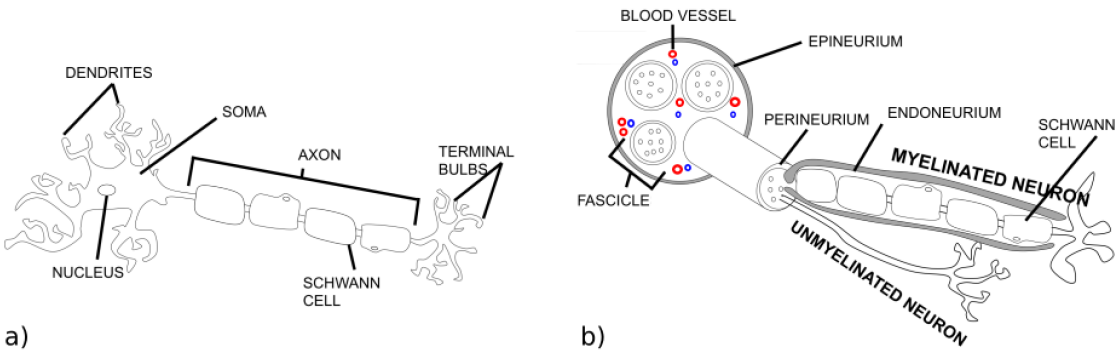

Figure 1.2: Schematic drawings of a) a neuron, and b) a peripheral nerve trunk.

1.1.1 The neuron

A neuron has a cell body, called the *soma*, dendrites and an axon (see Figure 1.2a). The axon can be myelinated or unmyelinated depending on whether it is encapsulated by a myelin sheath (Geuna et al., 2009). This myelin sheath provides insulation to enable efficient electrical conduction of a nerve impulse (Waxman, 1977), conducts the action potential much more rapidly (Gaudet et al., 2011), and is produced by Schwann (or neural support) cells (Geuna et al., 2009).

1.1.2 The nerve

A nerve, as represented in Figure 1.2b, is made up of bundles of nerves fiber called fascicles. Each nerve fiber and the surrounding Schwann cells are supported by collagenous endoneurium (Geuna et al., 2009; Kaplan et al., 2009b). The fascicle is delineated by a perineurium sheath and perineurial cell layer serving as a fluid barrier. Due to their structure, the epineurium and endoneurium provide elasticity to the nerve (Topp and Boyd, 2006). The epineurium is a loose connective-tissue that defines the nerve architecture. This tissue surrounds all fascicles and provides mechanical structural support for the nerve fascicles and blood vessels (Arslantunali et al., 2014; Grinsell and Keating, 2014).

1.2 Peripheral nerve injury

Peripheral nerve injuries occur in approximately 2.8% of trauma patients (Deumens et al., 2010) and often result in significant reduction of sensory/motor functions and neuropathic pain (Arslantunali et al., 2014). In Europe, over 300,000 people suffer from peripheral nerve injury annually (Gu et al., 2011) and 360,000 in the United States (Dodla et al., 2019). The likelihood of full functional recovery following severe nerve lesions, like a transection of the neuronal axon, is often unsatisfactory (Deumens et al., 2010; Sexton et al., 2012) and can result in life-long disability, compromising quality of life for patients, with major socio economic impact (Deumens et al., 2010; Arslantunali et al., 2014). To understand the challenges encountered in terms of functional outcome after injury, it is critical to know the severity of the injuries and understand the natural repair process taking place at the injury site.

1.2.1 Peripheral nerve injuries classification

Unlike the CNS, the PNS is not protected by the skull and spinal cord and can easily get damaged when exposed to external forces. When the mechanical trauma exceeds physiological levels, cells and tissues can be damaged (Topp and Boyd, 2006, 2012). The functional outcome of a peripheral nerve injury depends on the severity of the nerve trauma (Rickett et al., 2011). The first peripheral nerve injury (PNI) classification was published in 1943 by Sir Herbert Seddon (Seddon, 1943), and injuries were separated in three categories :

- *Neuropraxia*
- *Axonotmesis*
- *Neurotmesis*

These injury categories are described in more detail in Table 1.1. These categories

give an anatomical basis for PNI. In 1951, Sunderland expanded these categories and sub-divided the Neurotmesis into three additional grades. This classification informs current treatment strategies (Sunderland, 1951; Sunderland et al., 1990), e.g. in the case of large gap injury (>1-2 cm) (Deumens et al., 2010), a clinical decision is made to operate.

Seddon	**Description and Wallerian Degeneration**	**Prognosis**	**Sunderland**
Neuropraxia	Intact axon, localised conduction disruption, No degeneration	Full recovery (in days/week) without surgery	Type I
Axonotmesis	Disruption of the axon with intact endoneurium, conduction failure, Wallerian degeneration	Variable recovery	Type II
Neurotmesis	Endoneurium disrupted, preservation of the perineurium, Wallerian degeneration	Incomplete recovery (60-80%)	Type III
Neurotmesis	Endoneurium and perineurium disrupted, preservation of the epineurium, Wallerian degeneration	Surgical procedure required	Type IV
Neurotmesis	Complete transection of the nerve trunk, Wallerian degeneration	Surgical procedure required	Type V

Table 1.1: The Seddon (Seddon, 1943) and Sunderland (Sunderland, 1951) classifications to describe peripheral nerve injuries.

1.3 Nerve regeneration

Following injury, the PNS has the ability to spontaneously regenerate (Eric Huebner and Strittmatter, 2010). In this Section, the physiological regeneration process will be described and its limitations will be discussed.

1.3.1 Physiological nerve regeneration

After a nerve injury leading to axonal disruption or complete transection (Sunderland II-V, see Table 1.1), degenerative changes are initiated at the injured site within a few hours and this process is known as "Wallerian degeneration" (see Figure 1.3) (Deumens et al., 2010; Gaudet et al., 2011; Arslantunali et al., 2014). After two weeks, at the distal part of the transected area, the Schwann cells surrounding the axons stop producing myelin and the axons detach from their myelin sheath. Moreover, axonal, myelin and tissue debris are phagocytosed by Schwann cells and activated macrophages (Figure 1.3b) (Gaudet et al., 2011). Distal Schwann cells migrate towards the site of injury and form a solid supportive column called the Bands of Büngner which enable axonal regeneration (Figure 1.3c). During this process, regenerative axons from the proximal end encounter various chemical and mechanical guidance cues. These stimuli are provided by the surrounding substrate and the Schwann cells, and provide guidance cues to stimulate directed growth of neurons. The expected axonal growth is $\sim$1 mm.day^{-1} (Arslantunali et al., 2014). Axons regenerate towards the relevant target site. Initially, Schwann cells can remyelinate the smaller diameter regenerated axons with a thin myelin sheath (Gaudet et al., 2011). With time, the axon diameter is restored to normal dimensions (Nectow et al., 2012) (see Figure 1.3d and e).

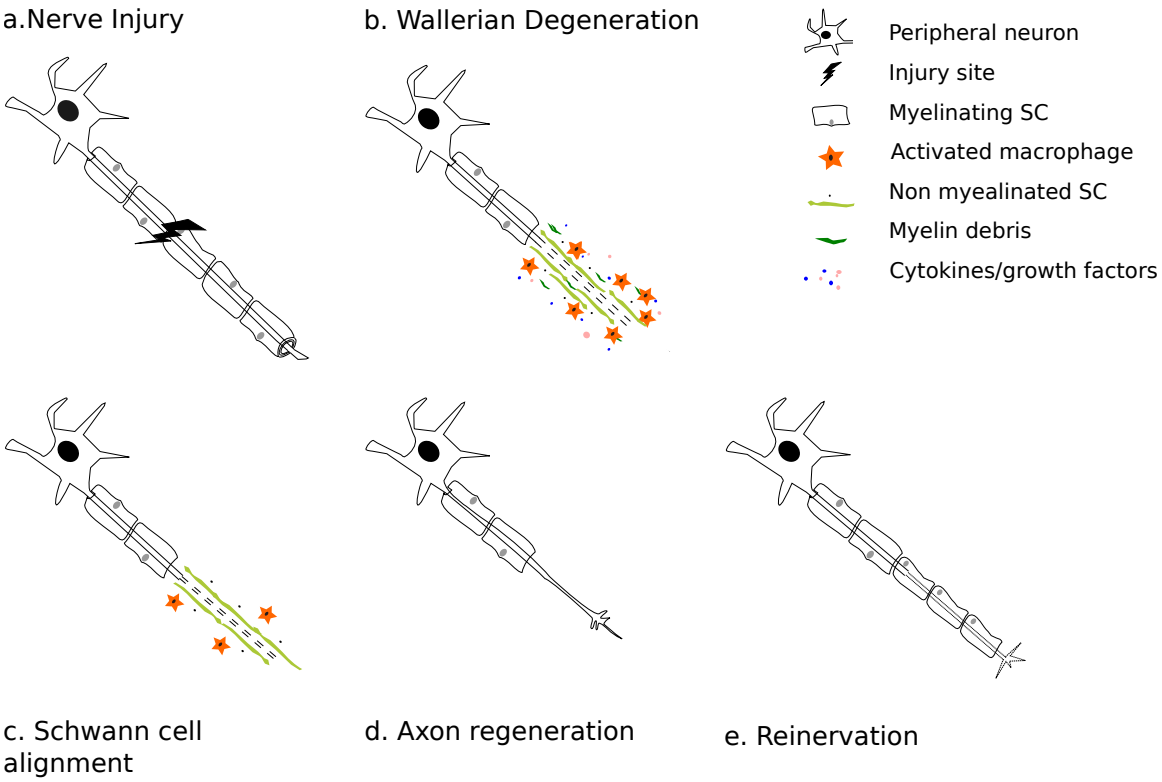

Figure 1.3: Schematic representation of the degenerative and regenerative events following a peripheral nerve injury. Within a week following a nerve injury, (a) Wallerian degeneration takes place: (b) Schwann cells stop producing myelin and debris are cleared by activated macrophages and Schwann cells. Distal non-myelinating Schwann cells migrate towards the site of injury, and (c) form a supportive substrate called bands of Büngner within the nerve basal lamina . Ultimately, axons begin to regenerate along the conduit formed by the bands of Büngner. Axonal growth is supported by physical and chemotactic stimuli provided by their surrounding environment and the Schwann cells (d) with a growth rate of $\sim$1 mm.day^{-1}. Then, the process of remyelination occurs. It is induced by the Schwann cells wrapping around the regenerating axons. Axonal growth continues until it reaches the target site of reinnervation (e) and the axonal diameter increases up the original dimensions. Adapted from Gaudet et al. (2011).

1.3.2 Nerve regeneration limitations

Even if a natural regenerative process occurs after a severe nerve injury (Sunderland II-V, see Table 1.1), it is frequent to observe aberrant axon sprouts leading to the formation of a neuroma at the proximal nerve stump, and causing pain to the patient (Kaplan et al., 2014). In most cases for large gaps, poor regeneration is observed and this results in incomplete/absent target reinnervation leading to muscle atrophy (Nectow et al., 2012; Hart et al., 2008). After 12 to 18 months of deinnervation, irreversible muscle atrophy occurs (Campbell, 2008; Sexton et al., 2012). As physiological regeneration is a slow process, the time of muscle deinnervation and distance required to bridge more proximal injuries ($>$ 30cm for braxial plexus injuries (Sexton et al., 2012)) are severe limitations. Indeed, the target reinnervation is time-dependant and meanwhile the target organ is not stimulated. This leads to atrophy followed by death of the neural cell bodies (Hart et al., 2008). The misdirection of the regenerating axons towards inappropriate targets can also have a major impact on the success of the motor and sensory outcome (Siemionow and Brzezicki, 2009; Jiang et al., 2010; Yao et al., 2010; Pfister et al., 2011). Furthermore, the success of the regeneration is highly dependant on the surrounding extracellular microenvironment and its ability to provide sufficient guidance cues (Jianming Li et al., 2010). In addition to the chemical cues, physical stimuli are now known to direct and aid nerve regeneration, and the lack of mechanical support during regeneration limits the repair process (Jianming Li et al., 2010).

All these aforementioned problems and limitations are extremely challenging and contribute significantly to poor functional recovery (Gordon, 2015). In order to support better regeneration, clinical solutions, dependant on the severity of the injury, are available and are presented in the next Section.

1.4 Peripheral nerve repair solutions

For severe peripheral nerve injuries (see Section 1.2.1), a surgical procedure is required. The clinical treatment options vary depending on the size of the nerve gap induced by the injury. For small nerve transections (Zhu et al., 2018), the most common surgical repair solution is a direct end-to-end surgery (Figure 1.4a). It involves the coaptation of the proximal and distal parts of the transected nerve using fibrin glue or sutures (Dodla et al., 2019). This technique can not be extended to large gap injuries (>1 cm) as the tension induced by the sutures results in inhibition of nerve regeneration and promotes the development of scar tissues (Fawcett et al., 1990; Siemionow and Brzezicki, 2009).

For peripheral nerve injuries larger than 1 cm, the clinical gold standard involves implanting an autograft into the injury site. A nerve graft is harvested from another site (Figure 1.4b), often the sural nerve, a sensory nerve in the calf region of the leg. It is used as it is a readily available, immunogenically inert scaffold which provides mechanical support to direct the sprouting axons toward the distal injury site, as well as providing growth factors and viable Schwann cells (Ray and Mackinnon, 2010). The graft is also permissive to the diffusion of chemical cues secreted by the distal part to guide/promote regeneration (Gu et al., 2011). However, as mentioned previously, autologous nerve grafts come with major disadvantages such as the requirement for a double surgery, donor site morbidity, a limited amount of nerve supply, nerve size and mismatch between sites, and possibility of painful neuroma formation (Hu et al., 2016; Sarker et al., 2018). In addition, nerve grafting is often unsatisfactory for the patient in terms of functional recovery (Sexton et al., 2012). The number of disadvantages associated with the current clinical solutions have motivated the investigation for developing alternative treatments. Tissue engineers are working on the development of nerve guidance conduit (NGC) to promote nerve regeneration and their main challenge is to achieve the functional outcome of nerve grafts and bridge the gap.

1.4.1 Tissue Engineered Nerve Guidance Conduits

The field of biomedical engineering contributes to the design, manufacture, storage, and application of synthetic conduits to overcome the limitations associated with autologous nerve grafts (Muheremu and Ao, 2015). Due to limitations of the autograft, neural tissue engineering research has focused on the development of nerve guidance conduits, tubular structures, that are implanted to the injury site to guide neurite growth (Figure 1.4c). The purpose of a nerve guidance conduit is to bridge the gap between the proximal and distal part of the sectioned nerve. These nerve scaffolds are often designed to mimic the architecture and extra-cellular matrix (ECM) of a healthy nerve. Their goal is to guide the axon sprouts to reach the distal injury site, by providing an adequate mechanical and chemical support to protect and stimulate the growing neurons (Thomson et al., 2017b). In addition to the crucial cellular, molecular and biomaterial components required, these scaffolds have to be biocompatible and biodegradable (Ratner et al., 2004; Stang et al., 2005). Permeability of the scaffold to ensure the sufficient exchange of gases and nutrients, is necessary (Hollister, 2005), and appropriate stiffness and flexibility have to be considered to support the regeneration and physical handling (Subramanian et al., 2009).

Intensive research is working towards an effective nerve guidance conduit (NGC) by investigating these aforementioned chemical and mechanical cues. They utilise biomaterials that support desired cellular functions and display appropriate mechanical and physical characteristics (Sarker et al., 2018). There is a large range of biomaterials available, e.g. synthetic and natural polymers are tested to generate improved NGC. As an example, the most common materials used for neural tissue engineering are chitosan and collagen among natural polymers, and polycaprolactone (PCL) and Poly(D,L-Lactide-Co-Glycolide) (PLGA) for the synthetic polymers (Barbarisi et al., 2015; Sensharma et al., 2017). Further discussion around biomaterials for neural tissue engineering is given in Section 1.5.1.

The ultimate goal is to reproduce the properties of the ECM and provide a favourable biochemical environment for regeneration. The interaction between these biomaterial and biochemical components and cells requires an in-depth understanding which in turn will aid the design of repair conduits.

Topographical structure, mechanical and chemical characteristics either combined or isolated are the main features that have been investigated in the literature. Recent studies have demonstrated various material processing techniques. For example, the fabrication of a multi-channel NGC to test the importance of linear and physical cues to guide regeneration across the lesion site (Pawelec et al., 2018), or spiral NGC with aligned nanofibers wrapped within a tube to create a multi-lumen conduit (Peng et al., 2017; Chang et al., 2018). Filament-loaded scaffolds have shown the importance of topography (e.g. a yarn structure) combined with biological cues (e.g. a laminin coating) (Wu et al., 2017). They have been developed to imitate nerve fascicular architecture and promote SC migration/ proliferation and guidance of neurite extension. Ryan et al. (2017), also combined physical and chemical cues to develop porous matrix loaded conduits supporting SC attachment and axonal outgrowth.

To conclude, multiple designs of NGC have been explored in order to promote axonal growth. Factors such as topography (Thomson et al., 2017a), stiffness (Willits and Skornia, 2004; Evans et al., 2018), porosity (Ryan et al., 2017), supporting cells (Hoke, 2006; Phillips, 2014), growth factors (Moore et al., 2006; Carballo-Molina and Velasco, 2015), and electrical simulation (Martin et al., 2014; Senger et al., 2018) can impact nerve regeneration and may be considered in the design of an optimal NGC (Sarker et al., 2018; Dodla et al., 2019; Jia et al., 2019) (see Figure 1.4). In the next Section, these key components, important for the development of an NGC that would mimic autograft features, will be described.

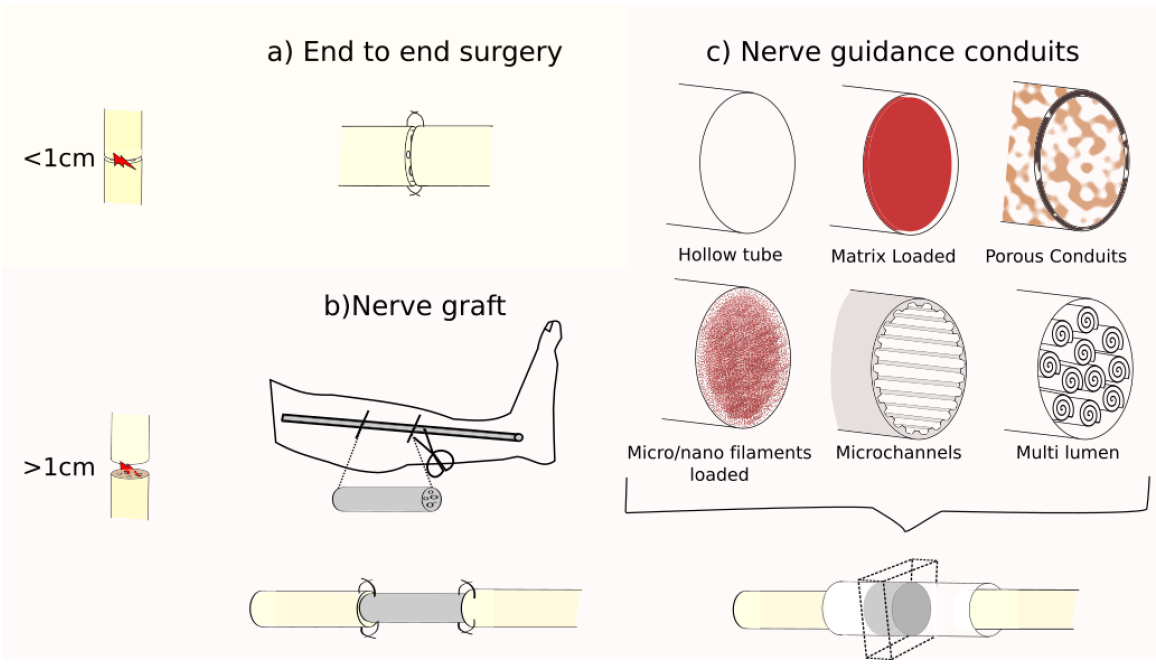

Figure 1.4: Schematic of the current clinical nerve repair solutions and the nerve guidance conduits investigated, using various guidance cues, to improve peripheral nerve repair.

1.5 Development of NGCs

1.5.1 Scaffold materials

The choice of scaffold biomaterial is generally the first step when designing a conduit because it forms the biological substrate. It is important that the chosen material is neither toxic nor triggers an immune response. Additionally, it should be biodegradable to avoid both compression and constriction around the regenerated nerves, chronic inflammation, as well as a second intervention to remove any non-degrading conduit. The optimal mechanical properties, and physical properties such as permeability, flexibility, and swelling are important factors that have an influence on the regeneration area, tissue interaction, effectiveness of supporting cells, and any drug diffusion/release (Subramanian et al., 2009).

Biomaterials are widely used in regenerative medicine and for the development of NGC to promote nerve regeneration (Nectow et al., 2012; Sensharma et al., 2017). They can be biopolymers, e.g. collagen, laminin, fibronectin, chitosan, or synthesised polymers, e.g. polyacrylamide (PAAm), poly(ethylene glycol)(PEG) (Carballo-Molina and Velasco, 2015; Du et al., 2018), gelatine (Sarker et al., 2018). Tissue engineers are focusing their work on numerous essential properties. The material must be biocompatible, permeable and not trigger an immunologic reaction. It should have controllable mechanical features and a degradation profile as well as the ability to encapsulate drugs and growth factors (Deumens et al., 2010; Gu et al., 2011). Natural materials tend to vary and can generate an immune reaction as they may contain antigenic components (Holmes, 2002; Carballo-Molina and Velasco, 2015). For this reason, synthetic material are widely investigated, however, they are not always compatible with the host site (Carballo-Molina and Velasco, 2015).

The materials found by the author to be currently approved by the Food and Drug Administration (FDA) and used for nerve guidance conduits are type I collagen, porcine small intestine submucosa, polycaprolactone (PCL), polyvinyl alcohol (PVA) and polyglycolic acid (PGA) (Kehoe et al., 2012) and more recently chitosan, with Reaxon Nerve Guide, the first chitosan tube approved for clinical use (Bąk et al., 2017).

Nevertheless, novel materials have been developed, optimised and multiple configurations in scaffolds have been investigated. Some materials known to induce cell changes in behaviour are described in Section 1.6. Having introduced examples of the materials currently used in studies to repair peripheral nerve injuries, the structural arrangement of these materials will be discussed next.

1.5.2 Scaffold architecture

The scaffold represents the main architecture of a nerve guidance conduit. It mechanically and physically supports the regenerative cells (Carballo-Molina and Velasco, 2015). The scaffold provides a substrate for cell adhesion and helps to direct axonal sprouting from the proximal to the distal injury site by containing and allowing diffusion of growth factors secreted by the distal stump (Gu et al., 2011). As shown in Figure 1.4c, various type of scaffold architectures have been investigated as an alternative to autografting for peripheral nerve injury repair. The structure of these scaffolds have greatly improved in the recent years (Du et al., 2018). The main parameters which have been investigated are the physical and mechanical properties of the substrate (Gentleman et al., 2003; Willits and Skornia, 2004; Mi et al., 2010; Bracaglia et al., 2017; Peng et al., 2017; Kim et al., 2018), cellular alignment within the biomaterial to guide regeneration (Georgiou et al., 2013), the topography (Hoffman-Kim et al., 2010; Kuo et al., 2012; Peng et al., 2017; Pawelec et al., 2018), overall porosity and the size of the pores (Jiang et al., 2010; Ryan et al., 2017; Tao et al., 2017) to

promote the infiltration of blood vessels and nutrient transport to support Schwann cell proliferation and axonal regeneration. Fibrous nerve conduits offer an increased surface area for cell attachment, permeability and also topographical cues (Rajangam and An, 2013).

To be translated from the lab to the clinic, tissue engineers must take into account various biomaterial dependant parameters when developing new designs. A neural scaffold must be easy to fabricate and sterilise, and easily implantable (Mobini et al., 2017). Furthermore, the stability over time of the implanted scaffold is to be considered as it impacts the biocompatibility and performance (Pawelec et al., 2018). These requirements should be met in order for a NGC to be successful.

1.5.3 Growth factors

Neurotrophic factors are cell-produced small proteins and peptides which play an important role in the survival, migration, proliferation and differentiation of various cells involved in nerve regeneration (Allen et al., 2006). The arrangement of trophic factors along a nerve conduit is continuously affected by the diffusion process. In addition, the supportive action in cellular production of growth factors from the distal part may also decline as a function of time (Höke et al., 2002). For this reason, there is widespread interest in investigating the optimal trophic factor distribution along a NGC and the delivery method for a time-controlled supply. Four different growth factors are commonly used: nerve growth factor (NGF), brain-derived neurotrophic factor (BDNF) and neurotrophin 3 and 4 (NT-3 and NT-4). They initiate and contribute to the growth and cell survival response. Moreover, these molecular players have been characterised and information on their properties is readily available, e.g. biological activity, half lives, potential toxicity. Indeed, cellular guidance due to chemical cues - known as *chemotaxis*- is well studied and researchers use experimental approaches (Cao and Shoichet, 2001; Lee et al., 2003; Kapur and Shoichet,

2004; Moore et al., 2006; Carballo-Molina and Velasco, 2015) and mathematical modelling (Tranquillo and Lauffenburger, 1987; Jabbarzadeh and Abrams, 2005; Tse et al., 2007) approaches to elucidate the underlying mechanisms.

1.5.3.1 Nerve growth factor

Nerve growth factor (NGF) is a neurotrophic factor, the first to be identified in the 1950s by Rita Levy Montalcini. It is involved in the regulation of PNS neuron growth, maintenance, survival and differentiation (Aloe, 2004, 2011). The regulation of NGF during peripheral nerve injury has been characterised (Heumann et al., 1987; Fine et al., 2002; Allen et al., 2006; Tse et al., 2007; Subramanian et al., 2009) and it has been shown that NGF has the capacity to help nerve regeneration (Terenghi, 1999; Fine et al., 2002; Tse et al., 2007). The pharmacokinetic properties of NGF have been defined and are valuable data for framework prediction (Tria et al., 1994). NGF is a chemical with the potential to modulate neuronal behaviour (Behar et al., 1994) and it has been shown that neurites respond to chemotactic gradients in NGF concentration (Cao and Shoichet, 2001; Kapur and Shoichet, 2004; Rosoff et al., 2004; Tse et al., 2007). To find an ideal arrangement of NGF along a conduit requires consideration of the NGF concentration (e.g. avoid critical concentration down regulating neurite growth) (Cao and Shoichet, 2001), diffusion (Tse et al., 2007) and the half life of this chemical.

1.5.3.2 Brain-Derived Neurotrophic Factor

Brain-derived neurotrophic factor (BDNF) is a growth factor which supports the survival of motoneurons (Sendtner et al., 1992), whilst promoting growth of motor and sensory neurons (Braun et al., 1996). BDNF has a shorter half life than NGF. This property should be taken into account of in defining the scaffold configuration, if BDNF is used as a guidance cue (Sakane and Pardridge, 1997) in combination with

NGF.

1.5.3.3 Neurotrophin 3 and 4

Neurotrophin 3 (NT-3) and neurotrophin 4 (NT-4) initiate and contribute to the survival response and differentiation of sensory and motor neurons (Davies et al., 1993; Yin et al., 2001). NT-3 may be involved in the maintenance of the adult nervous system and have been shown to help neurogenesis (Hagg, 2009). For example, a previous study has shown an increase in the number of myelinated axons using NT-3 spread throughout fibronectin mats and implanted into a 10 mm rat nerve gap (Sterne et al., 1997). Studies using NT-4 have also shown a possible amelioration of the regeneration process of a severed peripheral nerve (Yin et al., 2001). For these reasons, neurotrophin 3 and 4 can be eventually considered for use as chemical cues along a nerve conduit.

These different trophic factors could be used separately or in combination to help to improve the regeneration of different injuries, and even as a basis for treatment personalised to each patient, i.e. adapted to their type of injury.

To conclude, neurotrophic factors have been shown to be an efficient solution to increase the number, range, branching, length and growth rate of regenerating axons (Cohen-Cory and Fraser, 1995; Lentz et al., 1999; Cao and Shoichet, 2001). These neurotrophic factors can also work in complementary fashion (Maisonpierre et al., 1990). Thus, it is important to know how the biochemical cues impact neuronal behaviour to propose a drug efficient configuration for NGCs.

1.5.4 Growth Factor Delivery Configuration

Due to the numerous beneficial properties of growth factors, several studies have focused on improving the delivery of these proteins via tissue engineered conduits. This understanding of the different options could be exploited to regulate the spatiotemporal arrangement of growth factor along the conduit to support nerve regeneration.

The key features which can be controlled are the dosage, the arrangement of chemical along a conduit (taking into account factors such as diffusion, elimination, half lives, cell production/consumption), the duration of the therapy and the properties of the vector used for delivery (Pfister et al., 2007; Tayalia and Mooney, 2009). To date, NGC configurations have been tested with growth factors trapped directly in a hydrogel matrix (Terris et al., 2001; Lee et al., 2003; Midha et al., 2003). Other work has investigated release systems using microspheres, made out of biodegradable polymers, loaded with growth factors either in suspension in the conduit or dispersed in the hydrogel matrix for peripheral nerve regeneration (Xu et al., 2002; Rosner et al., 2003; Tabata, 2003; Xu et al., 2003). Support cells like Schwann cells (see Section 1.5.6) can also be considered as another source of growth factors. For instance, they can be injected in the nerve guidance conduit (Ansselin et al., 1997), or the matrix can be filled with glial cells (Guenard et al., 1992) that will then produce diffusible factors. These investigations give us the possibility to control the spatial distribution of growth factors, keeping in mind that they diffuse and are taken up, thus their spatial distribution varies as a function of time.

1.5.5 Supporting cells

Glial cells are non neuronal cells in the nervous system and are a critical cellular component for nerve regeneration and maintenance of the nervous system (Georgiou

et al., 2013; Gu et al., 2011). They are responsible for the maintenance of extra cellular homeostasis (buffer the pH, regulate ion and protein concentrations) and are involved in neuronal information processing (Noback et al., 2005; Bozkurt et al., 2009; Yao et al., 2010). Their incorporation in NGCs has been investigated due to their abilities to promote axon regeneration. They provide support and protection for neurons.

1.5.6 Schwann cells

Schwann cells are the principal glial cells in the PNS. They are wrapped around neurons and help in the myelination of the axons. Optimising migration and alignment of Schwann cells and other support cells, within a nerve gap, is critical for regeneration success as they play both structural and functional roles (Son and Thompson, 1995; Bozkurt et al., 2009; Georgiou et al., 2013). These cells are important as they provide a source of growth factors, crucial for neuronal support (Taniuchi et al., 1986; Hoke, 2006), such as NGF and BDNF (Gu et al., 2011) (see Section 1.5.3). In response to a peripheral nerve injury, Schwann cells undergo phenotype changes to activate their phagocytic activity, beneficial to support axon degeneration/regeneration (Hoke, 2006; Franze and Guck, 2010; Kaplan et al., 2014) (see Section 1.3). Due to their specific properties beneficial to peripheral nerve regeneration (Son and Thompson, 1995), they have been incorporated in engineered nerve scaffolds (Evans et al., 2002; Rajangam and An, 2013) to promote the formation of bands of Büngner and release growth factor. Therefore, investigations on Schwann cell alignment are significant. Georgiou et al. (2013) developed a technique to fabricate engineered neural tissue -EngNT-, a tissue engineered construct with aligned Schwann cells. However, to optimise their action on neurite regeneration, the behaviour of Schwann cells in response to chemical and mechanical stimuli is still under investigation (Evans et al., 2018).

Figure 1.5 summarises the key parameters desired for the design of artificial nerve

guidance conduits. As described in Section 1.5.3, for the development of nerve guidance conduits, the use of chemical guidance cues has been largely explored for the regulation of the neurite growth and regeneration (Tabata, 2003; Tayalia and Mooney, 2009; Steffens et al., 2018). However, there is increasing interest in mechanical properties of the surrounding environment and scientists are exploring the response of neuronal cells to various mechanical stimuli. The next Section will focus on the mechanical properties of biomaterial substrates for use in the development of NGCs.

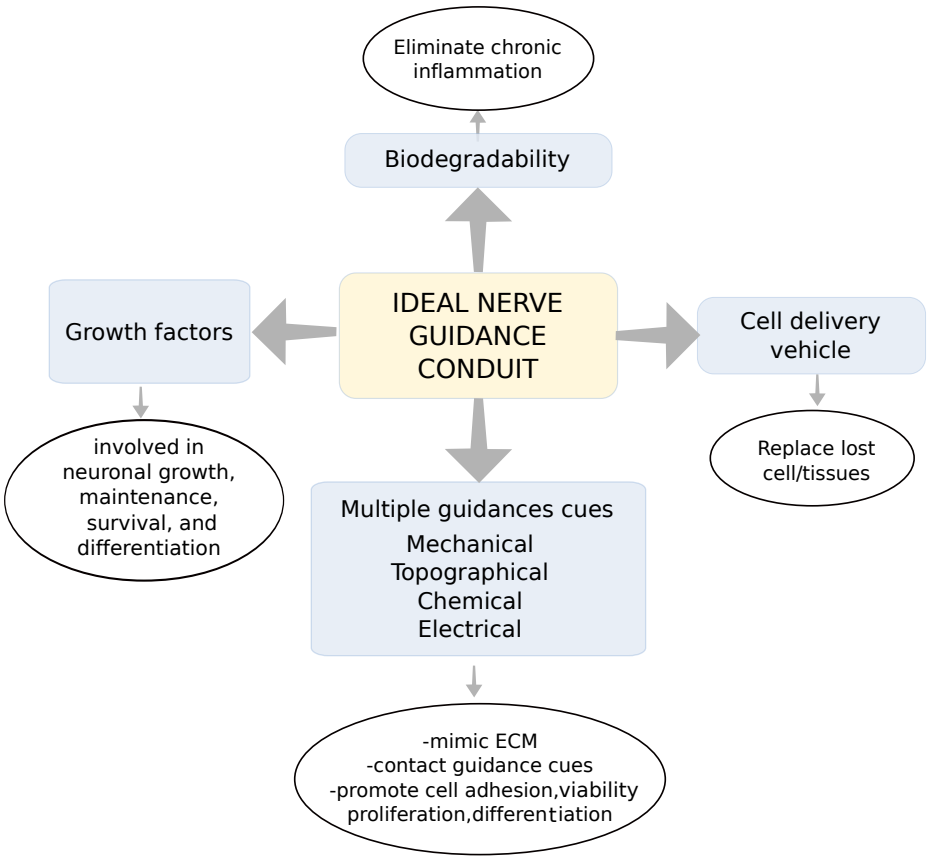

Figure 1.5: Key parameters to take into account for the development of the optimal nerve guidance conduit. Adapted from Subramanian et al. (2009).

1.6 Substrate mechanics for the development of nerve guidance conduits

Understanding of how neural and glial cell behaviour is influenced by their mechanical environment remains largely understudied and incomplete. Nonetheless, the investigation of the evidenced mechanosensitivity of these type of cells to their environment seems promising to help in designing the future generation of NGC. Accordingly, from now on, the work in this thesis will focus on tissue-mechanics and cell responses to it. This Section will describe the current understanding of PNS mechanobiology, the materials and the stiffness environments reported in tissue engineering to study neural cell mechanosensitivity in order to understand cell response and improve nerve repair solutions. Last but not least, the relevant mechanical tests available and used in the field to characterise material mechanical properties and help in the control/characterisation of mechanical features for the development of new materials will be discussed.

1.6.1 Mechanobiology

Neuronal cells are responsive to chemical and topographical cues and these phenomena are known as chemotaxis and haptotaxis respectively (Steffens et al., 2018). However, an increasing number of studies are investigating the cell response to mechanical guidance cues (Krieg et al., 2019; Hassanzadeh et al., 2018), known as *mechanotaxis* (Franze et al., 2013; Roca-Cusachs et al., 2013). Mechanobiology focuses on the mechanical properties of cells and tissues at various scale, i.e. proteins, cells, tissues, and the impact of the mechanical forces on cell behaviour, e.g. differentiation (Kuo et al., 2012; Rammensee et al., 2017; Hadden et al., 2017), migration (Rosso et al., 2017d), neurite branching and orientation (Flanagan et al., 2002; Koser et al., 2016).

The past two decades have been crucial for the field of mechanobiology as technologies have brought into the market new tools for investigation, e.g. atomic force microscopy (AFM), magnetic tweezers, and traction force microscopy (TFM). In 2000, Lo et al. (2000), reported for the first time the migration of fibroblasts from a soft to stiff region of a collagen coated polyacrylamide substrate (Figure 1.6). This phenomenon of cells sensing and responding to a stiffness gradient was then termed '*durotaxis*', after the Latin *durus* (hard) and *taxis* (directional arrangement in response to stimulus).

Cell sensitivity to their environment, referred to here as mechanosensing, involves conversion of a mechanical stimulus into an electrochemical activity (mechanotransduction) responsible for a change in cell behaviour, referred to here as mechanoresponse (Franze et al., 2013). The link between the mechanical forces and the biological system response is still poorly understood for the PNS (Rosso et al., 2017c,d; Evans et al., 2018).

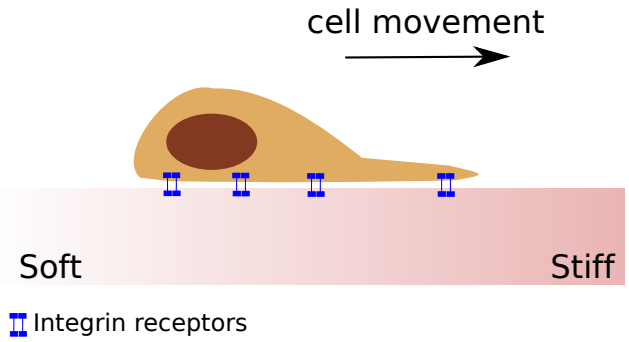

Figure 1.6: Durotaxis, guidance by stiffness gradient, which arise from the properties of the ECM. Adapted from Roca-Cusachs et al. (2013).

Reference	**Biomaterial**	**Stiffness range** kPa	**Stiffness gradient** kPa/mm	**Cell type**	**Mechanical test & stiffness type**
Wong et al. (2003)	Collagen coated PAAm	2.5-11	0.94	Human mesenchymal stem cells	Tensile test Young's Modulus
Zaari et al. (2004)	Collagen coated PAAm	3-40	12	Vascular smooth muscle cells	AFM Elastic modulus
Kloxin et al. (2009)	Fibronectin coated PEG	7-32	3	Myofibroblasts	Rheometry Storage modulus G'
Isenberg et al. (2009)	Collagen coated PAAm	1-8 	10 20 40	Vascular smooth muscle cells	AFM Elastic modulus
Cheung et al. (2009)	Fibrinogen coated PEGDA	0.7-50	74.7	Human foreskin fibroblasts	AFM Elastic modulus
Tse and Engler (2011)	Collagen coated PAAm	1-14	1	Human mesenchymal stem cells	AFM Elastic modulus
Kuo et al. (2012)	Poly(D-lysine) coated PAAm	-.3-1	47	Fibroblasts	AFM Elastic modulus
Sunyer et al. (2012)	Fibronectin coated PAAm	1-17 1-200 1-240	7.6 68 114	Fibroblasts	AFM Elastic modulus
Vincent et al. (2013)	Fibronectin coated PAAm	1-12 	1.4 10 275	Human mesenchymal stem cells	AFM Elastic modulus
Kidoaki and Sakashita (2013)	Gelatine sol	1-100	833	Fibroblasts	AFM Surface Young's modulus
Hartman et al. (2016)	Fibronectin coated PAAm or Laminin coated PAAm	10-170	72	Vascular smooth muscle cells	AFM Elastic modulus
Hadden et al. (2017)	Fibronectin coated PAAm	3.2-33	8.2	Human adipose-derived stem cells	AFM Surface young's modulus
Evans et al. (2018)	Laminin coated PAAm	0.05-0.55 0.71-12.6	0.04 0.95	Schwann cells	Rheometry Storage modulus G'

Table 1.2: Summary of current studies investigating durotaxis response to 2D stiffness gradient *in vitro*. (PAAm: Polyacrylamide; PEG: Poly(ethylene glycol) ; PEGDA: Polyethylene (glycol) Diacrylate).

1.6.2 Mechanical gradient

Both the CNS and PNS are mechanically heterogeneous tissues (Phillips et al., 2004; Mason and Phillips, 2011; Franze et al., 2013), thereby, neuronal and glial cells are likely to encounter regions with different stiffnesses. In the PNS, the microenvironment stiffness is likely to change during development (Franze et al., 2013; Rosso et al., 2017d), after an injury due to the development of scar tissues (Fawcett et al., 1990), or between different nerve regions (Phillips et al., 2004; Mason and Phillips, 2011).

For the past two decades, researchers have been studying cell durotaxis, the mechanosensitivity of cells to mechanical gradients (Lo et al., 2000). Multiple experimental approaches, on different cell lines, substrates and stiffness gradients have been investigated. This Section will describe these gradients and the resulting behaviour of cells growing on the surface of these type of substrates *in vitro*. A summary of the parameters used for each study is given in Table 1.2, a graphical representation of the stiffness gradients slope is plotted in Figure 1.7 and Figure1.8 is a diagram mapping the stiffness ranges for each study. Further details on the fabrication of these gradients will be given in Chapter 4.

Wong et al. (2003), Zaari et al. (2004) and Isenberg et al. (2009) investigated the behaviour of vascular smooth muscle cells (VSMCs) on collagen coated polyacrylamide gels (PAAm). Wong et al. (2003) used photopolymerisation and patterned filters (photomasks) to create a 0.94 kPa.mm^{-1}gradient slope. Zaari et al. (2004) and Isenberg et al. (2009) used microfluidic gradient generator combined with photopolymerisation and created gradient slope of 12 and [10-20-40] kPa.mm^{-1}, respectively. The VSMCs displayed durotaxis for the five gradients slopes created. They migrated preferentially toward stiffer substrates with a cell speed higher on softer substrate (Wong et al., 2003) and have shown more cell adhesion on a stiffer substrate (Zaari

et al., 2004). Tse and Engler (2011) used the photomask with radial grayscale pattern technique to create a collagen coated PAAm stiffness gradient of 1 kPa.mm^{-1}. They observed that human mesenchymal stem cells (MSCs) accumulated on stiffer regions, and independently of the local stiffness, migrated toward stiffer substrates. Cheung et al. (2009) also observed migration from compliant to stiff with fibroblasts on collagen coated PAAm substrate. They made their rigidity gradient using a microfluidic based lithography technique to micropattern cell-adhesive substrates (74.7 kPa.mm^{-1}). So, using PAAm gels offers the possibility to work with a wide range of stiffnesses using a large variety of techniques.

Furthermore, cells sense a stiffness gradient but are also responsive to the adhesion molecules involved in the binding between the cell surface and the ECM. These adhesion molecules can impact on cell response and therefore have been considered for the development of mechanical gradients. For instance, Hartman et al. (2016) have shown the importance of the choice of the adhesion molecule. They generated a PAAm stiffness gradient (72 kPa.mm^{-1}) using a surface tension based microfluidic device (UV initiated photopolymerisation) and compared fibronectin and laminin as coating on VSMCs. Migration of VSMCs toward stiffer regions was observed on fibronectin and no directed migration was observed on laminin. In comparison, Kloxin et al. (2009) used a fibronectin coated PEG gradient (3 kPa.mm^{-1}) and observed no significant directed cell migration nor effects on cell speed. On the other hand, Evans et al. (2018) worked with laminin coated PAAm gradients (0.04 and 0.95 kPa.mm^{-1}) on Schwann cells and observed morphological changes. Not only the stiffness gradient of the substrate, but also its surface adhesion ligands, impact substantially on cell behaviour. Furthermore, the behaviours observed are cell type dependant.

The study of durotaxis is challenging as it is difficult to uncouple the stiffness of a substrate from its pore size, ligand molecule coating density, and the thickness of the substrate itself (Roca-Cusachs et al., 2013). It is necessary to develop new assays

where the rigidity gradient is the only varying parameter to be able to compare studies. As mentioned in Section 1.6.1, recent studies have shown that SCs and PNS neurons are mechanosensitive (Rosso et al., 2017c,d; Evans et al., 2018). However the understanding of axon pathfinding (Koser et al., 2016), essential for the improvement of NGC, remain understudied.

In this thesis, it is proposed to use pure collagen gel to develop a controlled and characterised stiffness gradient, as pure collagen is the main component of PNS ECM. The next Section will describe the current knowledge about this material and the techniques that will be exploited for the experimental work of this thesis.

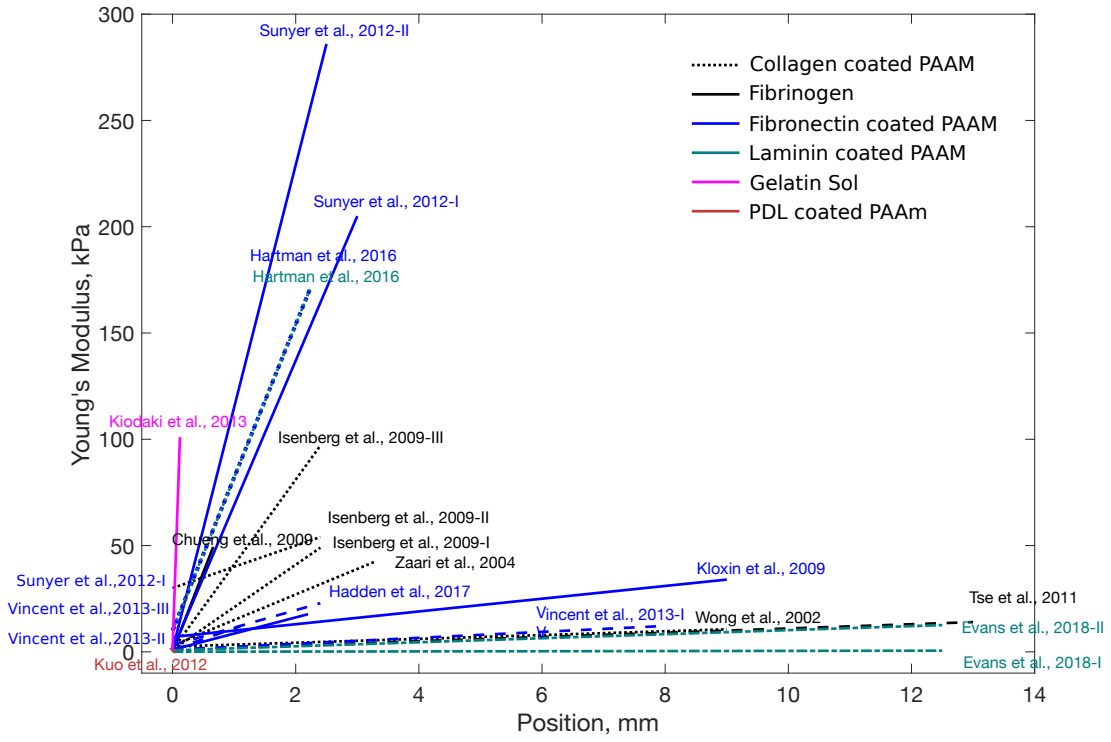

Figure 1.7: Graphical summary of the gradients and materials used to study durotactic behaviour *in vitro*, showing the Young's Modulus (kPa) as a function of the location on the samples (mm). Studies are categorised by material used, and the majority are using coated PAAm gels as it offers the possibility to work with a wide range of stiffness using a large variety of techniques (Wong et al., 2003; Zaari et al., 2004; Isenberg et al., 2009; Tse and Engler, 2011; Cheung et al., 2009; Hartman et al., 2016). This summary includes only 2D cultures.

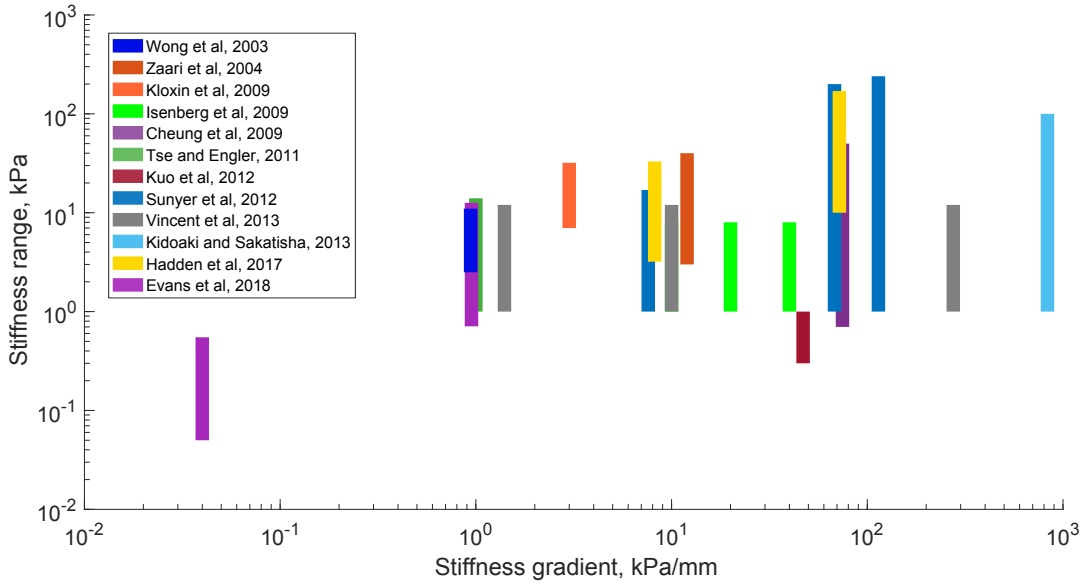

Figure 1.8: Diagram mapping the stiffness ranges (kPa) used to study durotactic behaviour *in vitro*, showing the modulus (kPa) range as a function of stiffness gradient (kPa.mm^{-1}. In this figure, the stiffness ranges are categorised by study (presented Table 1.2 and Figure 1.7).

1.6.3 Collagen gels

A wide variety of biopolymers have been used in NGC development and their mechanical properties have been studied extensively as they influence both cellular behaviour and tissue compatibility. Collagen is the major component of the ECM of the PNS and supports nerve function from the development of the PNS to adulthood (Koopmans et al., 2009). Collagen is known as a suitable cell substrate, is biocompatible (Neel et al., 2006) and has been explored extensively in the development of peripheral nerve repair solutions (Yang et al., 2004; Neel et al., 2006; Sundararaghavan et al., 2008; Stylianou, 2017; Ryan et al., 2017). To mimic the natural tissue mechanical and structural properties, collagen hydrogels used for tissue engineering purposes are often blended or cross linked in order to obtain replacement or repair solutions that would complement natural repair processes (Baranauskas et al., 1998; Banse et al., 2002; Krishnan et al., 2004), e.g. for wound healing and regenerative purposes (Ma et al., 2003; Yang et al., 2004; Madhavan et al., 2009; Tierney et al., 2009; Neel et al., 2013; Davidenko et al., 2015). However, without modification of the fully-hydrated collagen gel structure, there tends to be a mechanical and structural disparity compared with many mature body tissues, e.g. hydrated collagen gel is mechanically very weak (Brown et al., 2005; Saraf et al., 2007; Mi et al., 2010). Thus, the properties of collagen gels should be tuned to be specifically appropriate for the development of NGC.

A variety of methods exist to modify the mechanical properties of collagen, e.g. cross linking using enzymes or irradiation (Zaari et al., 2004; Sundararaghavan et al., 2008; Isenberg et al., 2009; Kidoaki and Sakashita, 2013) or blended collagen gels, e.g with PCL through electrospinning (Isenberg et al., 2009; Moskow et al., 2018; Schuh et al., 2018). These techniques alter the structure of the matrix and can result in the

addition of signalling cues which prevent the absolute understanding of the influence of an isolated collagen density gradient on neurite behaviour.

In 2005, Brown et al. (2005), developed a process to rapidly produce dense collagen matrix through plastic compression, i.e. gels do not rehydrate, opening a new route for the production of materials structurally and mechanically suitable for tissue engineering (see Figure 1.9a). The matrix produced by plastic compression, a combination of external mechanical loading and fluid absorption, is a dense collagen structure obtained by expulsion of 97% of fluid from the hydrogel (Brown et al., 2005). This process increases the strength and mechanical integrity of the hydrogel (Brown et al., 2005) and making it mechanically more comparable to soft human tissues. As shown in Brown et al. (2005), under tensile testing, the ultimate tensile strength of plastic compressed gels was 0.55 MPa, approaching soft tissue values. They also showed high cell viability for plastic compressed gels and compressed + tensioned gels (5-30% strain). They indicated minimal impact of the fluid removal process on cell survival (Brown et al., 2005), making it a promising technique for the biomaterial and tissue engineering field. Soon after this initial work, Neel et al. (2006) showed the importance of the level of hydration on the mechanical behaviour of collagen scaffolds (hyper hydrated, single (SC) and double compressed (DC)). For these studies, plastic compression was performed with a constant load of 60g per unit cross-sectional area (mm^2) to induce a downward fluid flow (Brown et al., 2005). The SC and DC constructs were shown to support cell seeding, their hydration level did not interfere with the cell viability and they have been used for numerous tissue engineering applications (Phillips, 2014).

More recently, Levis et al. (2015), extended the plastic compression approach to the commercially available Real Architecture For 3D Tissues (RAFT) kit, allowing confined compression (CC) of hydrogels with upward flow, known as RAFT-stabilisation, in collaboration with TAP Biosystems (Figure 1.9b). This method is

not experience-dependent and provides a rapid, simple and consistent way to fabricate engineered tissues able to withstand handling. It has been used to produce tissue engineered cornea (Levis et al., 2015), artificial cancer masses (Magdeldin et al., 2017), tissue engineered skin (Martin et al., 2017), and will be used in this thesis to fabricate RAFT-stabilised collagen gels for nerve tissue engineering purposes.

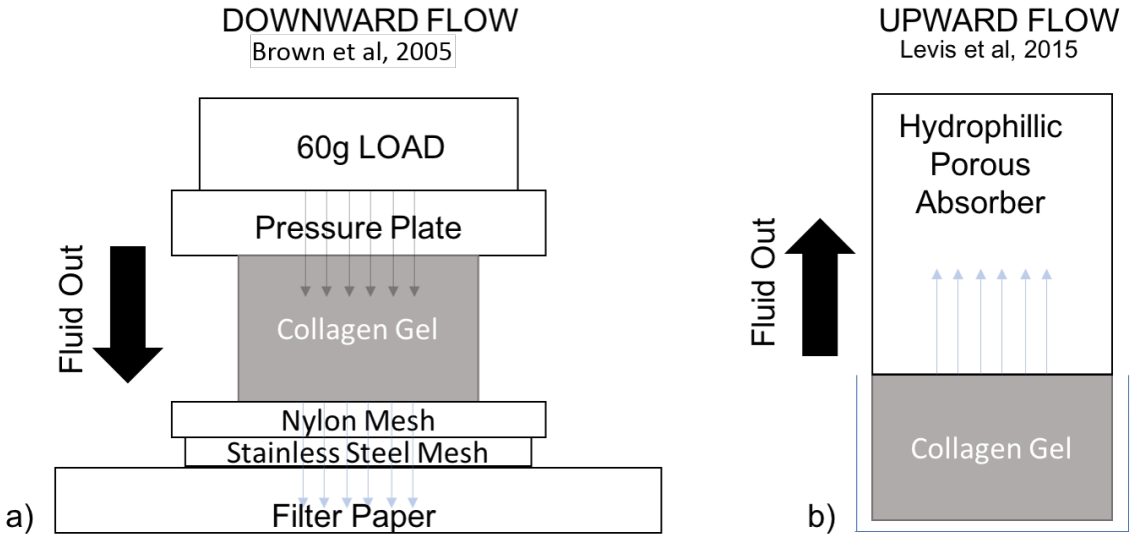

Figure 1.9: Difference between the processes in terms of fluid expulsion a)Brown et al. (2005) and the plastic compression (PC) process with downward fluid flow b)Levis et al. (2015), confined compression (CC) RAFT-stabilisation process with upward flow.

1.7 Characterisation of Mechanical Properties of Hydrogels

As summarised Section 1.6, cell behaviour, e.g. differentiation, migration, neurite branching and orientation, is impacted by the mechanical and structural properties of the substrate environment. Also, materials mechanically resistant to surgical handling and similar to the host site are required in tissue engineering to minimise the chance of an adverse host response. This characterisation can be seen as the study of the response of materials to applied load. If the material recovers its original shape and size after forces are applied on it, then the material is elastic. These materials have the capability to store the energy, whereas viscoelastic materials store the energy and dissipate it simultaneously. Typically, viscoelastic materials can change shape and flow away from the force to deform semipermantly. Their relationship between stress and strain is time and temperature dependant.

The mechanical characterisation of biomaterials is therefore crucial as it guides tissue engineers into developing tissue-like materials. The fundamentals of some of the mechanical tests used to characterise biomaterials (see Figure 1.10) will be described in this Section.

The stiffness of a material indicates the tendency for a material to resist deformation when subjected to a uniaxial force (tension or compression). It is related to the elastic modulus of the material (Young's modulus, E) which is the longitudinal stress divided by the strain (see Section 1.7.1). These material characteristics can be tested using static mechanical tests such as creep and stress relaxation tests. The stress relaxation is a time-dependent decrease in stress under a constant strain applied (at t=0). It informs the load required to maintain specimen deformation as a function

of time. The creep test is a time-dependent increase in strain under a constant stress initially applied.

The complex modulus, which is a measure of the resistance of a material to dynamic deformation can be measured using dynamical mechanical analysis (see Section 1.7.1) or rheology (see Section1.7.2).

The surface stiffness or hardness of a material is generally define as the resistance to local surface deformation as measured by forcing an indenter of specific geometry under a defined load, usually using atomic force microscopy or a Nanoindenter (see Section 1.7.3).

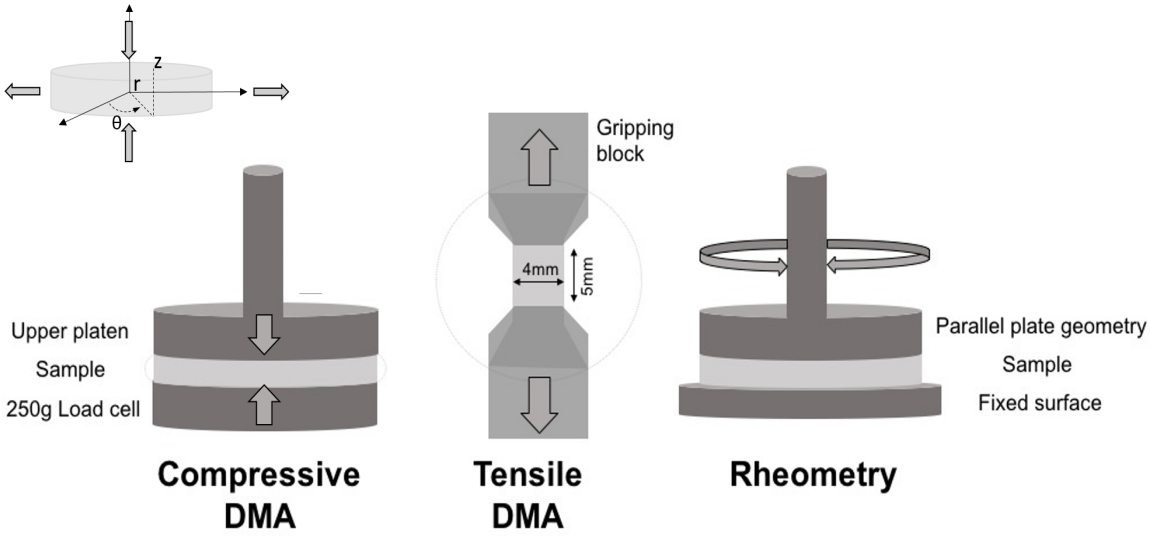

Figure 1.10: Schematic of the three different mechanical testing set ups used to investigate in detail the mechanical behaviour of collagen gels in a cylindrical coordinate system (r,θ,z).

1.7.1 Fundamental Principles of Dynamic Mechanical Analysis

Dynamic Mechanical Analysis (DMA) is a characterisation technique used to investigate the viscoelastic behaviour of polymers. A sinusoidal stress profile in time is applied to the material and the resulting sinusoidal strain is measured (see Figure 1.11). For purely elastic materials, the phase difference, (δ), between the stress and the strain wave is zero degrees, whereas, the phase difference is 90° for purely viscous material. Because of their viscoelastic nature, biopolymers exhibit a phase difference between those extremes ($0< \delta <90°$, see Figure 1.11). This phase difference, together with the amplitude of the stress and strain waves, is used to establish the properties of biomaterials, e.g. storage, loss modulus, and damping ($\tan\delta$) as they experience a periodic sinusoidal deformation. Figure 1.11 presents a typical force-displacement curve obtained by DMA.

DMA uses different deformation modes, i.e. tension and compression modes (Figure 1.10). This oscillating compressive or tensile force is called stress (σ, kPa) and can be expressed through

$$\sigma = F_n/A, \tag{1.1}$$

i.e. the ratio of an applied force F_n to the cross sectional area A on which the force is applied, to materials of known geometry in a cyclic manner. The material response to this stress, in the form of the dimensionless deformation, called strain (ϵ), which is defined by

$$\epsilon = \mathrm{dl}/\mathrm{l_i}, \tag{1.2}$$

where dl is the change of length and, l_i is the initial length.

The Young's Modulus of Elasticity, E (N/mm^2 or kPa), is the ratio of the stress to the strain.

$$E = \frac{\sigma}{\epsilon}. \tag{1.3}$$

This modulus represents the stiffness of a material by quantifying the deformation of a material within the elastic range when an uniaxial stress, whether tensile (extension) or compressive (compression), is applied.

For viscoelastic materials, the storage modulus, (E', kPa) is a measurement of the energy stored per cycle, representing the elastic response. The loss modulus, (E'', kPa), is a measure of the the energy dissipated per cycle, representing the viscous response. Under steady-states vibration conditions, a phase shift between stress and strain is caused and the modulus elasticity is then defined as the Complex Modulus (E^*, kPa) (see Figure 1.12). The complex viscoelastic response is depicted as follows

$$E^* = E' + jE'', \tag{1.4}$$

where j is the imaginary unit and $j^2 = -1$, the elastic component, E' is

$$E' = \frac{\sigma_0}{\epsilon_0} \cos\delta, \tag{1.5}$$

and the viscous component, E'', is defined by

$$E'' = \frac{\sigma_0}{\epsilon_0} \sin\delta. \tag{1.6}$$

The relationship between the Young's modulus and the Complex modulus is given by

$$E = |E^*| = \sqrt{E'^2 + E''^2}. \tag{1.7}$$

The damping, energy dissipation of the material under cyclical stress, is characterised by the tangent of phase difference, $\tan\delta$, which is the ratio of loss to the storage modulus,

$$\tan\delta = \frac{E''}{E'}. \tag{1.8}$$

This is an indication of the phase shift between displacement and load, and provides information on the relationship between the elastic and viscous components, i.e. storage and loss modulus.

The information obtained by DMA can be used in tissue engineering as it indicates if the replacement biomaterial used (in our case RAFT-Stabilised collagen, see Section 1.6.3), displays similar viscoelastic properties to the host tissue that requires replacing.

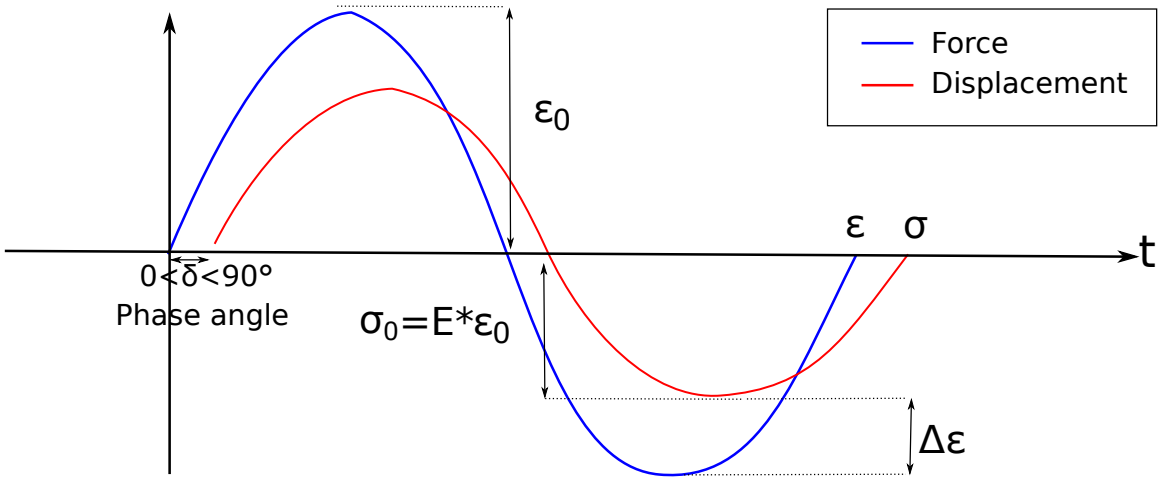

Figure 1.11: Typical force-displacement sine wave from DMA test, showing the stress (σ), and the strain (ϵ) as a function of time (t).

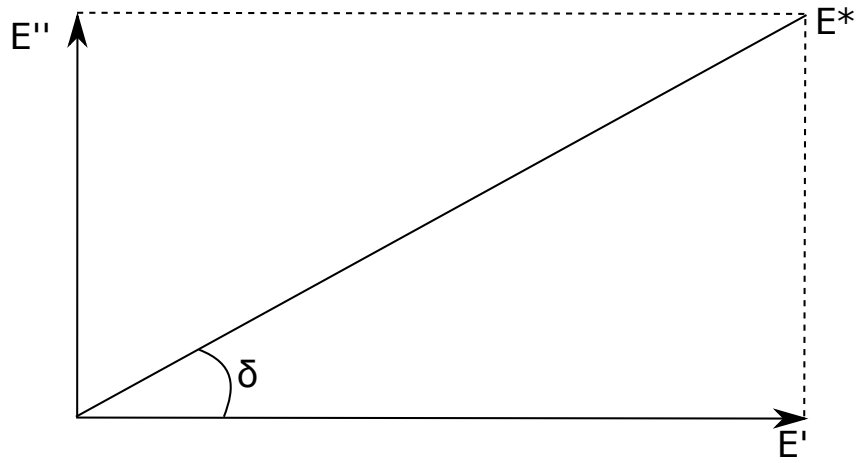

Figure 1.12: Relationship between E^*, E', E''.

1.7.2 Fundamental Principles of Rheometry

Rheology is commonly used to characterise the mechanical properties of polymers (Zuidema et al., 2014). This characterisation technique informs the relationship between the shear stress applied on a material (τ), and the deformation (γ) and flow of the material. For rheometry testing, various measuring geometries can be used to operate a rotational oscillation (see Figure 1.13) and to measure the properties of the material. These measuring systems are attached to the driving motor and rotate under specific conditions. Typical geometries are a concentric cylinder, a parallel plate and a cone and plate, as shown in Figure 1.13. Concentric cylinders are commonly used for very low to medium viscosity fluids. Cone and plate are used for very low to high viscosity fluids and parallel plates are used for very low viscosity to soft solid (Hackley and Ferraris, 2001).

Rheology provides information about the material's viscosity (η, Pa.s^{-1}) and viscoelastic properties given by the shear modulus (G, Pa) and shear $\tan\delta$. Fundamentally, a rotational rheometer controls and measures the torque (M(t), N m), the angular displacement (θ(t)) and the angular velocity of the plate (ω(t), rad.s^{-1}). In this thesis, rheological tests were conducted on collagen gels using a parallel plate geometry. In this scenario, the viscosity, η in Pa.s^{-1}, indicating the resistance of a fluid to a shear stress can be expressed as follows

$$\eta = \frac{\tau}{\dot{\omega}}, \tag{1.9}$$

where τ(pa) is the shear stress and $\dot{\omega}$ is the shear rate.

During a frequency sweep test, the sample is exposed to a sinusoidal strain (γ) at an angular frequency ω. For viscoelastic materials under dynamic testing, the strain

(γ) is a function of time, and uses the following relationship,

$$\gamma(\omega, t) = \gamma_0 \cdot \sin(\omega t), \tag{1.10}$$

where γ_0 is the maximum amplitude of the strain, $\omega = 2\pi f$ (f, frequency of the strain oscillation), t is the time, and δ the phase difference; as seen previously in Section 1.7.1, viscoelastic materials exhibit a phase difference between the strain and the stress ($0< \delta <90°$, see Figure 1.11). The stress resulting from the applied sinusoidal strain can be written

$$\tau(\omega, t) = \tau_0 \sin((\omega t + \delta), \tag{1.11}$$

or

$$\tau(\omega, t) = G' \cdot \gamma_0 \cdot \sin(\omega t) + G'' \cdot \gamma_0 \cdot \cos(\omega t), \tag{1.12}$$

where τ_0 the maximum amplitude of the stress, the shear storage modulus G' (Pa), represents the storage of elastic energy, i.e. the elastic component, and G" (Pa), the shear loss modulus, represents the viscous dissipation, i.e. the viscous component. Similarly to in Section 1.7.1, the complex shear modulus, G^* can be expressed as follows

$$G^* = G' + jG'', \tag{1.13}$$

where j is the imaginary unit and $j^2 = -1$. The relationship between the shear modulus, G, and the complex shear modulus G^* is also given by

$$G = |G^*| = \sqrt{G'^2 + G''^2}. \tag{1.14}$$

The shear modulus, G, can be compared to the Young's Modulus, E, by using the following relationship

$$G = \frac{E}{2(1+\mu)}, \tag{1.15}$$

where μ the Poisson's ratio.

A comparison between mechanical characteristics measured via DMA and rheology are given in Table 1.3.

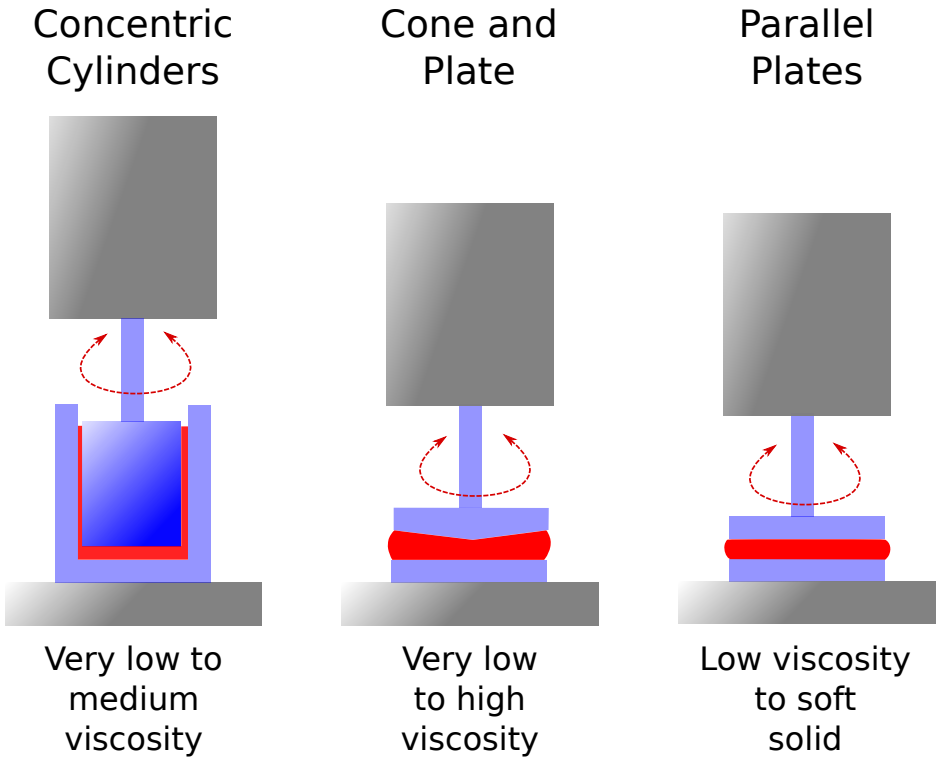

Figure 1.13: Typical rheometer geometry configurations. The rotational oscillation is represented by the double arrow; the measuring system rotates while the lower plate is stationary.

Name	DMA	Rheology	Definition	Units
Stress	σ	τ	Force/Area	Pa
Strain	ϵ	γ	Deformation	no units
Strain rate	$\dot{\epsilon}$	$\dot{\gamma}$	Velocity gradient	s^-1
Modulus	E	G	Stress/strain	Pa
Viscosity		η	Stress/strain rate	$Pa.s^{-1}$

Table 1.3: Glossary of mechanical measurement terms

1.7.3 Fundamental Principles of Atomic Force Microscopy

Atomic force microscopy (AFM) is a high-resolution scanning probe microscopy method (SPM) developed in 1986 by Binnig and colleagues (Binnig et al., 1986). The first commercialised AFM appeared in the early 1990s (Stylianou, 2017). It rapidly became a popular method as it can reach nanometer resolution. A tip mounted on a cantilever, usually made of silicon, is used to scan the sample surface. When a voltage is applied on the piezoelectric sample stage, the sample can accurately be moved in three-dimensions at a subnanometer scale (Leite et al., 2007; Stylianou, 2017; Krieg et al., 2019) (Figure 1.14a), and the sample can be imaged as shown in Figure 1.14b or mechanically characterised using atomic force spectroscopy (see Figure 1.14c). Both techniques will be detailed, respectively, in Section 1.7.3.1, and in Section 1.7.3.2. AFM is used to study nanoscale topography and mechanical characteristics of a broad range of samples, e.g. proteins, cells and tissues (Krieg et al., 2019).

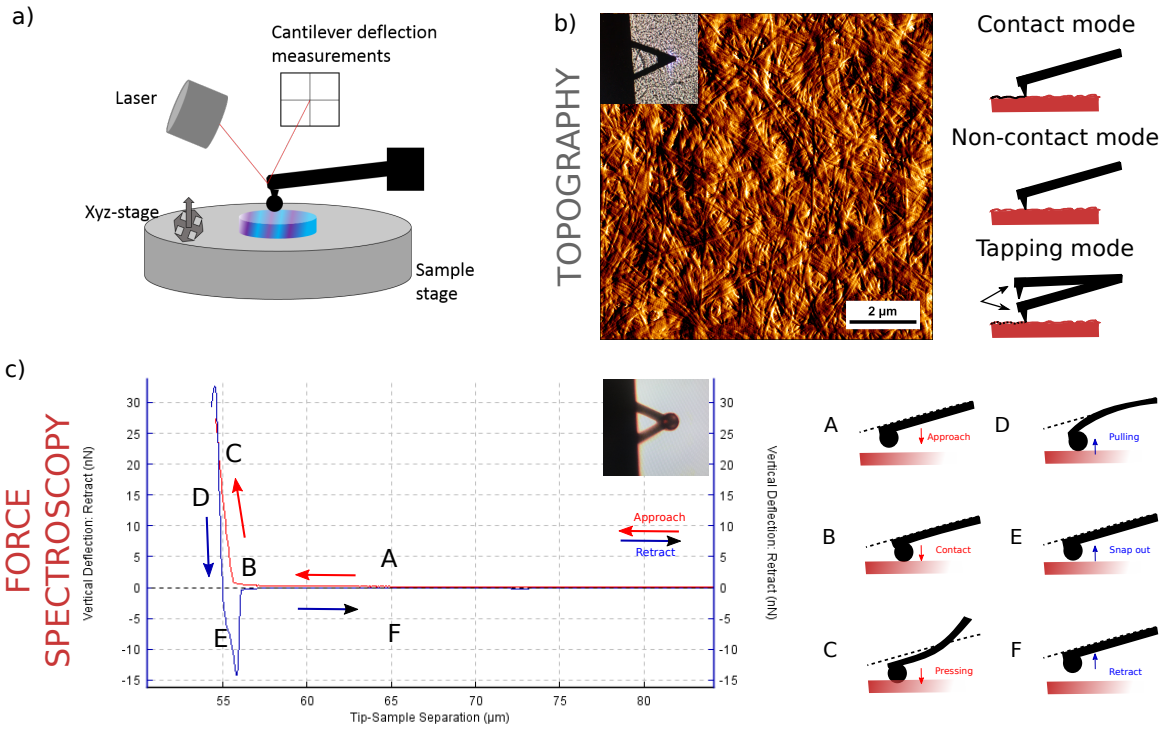

Figure 1.14: a) Schematic representation of the main components of an atomic force microscope. It consists of a probe (cantilever and tip), a laser, a piezoelectric sample stage, a photodetector to measure cantilever deflection and is all connected to a computer. b) Example of an AFM topography image taken with a pyramidal tip and the schematic representation of the commonly used imaging modes. c) Typical force-distance curve, divided in different segments (A-F) corresponding to the interaction between the scanning tip (spherical geometry) and the sample.

1.7.3.1 Topography

AFM can be used to obtain nanometer scale images of the surface of a large variety of samples e.g. biological samples, polymers, semi-conductors (Leite et al., 2007). To get an AFM image, the cantilever is brought to (or close to) the sample surface and a line-by-line image is formed according to the cantilever signal, itself detected using laser light, due to the probe-sample interaction (Leite et al., 2007). As represented in Figure 1.14b, three different imaging modes are commonly used.

- Contact mode: The probe is in close contact with the sample surface. It is the most common mode of operation but can also alter the sample.
- Non-contact mode: The probe is kept few Angstrom above the surface sample and is excited at its resonant frequency. Interaction forces between the tip and the surface are detected and used to generate an image.
- Tapping mode: This mode is used when the surface of a substrate is easy to damage. The cantilever is excited by an electrical oscillator and taps the surface as it goes through the area to image.

1.7.3.2 Force Spectroscopy

1) Force-Displacement curves: AFM is also used to investigate surface forces through force curves (see Figure 1.14c), used to measure the vertical force that the tip applies to the surface of the sample. This technique is called atomic force spectroscopy (AFS). In order to map the stiffness of biological or engineered substrates, AFS records single-point force-distance (FD) curves at each point of a map defined beforehand. It provides information regarding the tip-sample interaction at this particular location. Figure 1.14c shows a typical force-displacement curve. AFS records the force applied

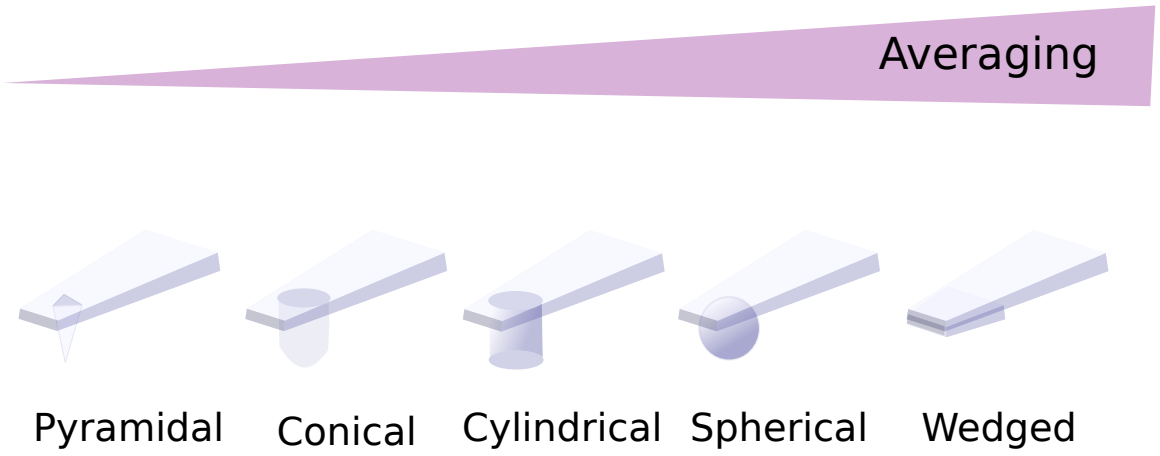

Figure 1.15: Various probe geometries used for the mechanical characterisation of biological samples. The larger the probe-sample contact area, the more the mechanical measurement will average out. Adapted from Krieg et al., 2017

by the probe into the sample during the indentation and the distance travelled by the probe. At first, the tip approaches the sample (A)(see Figure 1.14c), there is no interaction yet. When the tip gets close enough to the surface, various forces, e.g. electrostatic and Van der Waals forces, attract the cantilever and the tip jumps-to-contact (B). Then the tip applies a force on the surface (C) and this region (A-C), called the *approach curve*, measures the elastic properties (B-C) of the sample (Leite et al., 2007). Then, the tip is pulled off the surface (D) and the section (D-E) measures the adhesion forces formed during contact. Finally, the tip retracts and returns to its starting equilibrium position. This region (D-F) is called the *retract curve*.

2) Probe geometry and Hertzian Model: For the mechanical characterisation of biological systems, e.g. materials, or cells, various probe geometries can be used (Krieg et al., 2019). Sharp probes will allow local measurement with fine accuracy, e.g. measurement of the stiffness of a collagen fiber (Efremov et al., 2017). For larger probes, the mechanical properties of a bigger local area can be measured as shown Figure 1.15. Micro-beads or wedges can be glued to the cantilever to enable the mechanical measurement of a larger sample area (Krieg et al., 2019).

To extract the mechanical data from the force curves, an appropriate model must

be used. Although in most commercial AFM software programs models are implemented for data analysis, here will be described the most commonly used theoretical model. The Hertz model is often used to obtain the Young's Modulus from the FD curves and is dependant on the spherical probe geometry (see Figure 1.15). In this thesis a spherical probe was used for the mechanical characterisation of hydrogels. For a spherical probe as shown in Figure 1.16, the effective Young's Modulus, E_{eff}, most commonly reported parameter (Oyen, 2014), is expressed as

$$E_{eff} = F/[2(a^2 + {R_p}^2).\sigma - 2.a.R_p], \tag{1.16}$$

where σ, the indentation, is defined

$$\sigma = \frac{a}{2}.\ln\left(\frac{{R_p}^2 + a}{{R_p}^2 - a}\right), \tag{1.17}$$

and R_p is the radius of the indenting probe, a is the contact radius and F the indenting force (see Figure 1.16).

The Young's Modulus, E, for a compliant material can be expressed as a function of E_{eff},

$$E = E_{eff}(1 - \nu^2), \tag{1.18}$$

where ν is the Poisson's ratio generally set to 0.5 for soft tissue and tissue-like sample (Instrument, 2008) as they are considered as rubber-like incompressible materials (Chen et al., 1996).

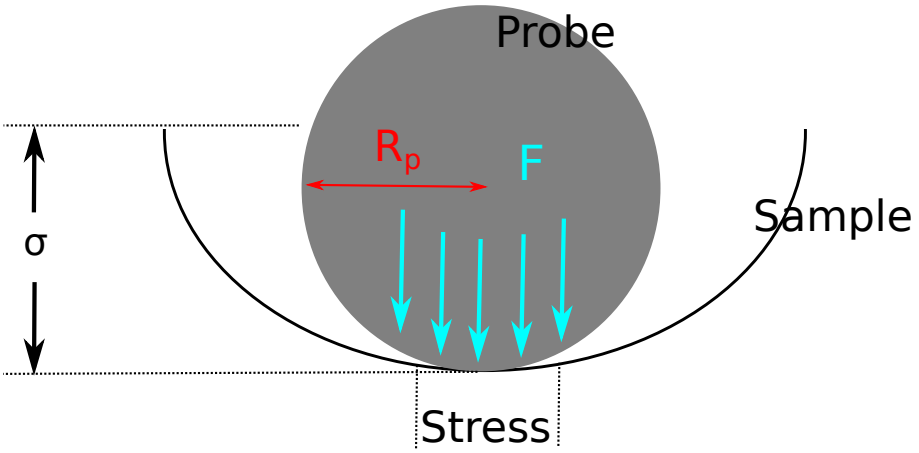

Figure 1.16: Schematic representation of a spheric probe and the key parameters used in the Hertzian model to extract mechanical data from force curves measurements. R_p is the radius of the indenting probe, σ the indentation and F the indenting force.

1.8 Mathematical Modelling

Experimental approaches can be very limited due to a wide variety of parameters and designs that require investigation. This is time-consuming, expensive and in some cases experiments can be ethically challenging due to animal experimentation. Mathematical modelling is a very useful and complementary approach that can minimise the need for laborious and expensive experiments (Coy et al., 2017). Computational models can help to test and to generate a design hypothesis to be tested experimentally. Coy et al. (2017) proposed a theoretical-experimental tissue engineering design workflow (see Figure 6.1) to be used to help with the development of NGCs to support neurite growth after an injury and increase their chance of translation to the clinic. A wide range of conduit designs have been developed in recent years and significant progress in understanding the importance of guidance cues has been made (see Section 1.5 and 1.6). However, the current design process has opportunity for improvement

in order to exceed the efficiency of the autograft and enhance nerve regeneration and functional recovery in the PNS (Jiang et al., 2010). Coy et al. (2017) proposed the integration of mathematical modelling into the NGC design workflow as follows; a preliminary *in silico* model is designed and parameterised using experimental parameters (obtained either from specifically conducted experiments or from the literature). Once the model has been informed, it can be used to simulate numerous scenarios and inform the efficacy of the tested designs quickly and in a cost-effective manner. Following the theoretical results, a refined set of experiments can be planned and executed. Data from these experiments can act to validate and/or refine mathematical models through an iterative process, allowing continuous improvement. In this thesis, both experimental and computational approaches are used following this aforementioned theoretical-experimental tissue engineering design workflow to investigate neurite elongation on stiffness gradient substrates.

Although various cell types will display different methods of locomotion, the cell migration process has been generalised and characterised to be a persistent random walk, similar to Brownian motion of small particles (Walmod et al., 2001) in the absence of guidance cues (Dunn and Brown, 1987; Walmod et al., 2001). It is now well established that cells are able to feel certain external signals and that their behavior is influenced by input signals from the surrounding environment, e.g. chemical, physical or structural. Furthermore, gradient of signalling cues can guide cell movement; Lo et al. (2000) reported for the first time the influence of the rigidity of the substrate, where cells were moving preferentially towards stiffer regions, phenomenon defined as *durotaxis* (see Section 1.6.1).

In order to provide some insight into the general aspects of cell migration, mathematical models have been developed and computational simulations used. Two principal types of models have been previously exploited to investigate cell migration pattern, the continuous approach and the discrete approach. For the continuous ap-

proach, the models are related to model of diffusion, and cell motility is modelled as a changes in time and space of the local cell concentration (Patlak, 1953; Painter, 2009; Moreo et al., 2008). This approach is used to describe cell population behavior and is generally based on Keller-Segel model (Keller and Segel, 1971). On the other hand, the discrete approach depicts single-cell trajectory (Alt, 1980; Dunn and Brown, 1987). For example, Zaman et al. (2005) proposed a discrete model based on the equilibrium of individual cells subjected to external forces in 3D (force-based dynamic approach).

Different types of cell migration in the absence or under signalling cues have been modelled using the discrete approach, e.g. random motility (Dickinson and Tranquillo, 1993; Zaman et al., 2005), chemotaxis (Tranquillo and Lauffenburger, 1987; Stokes and Lauffenburger, 1991; Jabbarzadeh and Abrams, 2005), haptotaxis (Dickinson and Tranquillo, 1993; Smith et al., 2004), durotaxis (Stefanoni et al., 2011). The discrete approach can easily be used to compare experimental data in which individual cell paths are collected. Therefore in this thesis, a discrete mathematical model of neurite motility informed by the experimental data collected in Chapter 4 and 5 is proposed to reproduce the influence of a stiffness gradient on neurite elongation. More details about the mathematical model are given in Chapter 6.

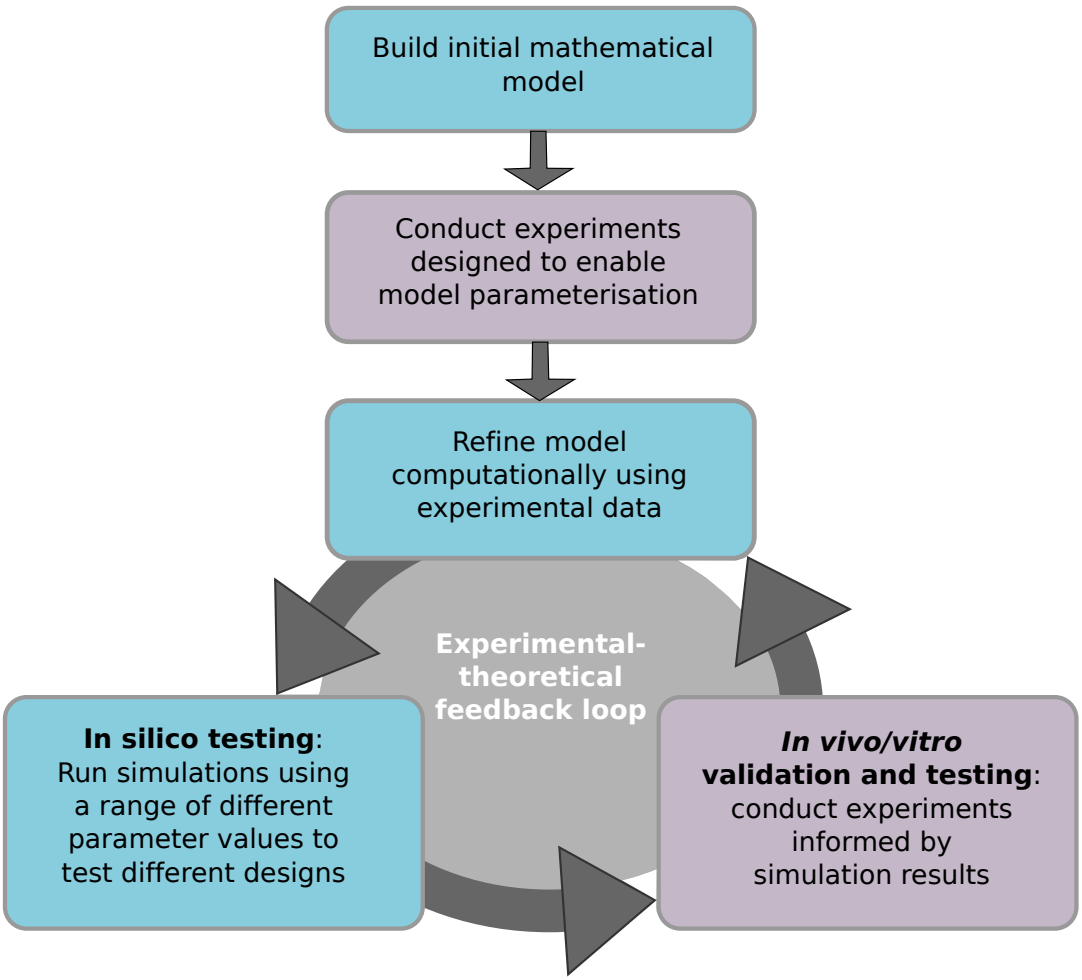

Figure 1.17: Theoretical-experimental tissue engineering design workflow. A mathematical model is initially built and parameterised using available data (either existing or specifically collected data). The model predictions help in the design of the next experiments and the obtained results are used to refine and expand the model entering the experimental-theoretical feedback loop. Adapted from (Coy et al., 2017).

1.9 Thesis Objectives

The overall aim of this thesis is to explore the effect of mechanical features of an optimised matrix on neuronal behaviour and use the results to propose a new design rationale for nerve tissue engineering, with four main objectives:

1. Investigate the mechanical properties of nerve tissue and engineer a material with similar properties.

2. Develop and optimise a technique to obtain a consistently reproducible and well characterised gradient material to enhance neuronal growth.

3. Use the gradient material to quantify/characterise the mechanosensitivity of neuronal cells

4. Develop a mathematical model with the collected parameters to predict the optimal spatial arrangement of mechanical properties within an engineered NGC, and therefore propose a new design rationale for nerve tissue engineering application.

To address the first objective, fresh rat sciatic nerves were mechanically tested, as reported in Chapter 2. As cell behaviour is influenced by the mechanical and structural properties of their substrate environment, a material with similar mechanical characteristics to nerve tissue was sought. Also, materials mechanically resistant to surgical handling and similar to the host site are required in tissue engineering to minimise the chance of an adverse host response. RAFT-Stabilised collagen gel was the chosen material. Properties of RAFT-stabilised collagen (RsC) gels are governed by the size, composition and arrangement of fibrils and their interaction with

the fluid trapped within the matrix. However, protocols to define and compare the physical properties and mechanical behaviour of RAFT-stabilised collagen gels are not standardised across the field. Chapter 3 specifically investigates the fundamental mechanical and structural properties of RsC gels, and proposes a new empirical relationship that correlates the measured stiffness of gels to varying frequency of strain oscillation (Objective 1).

Previous studies have explored the mechanical heterogeneity of the peripheral nervous system, e.g. during development stage or pathological differences. Here, based on defined mechanical cues, the use of mechanical gradient gels is explored to improve neuronal growth. Chapter 4 describes a new protocol for fabricating gradient gels, and presents a thorough characterisation of the physical and mechanical properties of the created gradients (Objective 2).

Following the creation of a mechanical gradients with physiologically relevant stiffness of collagen gels (Chapter 4), the next objective (3) of this thesis was to investigate the mechanosensitivity of neural cells cultured on the surface of the gradient and is described in Chapter 5.

The final part of this study, objective (4), was to use the experimental parameters to inform a discrete computational model to predict the most relevant gradient configurations to be further tested experimentally to control and improve neurites growth in a nerve guidance conduit (Chapter 6).

Chapter 2

Rat Sciatic Nerve Mechanics

2.1 Introduction

Biological tissues exhibit distinct mechanical properties related to their structure and function in the body (see Figure 2.1), e.g. the stiffest is bone tissue, to provide support to the body and protection to vital organs ($E > 10^9$ kPa) while the softest tissue is mucus, with a stiffness around 1 Pa. These properties, inform the overall organisation of the tissue and reflect the architecture and composition of the extracellular matrix, e.g. brain tissue, protected by the skull, is highly compliant due to the non-fibrillar nature of its ECM (Barnes et al., 2017). The biomechanics of tissues plays an important physiological role (Ju et al., 2017) and for peripheral nerves, understanding their mechanical properties will help develop artificial conduits to improve repair and regeneration (Chen et al., 2010b; Ju et al., 2017; Barberio et al., 2018).

Healthy peripheral nerve tissues exhibit viscoelasticity (Grewal et al., 1996; Topp and Boyd, 2012; Barberio et al., 2018) giving them the capacity to stretch, twist and bend to accommodate to compressive, tensile, or shear, forces that physiological limb movements create (Topp and Boyd, 2012; Shah, 2017). In the process of developing nerve repair strategies for large gap peripheral nerve injury, these properties have to be

taken into consideration to ensure tissue function, and avoid rejection of the implanted conduit, as it should match the host-site mechanical properties (Barnes et al., 2017). In addition, it is required for nerve substitutes to have coherent mechanical properties and sufficient tensile strength to face *in vivo* mechanical forces (Borschel et al., 2003).

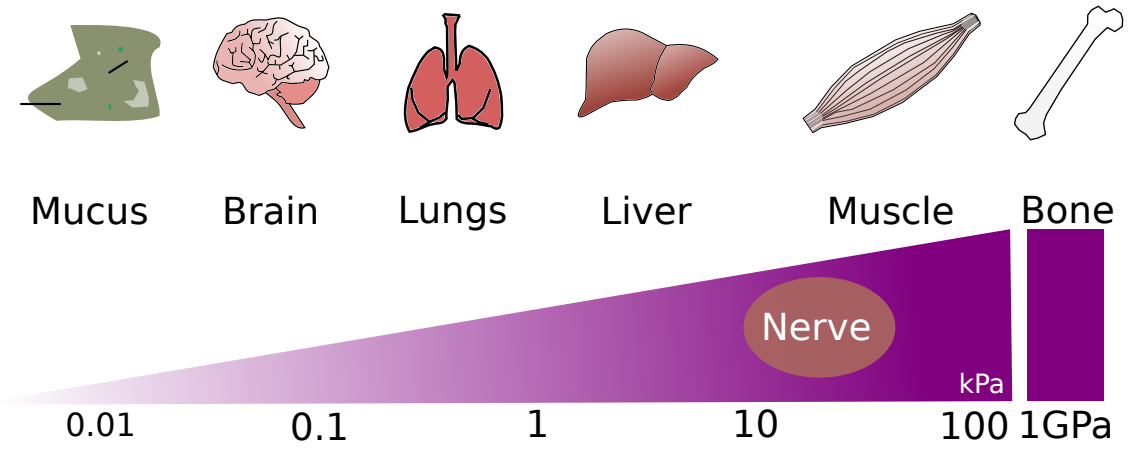

Figure 2.1: Stiffness properties of human tissues (E, kPa). The stiffest tissue is bone tissue with a stiffness in the order of magnitude in GPa, and the softest tissue is mucus, with a stiffness around 1 Pa. Lungs and brain are the softest organs ($E<4{\cdot}10^2$ Pa) and muscle tissue is intermediate (E between 10 and 100 kPa). Nerve tissue fits in a similar range of magnitude to muscle tissue as depicted on the image. Nevertheless, nerve tissues are softer than muscle fibers (Barnes et al., 2017). Adapted from Barnes et al. (2017).

Previous studies have investigated the static mechanical properties of nerves under parallel compression (Ju et al., 2004; Chen et al., 2010b; Rosso et al., 2017b); circular compression (Ju et al., 2006; Chen et al., 2010a) or tension (Tai et al., 2015). Ju et al. (2004) have found the Young's modulus, E, to be around 40 ±5 kPa for rabbit sciatic nerve, Chen et al. (2010b) found E to be around 115 ± 20 kPa for rat sciatic nerve, and Rosso et al. (2017b) found E to be around 30 ±10 kPa for mouse sciatic nerve. Under circular compression, the Young's modulus has been found to be generally higher, Ju et al. (2006) found E to be 70 ± 8 kPa for rabbit sciatic nerve and Chen et al. (2010a) found E to be 970 ± 650 kPa for rat sciatic nerve. All these studies used static stress-strain experiments on sciatic nerves from healthy animals (rabbit, rat, or mouse), and the previously reported mechanical properties are summarised in

Table 2.1. In addition, Georgeu et al. (2005), Phillips et al. (2004), and Mason and Phillips (2011) have shown the importance of the area of the nerve tested as nerve exhibits localised heterogeneity. For example, Mason and Phillips (2011) showed differences in stiffness between joint and non-joint regions of rat median and sciatic nerve due to a difference in collagen fibril diameter. The variability of tissue origin, e.g. species or anatomical position, along with the inconsistency across the testing methodologies generate important variations in the mechanical response measurement between studies (Valtorta and Mazza, 2005).

The most typical stress experienced by peripheral nerves is tension and the resulting deformation is shown in Figure 2.2, adapted from Topp and Boyd (2006). Indeed, more related to trauma and repair, researchers have focused on nerve biomechanics under longitudinal traction (Haftek, 1970; Topp and Boyd, 2006; Tai et al., 2015; Barberio et al., 2018). Even if peripheral nerves are known to be viscoelastic and constantly exposed to dynamic loading, the frequency-dependant viscoelasticity of peripheral nerve remains to be characterised. Dynamic mechanical analysis, DMA, is a dynamic testing method, described in Section 1.7.1, known to test the viscoelastic properties of a material and has been used to quantify the storage (elastic) and loss (viscous) properties of a variety of biological tissues (Sadeghi et al., 2015; Barnes et al., 2016; Lawless et al., 2016; Barnes et al., 2015; Burton et al., 2017). This method can be used to establish a more comprehensive viscoelastic profile, rather than static testing previously reported.

In 2013, Ma et al. (2013) demonstrated that human ulnar nerve exhibit a viscoelastic behavior by performing *in vitro* stress relaxation tests. More recently, Barberio et al. (2018) used DMA to determine the viscoelastic properties (storage and loss modulus) of embalmed human ulnar nerve. However, the use of embalmed nerve is a limitation in that study because the fixation process cross-link ECM and alter its mechanical properties when compared with fresh nerve.

This study focuses on the assessment of viscoelastic properties of fresh rat sciatic nerve under dynamic testing. Seeking to obtain a more comprehensive viscoelastic profile of fresh peripheral nerve to inform engineered replacement tissues, and aware of the ethical challenge to obtain fresh human nerve samples (Barberio et al., 2018), a compromise on fresh rat sciatic nerve has been found. This study investigated for the first time, the mechanical behaviour of fresh rat nerve under tensile DMA for frequency sweep at a constant strain. Preliminary ramp tests were conducted to characterise the stress-strain curve of rat sciatic nerve (see Figure 2.3).

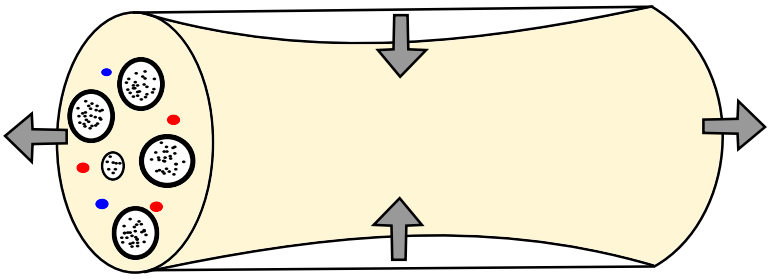

Figure 2.2: Physical stress experienced by a peripheral nerve. The tensile stress applied leads to a retraction of the cross sectional area called transverse contraction, greatest at the middle and an elongation of the nerve. Adapted from Topp and Boyd (2006).

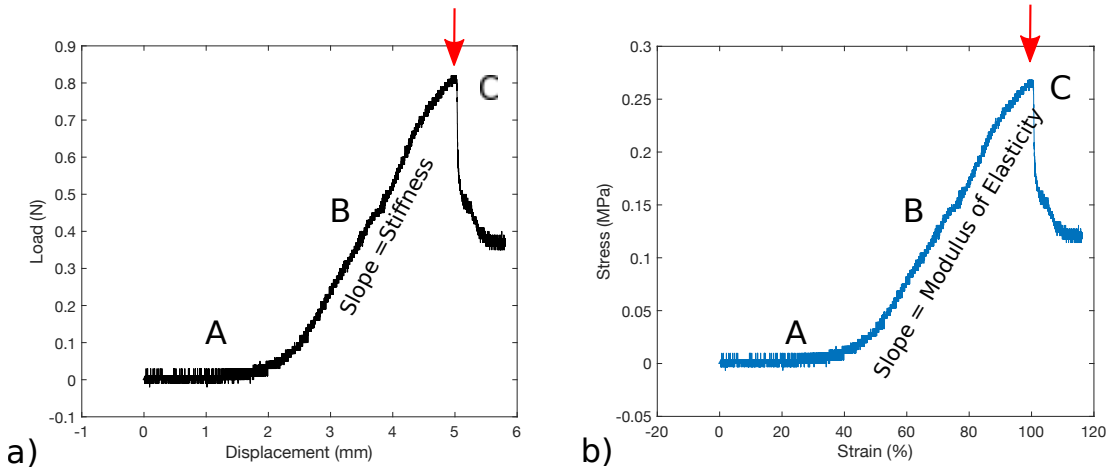

Figure 2.3: Typical Load-Displacement and stress-strain curves for a peripheral nerve (Topp and Boyd, 2006). The slope of the curves represents the stiffness of the nerve, called Modulus of Elasticity. The toe region (A), linear (B) and plastic (c) regions represent different structural and mechanical changes that the nerve will undergo under longitudinal tensile stress. The Ultimate load, represented by the red arrow is the highest load applied to the nerve before failure. Adapted from Topp and Boyd (2006).

Reference	Samples	**Mechanical Test**	**Elastic modulus**
Ju et al. (2004)	Rabbit sciatic nerve	*in vitro* parallel compression	41.6 ±5.0 kPa
Ju et al. (2006)	Rabbit sciatic nerve	*in situ* circular compression	66.9±8 kPa
Chen et al. (2010a)	Rat sciatic nerve	*in situ* circular compression	973±649 kPa
Chen et al. (2010b)	Rat sciatic nerve	*in situ* transverse, blood perfusion	116.3 ±22.3 kPa
Tai et al. (2015)	Rat sciatic nerve	*in vivo* tensile	not reported
Rosso et al. (2017b)	Mouse sciatic nerve	*ex vivo* compression	31.4±8.8 kPa

Table 2.1: Summary of biomechanical properties for healthy animal peripheral nerve evaluated under various mechanical testing methods.

2.2 Methods

2.2.1 Sciatic Nerve Harvest

Sprague Dawley male rats, weighing 370-480 g, were sacrificed by CO_2 inhalation then immediately dissected on ice to harvest the nerves. After exposing the sciatic nerve, a 5 mm gap was marked out before excision, to ensure that the *in situ* length was maintained. Both left and right sciatic nerves of each animal were harvested and stored in AQIX RS-I (solution used to preserve cell and tissue viability up to 72 hours) in ice. The time of death was recorded and for time 0 hours the nerve was tested within 30 minutes post-mortem. Care was taken to avoid stretching and touching the middle 5 mm gap, region to be tested.

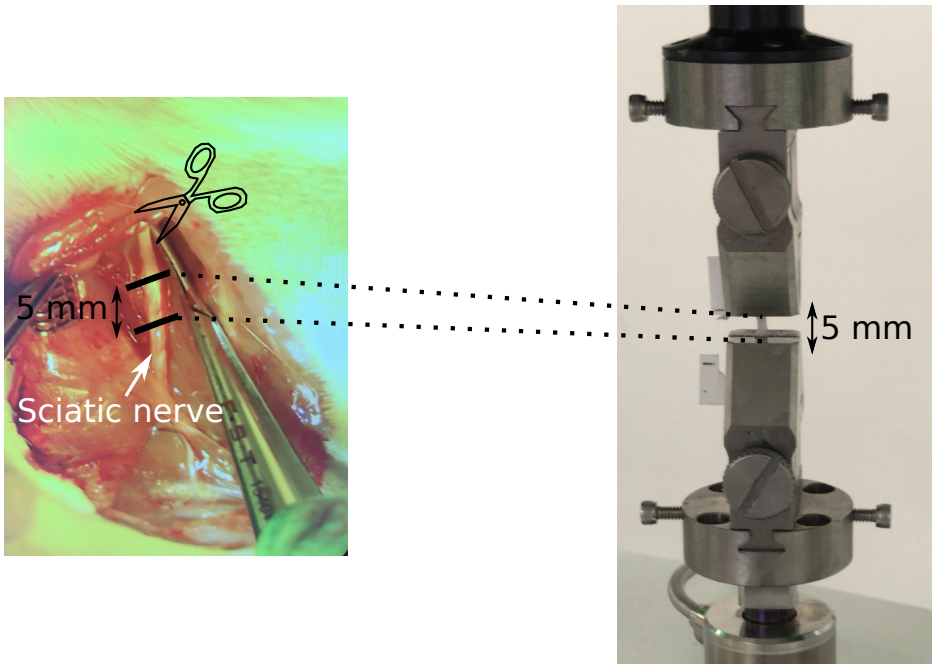

Figure 2.4: Experimental set up for the measurement of rat sciatic nerve mechanical properties under tensile DMA. A 5 mm gap is marked out on the nerve before excision and 1.5 cm of sciatic nerve is harvested on ice. The nerve is clamped to the grips with a gauge length of 5 mm. Nerves are kept hydrated during the testing procedure.

2.2.2 Ramp to failure

Preliminary ramp tests were conducted to characterise the stress-strain curves of fresh rat sciatic nerve. The sciatic nerve was clamped with a gauge length of 5 mm to a tensile testing machine BOSE-ElectroForce 3200 instrument (Bose Corporation, ElectroForce, System Group, Minnesota, USA) equipped with a 2500g load cell and Wintest DMA application software (Bose Corporation, ElectroForce, System Group, Minnesota, USA). A force/displacement curve was obtained at an extension rate of 10 mm.min^{-1}. Gauge length was measured using a caliper.

2.2.3 Dynamic mechanical tensile testing

To investigate the mechanical properties of rat sciatic nerve, the nerve was tested under tensile stress. The specimens (N=9) were secured using titanium grips as shown in Figure 2.4, and the middle 5 mm section was not touched to avoid any damage that could lead to a variation of the mechanical response. The specimens had a gauge length of 5.0 mm, and a diameter of 1.8 mm, measured with a caliper. The measurements were carried out also using a BOSE-ElectroForce 3200 instrument equipped but with a 250 g load cell and frequency tests were performed from 1Hz up to 10 Hz. To investigate the sweep frequency response, nerve samples were pre-extended by 10% of their gauge length, to reproduce the nerve *in situ* scenario where nerve is under some tensile load (evidenced by the fact that nerves retract when severed) (Topp and Boyd, 2006). Then the sample is dynamically tested with sinusoidal extension over the aforementioned range of frequencies for a displacement amplitude of $\pm 1\%$ of the gauge length of the nerve, which based on preliminary data (Section 2.2.2) does not induce irreversible damages. Nerves were kept hydrated during the testing period. Nerves were tested at t=0, 2 and 3 hours after dissection to investigate the impact of the time on *post mortem* nerve mechanics. 3 nerves samples were tested for each time point.

2.3 Results

2.3.1 Ramp to failure

Figure 2.5a shows a typical force/displacement curve obtained for fresh rat peripheral nerve (sciatic). It is characterised by the three distinct regions, depicted in Figure 2.3, the toe region for 0-40% strain, the linear region for 40-100% strain and after 100% strain, the nerve began to demonstrate signs of damage, the plastic region was reached. Figure 2.5b shows a typical stress/strain profile for fresh peripheral nerve. The curve showed that it could extend up to 30% strain before any stress transmission could be measured, i.e from toe region to linear region. Afterwards, the stress increased steeply with increasing strain.

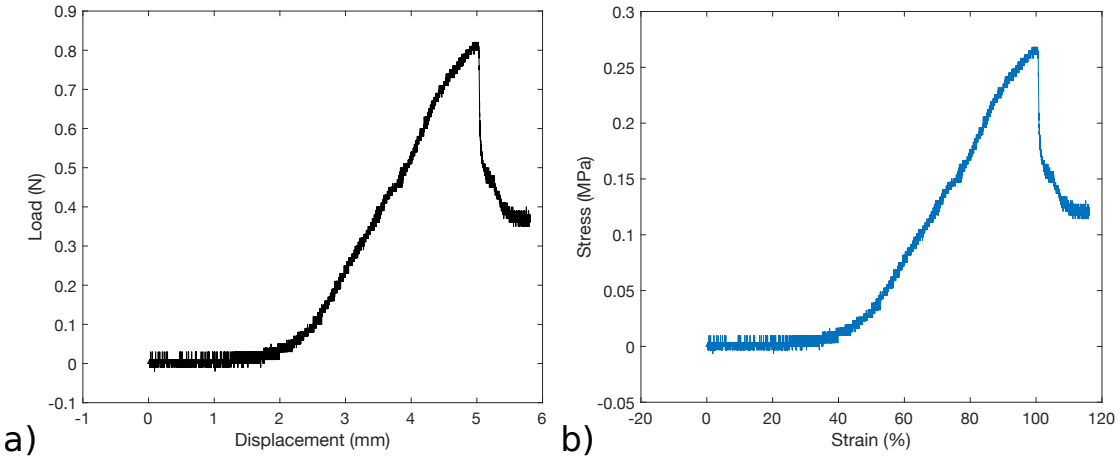

Figure 2.5: a) Curve showing force (N) against the displacement (mm) of a rat sciatic nerve. b) Strain-stress curve giving the modulus of elasticity ($\sim 80 \pm 5$ kPa) of the nerve.

2.3.2 Dynamic mechanical tensile testing

Figure 2.6 shows the effect of a frequency sweep on the viscoelastic properties, reported as the complex modulus, E^*, under dynamic tensile testing, as well as the storage (E') and loss (E'') modulus, respectively the elastic and viscous components

for three different time points (t=0, 2, and 3 hours). For all the time points, the elastic component appears to be around 5 times higher than the viscous component. For increasing frequencies, at t=0 hours, the complex modulus increased from ∼47 kPa to ∼63 kPa, which represents a 34% increase. At t=2 hours, the complex modulus increased from around 41 kPa at f=1Hz to ∼59 kPa at f=10Hz, which represents a 44% increase. At t=3 hours, 8% increase is reported for the complex modulus between f=1Hz and f=10Hz. Over time, a reduction of the standard deviation shows that the variability between samples reduces, possibly due to the stabilisation of the tissue sample in the preserving solution.

Figure 2.7 shows the ratio of the loss modulus to the storage modulus, tanδ as a function of frequency for three different time points(t=0, 2, and 3 hours). For increasing frequencies, at t=0, 2 and 3 hours, tanδ is quasi constant with a value of 0.20± 0.03 and 0.20± 0.05 and 0.17±0.02 respectively. There is no significant difference in tanδ between the different time points. Table 2.2 summarises the mean of E^*, E', E'' and tanδ for the three different time points. Between t=0 and t=3 hours, the nerve seems slightly stiffer with respective complex modulus value of $E_0^* = 53.3 \pm 5.3$ kPa, and $E_3^* = 59.3 \pm 2.8$ kPa. Nevertheless, the mechanical properties of the rat sciatic nerve under dynamic tensile testing did not show any significant variation within a three hours time window. The elastic component, shown as the storage modulus E', clearly predominates (53.4 ± 5.0 kPa) compared to the viscous component (loss modulus, E'',10.2 ± 1.1 kPa).

The complex modulus E^* of rat sciatic nerve remains roughly constant, 54.4 ± 5.0 kPa, and does not show signs of permanent deformation within this frequency range.

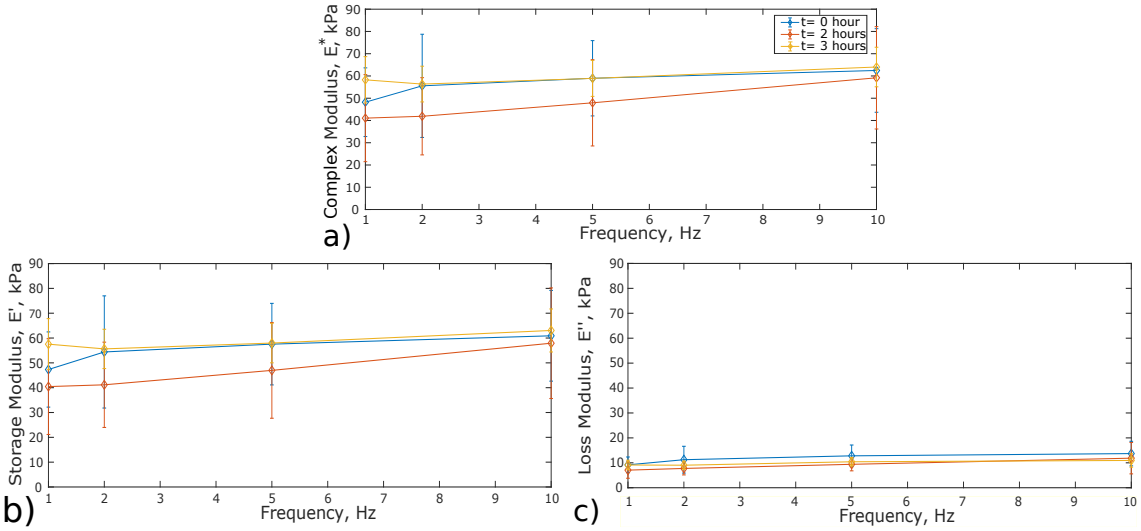

Figure 2.6: a) Complex Modulus (E^*, kPa), b) Storage Modulus (E', kPa) and c) Loss Modulus (E'', kPa) as a function of the frequency (Hz) for fresh rat sciatic nerve at three different time points (t= 0, 2, and 3 hours) under a sinusoidal extension [1-10]Hz. N=3.

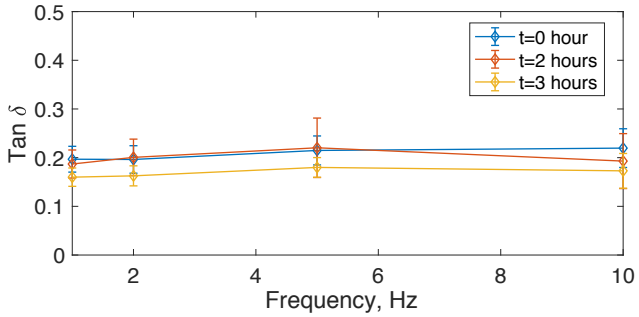

Figure 2.7: Tanδ as a function of the frequency (Hz) for fresh rat sciatic nerve at three different time points (t= 0, 2, and 3 hours). N=3.

Time Point	E*	E'	E"	tanδ
hours	kPa ± std	kPa ± std	kPa ± std	
0	53.3 ± 5.3	55.0 ± 5.0	11.7 ± 1.7	0.20± 0.03
2	47.5 ± 7.2	46.6 ± 6.9	9.0 ± 1.8	0.20±0.05
3	59.3 ± 2.8	58.5 ± 2.7	9.88 ± 0.8	0.17±0.02
Mean	54.4 ± 5.0	53.4 ± 5.0	10.2 ± 1.1	0.19±0.02

Table 2.2: Viscoelastic properties of rat sciatic nerve under tensile DMA at 2% strain for t= 0, 2, 3 hours.

2.4 Discussion

This study characterised the viscoelastic properties of rat peripheral nerve using DMA for the first time in unfixed animal samples, tested across a relevant frequency range Barberio et al. (2018). In response to a preliminary ramp test, the stiffness of the rat sciatic nerve was ∼80 kPa. As referred by Topp and Boyd (2006), the transition between the toe region and the linear region in a strain-stress curve corresponds with the *in situ* strain. In Figure 2.5, this transition region occurs around 30-40% strain, which is within the wide range of *in situ* strains reported by Barberio et al. (2018) to be within 0 and 69% (Toby et al., 1998; Ochi et al., 2013; Barberio et al., 2018, 2019).

Under dynamic tensile stress, nerve samples were pre-extended (10%, based on previous literature Topp and Boyd (2006)) and a frequency test was run for constant strain (1%). These conditions were based on our preliminary test and backed up by previously reported results (Grewal et al., 1996) so the nerve is under tension and the critical limit of elongation is not reached. These testing conditions were selected based on the *in situ* scenario to characterise relevant viscoelastic properties with conditions comparable to previously published work (1-2%; (Willits and Skornia, 2004; Barberio et al., 2018). Indeed, the nature of the mechanical load applied on the nerve results in variability in the mechanical response obtained, as it depicts different scenarios, e.g. physiological rate of loading or trauma (Valtorta and Mazza, 2005). The complex modulus measured, E^*, was ∼55 kPa, comparable to animal sciatic nerve elastic modulus measured by Ju et al. (2004, 2006, 2017), and Rosso et al. (2017b), detailed in Table 2.1, and corresponded to the range of magnitude expected from the mechanical properties of soft tissues, i.e. $10 < E < 100$ kPa (Barnes et al.,

2017) (see Figure 2.1). Fresh rat nerve samples were tested at three different time points (t=0, 2, 3 hours), and for each time points, the complex modulus increased by respectively 34%, 44% and 8% for increasing frequencies (1-10Hz). By comparison, an 8% increase has been indicated previously for embalmed human ulnar nerve, by extrapolating Barberio et al. (2018) data; $E^* = 7.89$ MPa at $f = 1$ Hz and $E^* = 8.54$ MPa at $f = 10$ Hz.This variation may be related to the nerve microstructure. This observation underlines the frequency-dependant viscoelasticity of nerve tissues. Fresh rat sciatic nerve displayed a viscoelastic behaviour for frequencies between 1-10 Hz under a 1% strain. The elastic component was predominant with E' ∼50 kPa, 5 times higher than the viscous component, E" ∼10kPa. Barberio et al. (2018) have investigated the viscoelastic properties of embalmed human ulnar nerves under a frequency sweep, and reported a similar behaviour; they reported E' to be around 10 times higher than E" for embalmed nerve samples. This observation is supported by the resulting low tan delta, indicating that fresh rat sciatic nerve acts more elastic when a load is applied, and therefore, has more potential to store the load rather than dissipating it.

The effect of *post-mortem* changes on tissue mechanics has been previously investigated as it is usually challenging to coordinate the excision of tissue from animals or patients with the timing of the mechanical testing experiment (Black, 2018). Common patterns of increasing stiffness for increasing time after death as been previously reported, e.g. for brain tissue changes happen within minutes *post-mortem* (Weickenmeier et al., 2018), or for tendons an increasing pattern is observed within hours *post-mortem* (Matthews and Ellis, 1968). This phenomenum could be explained by the significant modification of the environment, e.g. polarisation, oxidation, or perfusion (Weickenmeier et al., 2018). *In vitro* measurements of the mechanical properties of fresh nerves over a period of time of 3 hours revealed no significant increase. These results could support future investigations of fresh human nerve mechanical properties

occurring within a 3 hours time window.

These results highlighted similar biomechanical behaviour for nerve tissues, i.e. frequency-dependant viscoelastic properties, but also underlined the disparity between species and storage/preservation techniques (embalmed (Barberio et al., 2018) versus fresh) which might explain the large differences observed in stiffness measured.

Overall, fresh rat sciatic nerve displayed frequency-dependant viscoelastic properties, with the storage modulus consistently greater than the loss modulus over time. The characterisation of the mechanical properties of soft tissues is still a challenge due to the variability of the tissues themselves, e.g nerves are non-homogenous tissues and their structure varies throughout and between individuals (Mason and Phillips, 2011), the inconsistency across the mechanical testings as well as the various amount of storage/preservation techniques available (Barberio et al., 2018). Nevertheless, to improve the success of NGCs and the understanding of the impact of the mechanical properties on nerve injury and repair, a good mechanical characterisation of the host site is required. These results presented in this Chapter showed a comprehensive viscoelastic profile of fresh peripheral nerve under dynamic testing, adding general knowledge to the previous literature reporting mostly the mechanical properties of peripheral nerve under static testing (Haftek, 1970; Topp and Boyd, 2006; Tai et al., 2015) or under dynamic testing for embalmed nerve (Barberio et al., 2019). This work will contribute to the development of engineered replacement tissues matching natural tissue properties, and therefore assist in the development of nerve repair strategies.

Chapter 3

Physical and Mechanical characterisation of RAFT-stabilised collagen gels for tissue engineering application

This Chapter is adapted from the paper entitled "*Physical and Mechanical Properties of RAFT- Stabilised Collagen Gels For Tissue Engineering Applications.*" By Celine Kayal, R.J. Shipley and J..B. Phillips, Journal of the Mechanical Behavior of Biomedical Material, November 2019 (Kayal et al., 2019)

When developing engineered tissues, various parameters are to be taken into consideration. For the development of nerve scaffolds, tissue engineers want to minimise the chance of an adverse host response by fabricating materials that are mechanically similar to the host site. These materials needs to be compliant (a property of the macroscale mechanics) and are known to impact cell behaviour (which is influenced by microscale mechanics). RAFT-Stabilisation is a commercially available technique

for creating stabilised hydrogels for tissue engineering applications (see Section 1.6.3). Characterising the mechanical properties of RAFT-stabilised collagen (RsC) gels is critical to ensure that their viscoelastic properties match those of the host tissue (see Chapter 2). It can also enable the interpretation of cell-substrate interactions and the correlation between changes in cell behaviour and these mechanical properties. Collagen gel is a viscoelastic material and its properties are governed by the size, composition and arrangement of the fibrils and their interaction with the fluid trapped within the matrix. The stabilisation process for collagen gels, using hydrophilic porous absorbers, produces dense matrices by rapid expulsion of fluid, and the structure obtained has mechanical properties suitable for tissue engineering purposes. However, protocols to define and compare the physical properties and mechanical behaviour of RAFT-stabilised collagen gels are not standardised across the field.

In this Chapter, the mechanical properties of RsC gels are investigated, and a new empirical correlation that correlates the measured stiffness of gels to varying frequency of strain oscillation is proposed. RAFT-stabilised collagen gels were fabricated and tested using compressive and tensile dynamic mechanical analysis (DMA) (see Section 1.7.1) and rheology testing (see Section 1.7.2). These frequency-dependent measurements allow a detailed quantification of the viscoelastic properties.

3.1 Background

The extra cellular matrix (ECM) in the human body is composed mostly of collagen (Yamazaki et al., 2010) and, among the 28 types of collagen identified (Shoulders and Raines, 2009), collagen type I is predominant. Thus, collagen type I is a natural polymer commonly used as a biomaterial in tissue engineering for numerous applications such as peripheral nerve regeneration (Bellamkonda, 2006; Neel et al., 2013), bone reconstruction (Ferreira et al., 2012; Neel et al., 2013), drug delivery (Rosso et al.,

2004; Wallace and Rosenblatt, 2003), and skin reconstruction (Ma et al., 2003; Neel et al., 2013). Its biodegradability, biocompatibility, high versatility and its ready availability are major advantages for application in the field of tissue engineering (Parenteau-Bareil et al., 2010) and makes collagen type I suitable for implantation (although a very small proportion of the population is allergic to it (Charriere et al., 1989)). Collagen provides both structural support and guidance cues which influence cell proliferation, differentiation, and migration when cells are cultured in/on a collagen hydrogel substrate (Pelham and Wang, 1998; Besseau et al., 2002; Flanagan et al., 2002; Willits and Skornia, 2004; Harley et al., 2006; Levis et al., 2010; Ferreira et al., 2012; Cheema and Brown, 2013). This is key to mimicking the environment in the body, where cell interactions with the extra-cellular matrix (ECM) produce a traction-induced signal directly dependent on the mechanical constraints provided by the ECM (Baranauskas et al., 1998; Ghosh et al., 2007; Yamazaki et al., 2010; Neel et al., 2013). Indeed, it is now widely accepted that the stiffness of the substrate has a direct influence on cell behaviour (Discher et al., 2005).

The mechanical characterisation of biomaterials is a well-established field and a range of different tests and techniques are commonly used (e.g compression, uniaxial tension, shear stress) to establish viscoelastic properties for isotropic and homogeneous materials (Buffinton et al., 2015). As the mechanical values obtained depend on the type of stress applied, it is important to do an extensive analysis using multiple approaches.

The aim of this study was to characterise thoroughly the mechanical behaviour of RsC gels. RsC gels were fabricated using multiple initial volumes, in either 24 or 96 well-plates, using the CC RAFT process (Levis et al., 2015). First of all, the collagen density was calculated based on measurements of the final dimensions of the gels, and variation in mechanical response of RsC gels under a sinusoidal load with frequency-dependent oscillations was reported. Next, RsC matrices were

tested under compressive, tensile and shear stress across a range of frequencies and their mechanical behaviour was analysed and correlated to the physical properties. Finally, new empirical relationships were determined which link Young's modulus to frequency for each of compressive, tensile and shear loading. These were determined based on regression analysis on the experimental data obtained for each mechanical test, and provide a useful predictor of RsC matrices for future studies.

3.2 Materials and methods

3.2.1 Preparation of RAFT-stabilised collagen gels

The collagen solution was formed using acid-solubilised type I collagen solution from rat tail tendon (2 mg.mL^{-1} in 0.6% acetic acid; First Link, UK). For each collagen solution, the following components kept on ice, and their respective percentage of the final volume, were mixed, in order : 80% (v/v) rat tail collagen type I, 10% (v/v) 10×Minimum Essential Medium (MEM), 5% (v/v) Dulbecco's modified eagle's medium (DMEM), and was neutralised with 5% (v/v) 0.325M sodium hydroxide to achieve physiological pH, thus inducing the collagen gelation process (Ngo et al., 2006; Willits and Skornia, 2004). The collagen solution was pipetted into well plates ($gel_{concentration}$ = 1.64 mg.mL^{-1} and area covered per well plate being 201 mm^2 for 24 well plates and 29.6 mm^2 for 96 well plates) and kept in a humidified cell culture incubator (37°C, CO_2 = 5%) for 10 min to allow gelation. Then, gels were RAFT-stabilised for 15 min using RAFT-absorbers fitting the well plate size (96 and 24 well plates) (Startorius Stedim/Lonza). This step rapidly removes most of the fluid of the hydrogel through the top surface of the gel and so increases the density of the collagen matrix (see Section 1.6.3, Figure 1.9). RAFT-stabilised collagen gels (RsC) were stored in phosphate buffered saline (PBS) solution at 4°C for 24 hours, then measured and tested. For compressive DMA and rheology testing, 4 different batches

of RsC gels (n=4), with three repetitions, were tested, each for five initial volume conditions, $[100; 150; 200; 250; 300]$ μl. For tensile DMA, 4 different batches of RsC gels (n=4), with three repetitions, were tested, each for four initial volume conditions, $[0.8; 1; 1.2; 1.5]$ ml. A total of 108 RsC gels were used. All gels were tested submerged in fluid during mechanical testing.

3.2.1.1 Density of collagen of RAFT-stabilised gels

Gels made in well plates have a uniform and definite distribution of collagen. To define the density of collagen, it was assumed that the well plates are perfectly cylindrical. In the first instance, the volume of the stabilised hydrogel $V_{ps}(ml)$ is defined as

$$V_{ps} = h_{coll} \cdot \pi \cdot R^2 \tag{3.1}$$

where h_{coll}(mm) is the height of the gel measured with the OCAM (see Section 3.2.2) and depends on the initial volume of fully hydrated solution, and $R = 3.25$ mm (the radius of the 96 well plate cylinder). The mass of collagen, m_c (mg), is then found using the following

$$m_c = V_{sol} \cdot 0.8 \cdot 2.05, \tag{3.2}$$

where V_{sol} is the initial volume and the 2.05 mg.mL^{-1} collagen solution represents 80% of the gel solution. Combining Eq.(3.1) with Eq.(3.2) yields

$$\rho_{coll} = \frac{m_c}{V_{ps}}, \tag{3.3}$$

where ρ_{coll} (mg/ml) is the density of collagen in the stabilised matrix.

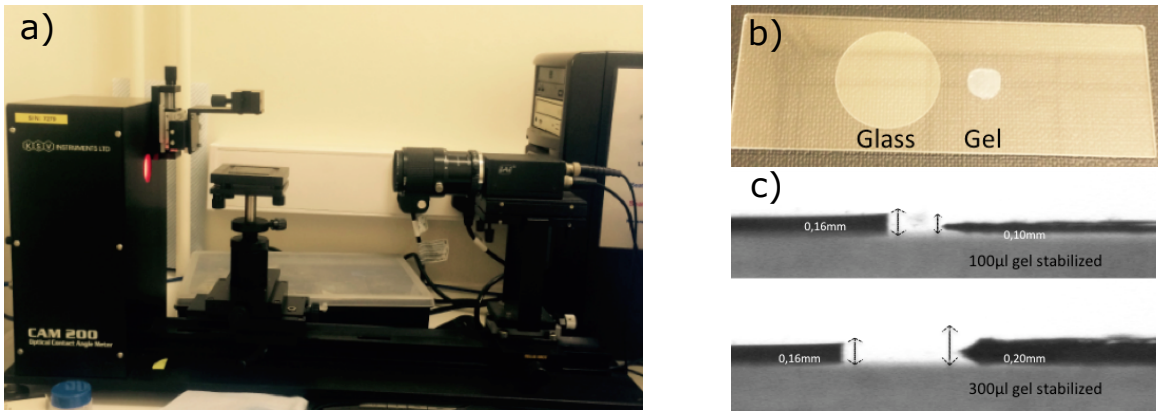

Figure 3.1: Measurement of the thickness of different stabilised collagen gels using a) the KSV's CAM 200 (right picture). b) The gels were put as flat as possible next to a microscope glass of 0.16 mm thickness. c) Example for one 100 μl gel and one 300 μl gel on ImageJ.

3.2.2 Gel Thickness Measurements

The height (thickness) of each RsC gel was measured using an optical contact angle meter (OCAM) (KSV CAM 200), (see Figure 3.1), to establish the new volume of the RsC gel after RAFT-stabilisation. The OCAM is an instrument controlled by a computer and is based on image capture. Images are captured using a camera (512×480) with telecentric zoom optics. This is combined with LED based background lightning at frame intervals from 10 ms to 1000 ms. Mean thickness for each RsC gel was determined from measuring three different positions within the gel.

3.2.3 Dynamic Mechanical Analysis (DMA) of RsC gels

To quantify the viscoelastic behaviour of RsC gels, compressive and tensile Dynamic Mechanical Analysis (DMA) was performed at room temperature (21°C). The measurements were carried out using a BOSE-ElectroForce 3200 instrument (Bose Corporation, ElectroForce, System Group, Minnesota, USA) equipped with a 250g load cell and Wintest DMA application software (Bose Corporation, ElectroForce, System Group, Minnesota, USA), and frequency tests were performed from 1 Hz up to 70 Hz.

3.2.3.1 Compressive DMA

The specimens were disk shaped RsC gels made in 96 well plates with a 6.4 mm diameter. To initiate an experiment, the upper plate was lowered until just touching the upper surface of the RsC gel sample, identified by the load cell properties. To investigate the linear viscoelastic response of the material, tests were run at a constant frequency of 5 Hz for strain amplitudes of $[0.1 - 5]\%$ of the thickness of the RsC gel. To investigate the sweep frequency response, contact was established between the RsC gel and the load cell, the sample was precompressed by 15% of its thickness and then dynamically tested with sinusoidal compression over the following range of frequencies $[1 - 70]$ Hz for a displacement amplitude of $\pm 2\%$ of the thickness of the RsC gel.

3.2.3.2 Tensile DMA

For tensile experiments, the specimens were shaped using a cutter to provide a tapered shape with flared ends and a narrower central section (Figure 3.2). The flared ends of the gel were secured using titanium grips (Figure 3.2). The specimens had a gauge length of 5.0 mm, a width of 4.0 mm, and a thickness depending on the initial volume. To investigate the sweep frequency response, RsC samples were pre-extended by 10% of their gauge length and then dynamically tested with sinusoidal extension over the following range of frequencies $[1 - 70]$ Hz for a displacement amplitude of $\pm 2\%$ of the gauge length of the RsC gel.

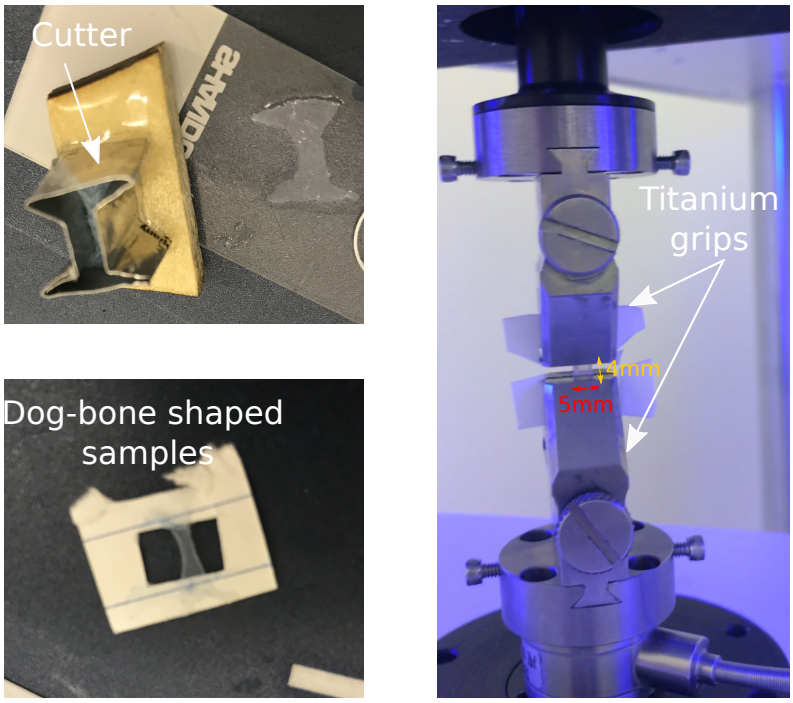

Figure 3.2: Dog-bonne shaped samples preparation process for tensile DMA.

3.2.4 Rheometry

The rheology test was performed using a Discovery Hybrid Rheometer HR-3. An 8 mm diameter parallel plate configuration was used. The sweep frequency response was established at a frequency range $[1 - 20]$ Hz for a 2% applied shear strain to cylindrically shaped RsC gels (initial volume =[150, 200, 250, 300] μl) and the complex shear modulus G^* was measured. The upper limit was determined to eliminate the effect of instrument inertia (Schroyen et al., 2017) leading to major variations.

To investigate linear viscoelasticity, the tests were run following the TA instruments protocol (TA Instruments) at a constant frequency of 5 Hz for an oscillation strain varying in the range of $[0.1 - 100]\%$.

Relation between Young's modulus E and Shear Modulus, G. The orientation of fibres within the stabilised collagen gel is random (Neel et al., 2006) so can be assimilated to homogeneous and isotropic material at a macro-scale. Also for

collagen, the Poisson's Ratio is assumed to be $\mu = 0.5$ (Ahearne et al., 2005; Castro et al., 2016). These assumptions allow us to use the following relationship between the Young's modulus, (E) and Shear modulus, (G) in order to compare results from different types of testing:

$$E = 2G(1 + \mu), \tag{3.4}$$

(see Section 1.7).

3.2.5 Scanning Electron Microscopy of the RsC gels

To determine the impact of mechanical testing on the arrangement of the collagen fibrils within the RsC gels, the samples were observed using scanning electron microscopy (SEM). Samples were fixed in 2% glutaraldehyde solution dissolved in 0.1M cocadylate buffer at $4°C$ for 24 hours. The samples were dehydrated using a graded series of ethanol dilutions in water: 70% for 5 min; 90% for 10 min and 100% absolute ethanol for 3×5 minutes. Finally, the dehydrated RsC gels were mounted on specimen stubs, sputter-coated with gold/palladium alloy, and examined under SEM at 5 kV.

3.2.6 Statistical test

Results are expressed as mean $\pm$ standard deviation. A normality test was conducted. One-way ANOVA test was performed to evaluate the difference between means. A Mann-Whitney U test was used for non normally distributed data. Statistical significance was taken at $p < 0.05$.

3.3 Results

3.3.1 Control of the stabilisation process

A range of initial volumes were used in both 24 and 96 well plates, in order to establish the impact of initial volume on physical properties after the RAFT-stabilisation process. Results are reported in Table 3.1. To quantify the reproducibility of the protocol, the intra-experiment variability (SD_{intra}) for each initial volume (n=12), and the inter-experiment variability (SD_{inter}) describing the variability within all the different batches of gels of the same volume and shape (n=4) were tested. Figure 3.3 shows the SD_{intra} and SD_{inter} represented by the x-axis and y-axis standard deviation values respectively for the thickness of the RsC gels (Figure 3.3a), the percentage of fluid expelled after RAFT-stabilisation (Figure 3.3b) and the collagen density of RsC gels (Figure 3.3c). Results are shown for gels with a top surface area of 210 mm^2 (RsC_{24}), and gels with a top surface area of 30 mm^2 (RsC_{96}).

Figure 3.3a shows the mean thickness (T) of stabilised gels for the nine different initial volumes. The height variability across all the samples was observed to be an average SD_{intra} value of $\pm 3.3 \times 10^{-2}$ mm for RsC_{24}, and $\pm 3.7 \times 10^{-2}$mm for RsC_{96}. Thickness variability across all the different batches was observed to be an average SD_{inter} value of $\pm 2.2 \times 10^{-2}$ mm.

In addition, the fluid loss due to the stabilisation process was calculated via volume changes and is shown in Figure 3.3b. The stabilisation process used RAFT absorbers and produced dense RsC gels by expulsion of $97.2\% \pm 0.3$ fluid for RsC_{24} gels and $96.2\% \pm 0.3$ for RsC_{96}. The fluid expelled for the five initial volume conditions of RsC_{96}, and four initial volume conditions of RsC_{24}, were not significantly different. However, the amount of fluid expelled for RsC_{96} and RsC_{24} gels was significantly

different ($p < 0.0001$).

Figure 3.3c shows the calculated collagen densities with the corresponding standard deviations. The average standard deviation across the RsC_{96} samples was ± 11.6 mg.mL^{-1} and was ± 7.1 mg.mL^{-1} for the RsC_{24} gels. The difference in collagen concentration for the fives initial volume conditions for RsC_{96} was not significant, and this was also true for the four initial volume conditions for RsC_{24}. However, the collagen densities for RsC_{96} and RsC_{24} gels were significantly different, with a p value < 0.0001.

The protocol showed greater reproducibility for the samples with the biggest surface area with a standard deviation of only ± 4.1 mg.ml^{-1}, whereas the smaller gels had a standard deviation ± 8.1 mg.ml^{-1}. The density of collagen varied from the lowest value of 38.1 mg.mL^{-1} for a stabilised thickness of $T_{Stabilised} = 0.25$ mm to the highest collagen density value of 67.3 mg.mL^{-1} for $T_{Stabilised} = 0.13$ mm (Table 3.1). Overall, the average collagen density of the stabilised collagen gel was 61 mg.mL^{-1} for RsC_{96} and 50 mg.mL^{-1} for RsC_{24}. The initial gel geometry induced a significant difference in fluid removal and produced more diluted gels for RsC_{24} than RsC_{96} ($p < 0.0001$).

3.3.2 Mechanical properties of stabilised collagen gel

3.3.2.1 Linear viscoelasticity

Usually, the mechanical properties of a viscoelastic material are independant to the strain applied up to a critical strain level. Beyond this point, the modulus declines, the material's behaviour is non-linear. The linear viscoelastic regime was explored using compressive DMA and rheology under a strain sweep test to determine suitable test conditions for subsequent experiments. For small strains, the compressive DMA results were subject to significant variability due to the limitations of the device in terms of noise. However, for compressive DMA testing, a linear elastic modulus

	Top surface area (mm^2)	Initial Volume (ml)	$T_{Hydrated}$ (mm)	$T_{Stabilised}$ (mm)	Collagen gel density (mg/ml)	Collagen w/v	Fluid Expelled (%)
RsC_{96}	29.76	0.10	3.38	0.09	63.53	6.35	97.23
		0.15	5.07	0.13	67.28	6.73	97.50
		0.20	6.76	0.20	58.14	5.81	97.07
		0.25	8.45	0.25	56.10	5.61	97.04
		0.30	10.14	0.29	58.86	5.88	97.13
RsC_{24}	201.00	0.80	3.98	0.18	38.06	3.80	95.60
		1.00	4.98	0.19	45.25	4.53	96.32
		1.20	5.97	0.22	46.37	4.64	96.38
		1.50	7.46	0.26	50.18	5.02	96.56

Table 3.1: Physical parameters defining the collagen matrix after RAFT-stabilisation for different initial volumes and in 24 (RsC_{24}) or 96 (RsC_{96}) well-plates.

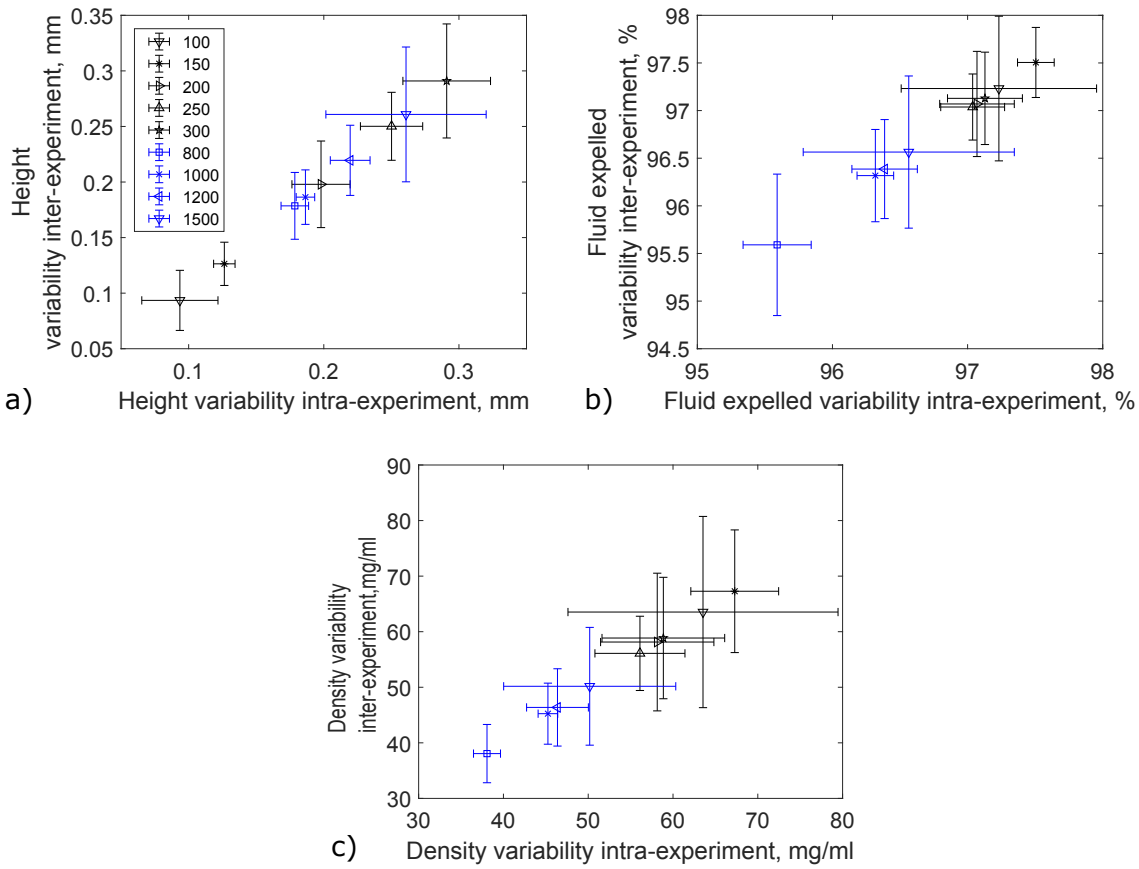

Figure 3.3: a) Mean thickness of RsC gels in mm, b) fluid expelled after stabilisation(%) and c) collagen density for RsC gels in mg.ml^{-1}. The physical properties of the RsC gels are shown for each initial volume (± SD), in blue for gels stabilised in 24 well-plates (RsC_{24}) and black for gels stabilised in 96 well-plates (RsC_{96}).

trend was displayed from 0.01% up to 1.5% strain (Figure 3.4a). So, the viscoelastic properties observed are independent of strain levels in this region, and beyond this point, the elastic modulus drops, and a constant viscosity coefficient can not be defined. Due to the variability of the results, the dynamic properties of the stabilised collagen gel were also analysed under an imposed shear stress. The linear relationship between strain and stress was sustained below approximately 2% strain for both compressive testing and rheology (Figure 3.4b). Therefore, the linear viscoelastic limit was chosen to be at 2% strain, above which the stress-strain relationship is non-linear, in agreement with some previous literature values (Cho et al., 2017)

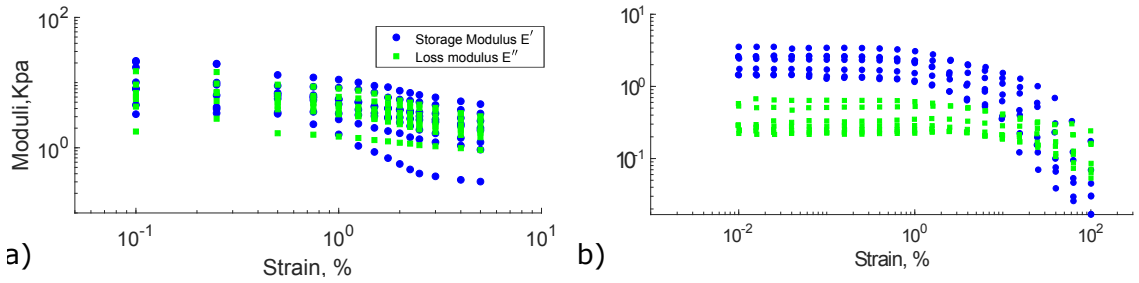

Figure 3.4: Determination of the linear viscoelastic region of RsC gels at 21°C and constant frequency of 5 Hz, a) for an oscillation strain varying in the range $[0.1 - 5]\%$ for compressive DMA testing or b) an oscillation strain varying in the range $[0.1 - 100]\%$ for rheometry testing.

3.3.2.2 Temperature control

As RsC gels properties are investigated to be used as a material for NGC, it is important to be aware of the effect of temperature on the mechanical properties. To establish if the properties of RsC material is temperature-dependant, the viscoelastic properties of the RsC gels were measured under room and body temperature, respectively 21°C and 37°C, under rheology testing. Figure 3.5a shows the complex modulus of RsC gels under a frequency sweep (1-15 Hz). At 37°C, the mean complex modulus was measured to be 7.0 ±0.7 kPa and 6.4 ± 0.9 kPa at 21°C. The difference between body temperature and room temperature does not affect significantly the viscoelastic properties of the RsC gels.

The viscosity of the gel was extracted from the rheology measurements. Figure 3.5b shows the viscosity of RsC gels under a frequency sweep. For a constant strain of 2%, increasing the frequency reduces dramatically the viscosity. This phenomenon characterising pseudoplastic behaviour is observed at both temperature conditions and has been observed previously for hydrated collagen gels (Shivakumar and Maffia, 2014; Cho et al., 2017; Popa et al., 2017).

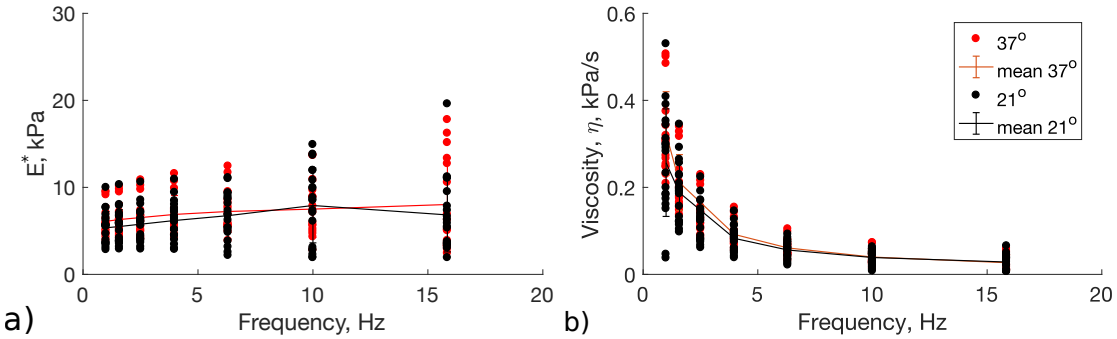

Figure 3.5: Effect of temperature on the rheological behaviour of the RsC gel. a) Complex modulus E* (kPa) of RsC gels function of frequency for T=21°C and 37°C. b) Dynamic viscosity (kPa.s^{-1}) of RsC gels at 21°C and 37°C.

3.3.2.3 Compressive DMA- Frequency Sweep

The complex modulus values E^* (kPa) measured for the stabilised collagen gels under uniaxial compression are presented in Figure 3.6a for eleven different frequencies, in the range $[1-70]$ Hz. The data shown are the mean numbers of $n = 4$ different batches of gels with three repetitions for each of the five different initial volume conditions. A continuous increase of E^* with increasing frequencies was observed with no significant differences between initial volumes. For each frequency, E^* ranges were overlapping. This indicates that all RsC gels behaved similarly under compression.

3.3.2.4 Tensile DMA- Frequency Sweep

Figure 3.6b shows the effect of a frequency sweep ($[1 - 70]$ Hz) on E^* under tensile testing for each of the four different initial volume conditions. E^* remained roughly constant (100 kPa) up to the yield point at 15 Hz before collapsing, characterising permanent elongation. All RsC gels exhibited a similar behaviour under tensile DMA.

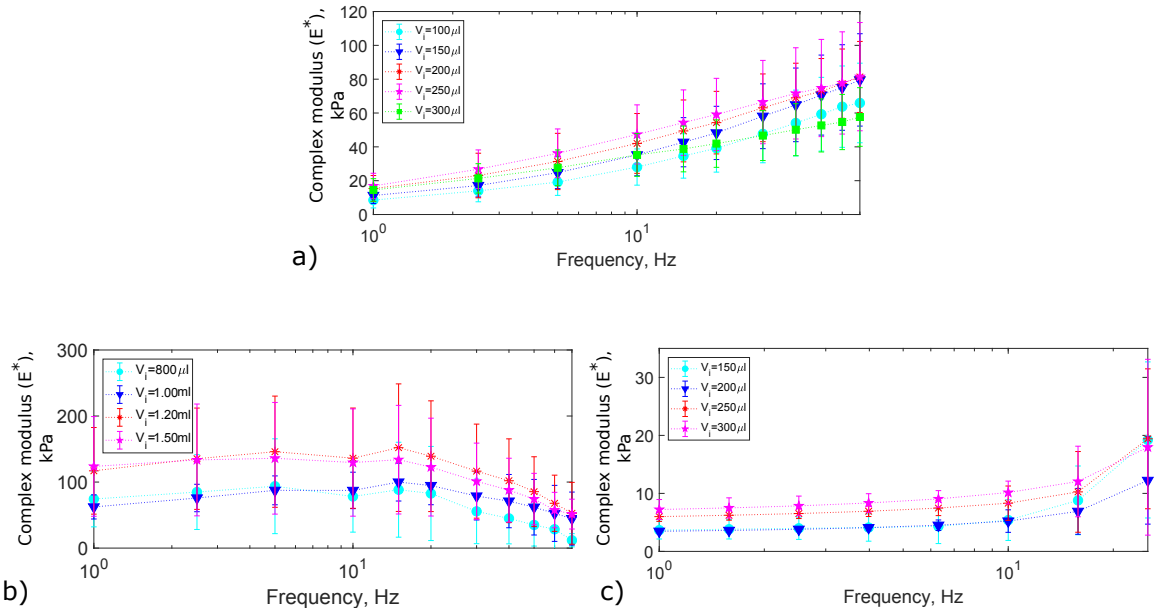

Figure 3.6: The complex Modulus (E*, kPa) as a function of the frequency (Hz) for each initial volume condition of the RAFT-stabilised collagen gels (a) for a sinusoidal compression [1-70]Hz, (b) for a sinusoidal extension [1-70]Hz, (c) for an oscillating shear strain [1-15]Hz.

3.3.2.5 Rheometry- Frequency Sweep

Four different initial volumes were analysed using rheometry (Figure 3.6c). The complex shear modulus G^* values obtained were converted to E^* using Eq.(3.4). As observed under tensile testing, E^* remained constant up to 15 Hz across all samples (Figure 3.6c).

RAFT-stabilised gel behaviours in each of the three dimensions were analysed using different techniques. Under uniaxial compression (Figure 3.7a), the RsC gels had a viscoelastic response. From 1 to 30 Hz, the viscous component, the loss modulus (E") ranged from 10 to 40 kPa, and was consistently ∼2.5 kPa higher than the elastic component, storage modulus (E'). Comparatively, from 40 to 70 Hz, the tendency changed and the behaviour seemed to become more elastic.

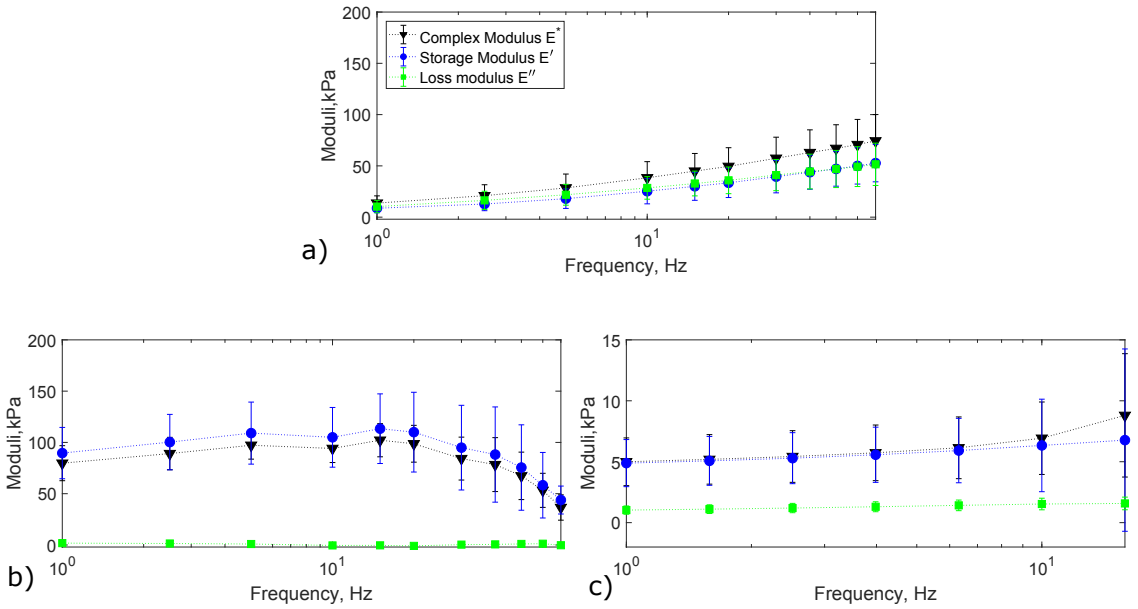

Figure 3.7: Complex Modulus (E*, kPa), storage modulus (E′, kPa) and loss modulus (E″, kPa) as a function of frequency (Hz) at strain amplitude of ±2% for (a) Compressive DMA (b) Tensile DMA and (c) Rheology testing.

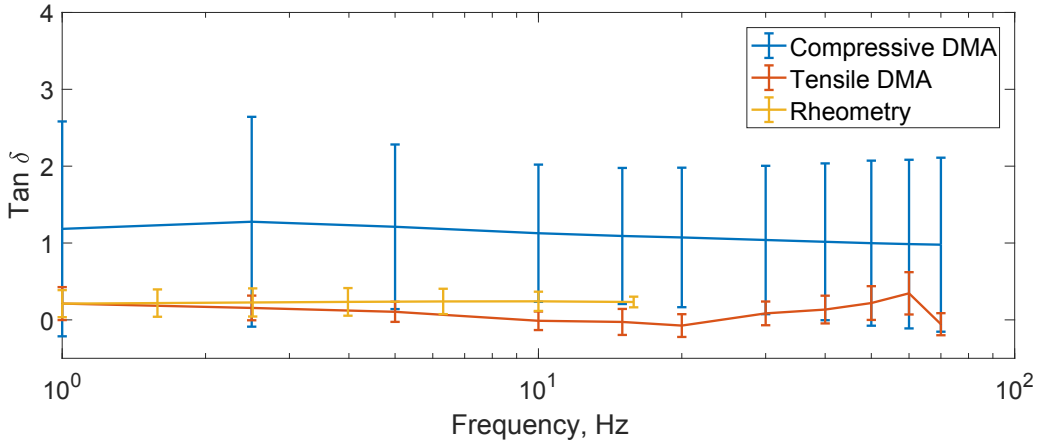

Figure 3.8: Tanδ as a function of frequency (Hz) for compressive DMA (in blue), tensile DMA (in orange) and Rheology (in yellow).

By comparison, Figure 3.7b shows the mechanical behaviour under tensile testing. The elastic component, E', clearly predominates as the value of the loss modulus was almost zero kPa for all the frequencies. So under tensile load, the dense collagen matrix gels displays an elastic behaviour. Also, it can be reported that the tensile modulus is 1.4 to 7.7 times bigger than the compressive modulus.

For the rheometry measurements (Figure 3.7c), the behaviour was viscoelastic as the E" value was non negligible. The stiffness of the gel under shear stress was around 5 kPa, so 2.6 times softer than under compression, for the corresponding range of frequency ($[1 - 15]$ Hz).

In order to compare the absolute value of dynamic properties under different loading, Figure 3.8 shows tanδ, the ratio between the loss and storage modulus and indicates how the RAFT-stabilised collagen gels absorbs and disperses energy under different loading conditions. Under compressive DMA, tan$\delta \geq 1$, the material displays viscoelastic behavior with a tendency to be more viscous. However, under tensile DMA and shear stress the RAFT-stabilised collagen gel is more elastic tanδ ≤ 0.5.

3.3.2.6 Effect of frequency on mechanical properties

In order to characterise the relationship between mechanical properties and frequency, a regression analysis was performed to find an empirical expression which closely correlated the experimentally measured data to the strain rate. A set of formulae was produced to describe the correlation between the complex modulus (E^*) and frequency for rheometry, compressive and tensile DMA, through numerical fitting. The effects of the frequency sweep on the complex modulus for the compressive DMA, tensile DMA and rheology were formulated as :

$$E^*_{compressive}(f) = 15.93 * \log(f) + 4.348, \quad R^2 = 0.9803, \tag{3.5}$$

$$E^*_{tensile}(f) = 96.37 * \exp^{-((f-17.36)/53.41)^2}, \quad R^2 = 0.9525, \tag{3.6}$$

$$E^*_{rheology}(f) = 4.881 * \exp^{(f*0.037)}, \quad R^2 = 0.9966, \tag{3.7}$$

where the complex Modulus E^* is in kPa and the frequency f is in Hz (Figure 3.9a-c). The fitted logarithmic, Gaussian and exponential curves are appropriate models to describe the effect of frequency sweep on the stiffness of RsC gels, and the comparison with the experimental data is shown in Figure 3.9.

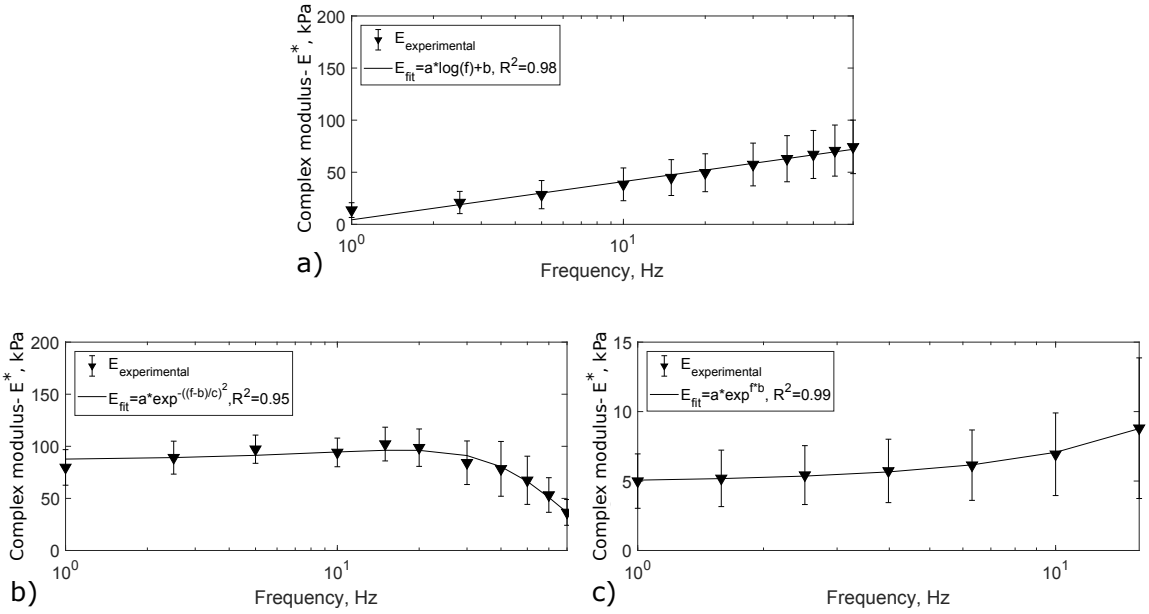

Figure 3.9: Fitted curves to describe the relationship between complex modulus (E^*, kPa) and frequency (Hz) for (a) Compressive DMA (b) Tensile DMA and (c) Rheology.

3.3.2.7 Morphological characterisation

Figure 3.10 shows SEM micrographs of the top surface of RAFT-stabilised collagen gels after various types of mechanical loads. Figure 3.10a shows the surface image of a RsC gel and Figures 3.10b, 3.10c and 3.10d show RsC gels after compressive, tensile and rheology analysis, respectively. Before any testing, the RsC gels displayed a randomly orientated porous architecture with visible and entangled fibrils. The same pattern was observed for the gels after tensile testing. RsC gels after rheology and compressive testing (Figure 3.10b and 3.10d) demonstrated a more compact and less porous surface matrix where the collagen fibrils seemed to have merged together and were harder to distinguish. The images show that the seemingly random organisation of the fibrils on the surface was not disturbed by the mechanical characterisation analysis.

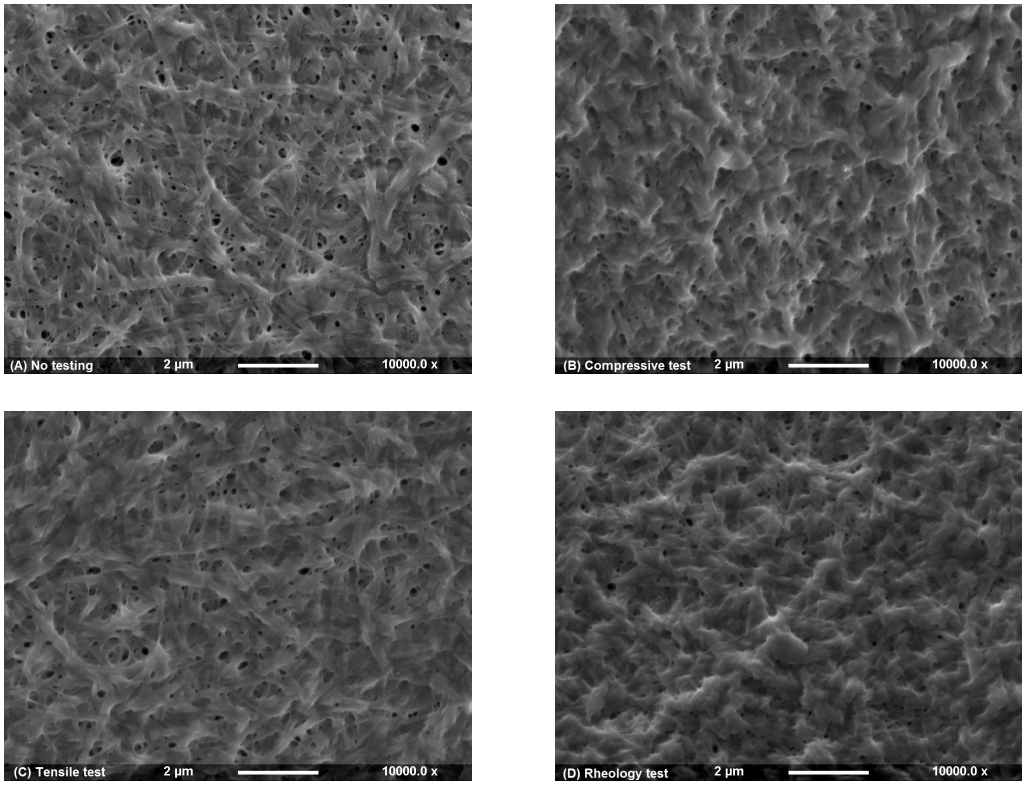

Figure 3.10: Scanning electron microscopy images. Top surface view of RAFT-stabilised collagen (RsC) gels (A) Before testing then following (B) Compressive load, (C) Tensile load, and (D) Rheology. (Scale bar = 2 μm).

3.4 Discussion

The RAFT-stabilisation process (Levis et al., 2015) was applied to mechanically weak, fully-hydrated collagen hydrogels (Willits and Skornia, 2004; Brown et al., 2005), as this has been shown previously to produce collagen structures with improved mechanical stiffness comparable to soft tissue values, by the rapid removal of fluid (Brown et al., 2005; Neel et al., 2006; Cheema and Brown, 2013). This technique has many tissue engineering applications (Levis et al., 2015) (see Section 1.6.3) and is now standardised, rapid, simple and not experience-dependent, through the use of commercially available RAFT-absorbers. The stiffness parameters characterising this type of stabilised collagen within the literature (Neel et al., 2006; Bitar et al., 2007; E.Hadjizadeh, V. Mudera, 2009) have been defined using multiple methods, across a range of gel compositions, and therefore values are not directly comparable.

Levis et al. (2015) provided a qualitative analysis showing that the dense collagen matrices obtained after RAFT-stabilisation were able to withstand handling and be attached to *in-vivo* like tissues using fibrin glue or similar. In this study, the physical and viscoelastic properties of RAFT-stabilised collagen gels were assessed for the first time, using a comprehensive range of quantitative measurements techniques. Physical properties, such the collagen gel density and the fluid loss due to the stabilisation, were assessed for two different dimensions of gels made in standard multi-well plates ($RsC_{24} = 29.76$ mm^2 and $RsC_{24} = 201$ mm^2) with a range of different initial volumes of collagen solution.

It has been reported previously that during plastic compression about 97% of fluid is expelled (Neel et al., 2006) by a downward fluid flow (Brown et al., 2005), which is consistent with the 96-97% measured in this study for the upward fluid expulsion.

Furthermore, for RsC_{96} gels, 1% more fluid was removed compared to the RsC_{24} gels, and this has a direct impact on the final concentration of collagen gel (61 $mg.mL^{-1}$ for gels in RsC_{96} versus 50 $mg.mL^{-1}$ for gels in RsC_{24}). This phenomenon could be due to the use of different sizes of hydrophilic porous absorbers (Levis et al., 2015) for stabilisation. The surface area covered for the RsC_{24} gels is larger and so the weight of the fluid absorbed is differently distributed. For a given surface area and volume, the thickness of the RsC gels can be consistently predicted and so defined using industrial absorbers.

The dense collagen type I structure retained approximately 3% of the initial fluid volume trapped within the fibres, and displayed a viscoelastic behaviour under compressive DMA ($\tan\delta \sim 1$). Under shear stress, the material displayed a more elastic behavior with a $\tan\delta < 0.5$.The RsC gels were two orders of magnitude stiffer than fully hydrated 1.5 $mg.mL^{-1}$ collagen gels under a 2% shear stress reported in previous studies (Willits and Skornia, 2004). This result confirms the production of a stiffer matrix by the fluid removal process (Brown et al., 2005; Neel et al., 2006) with a tissue-like mechanical strength (Brown et al., 2005; Levis et al., 2015). The storage modulus of RsC gels under compressive and shear dynamic loading is of the same order of magnitude as soft human tissues such as brain ($[0.1-1]$ kPa), fat ($[0.5-5]$kPa), kidney (2.5 kPa), lung ($[2.5-9]$kPa), liver ($[3-5]$kPa), cornea (50 kPa) (Saraf et al., 2007; Geerligs et al., 2008; Sachot et al., 2014; Seifert et al., 2014), which makes RsC gels attractive for various medical applications.

Under tensile stress, the RsC gels displayed an elastic behaviour (low $\tan\delta$). After 15 Hz, the cross sectional area of the sample is probably decreasing. As the value of E^* after 15 Hz is calculated on original cross sectional area, then it appear to decrease, this phenomenon is in fact called necking and failure will occurs soon after. Consistent with the Buffinton et al. (2015) study, the yield point is hypothesised to be reached due to decreasing hydration level of the gels, which causes a strength loss inducing

deformation that will potentially leads to a material fracture. The collagen structure obtained is also 20 times stronger (approximately 100 kPa) than fully-hydrated collagen gels (5 kPa for a collagen concentration of 1.5 mg.mL^{-1})(Krishnan et al., 2004) under tensile testing (at 5 Hz and 2% strain), which is consistent with previous studies (Buffinton et al., 2015; Neel et al., 2006) reporting increased tensile strength after stabilisation. After stabilisation, the collagen gels display similar viscoelastic properties, under tensile testing, than previously measured fresh rat sciatic nerve in Chapter 2, which also displayed a predominant elastic behaviour confirm by the constant low tanδ observed over the frequency sweep.

The results reported here are consistent with previous studies showing the moduli of hydrogels measured in tension is higher than moduli measured in compression(Buffinton et al., 2015) which can be explained by the flow of fluid within the hydrogel during the testing. For RsC gels, the tensile modulus was measured to be 1.4 to 7.7 times stiffer than the compressive modulus, and viscoelastic properties under tensile DMA were similar to those of fresh rat sciatic nerve measured previously in Chapter 2. This confirms that RsC gels have potential to be taken forward for nerve tissue engineering approaches.

The data reported here can be used to predict the behaviour of RAFT-stabilised collagen gels under different mechanical loads, for example to identify limitations such as material failure during tissue engineered scaffold applications (Drobnič et al., 2006). The numerical fitting performed on the experimental data provides a set of predictive formulae (Eq.(3.5)-(3.7)) to describe the correlation between the dynamic modulus, E^*, and the frequency for rat tail collagen. This will be of use in the field of tissue mechanics, as well as studies establishing the fundamentals of the cell-substrate interaction using collagen-based materials.

SEM images indicated random fibrils orientation so the RsC matrix can be assimilated to an isotropic material at a macro scale. The fibrils have a less distinct

fibrillar structure to that shown in the literature for the plastic compression protocol (Neel et al., 2006). In Neel et al. (2006) study, a dense and compacted appearance of fibrils was observed after double compression. A similar organisation was observed for the RsC gels after both compressive DMA and rheology. The recurrence of these tests for each frequency can cause a reorganisation of the collagen fibrils and lead to analogous pattern that resembles gels after a second compression (Neel et al., 2006). Also, the extension test on the RsC gel did not impact the random orientation of the collagen at the fibrils scale (Neel et al., 2006).

Overall, results demonstrated that the final collagen gel density and fluid loss percentage under RAFT-stabilisation depended on the initial geometry used. A viscoelastic response was induced by both compressive and shear stress under a frequency sweep test. Under a tensile stress frequency sweep, the RsC gels exhibited predominant elastic behaviour also observed with fresh rat sciatic nerve tissue, and reached a permanent deformation at 15 Hz. Different initial volumes of collagen solution used did not impacted the stiffness of RsC gels for a given geometry. These results provide quantitative data, and this material, RAFT-stabilised collagen will be used to develop a stiffness gradient model, to guide future studies into cell-collagen interactions.

Chapter 4

Development, optimisation and characterisation of collagen gel stiffness gradients

The second part of this Chapter is adapted from the paper entitled "*Mechanoresponse of neural cells to physiological stiffness cues.*" By Celine Kayal, E. Moeendarbary, R.J. Shipley and J.B. Phillips. *Under revision*

This Chapter focuses on the creation of a collagen stiffness gradient with physiological mechanical properties to be used as an optimised matrix for nerve regeneration. First of all, the development and optimisation of a design and protocol to fabricate collagen defined-stiffness gradient profiles is described. Secondly, the geometrical, physical and mechanical properties of the created gradients are characterised, before moving on to test neuron mechanosensitivity to these gradients in the next Chapter.

4.1 Introduction

The extracellular environment is physiologically and mechanically inhomogeneous, therefore the use of hydrogel substrates with stiffness variation or gradient have the potential to mimic the natural or pathological ECM (Lee et al., 2018). In addition, two recent studies have highlighted the response of neural and supporting cells to stiffness gradients (Koser et al., 2016; Evans et al., 2018), referred to as durotaxis (Lo et al., 2000) (see Section 1.6.1), highlighting the current relevance of exploring rigidity gradients for peripheral nerve tissue-engineering. Indeed, improved peripheral nerve repair strategies need to be developed and one of the emerging research avenues in tissue engineering is the study of cell-substrate interactions to underpin the design of conduits that support and guide neuronal regeneration. The stiffness of the extracellular matrix significantly influences cell behaviour (Franze et al., 2013), and there is growing interest in understanding the complexity of cell-substrate mechanobiological interactions (Smith Callahan, 2018). Although previous studies have focused on how PNS cells respond to a substrate of uniform stiffness (Rosso et al., 2017d,c), the physiological extracellular environment is mechanically inhomogeneous (Sunyer et al., 2012; Lee et al., 2018). These stiffness differences play a substantial role on cell behaviour, i.e. differentiation, migration, shape and directionality (Franze et al., 2013; Hadden et al., 2017; Rosso et al., 2017b; Krieg et al., 2019), and tissue engineers have been working on multiple methods to optimise the matrix organisation (Smith Callahan, 2018).

Over the past 15 years, several techniques have been developed to fabricate hydrogels with stiffness variations or gradients. The most common approach is to modify the polymer concentration within the pre-polymer solution leading to a gradient of

stiffness after polymerisation. To do so, some groups are using microfluidic channel devices (Burdick et al., 2004; Zaari et al., 2004; Isenberg et al., 2009; Sundararaghavan et al., 2009; Orsi et al., 2017; Hartman et al., 2016), or a non-microfluidic gradient maker (Du et al., 2009; Nemir et al., 2010; Diederich et al., 2013; Hadden et al., 2017).

Another existing technique is Ultraviolet (UV)-Photopolymerisation, where the degree of polymerisation or cross linking is controlled by the penetration depth of the UV irradiation. To change the polymerisation, a photomask (Wong et al., 2003; Kidoaki and Matsuda, 2008; Marklein and Burdick, 2009; Nemir et al., 2010; Khetan and Burdick, 2010; Tse and Engler, 2011; Vincent et al., 2013; Stowers et al., 2015; Evans et al., 2018) or a sliding mask (moving opaque mask) (Johnson et al., 2005; Marklein and Burdick, 2009; Kloxin et al., 2009, 2010; Sunyer et al., 2012; García et al., 2014; Hasan et al., 2018; Tong et al., 2016) are used to vary the hydrogel light exposure time. A localised light irradiation by microprojection of a focused beam can also allow the formation of a stiffness gradient (Kawano and Kidoaki, 2011; Mosiewicz et al., 2014; Stowers et al., 2015; Yanagawa et al., 2015).

Less widespread techniques, such as microfluidic based lithography (Cheung et al., 2009; Kuo et al., 2012), control of the thickness of the gels (Kuo et al., 2012; Chao et al., 2014; Shu et al., 2017), micropatterning (Gray et al., 2003) or temperature control (freezing/thawing) (Kim et al., 2015) have been developed to fabricate hydrogel stiffness gradient with variable mechanical properties. However, these techniques are limited by the use of specialised apparatus or specific material requirements (Li et al., 2019).

The material used in the majority of cases in the literature is polyacrylamide (PAAm) gel (Wang et al., 2001; Wong et al., 2003; Zaari et al., 2004; Isenberg et al., 2009; Cheung et al., 2009; Tse and Engler, 2011; Kuo et al., 2012; Sunyer et al., 2012; Vincent et al., 2013; Diederich et al., 2013; García et al., 2014; Hartman et al., 2016; Hadden et al., 2017; Evans et al., 2018; Lee et al., 2018). This hydrogel has the

advantage of being transparent and its stiffness can be varied readily across a wide range by modifying the monomer and cross-linker concentration (Lee et al., 2018). Other commonly used hydrogels are Poly(ethylen glycol) (PEG) (Burdick et al., 2004; Du et al., 2009; Kloxin et al., 2009, 2010; Nemir et al., 2010; Mosiewicz et al., 2014; Yanagawa et al., 2015; Tong et al., 2016) and polydymethylsiloxane (PDMS) (Gray et al., 2003; Wang et al., 2012; Chao et al., 2014; Shu et al., 2017). Finally, some less popular hydrogels are used in tissue engineering for the fabrication of stiffness gradient, such as gelatine (Kidoaki and Matsuda, 2008; Kawano and Kidoaki, 2011; Kidoaki and Sakashita, 2013), hyaluronic acid (HA) (Marklein and Burdick, 2009; Khetan and Burdick, 2010), alginate (Stowers et al., 2015), Polyvinyl alcohol (PVA) (Kim et al., 2015) and collagen (Hadjipanayi et al., 2009; Cheema and Brown, 2013).

For the development of nerve repair solutions, collagen is a good candidate as it represents the major component of the extra cellular matrix of the peripheral nervous system and supports cellular nerve function from development to adulthood (Koopmans et al., 2009) (see Section 1.6.3). It is also known as a suitable cell substrate for use in nerve tissue engineering (Sundararaghavan et al., 2008; Neel et al., 2006; Yang et al., 2004; Phillips et al., 2005; Georgiou et al., 2013; Stylianou, 2017).

Several methods can be used to modify the mechanical properties of collagen, such as cross linking collagen using enzymes or irradiation (Zaari et al., 2004; Sundararaghavan et al., 2008; Isenberg et al., 2009; Kidoaki and Sakashita, 2013) or blending collagen with other polymers, e.g. with fibrin (Schuh et al., 2018). However, these techniques alter the structure of the matrix and can result in the addition of signalling cues and other variables that confound studies seeking to isolate the influence of material gradients on neurite behaviour.

Here, a robust and reproducible protocol for fabricating collagen-based hydrogels with defined gradient fields is presented, where the structure of the collagen fibrils is not altered and collagen concentration is the only varying parameter. In Chap-

ter 3, the mechanical properties of collagen gels were shown to depend on collagen density and the hydration rate, which affect the positioning of collagen fibres. Here, this information is used as a starting point to develop a 'gradient maker' which is cost-efficient, easy-to-use and non experience-dependent, in order to make rapidly reproducible, well-defined stiffness gradient gels by varying the collagen concentration. Several methods were adapted and a protocol was refined based on a trial-and-error optimisation. This work is described in the first part of this Chapter. It led to the adaptation of a tissue engineering technology for generating gradients within RAFT-stabilised collagen gels (Levis et al., 2015; Cheema and Brown, 2013), designing and 3D printing moulds to yield model collagen hydrogels with defined gradients of stiffness. Physical and mechanical properties of the gradient gels were established using atomic force microscopy (see Section 1.7.3). Overall, a new protocol to fabricate 2D collagen gradient culture model is proposed to be used in the future for the investigation of the influence of various mechanical signals on neural growth.

4.2 Design and development of the gradient device

Here is described the development of a quick and reproducible method to fabricate pure collagen concentration gradients, and therefore stiffness gradients without altering the properties of the matrix for the field of tissue engineering. In order to do so, it is helpful to follow the steps of the conventional design process as shown in Figure 4.1.

First of all, the main product specifications must be defined, e.g. intended use, product characteristics, and the requirements expected for the device have to be set. For an hydrogel gradient maker, the device/method should :

1. allow fabrication of reproducible defined concentration/stiffness gradient
2. be easy to manufacture
3. be easy to manipulate in a culture lab, i.e. sterilisation
4. allow a quick learning curve for the user
5. be non experience-dependant
6. allow cost-effective experiments

The specifications can be updated as the device/protocol is developed or modified. Initially, a first idea is explored, tested and then modified/optimised if necessary following a trial and error process. In this Section, the numerous steps leading to the development of the right design of collagen gradient maker following this trial-and-error optimisation process will be detailed. The collagen solution used to test the gradient maker was prepared following the protocol described in Section 3.2.1. After alteration of the collagen density, the gels were stabilised following either the

protocol described in Section 3.2.1 (RAFT-stabilisation) or the protocol described by Brown et al. (2005) (plastic compression) depending on the shape of gels to obtain a tissue-like collagen sheet. The protocol used is described as required. A summary of the several protocols and designs used is given in Table 4.1 and the final product specifications are given in Table 4.2.

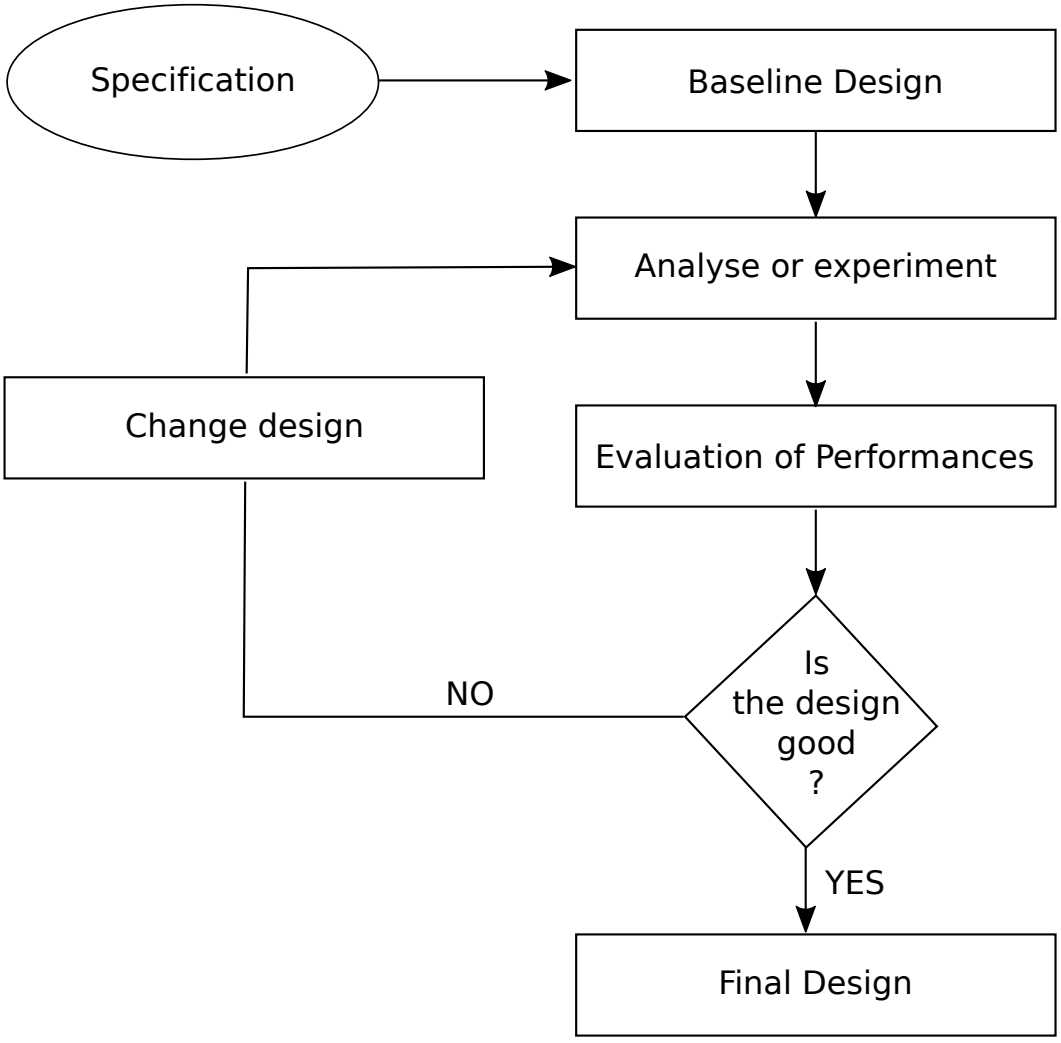

Figure 4.1: Conventional design process.

4.2.1 Trial-and-error optimisation

As shown in Chapter 3, the mechanical properties of collagen gels depend on the collagen concentration. Therefore, for the development of a collagen gradient maker, it seemed sensible to find a consistent way to vary and control collagen density to produce well-defined stiffness gradient substrates.

4.2.1.1 Collagen gradient using centrifugation

Centrifugation is a separation process using centrifugal forces to spin down molecules depending on their size, and in the collagen preparation, the collagen protein is the biggest molecule. Thus, the first hypothesis was to use centrifugal forces to induce a collagen density gradient within a collagen solution.

As a first attempt, Eppendorf tubes (Design 1), were filled with collagen solution and centrifuged at different time periods (in minutes) and spinning rates (in rotation per minutes, rpm) at 4° Celsius to avoid gelation during the centrifugation step. Then, gels were kept 10 min in the incubator to allow gelation of the gradient gel. The design of the Eppendorf tube, with a lid at the top was a great feature to avoid any contamination when moved from the centrifuge to the incubator. To the author's knowledge, no other studies have investigated the use of the centrifugation to obtain a collagen gradient. The collagen solution turned into a gel after undergoing centrifugation, suggesting that collagen fibrils were potentially not altered during the centrifugation process. This process allowed the formation of a visible collagen density gradient (see Figure 4.2a). However, the action of removing the gel from Design 1 damaged the gels, and therefore also the gradients obtained. In addition, the cylindrical geometry of Design 1 led to the formation of a cylindrical collagen gel and so, added an additional spatial variation of the collagen density after plastic

compression. Details are given in Table 4.1.

Following the conventional design process, Design 1 had to be adapted. Taking into account the first observations, Design 2 had to allow manipulation of the gel without damaging the matrix structure. Also, the shape of the design had to be uniform to not add additional spatial variation of the collagen solution that could lead to an additional collagen concentration variation after the stabilisation process.

As Design 1 was not satisfactory, specific moulds were developed using a CAD design software to overcome the limitations observed, such as the container geometry and the poor accessibility to the gel. A square tube was 3D designed (Design 2), with a sliding side using Catia (CAD design software, Dassault Systems, France) in order to address the limitation related to the cylindrical shape. The addition of an open side allowed an easy access to the gradient gel and a lid was added to limit the risk of contamination when moved from the centrifuge to the incubator (feature kept from Design 1). Design 2 is shown in Figure 4.2b and details are given Table 4.1.

The body part of Design 2 was made with simple slots to maintain the sliding side in place (dimensions (W $\times$ D $\times$ H): $15 \times 15 \times 35$ mm, and wall thickness 2 mm). Two different versions were printed (horizontally and vertically) using polylactic acid (PLA) with 40% to 90% infill density, representing the amount of PLA filaments printed inside the object. The printing time was $\sim 10 - 20$ hours for 8 moulds, including the three parts: the body, the lid and the sliding side (see Figure 4.2b), using low accuracy (0.12 mm) printing and material filling density of 40%.

3D printing vertically using 90% infill density gave better quality moulds than printing horizontally using lower accuracy. With lower accuracy settings, holes were visible in the printed mould. The printed moulds were 0.05 to 0.01 mm bigger than the initial design measures due to the accuracy of the 3D printer. In addition, moulds were very fragile and collagen solution was leaking from the grooves, therefore Design 2 was not investigated further under centrifugation forces. To address this problem,

Design Version Version	**CAD Software**	**Device**	**V_{max}** mg.ml^{-1}	**Technique**	**Observation**
1	N/A	Eppendorf tube	1.5	Centrifuge gel in the tube	Visible Gradient. Removal destroy the gel.
2	CATIA	3D printed square tube	6	N/A	Weak design. Important liquid Leakage.
3	AutoCAD	3D printed square tube	7.68	Centrifuge gel in the mould	Not watertight.
4	AutoCAD	3D printed square tube with plexiglass side	3.36	Centrifuge gel in the mould	Leaky under centrifugation.
4	AutoCAD	3D printed square tube with plexiglass side	3.36	Add collagen solution with different concentrations step-by-step	Waterproof. Gradient shape. not predictable.
4	AutoCAD	3D printed square tube tube with plexiglass side	3.36	Add collagen solution with different concentrations in one go	Waterproof. Gradient Shape not predictable.
5	AutoCAD	3D printed well plate	1.5		Success. Final Design.

Table 4.1: Optimisation of the Gradient Maker.

the next design had to be reinforced by increasing the thickness of the walls and made watertight by modifying the groove system.

A new version of the mould, Design 3, was designed using *AutoCad*, a more user-friendly CAD design software, and improved, to take into account failures from the previous trial. The thickness of the design was increased (dimensions: $24 \times 24 \times 35$ mm, and wall thickness 4 mm). To address the watertightness limitation, additional slots were added, and grooves were added in the slots.

The printing time was approximately 15 hours for 1 mould with high accuracy printing (0.06 mm) and a high material filling density of 90%. This new design was physically more resistant. To reduce the printing time, another trial using 50% filling density ($\sim$10 hours) showed no holes in the printed structure and produced an equally resistant mould. To avoid any fitting problems, the fitting parts (lid and sliding side) were designed 0.1 mm smaller than the body part (see Figure 4.2c). Collagen solution was used to test Design 3.

Increasing the thickness of the walls of Design 3 gave a more resistant mould, tested using collagen solution. The addition of the grooves within Design 3 were not sufficient to retain the collagen solution, leakage also occured at the groove site. Leakage remained a serious limitation. Moreover, for Design 3, the inside volume was $7.68ml$, which, in the future, will not allow for cost-effective experiments as a large volume of collagen solution would be required for each experiment. In terms of limitations to address, the total inside volume of the design had to be redefined and a solution had to be found to improve the waterproof characteristics.

For Design 4, the walls were kept thick (4 mm) and the total volume inside was reduced to $V_{tot} = 3.36$ ml to make it more suitable for future experiments, i.e. more cost-effective. In order to address the watertightness issue, the additional grooves were removed, but the sliding part and the slots were kept to hold the sliding side and to allow access to the gel (see Figure 4.3). Plexiglass was used for the sliding

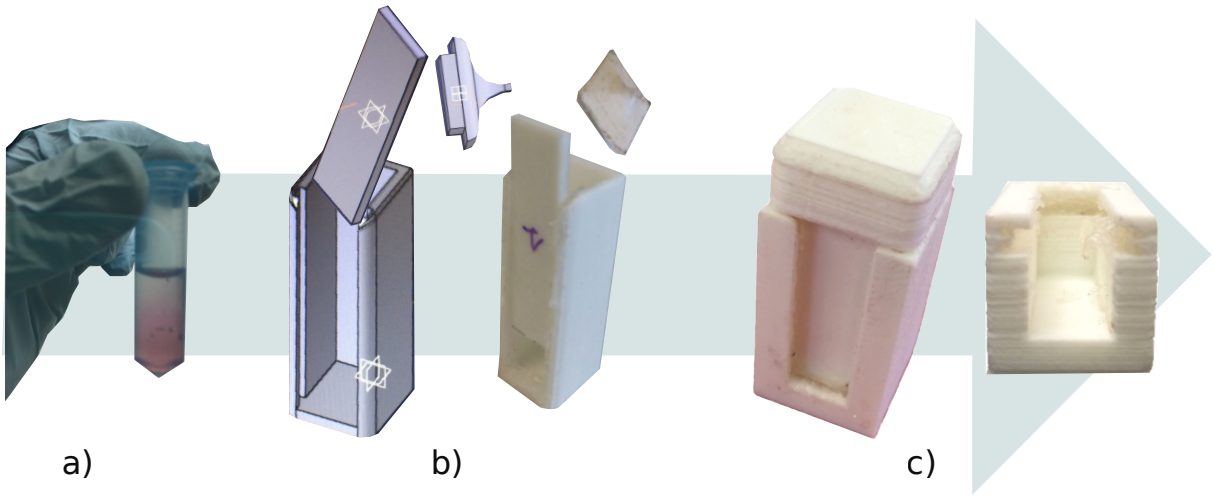

Figure 4.2: a) Gradient of collagen density obtained by centrifugation of collagen solution in an Eppendorf tube (Design 1). b) CAD design of Design 2 (body part, sliding part and lid), and the corresponding image of the 3D-printed version. Dimensions (W × D × H): 15 × 15 × 35 mm, and wall thickness 2 mm. c) 3D printed version of Design 3, more robust, but not watertight. Dimensions: 24 × 24 ×35 mm, and wall thickness 4 mm.

part (see Figure 4.4a).

Tests with collagen gel solution using Design 4 showed that if not centrifuged the mould was not leaking and retained the collagen solution, and therefore could be a good candidate to make square shaped collagen gels that would not induce an additional variation in collagen concentration after stabilisation. The waterproof property was not satisfied under centrifugation forces (Table 4.1). The plexiglass sliding side allowed the visibility of the collagen gel in the tube which was useful to check the formation of a density gradient (see Figure 4.4a). It was also possible to access and manipulate the gel, allowing plastic compressed stabilisation without destroying the collagen structure. In addition, Design 4 was easy to use, to sterilise and allowed cost-efficient experiments. After several design modifications, and still facing serious watertightness limitations under centrifugation, the next step was to test Design 4 using a different protocol.

4.2.1.2 Collagen gradient using diluted collagen solutions

As tests on Design 4 showed it to not leak if not under centrifugation forces, two other methods to make collagen density gradients were investigated. The two methods required collagen solutions of different concentrations (0.80, 1.00, 1.25, 1.50, 1.64 $mg.ml^{-1}$), diluted using hydrogen chloride (HCl) (see Figure 4.4). The range of collagen concentrations varied from normal collagen solution (1.64 $mg.ml^{-1}$) to the most dilute solution allowing formation of a visible collagen gel (0.80 $mg.ml^{-1}$).

1) Step-by-Step gradient: For the method (1) a density gradient was made using the aforementioned dilutions of collagen solution. Each solution, from the more concentrated to the more diluted were added on the top of each other (see Figure 4.4b). Between each step, the solution was left to set for 10 min at room temperature (21°C). After adding the last solution, the resultant collagen gel was left in an incubator (37°C) for 10 min for total gelification to occur and was then stabilised using plastic compression.

2) Smooth gradient: For the method (2), the creation of the collagen density gradient required the addition of all the different solutions, from the more concentrated to the more diluted, carefully on the top of each other, within a short time (seconds) to encourage mixing and therefore avoid a sharp interface (see Figure 4.4c). The resultant collagen solution was then left in an incubator (37°) for 10 min for the gelification to occur and stabilised using plastic compression.

Gels were stained using Toluidine blue to visualise collagen distribution. Collagen concentration gradients were formed using Design 4 for both methods (1) and (2). After stabilisation, surface variations of the top surface of the gels were observed at the macro scale (see Figure 4.4b and c), adding topographical cues for both methods. Furthermore, repetitions of the methods (1) and (2) using Design 4 showed

that resulting gradient gels were not predictable and could not be reproduced consistently, as the obtained gradient gels were always different at a macro-scale, with different shapes, collagen distribution and distinct topography. Accordingly, these two aforementioned methods were rejected.

Overall, Design 1-3 and 4 have been tested in the centrifuge and none of them matched the requirements for regular use. The initial Design 1 had been optimised to Design 4, which seemed initially promising. It was easy to sterilise, easy to use, did not leak, allowed easy access to the gel and the formation of a density gradient by addition of various collagen dilutions. However, when repeated, method (1) and (2) (Table 4.1), using the addition of various concentrations of collagen solution, have proven to be not reliable. As such, the design of a mould to make a reproducible, cost efficient and fast collagen gradient was completely rethought.

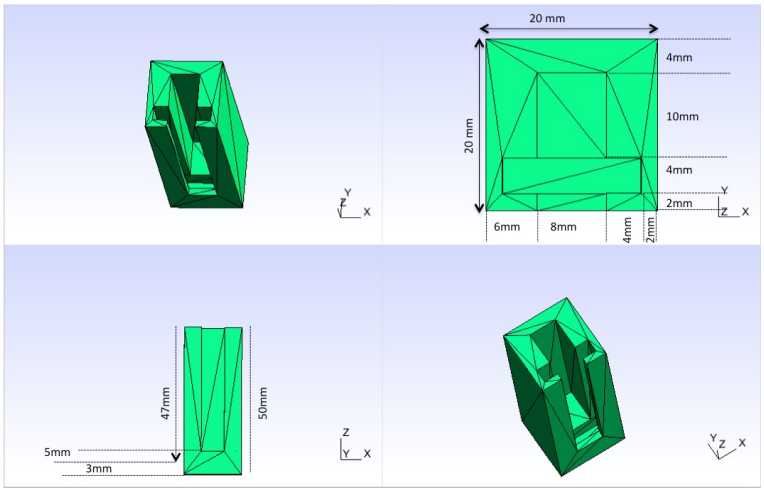

Figure 4.3: CAD-Design of Design 4 obtained after optimisation. The mould was not waterproof under centrifugation but has been used to test a second method, the addition of various concentration of collagen solution in the mould. Results obtained with the mould were not reproducible.

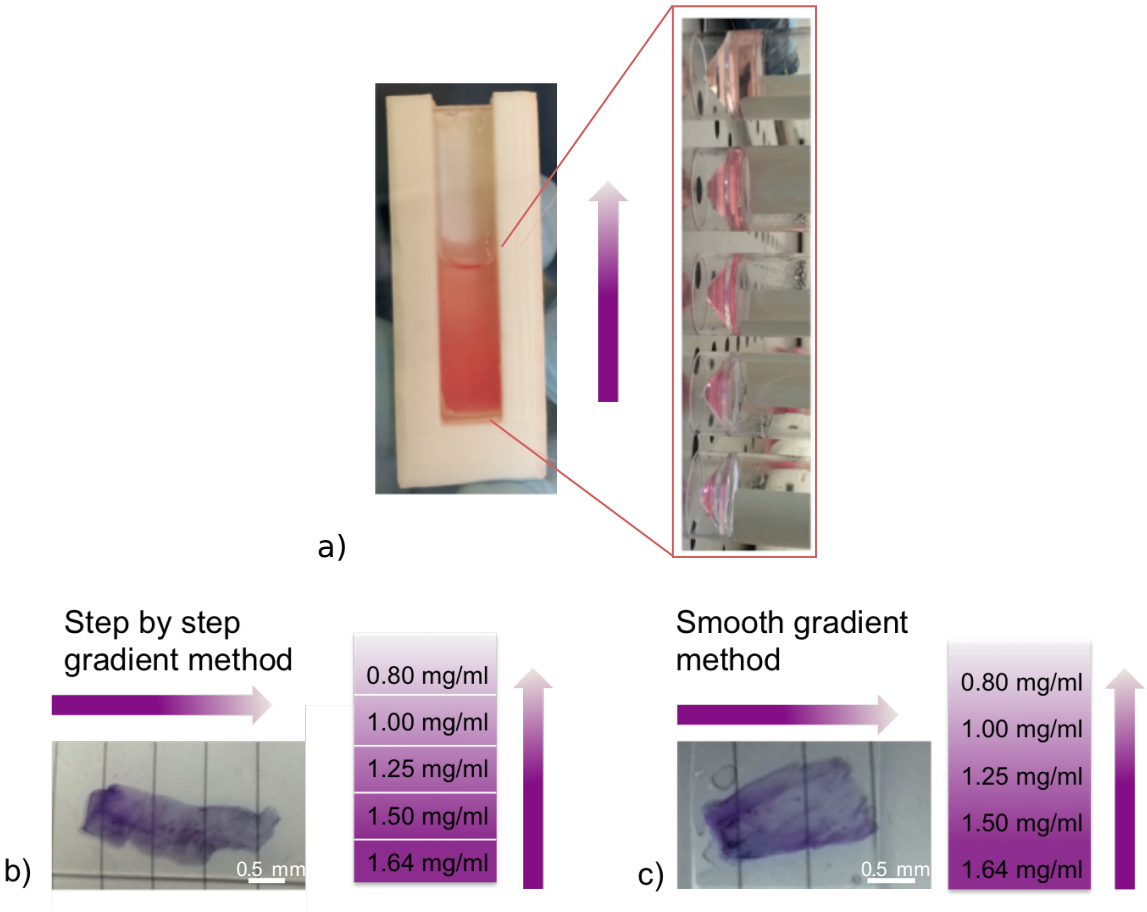

Figure 4.4: Image of the 3D-printed version of the third design, with the plexiglass side. a) Different dilutions of collagen solution were added on the top of each other in the mould in order to form a collagen concentration gradient. b) Result of the stabilised collagen gel gradient obtained following the step-by-step method. c) Example of the stabilised collagen gel gradient obtained for the smooth gradient method. Gels were stained using Toluidine Blue after stabilisation.

4.2.1.3 3D printed collagen gradient mould

Taking a step backward, the use of a square tube mould was revisited. Based on the 24 well plate geometry, a 16 gradient shaped-well-mould, Design 5, was designed (see Figure 4.6) in order to use a cost-efficient amount of solution ($V = 1.4$ml). The geometry of already manufactured well plates was chosen to help with the stabilisation process, as there are commercially available 24 wells plate RAFT-absorbers (Levis et al., 2015). In addition, Design 5 offers the possibility to set multiple collagen hydrogels simultaneously, and after gelation, gels were easy to access. Design 5 is easy to manufacture and sterilise and a lid was made to limit contamination (based on previous features). To produce a gradient, ridges were introduced in the casting mould as visible in Figure 4.5a. As a result, collagen gels with a volume variation due to the ridges were made and density gradients were obtained after RAFT-stabilisation. This version of mould has been thought to make collagen gradient in a reproducible (see Section 4.4), quick, cost-effective and reliable manner. Figure 4.5a shows the geometry of one of the gradient mould design. The shape of the mould was thought to be easy to adapt, e.g. can be modified to be able to create a gradient of collagen along a conduit, eventually suitable for making nerve repair conduits (see Figure 4.5b).

The 3D printed version of Design 5 is represented Figure 4.6 and the specifications of the product are detailed Table 4.2. Design 5 allowed the fabrication and access to collagen gels with controlled volume variations. After RAFT-stabilisation, collagen density gradients were visible in the gels at the macro-scale with no apparent surface variations (see Section 4.3.2). It was easy to sterilise and an additional lid on the top was added to avoid any contamination. Therefore, Design 5 was selected as the optimal design, and a full characterisation of the hydrogel gradients fabricated was

performed. Hence, a detailed description of the protocol and the characteristics of the collagen gradient gels, i.e. concentration gradient, stiffness profile, topography, parameters of high interest for the tissue engineers, will be given in the next Section.

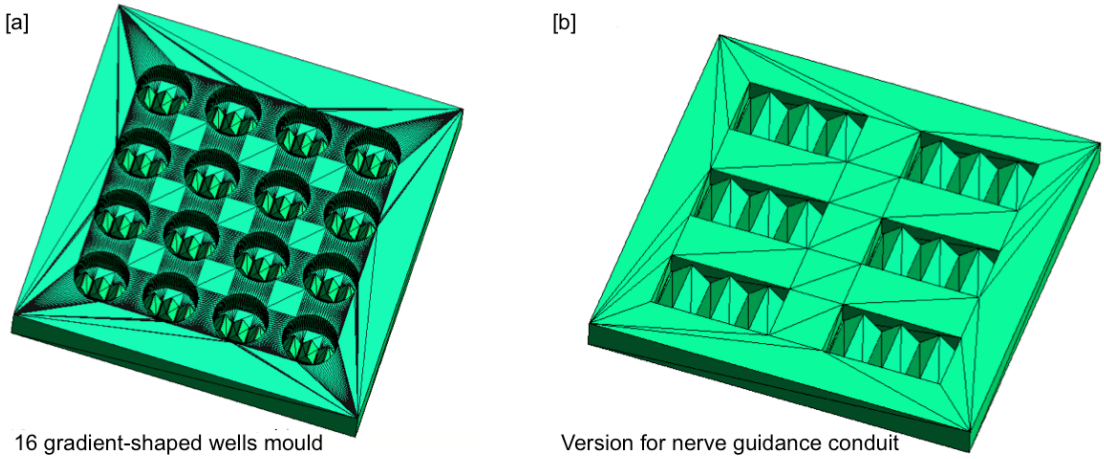

Figure 4.5: a) Geometry displaying one final gradient moulds' design (Design 5) (10 × 10 cm) and b) another 3D design showing the possibility to adjust the final mesh to make the gradient maker suitable to create nerve guidance conduits (10 × 10 cm).

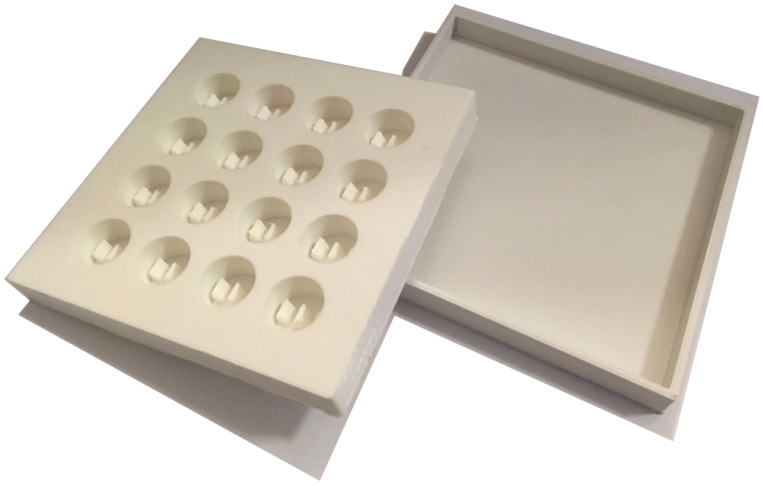

Figure 4.6: The final 3D printed mould (Design 5) used to make collagen defined-stiffness gradient profiles (10 × 10 cm).

Product specification	
Name	3D-printed gradient mould
Intended use	Hydrogel gradient maker
Material	PolyLatic Acid
Stability	OK
Type of gradient	2 (lower and higher)
Volume plate	1.5 mL
Sterilise	Yes
Product size	10 ×10 cm
Lid	Yes

Table 4.2: Final gradient maker specification sheet.

4.3 Material and Methods

4.3.1 Gradient CAD-design

For this study, the gradient moulds were designed using the computer-aided design (CAD) software Autocad, and 3D printed from polylactic acid (PLA) using an Ultimaker 2. Two different multi-well moulds were produced, each of which contained wells of the same dimensions as a standard 24-well plate and therefore could be used to cast multiple equivalent collagen hydrogels simultaneously. The bottom surface of each mould well was shaped to include 3× equally-spaced raised ridges, conferring a pattern of varying depth on the collagen hydrogels cast in the moulds subsequently (Figure 4.7). One of the mould designs had ridges of height 5 mm to create a shallow gradient (lower), the other had ridges of height 8 mm to create a steeper gradient (higher). Moulds were sterilised by immersion in 70% ethanol overnight.

4.3.2 Raft-stabilised collagen gel gradients substrate fabrication

The collagen solution was made following the protocol described Section 3.2.1. A volume of 1.4 ml of the collagen solution was pipetted into the printed moulds (lower and higher) and into a standard 24 well plate for the control (Control), and kept in a humidified cell culture incubator (37°C, 5% CO_2) for 10 min to allow gelation.

Once set, gels were flipped from the printed moulds into a standard 24-well plate and were RAFT-stabilised for 15 min using RAFT®absorbers (Startorius Stedim/Lonza). This step rapidly removes most of the fluid of the hydrogel through the top surface of the gel and resulted in gels obtained with a flat top and bottom surface,

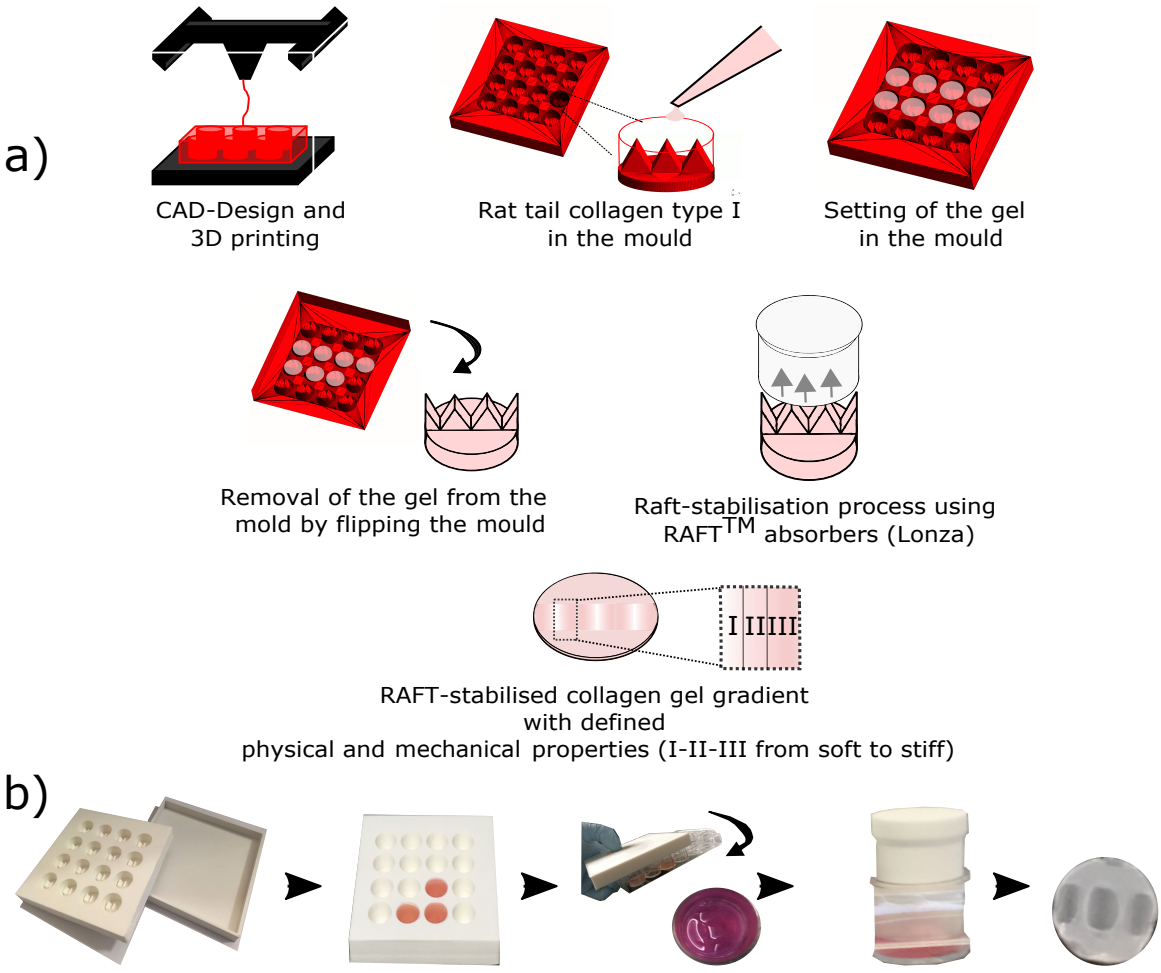

Figure 4.7: Schematic diagram showing the fabrication process of the collagen gradient gel mould with defined geometry. a) Moulds were CAD-designed and 3D printed using PLA. Collagen gel solution was pipetted in moulds and gels were let to set for 15 min in a humidified incubator then flipped to a standard 24-well plate. Then, gels were RAFT-stabilised for 15 minutes. The gel obtained are RAFT-stabilised collagen gel gradients with defined physical and mechanical properties. The gels are segmented in three separate area (I-II-III) from soft to stiff. b) Pictures of the experimental set up to make gradients gels.

but with gradients of collagen density resulting from the variation in gel height as a consequence of the ridges in the original casting mould (Figure 4.7). Gels were covered with serum free DMEM and kept in a humidified incubator.

4.3.3 Physical characterisation of collagen substrates

4.3.3.1 Gel thickness

The height of the gels was measured following the protocol described in Section 3.2.2. The images were extracted and analysed on ImageJ. For accuracy, three measurements of the height of each gel were taken and averaged.

4.3.3.2 Density of Collagen for stabilised gradient gels

The gradient gels are the inverse of the 3D printed mould design. Knowing the geometric shape of the hydrated gel, the volume of the fully hydrated gel was calculated in a 3D-*Cartesian Coordinate* system. The gel was cut into two distinct components (see Figure 4.8): V_{cyl} a partially full cylindrical part ($\times 2$ sides) and V_{grad} the actual gradient. The volume V_{cyl} was calculated using the following equation

$$V_{cyl} = 2 \cdot y \cdot \left[\cos^{-1}\left(\frac{R-h}{R}\right) R^2 - \sqrt{R^2-(R-h)^2}(R-h) \right], \tag{4.1}$$

where y (mm) is the height of the gel, R the radius of the cylinder (here R = 8 mm, radius of a 24 well plate) and finally h (mm) is the width of the partial cylinder (see Figure 4.8).

For the second volume V_{grad}, the base of the gel is defined by x and z axis, fixed in space and can be associated to a rectangular domain and the shape of the gradient is defined by $f(x)$ (see Figure 4.8). The volume of the three-dimensional region D is given by the integral,

$$\begin{aligned} V_{grad} &= \iiint_D \mathrm{dV} \\ &= \iiint_D \mathrm{dzdydx}, \end{aligned} \tag{4.2}$$

where D is defined as follow

$$D = [x_a; x_b] \times [0; f(x)] \times [z_a; z_b],$$

where $[a, b]$ is a closed interval contained in D and $f(x)$ the function defining the gradient pattern. Consequently

$$V_{grad} = \int_{x_a}^{x_b} \int_{0}^{f(x)} \int_{z_a}^{z_b} \text{dzdydx}. \tag{4.3}$$

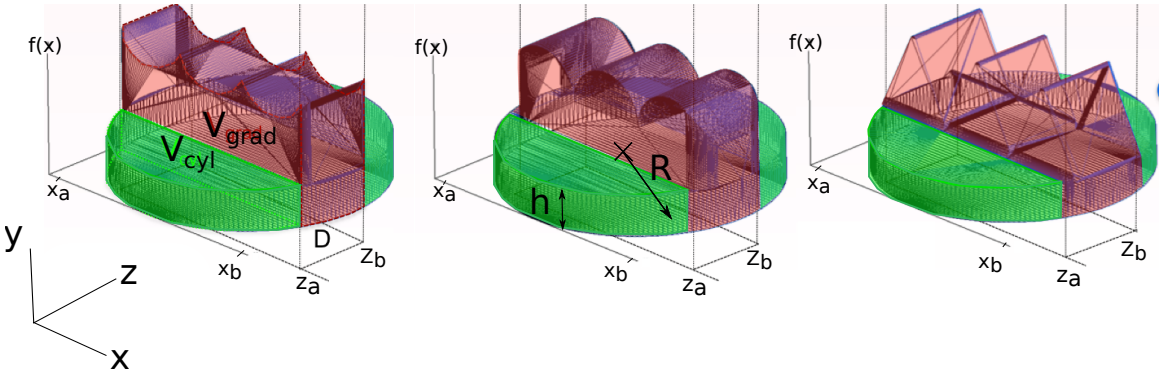

Figure 4.8: Three examples of the volume of hydrated collagen gels and the volume separation for integral calculation.V_{cyl} is represented by the area in green and V_{grad} is represented by the area in red.R is the radius of the cylinder and h is the width of the partial cylinder.

Riemann Sum Approximation, volume post-stabilisation and collagen density Riemann Sum approximation was used to determine the volume of the fully hydrated collagen gradient gel. Let $f(x, z)$ be the shape of the gel defined over the base $[x_a; x_b] \times [z_a; z_b]$ (see Figure 4.8). Then, the base of the gel was divided into rectangles of area $\Delta A = \Delta x \cdot \Delta z$. On each rectangle, the value $f(x_k, z_j)$ was used to approximate $f(x, z)$ on this rectangle. The volume of gel over each rectangle (see Figure 4.9) is approximated by

$$\Delta V = f(x_k, z_j)\Delta A = f(x_k, z_j)\Delta x \Delta z. \tag{4.4}$$

The gradient gel was separated in three different parts (see Figure 4.9). This was defined as such to check the density variation and also to be able to define specific fields for future mechanical analysis measurements and cell experiments,

$$V_{gradapprox} = \sum_{k=1}^{n} \sum_{j=1}^{m} f(x_k, z_j) \Delta z \cdot \Delta x. \tag{4.5}$$

Since the initial volume of hydrated collagen is known for all three parts, the mass of collagen in each of them using Eq.(3.2) can be calculated. Next, using the height measures, for the different sections A-B-C (see Section 3.2.2-Figure 3.1) the volume after stabilisation can be approximated as

$$V_{ps} = \text{Length} \cdot \text{Height} \cdot \text{Width} = x \cdot y \cdot z. \tag{4.6}$$

Thus, the collagen concentration is calculated using Eq.(3.3) in Section 3.2.1.1.

Using the concentration approximations for each part of the gradient, the regular gels density and the density of collagen over the gradient can be linked. These data are used to correlate the mechanical stiffness properties (see Section 4.3.5) of each type of gel (see Figure 4.10), known to be dependent on collagen density, as seen in Chapter 4.

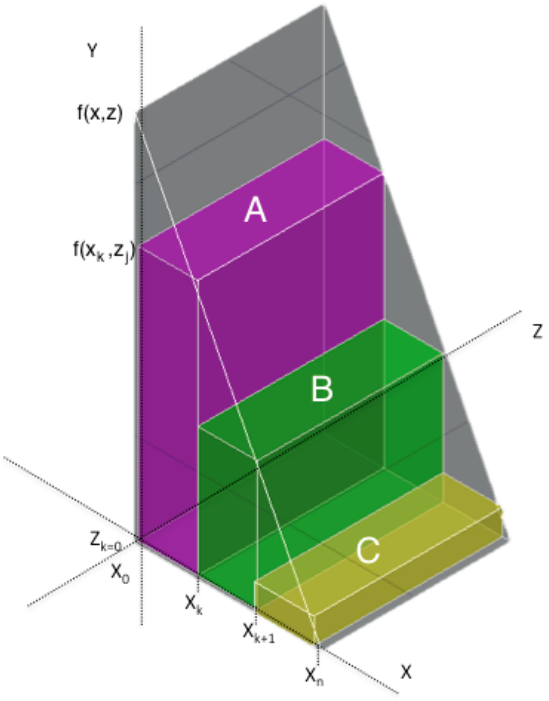

Figure 4.9: The Riemann Sum Approximation.

4.3.4 AFM topography

A JPK Nanowizard 1 AFM (JPK Instruments Ltd, Germany) was used to obtain 10×10 μm high-resolution topography images (1024×1024 pixels) from each segment (I-II-III of the lower and higher gradient gels and the control gel shown in Figure 4.7a) (see Section 1.7.3.1). Gels were kept for 24 hours in PBS and rinsed using distilled water. Imaging was conducted using MSNL-10-A tip cantilevers (Bruker Ltd, France) with the following characteristics: F_{res} ∼22 kHz resonant frequency and ∼0.07 N.m^{-1} nominal spring constant. JPK/SPM data processing software was used to extract data and height profiles were obtained for 5 x-lines across the images (each 20 y-pixels).

4.3.5 Mechanical characterisation of collagen substrates

In order to quantify the effect of collagen concentration on mechanical properties of the material, a series of force mapping experiments were performed to yield a stiffness map using AFM-force spectroscopy. Indentation measurement were performed using a JPK Nanowizard CellHesion 200 with motorised precision stage (JPK Instruments AG, Berlin, Germany). Solid soda-lime glass microspheres (S-SLGMS, diameter 50-53 μm, Cospheric, Santa Barbara, CA) were glued (light cure adhesive, Loctite 349 IMPRUV® ,R. S. Hughes Company, Plymouth, MI) to non conductive silicone nitride and triangular tip-less cantilevers (NP-O10, Brukers, spring constant ∼ 0.35 N.m^{-1}). Experiments were carried out using force mapping over 1×2.5 mm area, covering the segments I-II-III, at room temperature. The collected force curves were batch-analysed using JPK/SPM data processing software (JPK Instruments Ltd, Germany). A Hertz model was used for determining the Young's Modulus E (kPa), with a Poisson ration (ν) set to 0.5 (Instrument, 2008), (see Section 1.7.3.2).

4.4 Results

Two different collagen gradients (lower and higher) were created and compared to control RAFT-stabilised gels with no gradients. The density of collagen ranged from 67±4.2 to 79±7.1 mg.ml^{-1} and the surface stiffness ranged from 1.7±0.3 to 2.0±0.2 kPa for the lower gradient. The density of collagen ranged from 73±7.1 to 122±4.8 mg.ml^{-1} and the surface stiffness ranged from 1.5±0.6 to 7.1±1.9 kPa for the higher gradient (see Table 4.3 and Figure 4.10a). The gradient slope, reported as a function of change in stiffness over distance, was 0.85 kPa.mm^{-1} for the Lower gradient and 7.96 kPa.mm^{-1} for the higher gradient (see Table 4.3 and Figure 4.10b). Stiffness maps (1×2.5 mm) of gradients are shown in Figure 4.11. The substrate stiffness characterisation was performed using AFM-force spectroscopy (Stylianou, 2017). The gradient substrate stiffness was directly related to the collagen density as expected and the correlation is established Table 4.3. Increasing the collagen density also increased the stiffness of the collagen gels. Collagen substrates with stiffnesses of physiological relevance to the peripheral nervous system (PNS) have been fabricated (Evans et al., 2018; Rosso et al., 2017d, 2014) by varying the collagen concentration using bespoke 3D-printed moulds and the RAFT-stabilisation process.

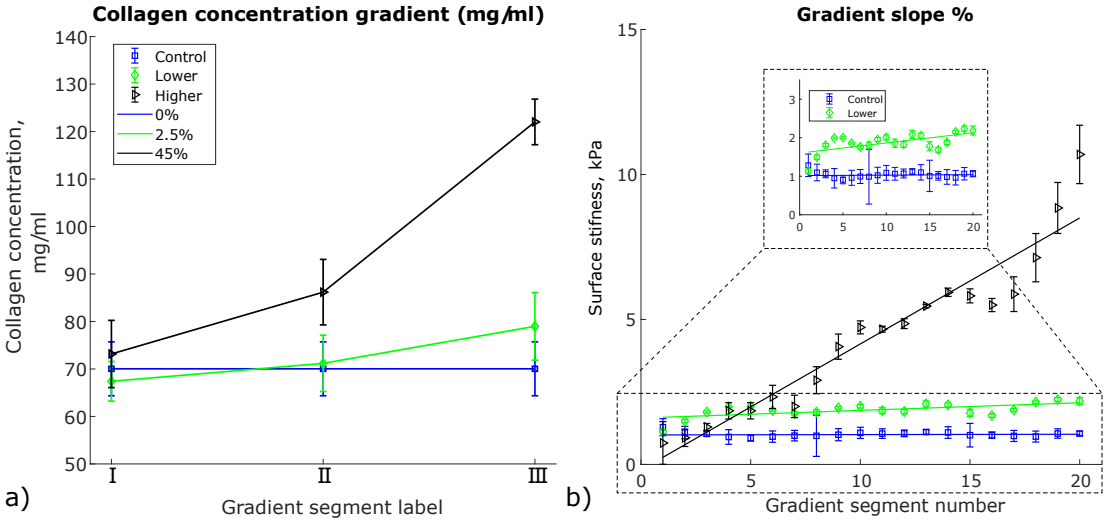

Figure 4.10: a) Mean collagen concentration for each segmented area (I-II-III) of the gradient gels. b) Mean surface stiffness value for 20 segments (125 μm each) (60-110 points for each segment)± SD and corresponding gradient slope (control (0%), lower (2.5%), higher (45%)).

Gradient	**Segment label**	**Slope** (kPa.mm^{-1})	**Collagen density** (mg.ml^{-1} ±SD))	**Collagen** (w/v± SD)	**$\sim$ E** (kPa ± SD)
Control	-	0	70±5.7	7±0.57	1.0±0.2
Lower (0.85 kPa/mm)	I	0.85	67±4.2	6.7±0.42	1.7±0.3
	II		71±5.9	7.1±0.59	1.9±0.1
	III		79± 7.1	7.9±0.71	2.0±0.2
Higher (7.96 kPa/mm)	I	7.96	73± 7.1	7.3±0.71	1.5±0.6
	II		86±6.9	8.6±0.69	4.1±1.1
	III		122±4.8	12.2±0.48	7.1±1.9

Table 4.3: Characteristics of RAFT-Stabilised collagen substrates. Noted in the table are the collagen density (mg.ml^{-1}) and the corresponding surface stiffness (E, kPa) for the control and the segmented area (I-II-III) of the gradient gels measured using AFM-Force spectroscopy. Data are presented as mean ± SD.

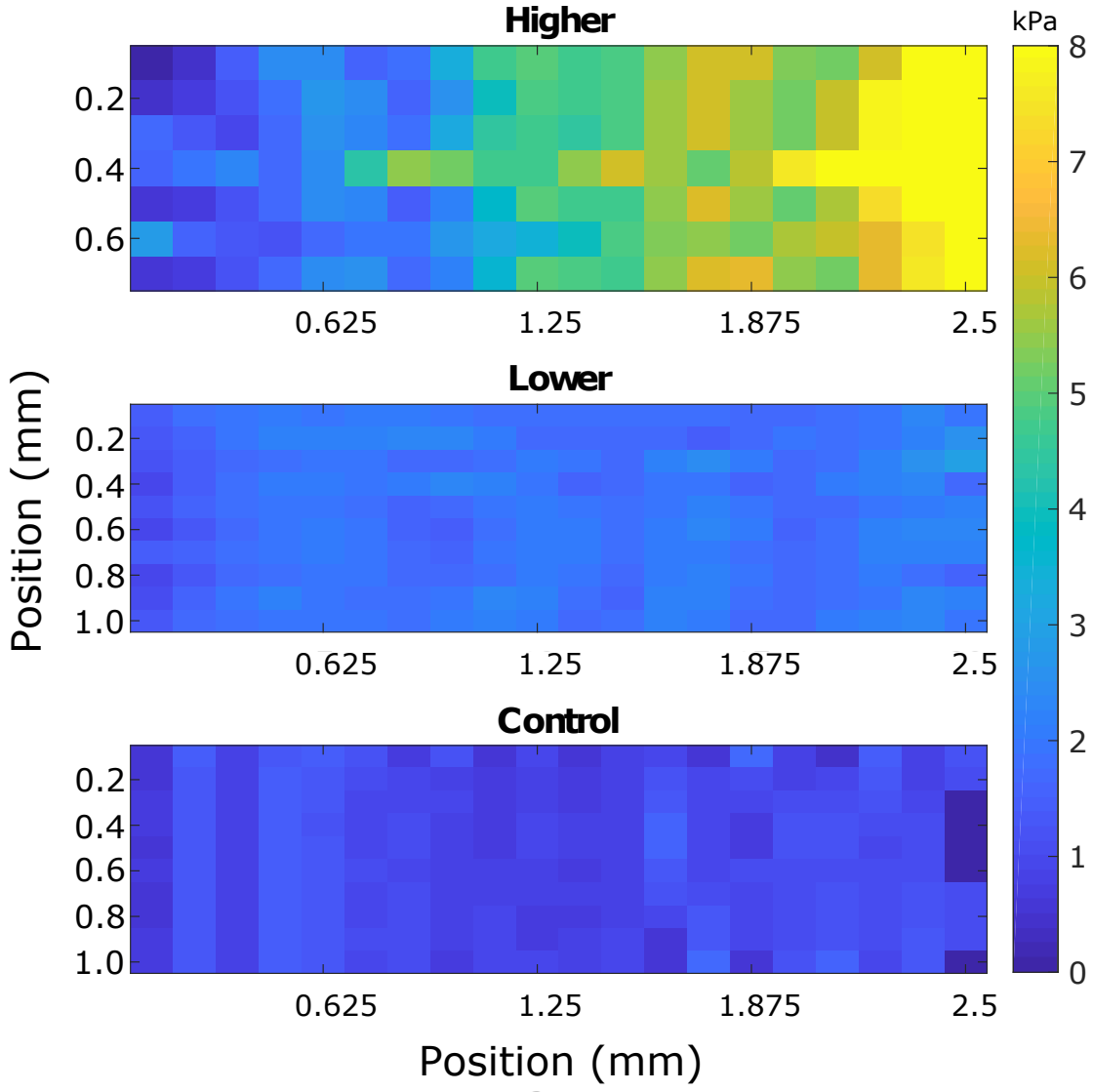

Figure 4.11: Spatial mapping of the surface stiffness of Control gel, lower and higher gradient gels.The stiffness at each pixel is the mean of five measurements (N=3 separate gels) taken by AFM spectroscopy and is represented as a rainbow-coloured palette map with blue denoting softer and yellow corresponding to stiffer regions; scale bar = 0-8 kPa.

4.4.1 Topography of collagen gradients

AFM imaging was used to examine the topography of the collagen gels and investigate any surface modification induced by the gradient making process (Stylianou, 2017). Figure 4.12, 4.13 and 4.14 show AFM images of the different segments (I-II-III, see Table 4.3) for the lower and higher gradient gels, and the control gel. The three types of substrate exhibited a similar dense surface structure with distinctive collagen fibrils detected. The collagen fibrils were randomly oriented in the three different types of substrates and did not present any apparent topographical directional cues. The measured height showed the roughness of the gels was lower than 1 μm with a maximum variation of 745 nm for Lower-III, therefore the overall surface topography of the gels was considered as flat (Li et al., 2017).

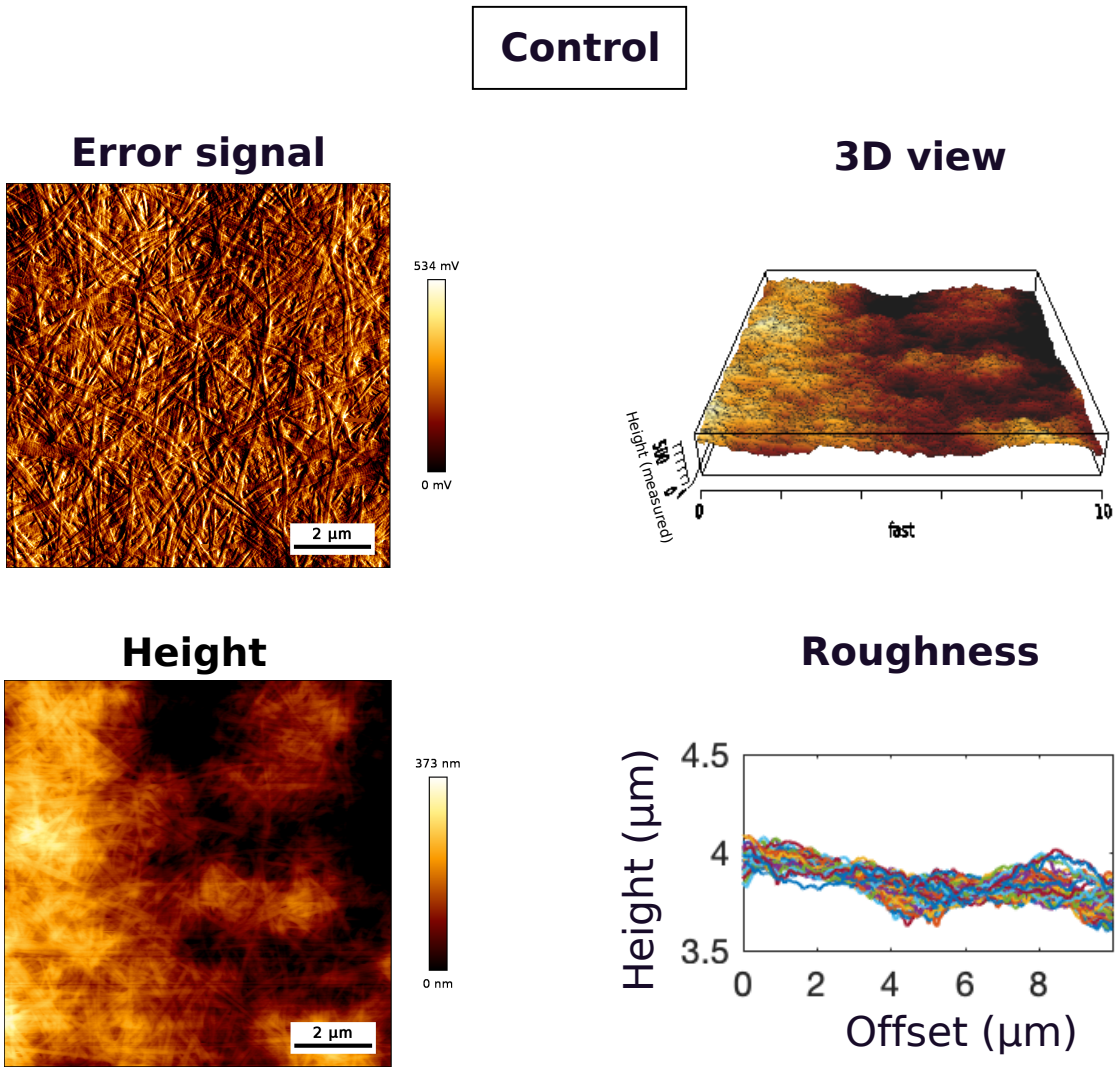

Figure 4.12: AFM topography images (10 × 10 μm, 1024×1024 pixels) of RAFT-stabilised collagen gels for the control gel showing the 3D and 2D view of the relative value of the height of the gels (scale bar in nm), then the error signal (mV) show the surface of the collagen gels where the banding pattern of collagen type I fibrils is visible. The surface roughness of the gels is indicated by the height profiles.

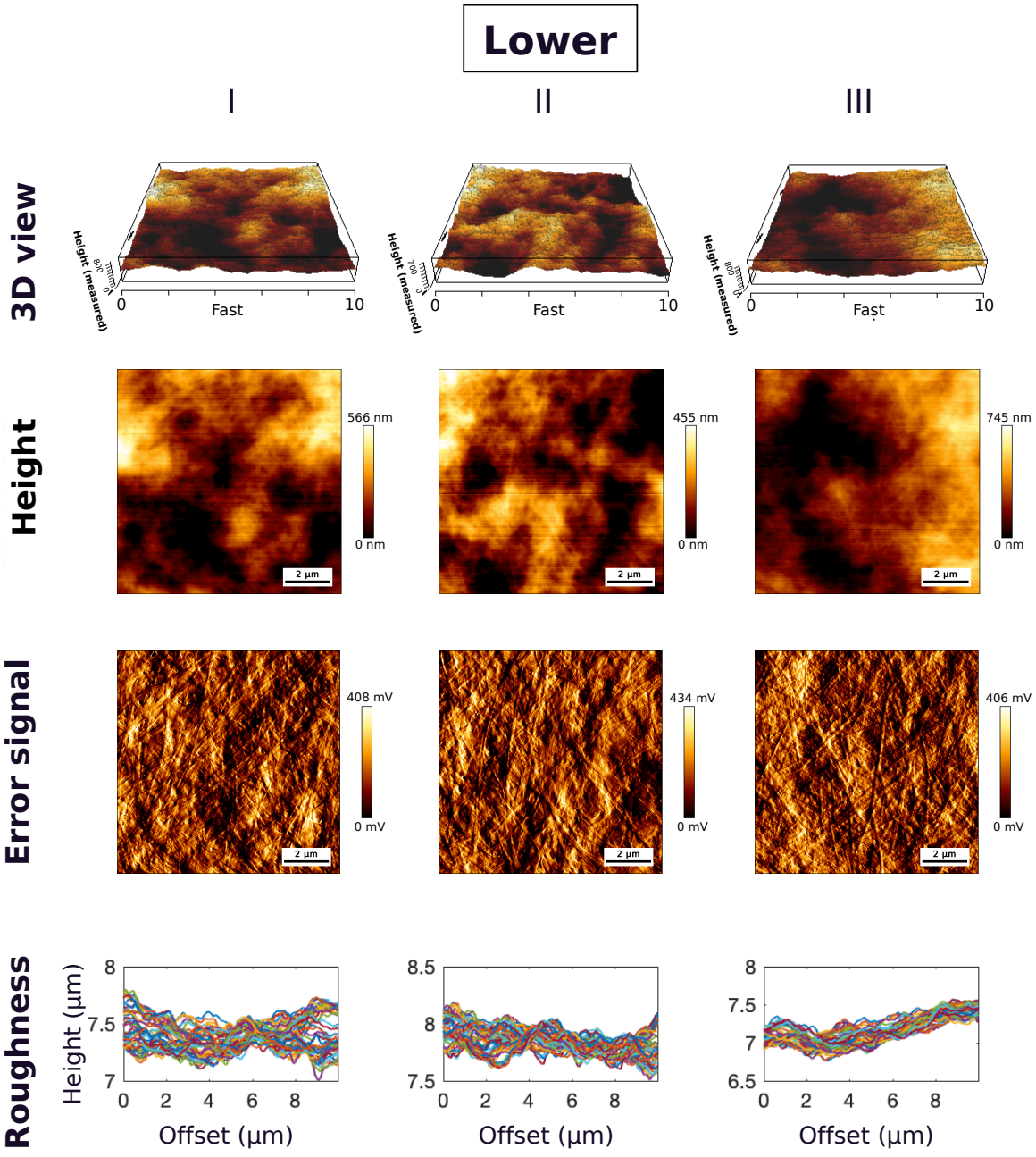

Figure 4.13: AFM topography images (10 × 10 μm, 1024×1024 pixels) of RAFT-stabilised collagen gels for the three sections (I-II-II) of lower gradient gel. The first two columns show the 3D and 2D view of the relative value of the height of the gels (scale bar in nm), then the error signal (mV) shows the surface of the collagen gels where the banding pattern of collagen type I fibrils is visible. The surface roughness of the gels is indicated by the height profiles.

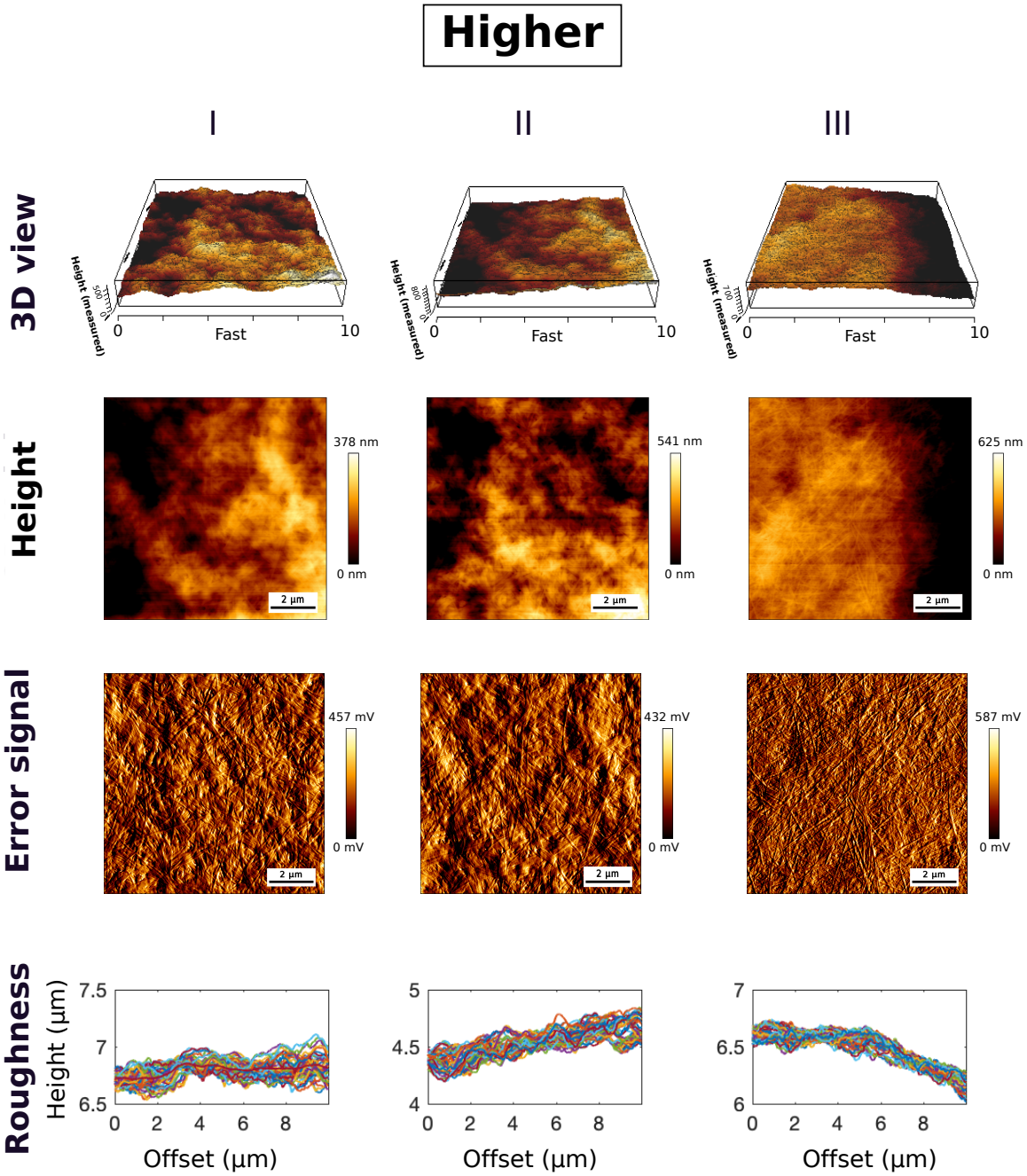

Figure 4.14: AFM topography images (10 × 10 μm, 1024×1024 pixels) of RAFT-stabilised collagen gels for the three sections (I-II-II) of higher gradient gel. The first two columns show the 3D and 2D view of the relative value of the height of the gels (scale bar in nm), then the error signal (mV) show the surface of the collagen gels where the banding pattern of collagen type I fibrils is visible. The surface roughness of the gels is indicated by the height profiles.

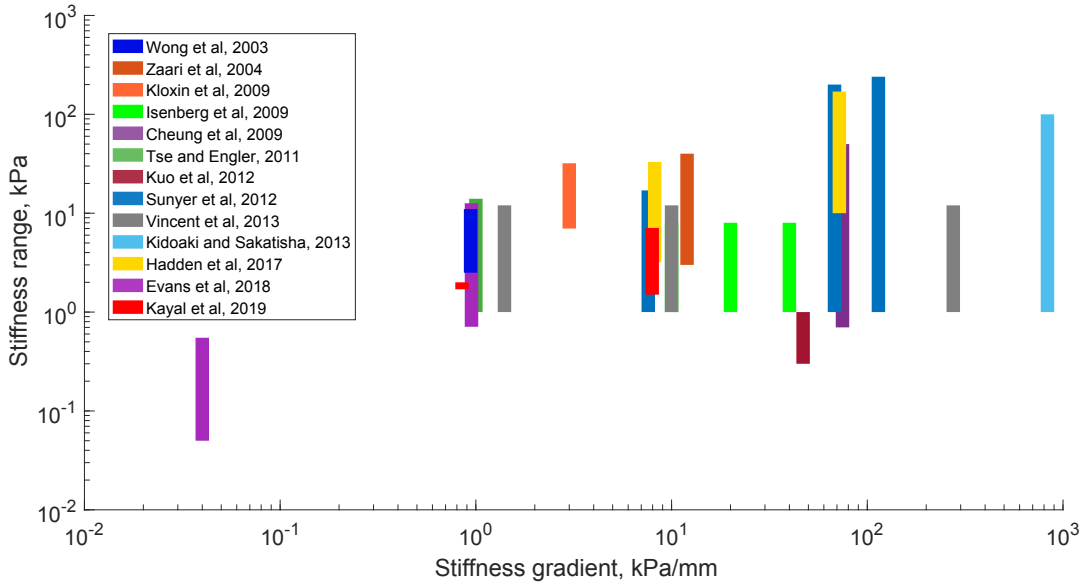

Figure 4.15: Diagram mapping the stiffness ranges (kPa) used to study durotactic behaviour *in vitro*, showing the modulus (kPa) range as a function of stiffness gradient (kPa.mm^{-1}). For clarity, in this figure, the stiffness ranges are categorised by study (same as the ones presented Figure 4.16), and include the stiffness gradient proposed in this Chapter (in red).

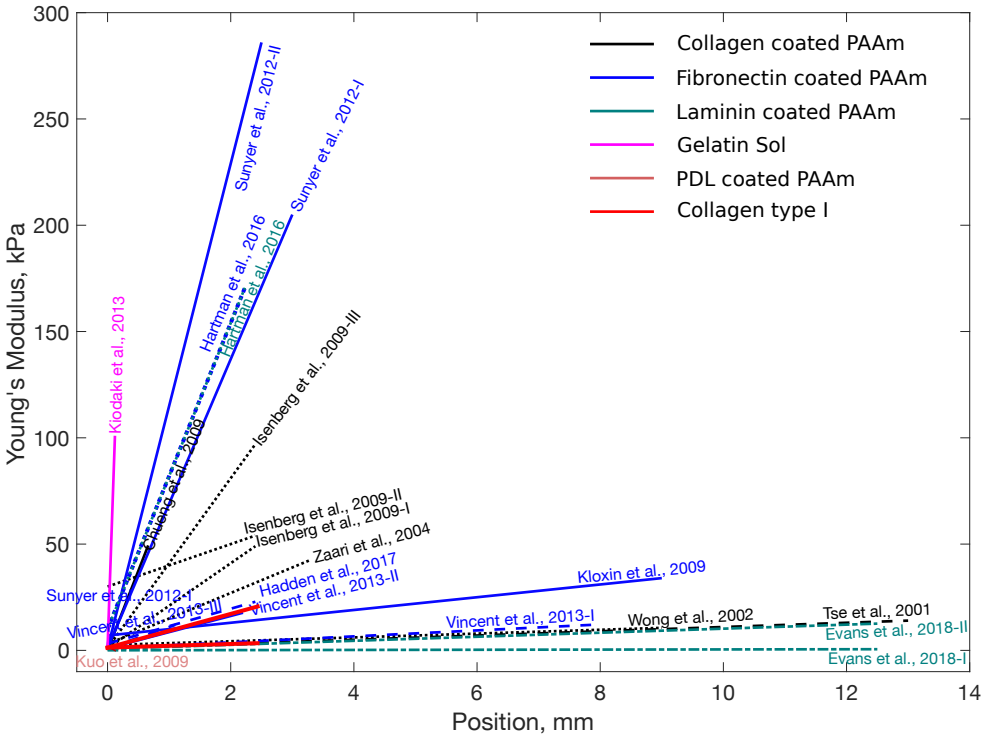

Figure 4.16: Graphical summary of the gradients and materials used to study durotactic behaviour *in vitro*, showing the Young's Modulus (kPa) as a function of the location on the samples (mm). Studies are categorised by material used, and the majority are using coated PAAm gels as it offers the possibility to work with a wide range of stiffness using a large variety of techniques (Wong et al., 2003; Zaari et al., 2004; Isenberg et al., 2009; Tse and Engler, 2011; Cheung et al., 2009; Hartman et al., 2016). This summary includes only 2D cultures. The study of durotaxis is challenging as it difficult to uncouple the stiffness of a substrate to its pore size, ligand molecule coating density, the height of the substrate itself (Roca-Cusachs et al., 2013). This study proposes to use pure collagen gel to develop defined stiffness gradients, represented by the red lines (lower and higher) and shows the fit of the proposed technic with the current literature.

4.5 Discussion

The goal of this Chapter was to design a flat substrate with a stiffness gradient to study cell responses to mechanical cues in 2D. Physiologically relevant stiffness gradients were created within the range of modulus values reported previously for PNS tissue (Evans et al., 2018; Rosso et al., 2017d) using tissue engineering techniques to control collagen matrix density (Levis et al., 2015; Cheema and Brown, 2013) and the fit of our produced stiffness gradient and stiffness range is compared to the literature Figure 4.15. Collagen gels were generated and characterised, exhibiting a flat surface topography and continuous linear gradients of defined density, which correlated to the stiffness (Tierney et al., 2009; Hadjipanayi et al., 2009).

Previous studies to create 2D substrates with continuous stiffness gradients have used coated polyacrylamide gels (PAAm) gels as well as proteins such as fibrin and gelatin. The range of stiffnesses obtained vary over several orders of magnitude (Sunyer et al., 2012) and the various stiffness gradients used previously to investigate cell mechanosensitivity are shown in Figure 4.16, categorised according to the type of material used (Tse and Engler, 2011; Kuo et al., 2012; Zaari et al., 2004; Kidoaki and Sakashita, 2013; Isenberg et al., 2009; Wong et al., 2003). Type I collagen is an appropriate choice for studying neuronal responses since it is a major component of nerve tissue. Previous studies using collagen to form gradients have tended to combine the protein with PAAm and gradients have been generated via cross linking with enzymes, ultra-violet light or temperature (Sant et al., 2010). Such cross-linking can modify the protein structure (Buehler, 2008; Tierney et al., 2009) which can potentially add confounding signalling parameters that can influence cell behaviour.

By contrast, the approach used here does not affect the microstructure of the

collagen fibrils and the banding pattern is conserved after gel stabilisation, offering a way to make gradients purely of collagen, in a simple, controlled and reproducible way. Previous studies have reported the effects of similar substrate stiffness profiles for other types of cells (including human adipose-derived stem cells (Hadden et al., 2017), human mesenchymal stem cells (Tse and Engler, 2011; Vincent et al., 2013), vascular smooth muscle cells (Wong et al., 2003), fibroblasts (Kloxin et al., 2009; Sunyer et al., 2012) and Schwann cells (Evans et al., 2018)). Focusing on the improvement of nerve repair solutions, Evans et al. (2018) have shown that a 0.95 kPa.mm^{-1} gradient induces Schwann cell durotaxis. Our lower gradient (0.85 kPa.mm^{-1}) therefore could potentially be used to modulate both Schwann cells and neural cells combined for the improvement of nerve guidance conduits.

Moreover, Hadjipanayi et al. (2009) developed a 3D model to study the impact of compressed collagen gradient on fibroblasts, and Georgiou et al. (2013) developed an engineered neural tissue on collagen gels seeded with Schwann cells and both have shown that the stabilisation process via plastic compression does not affect cell viability (Levis et al., 2015; Georgiou et al., 2013). This technic could be extended in the future to a cellular substrate gradient allowing the study of overlapping chemical and mechanical cues for a better understanding of cell response to their environment.

Chapter 5

Mechanoresponse of NG108-15 cell line on characterised RAFT-stabilised collagen gel gradients

This Chapter is adapted from the paper entitled "*Mechanoresponse of neural cells to physiological stiffness cues.*" By Celine Kayal, E. Moeendarbary, R.J. Shipley and J..B. Phillips.(*Under revision*)

This Chapter focuses on the cell-substrate interaction. It reports the investigation of the mechanoresponse of neural cell to defined-stiffness gradient profiles, developed and characterised Chapter 4.

5.1 Introduction

The interaction between the tissue and the cell is a key factor in controlling the fate of the latter (Discher et al., 2005; Saha et al., 2008; Wells, 2008; Franze, 2011; Seidi et al., 2011; Koser et al., 2016). Cells exert forces on and sense the stiffness of the surrounding extracellular matrix (Discher et al., 2005). The mechanical properties of the local environment have important implication in cell differentiation (Tse and Engler, 2011; Rammensee et al., 2017), proliferation (Leipzig and Shoichet, 2009) and migration (Wu et al., 2012; Evans et al., 2018). For nervous system cells, neurite outgrowth and branching patterns have been shown to be depending on substrate stiffness (Flanagan et al., 2002; Koch et al., 2012; Koser et al., 2016; Rosso et al., 2017d). Moreover, the peripheral nervous system (PNS) (Phillips et al., 2004; Tillett et al., 2004; Mason and Phillips, 2011) and central nervous system (CNS) (Koser et al., 2016; Moeendarbary et al., 2017) native tissues are mechanically heterogeneous; therefore, neurites are likely to encounter regions with distinct mechanical properties. Although several studies have shown the importance of chemotactic, haptotactic and topographical guidance cues, there is still limited understanding of how the mechanical cues influence the neurite outgrowth and branching pattern. Providing information to promote the current knowledge would help nerve tissue engineers to make a step forward to designing optimised nerve repair solutions.

Recent studies have characterised the mechanosensitivity of PNS neuronal cells on various stiffness substrate (Rosso et al., 2017d,c) and highlighted the cell response to a stiffness gradient (Koser et al., 2016) referred to as durotaxis (Lo et al., 2000; Franze, 2011). Biomimetic mechanical gradients have the potential to be used in the construction of nerve repair materials, to improve axon pathfinding and accelerate

nerve repair by controlling the orientation of neurite regeneration (Sundararaghavan et al., 2008; Koser et al., 2016; Rosso et al., 2017d; Evans et al., 2018).

In the study presented in this Chapter, NG108-15 cells were cultured on the substrates developed in Chapter 4 to explore the influence of stiffness gradient and magnitude on neuronal regeneration *in vitro*.

5.2 Material and methods

5.2.1 Neuronal cell culture

5.2.1.1 NG108-15 cell culture

NG108-15 neuronal cells are a hybrid cell line derived from mouse neuroblastoma and rat glioma cells. NG108-15 cells were cultured in Dulbecco's modified Eagle Medium (DMEM)(SigmaAldrich, St Louis, Missouri) supplemented with 10% (v/v) Fetal Bovine Serum (FBS) and 1% (v/v) Penicillin-Streptomycin (PS). *In vitro* experimentations were conducted between passage 14 and 18.

5.2.1.2 Investigation on the effect of serum on neurite behaviour

To study the impact of the substrate on the neurite behaviour, the choice of the cell line went towards NG108-15 as it does not require the addition of growth factor (external signalling cues) to elongate neurites.

The effect of serum on neurite extension, was investigated. NG108-15 neuronal cells were seeded on the top of RAFT-stabilised collagen gels at a density of 5×10^5 per 24 well plates in either serum-free DMEM or complete medium (DMEM with 10% (v/v) FBS, 1% (v/v) PS). For both conditions cells were maintained in 1.4 ml of culture medium in 24 well plates. Cells were incubated in a humidified incubator with 5% CO_2 at 37°C for two days.

5.2.1.3 NG108-15 neuronal cell culture on stiffness gradient gels

NG108-15 were trypsinised and 1×10^5 cells were seeded per gel onto RAFT-stabilised collagen gradient gels (lower and higher gradient and control gradient) contained in 24-well plates, in serum-free cell culture medium (Ghahary et al., 1989). Cultures

were maintained for two days (t= 48 hours) in a humidified incubator (5% CO_2 at 37°C). The cells were only exposed to different mechanical signals, their chemical environment was kept similar and cell density was defined to avoid cell-cell interaction (see Figure 5.1).

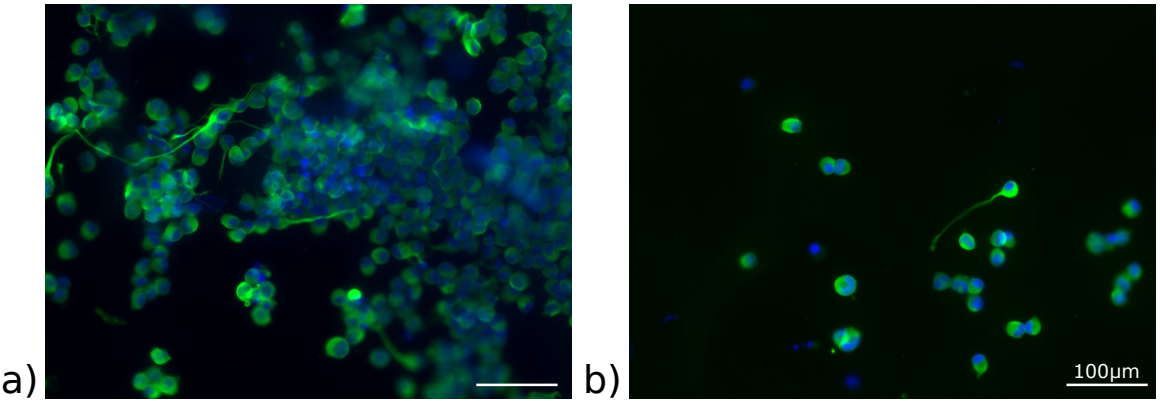

Figure 5.1: NG108-15 cells for : a) Cell density: 5×10^5 per gel. b) Cell density: 1×10^5 cells per gel. Hoechst staining for the nuclei (blue), β-III-tubulin staining for neurons (green). White scale bars : 100μm.

5.2.2 Cell immunolabelling and fluorescence imaging

Cultures were fixed with 4% paraformaldehyde overnight at 4°C and permeabilised using 0.5% Triton X-100 for 30 minutes. Non-specific bindings were blocked with 5% normal goat serum. Nuclei were labelled using Hoechst (1:1000). Mouse anti-β-III-tubulin primary antibody (1:400, incubated overnight at 4°C) and dylight goat anti-mouse 488 (1:300, for 90 minutes) were used to detect the neurites. Samples were rinsed using phosphate buffered saline (PBS) solution between each step.

Fluorescence microscopy (Zeiss Axio Lab.A1, Germany) was used to acquire images of NG108-15 cell line on the gels. Images were captured using a 10× lens, and were analysed using ImageJ software (US National Institutes of Health)(Abramoff et al., 2004).

5.2.3 Data analysis

Neurite response to collagen gradients has been quantified using measures previously described (Hoffman-Kim et al., 2010) in terms of the number of cells forming neurites; the mean number of neurites per cell; the mean neurite length per cell. Neurite length was determined using the freehand line selection tool and measure function. The angle of each neurite was measured from the long axis of the gradient (see Figure 5.2). Orientation was classified into three different categories: a) neurite elongating up the gradient, toward stiffer substrate region ([-60;60]^o), b) neurite elongating down the gradient, toward softer substrate region ([-120;120]^o), and c) neurite elongating perpendicular to the gradient. The categories are represented in Figure 5.2.

5.2.4 Statistical analysis

Statistical analysis was performed using JMP Pro 13 software (JMP SAS Institute, Marlow, Buckinghamshire, UK). Data are presented as mean values ± standard deviation (SD). Differences among the gradients and the different segments were assessed using one way ANOVA with a multiple comparison analysis to identify the statistical differences. Statistical significance was taken at $p < 0.05$

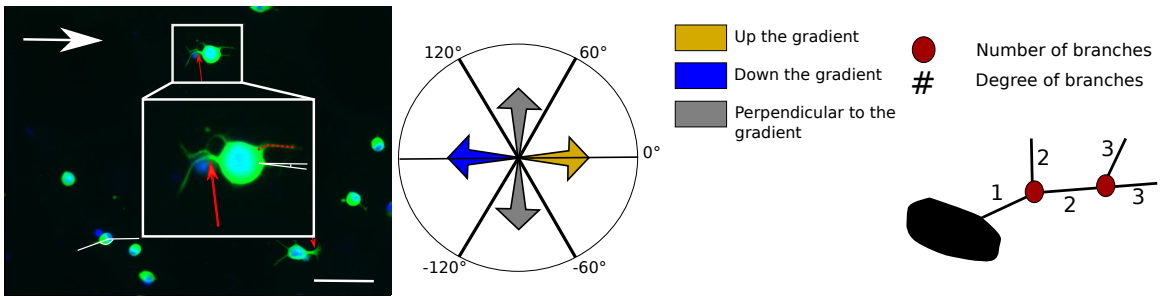

Figure 5.2: Fluorescence micrographs show sprouting of neurites; red dashed line indicates neurite length, branching spots are indicated by red arrows and neurite orientation was measured as indicated by the white line. The white arrow indicates the direction of the gradient. A classification of the neurites orientation has been used to quantify their sensitivity to the stiffness gradient and was defined as such: neurite were considered growing up the gradient for all the angles between [-60,60]° (yellow), down the stiffness gradient for the angles between [-120, 120]°(blue) and neurite growing perpendicular to the gradient otherwise (grey). The branching quantification was made based on the following branching tree.

5.3 Results

5.3.1 Investigation on the effect of serum on neurite behaviour

NG108-15 cells proliferated when cultured in serum supplemented DMEM but did not extend neurites. In contrary, when cultured in serum free DMEM, NG108-15 cells differentiated but did not proliferate. These results agreed with Ghahary et al. (1989), who have shown that the addition of serum in the media induces neurites retraction of the differentiated NG108-15 cells.

5.3.2 Mechanosensitivity of NG108-15 cells to the stiffness gradient gels

The behaviour of NG108-15 cells was evaluated on lower gradient (0.85 kPa.mm^{-1}) and higher gradient (7.96 kPa.mm^{-1}) gels, for each segment area (I-II-III; representing a specific absolute stiffness value (details in Table 4.3), and compared to cell behaviour on mechanically uniform control gels (Figure 5.3a-e).

Results indicated that the amount of cell expressing neurites, and the amount of neurite per cells were not influenced by neither the absolute stiffness of the stiffness gradient of the substrate. Overall, ∼29% of cells expressed neurites (∼2 neurites per cell). The mean neurite length for the gradient gels, taken from the longest branch of each neurites, was 116.4±66.5 μm for the higher gradient and 117±42.3 μm for the lower gradient, which was not significantly different to the 122±60.0 μm reached by neurites on the mechanically uniform substrates. These data give an average neurite growth rate of 2.5±1.1 μm.h^{-1}.

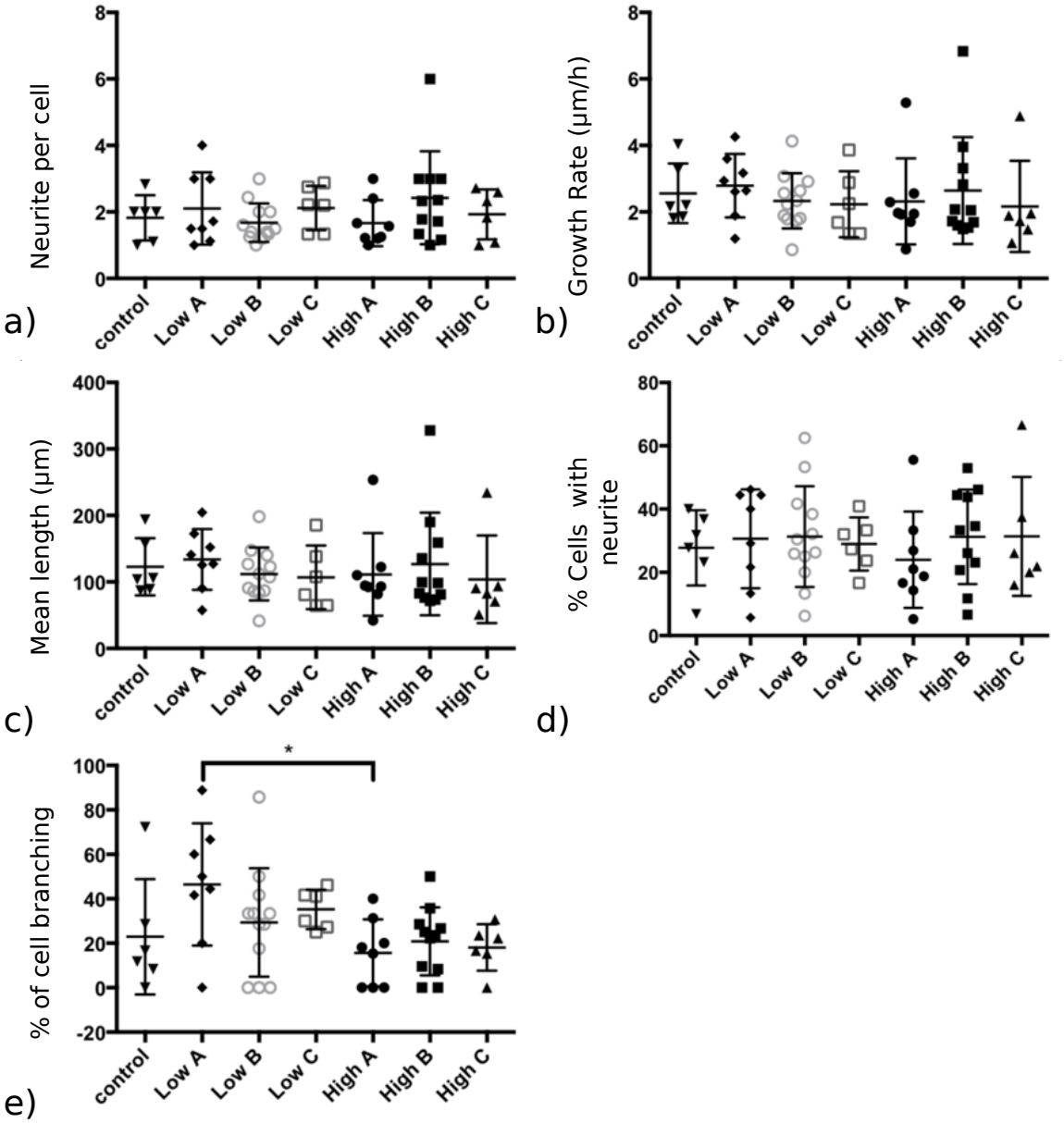

Figure 5.3: Behaviour of NG108-15 cells evaluated on lower and higher gradient gels and compared to cell behaviour on mechanically uniform control gels. Cells were cultures on two different gradient slopes (lower and higher) and on a Control gel. a) Mean number of neurites per cell, b) mean neurite growth rate (μm/h), c) mean neurite length (μm), and d) percentage of NG108-15 cells expressing neurites do not vary according to the presence of a gradient and differences in absolute stiffness value. However, e) the percentage of neurite branching is affected by the stiffness gradient. Data are shown for the different segments (I-II-III) of each gradient type (lower and higher) and the control. Results are shown as mean$\pm$ SD, $p < 0.05$ (*).

5.3.3 Neurite branching pattern and orientation

Figure 5.3e shows that after 48 hours, neurites branched differently depending on the growth region. Neurite were significantly more likely to branch on the segment Lower-I of the lower gradient (E ∼1.7 kPa) compare to the segment Higher-I of the higher gradient (E ∼1.5 kPa), suggesting that NG108-15 cells were mechanosensing the imposed gradient as seeded on a mechanically comparable absolute stiffness area. This phenomenon can be observed Figure 5.5.

Figure 5.4 and 5.5 show how the neurites explore their environment. On softer substrate's segments (Lower-I and Higher-I) and the control, respectively 1.7, 1.5 and 1.0 kPa, neurites did not elongate toward any preferential directions (see Table 5.1, column orientation). On the stiffer region of both gradient gels, a more persistent directionality was observed along the gradient, regardless of the absolute stiffness value. For the lower gradient, neurites on the stiffer segment (Lower-III, E=2.0 kPa), elongated preferentially up the gradient, toward stiffer regions. Contrarily, on the stiffer segment of the Higher gradient, (Higher-III, E=7.0 kPa), neurites elongated preferentially toward the softer region, down the gradient. Overall, the NG108-15 cells responded to the mechanical signals induced by the collagen gradient gels by modifying their branching behaviour and orientation pattern.

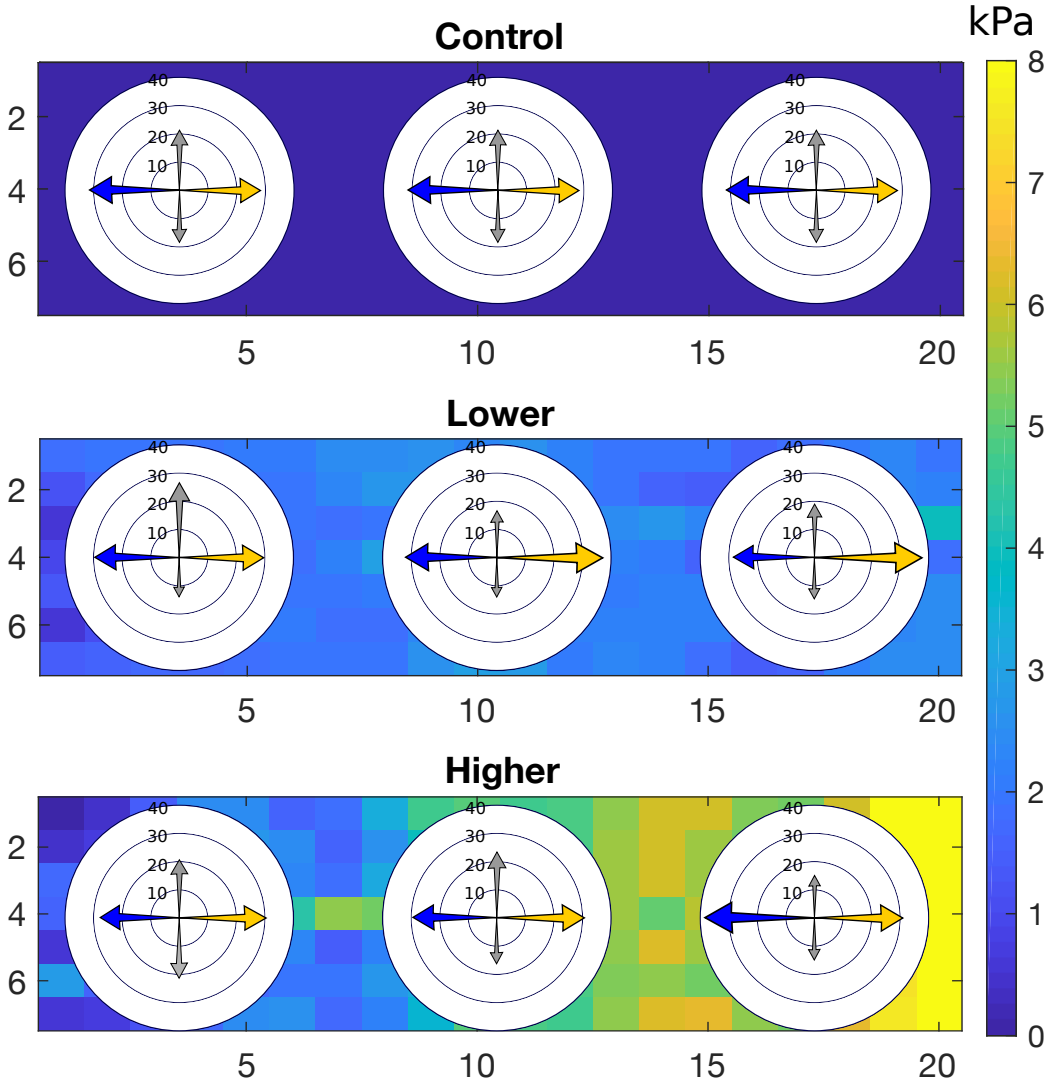

Figure 5.4: Percentage of elongation toward a given direction for each segment of the control and both gradient gels.The measures have been done per fields for each gradient segment labels (I-II-III) (N=3,n=3).

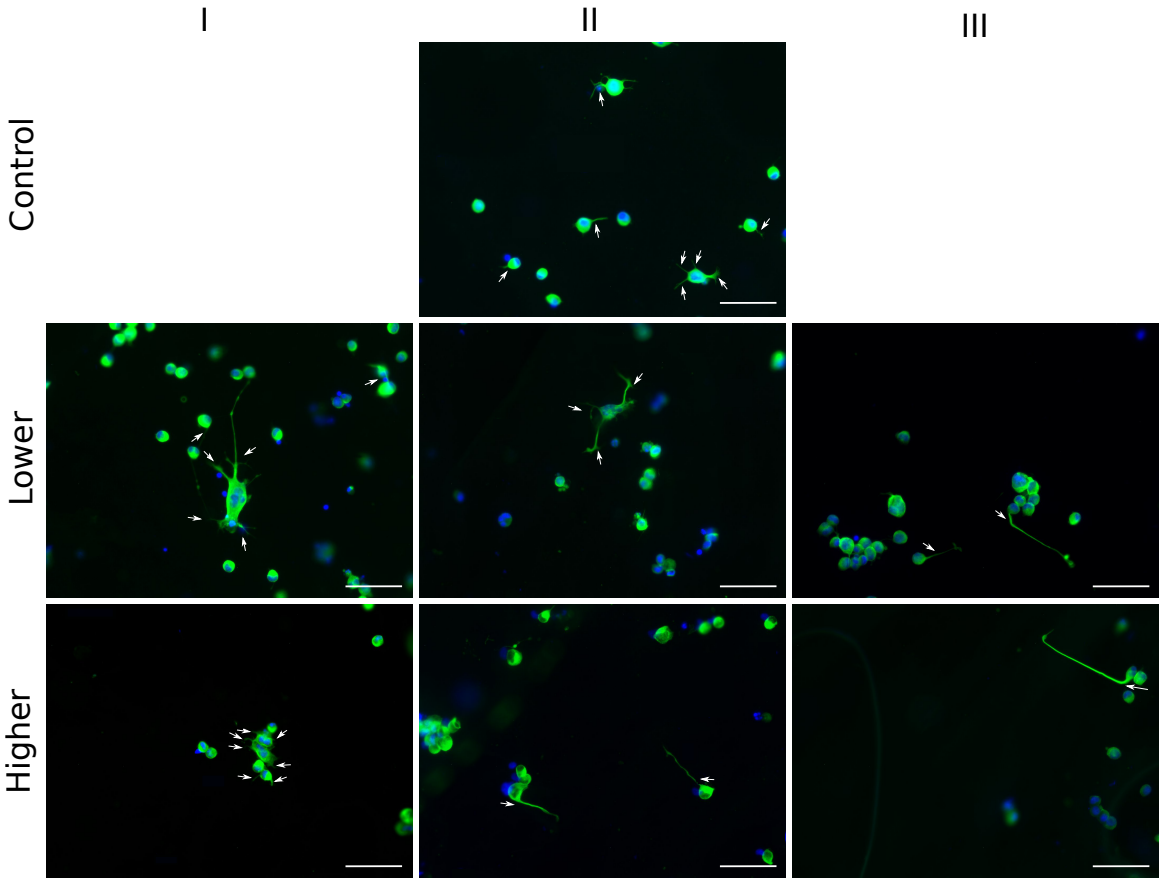

Figure 5.5: Representative merged images taken from immunolabeled NG108-15 treated with DAPI (blue) and β-III-tubulin (green) on each part (I-II-II) of the Lower and Higher gradient and on the control. White scale bars : 100μm.

Gradient	**Segment label**	**Slope** (kPa.mm^{-1})	**Density** (mg.ml^{-1} ±SD))	**$\sim$ E** (kPa ± SD)	**Orientation** (Along the gradient%)
Control	-	0	70±5.7	1.0±0.2	60.6
Lower (0.85 kPa/mm)	I	0.85	67±4.2	1.7±0.3	60.0
	II		71±5.9	1.9±0.1	**70.1**
	III		79± 7.1	2.0±0.2	**67.0**
Higher (7.96 kPa/mm)	I	7.96	73± 7.1	1.5±0.6	58.7
	II		86±6.9	4.1±1.1	61.1
	III		122±4.8	7.1±1.9	**70.2**

Table 5.1: Characteristics of RAFT-Stabilised collagen substrates. Noted in the table are the collagen density (mg.ml^{-1}) and the corresponding surface stiffness (E, kPa) for the control and the segmented area (I-II-III) of the gradient gels measured using AFM-force spectroscopy. The percent orientation of neurite elongating along the gradient on each segment is reported for each stiffness absolute value and gradient slope characteristics. Data are presented as mean ± SD.

5.4 Discussion

The objective of this work was to induce a neural cell change in behaviour in response to the substrate properties only. The study presented in this Chapter provides the first evidence that neurite elongation can be influenced by a combination of substrate stiffness absolute value and the steepness of the gradient slope, suggesting that neurons have the potential to process a combination of mechanical guidance cues.

Neurite branching is potentially an important parameter for the establishment of synaptic connections (Flanagan et al., 2002), needed for successful regeneration (Nectow et al., 2012; Moskow et al., 2018). Franze and Guck (2010), and Franze et al. (2013) have shown the influence of substrate compliance on neurite branching and neurite orientation, and the rigidity range are investigated towards an optimal ECM-growth cone interaction (Balgude et al., 2001; Flanagan et al., 2002; Sundararaghavan et al., 2009; Rosso et al., 2017d). Here, consistently, a higher percentage of cells presented neurites branching on the more compliant area of the lower gradient (I_{Lower}). A similar phenomenon was reported by Flanagan et al. (2002) and Franze et al. (2013). However, when comparing the substrate zones with similar absolute stiffness value (Control, I_{Lower} and I_{Higher}), the percentage of cell presenting neurites branching was significantly greater on the Lower gradient. This observation highlights the potential of neuronal cells to be mechanosensitive to specific stiffness gradient slopes as opposed to only the absolute stiffness value of the substrate. Rosso et al. (2017d) investigated neurite orientation on mechanically uniform substrates of different stiffnesses (1-10-20 kPa), and their results suggested that within the physiologically relevant stiffness range tested (Rosso et al., 2014), the directionality of neurite outgrowth was substrate-stiffness sensitive. In this study, the neurites did not

orientate in a particular direction on the soft areas (Control, I_{Lower} and $I_{Higher} \sim 1$ kPa). However, on the stiffest area of the Lower gradient gel ($III_{Lower} \sim 2$ kPa), a preferential orientation towards stiffer areas was observed. A preferential orientation was also observed on the stiffest region ($III_{Higher} \sim 10$ kPa) towards softer areas. It is known that the growth cone detects guidance cues and has a major role in neurite orientation (Franze and Guck, 2010; Rosso et al., 2017d; Franze et al., 2013; Balgude et al., 2001). This observation supports the possibility that both the absolute stiffness of the substrates and the substrate gradient slope influence neuronal behavior. Further work will be required to allow a better understanding of how neuronal growth cones process and convert the combination of gradient slope and absolute stiffness value into intracellular biochemical signals leading to neurite reorientation.

Neurons on different part of the stiffness gradient gels did not exhibit significant differences in neurite length, proportion of cells presenting neurites and number of neurite per cell (from 1 to 10 kPa). This result is in contrast with Rosso et al. (2017a), who noted that length of neurite outgrowth from embryonic DRG explants was substrate stiffness-sensitive (between 1 and 10 kPa). In addition, Leach et al. (2007), have shown that neurite were longer, more branched and a greater percentage of cell presented neurites on stiff substrates (stiffness between 10^2-10^4 Pa) compared to soft substrates (10 Pa). However, in their study no significant differences were found on substrate with a stiffness greater than 10^2 Pa. The difference observed could potentially be explained by the difference in the cell type used for the study, the difference in the substrate composition, the absence of additional external cues (e.g. external growth factors) or the introduction of a stiffness gradient slope as previously hypothesised by Leach et al. (2007) . Related work has investigated neurite growth behaviour within 3D substrates with varying stiffnesses (Sundararaghavan et al., 2009), however the focus of this study was restricted to neuronal behaviour on surfaces of substrates with defined stiffness environments. Further studies would be

required to separate the influence of absolute stiffness and stiffness gradient slope in order to investigate the effects on neuronal growth further.

This Chapter provides relevant information on neuronal growth-cone durotaxis, demonstrating neurite orientation in response to the presence of a stiffness gradient, revealing previously unreported sensitivity to the combination of gradient slope and absolute stiffness. Neurites grew toward stiffer or softer substrate regions, depending on the gradient/absolute stiffness combination, highlighting how both cues combined can affect orientation. With the intention of informing the next generation of PNS injuries treatments strategies, this precious set of data will be used to enable the parameterisation of a mathematical model to predict the next experimental design to be tested.

Chapter 6

Mathematical modelling informed design of NGCs

6.1 Introduction

As mentioned previously in Chapter 1, for large gap injuries, a surgical procedure is required to bridge the gap and improve the connection from the proximal part to the distal stump. A tubular structure, e.g. nerve graft or nerve guidance conduit, is sutured in the nerve injury site to support neurite growth. However, finding the optimal design of the nerve conduit is a work in progress in the community. While there are likely various reasons why neuronal growth in a NGC may not exceed autograft outcomes, the physical features and mechanical cue environments is likely to play a key role. Mechanical guidance cues, provided by the structural and physical properties of the ECM, are known to affect cell migration (Zaman et al., 2005; Stefanoni et al., 2011). Lo et al. (2000) defined as durotaxis the phenomenon by which cells sense the mechanical environment and adapt their movement in response to a stiffness gradient. In previous studies, the moving cells seemed to be preferentially directed towards stiffer regions, e.g. for VSMCs responding to stiffness gradient (Wong et al.,

2003; Zaari et al., 2004; Isenberg et al., 2009) (see Section 1.6.2), or to show more cell adhesion on stiffer substrates (Zaari et al., 2004). Seeking to understand these phenomena, several mathematical models have been developed, e.g. Stefanoni et al. (2011) have developed a mathematical model for durotaxis based on the experimental studies of Lo et al. (2000).

Here, it is proposed that adapting the spatial arrangement of the mechanical properties within a NGC could lead to better growth. In previous work, described in Chapters 4 and 5, a new experimental 2D stiffness model to investigate the behaviour of neuronal cells in response to various mechanical gradients *in vitro* was developed. Neurite branching and orientation were two behavioural responses shown to be dependent on both the stiffness gradient and absolute stiffness value of the substrate. Seeking to accelerate the design process of NGCs, to reduce financial expense, and to minimise animal based experiments, mathematical modelling can be used as a powerful tool to direct experimental work (Coy et al., 2017) (Section 1.8). Based on the framework of Stefanoni et al. (2011), modelling cell durotaxis, and adapted to the specific experimental data obtained previously, an *in silico* model was developed to test the hypothesis that a stiffness gradient within a NGC can improve guided neurite growth and improve the performance of the device.

Following the experimental-theoretical feedback loop described by Coy et al. (2017), a computational model was developed and parameterised using experimental data to predict the next experimental set up to be investigated (see Figure 6.1). Mathematical modelling provides an additional rationale for experimental design decisions. Although computational work does provide its own challenges, such as the dilemma of initial mathematical model choice, the need for sufficient quality and quantity of data for robust parameterisation, it offers a cost and time-efficient way to narrow down the most important experimental designs to be investigated further (Gutenkunst et al., 2007).

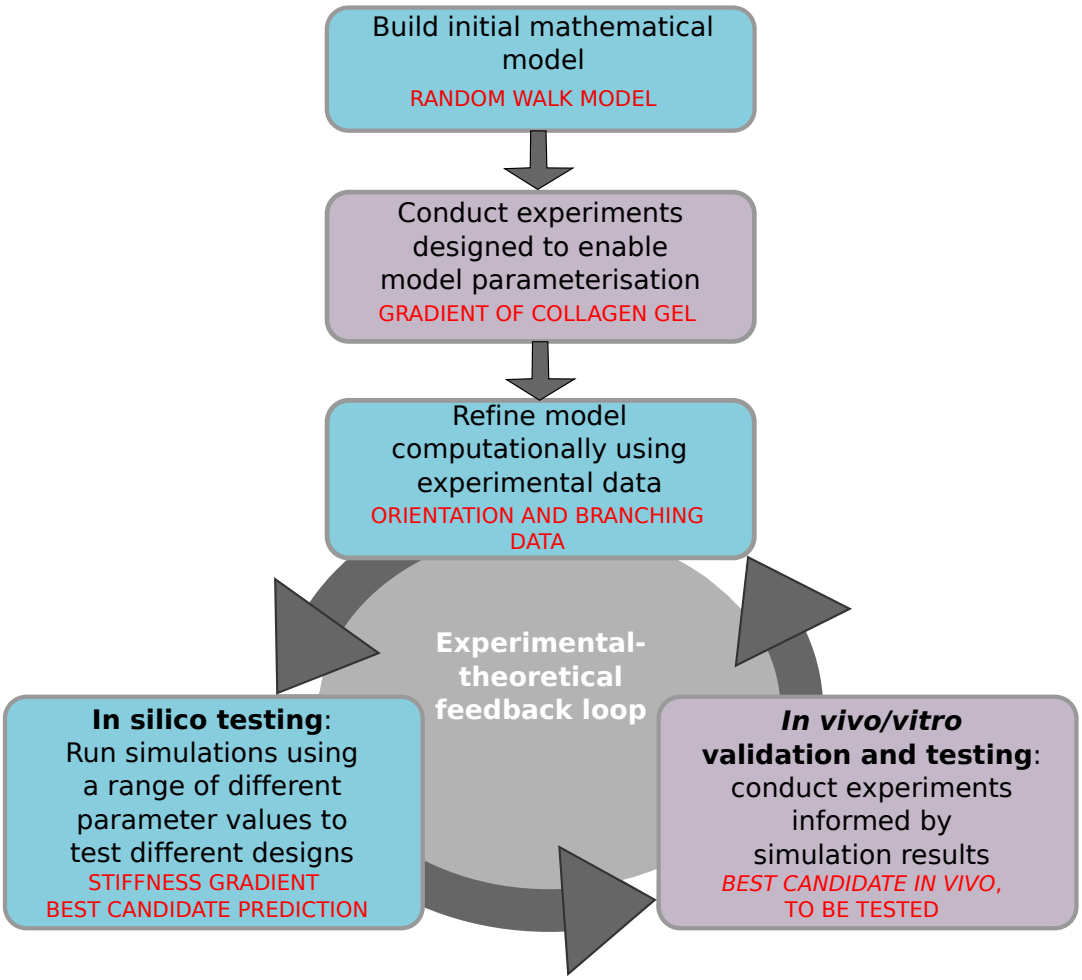

Figure 6.1: Theoretical-experimental tissue engineering design workflow adjusted to this study. A random model is initially built and parameterised using experimental data presented in Chapter 5. The model predictions help in the design of the next experiments and the obtained results are used to refine and expand the model entering in the experimental-theoretical feedback loop. Adapted from Coy et al. (2017).

In order to model cell migration, two principal types of models have been used, namely continuous approaches and discrete approaches. Cell migration is a process involving the translation of a cell in a particular direction and towards a specific location. The use of mathematical modelling to study this phenomenon is not novel. In the absence of cues, cell motility has been found to correlate well to a specific case of a random walk called Brownian motion of a particle (Dunn and Brown, 1987; Walmod et al., 2001). This mathematical framework can be extended to describe different kinds of cell motility such as random motility (Dickinson and Tranquillo, 1993; Zaman

et al., 2005) or in response to a range of external stimuli, or guidance cues, such as chemical signals (chemotaxis) (Tranquillo and Lauffenburger, 1987; Stokes and Lauffenburger, 1991; Jabbarzadeh and Abrams, 2005); and haptotaxis (Dickinson and Tranquillo, 1993; Smith et al., 2004). Most recently, studies have focused their computational work on durotaxis (Moreo et al., 2008; Stefanoni et al., 2011), the ability of certain types of cells to recognise and respond to the mechanical properties of their environment (Lo et al., 2000). This physical mechanism has been studied using a continuous model by Moreo et al. (2008). Stefanoni et al. (2011) proposed a 2D discrete model for durotaxis to simulate cell movement influenced by the mechanical environment. These studies help understand the basic mechanisms implied in the cell migration process, cell-substrate interaction and the change in speed or direction of cells over time.

Here, the first, validated, discrete mathematical model of neurite motility in response to durotaxis is presented. The model presented in this Chapter predicts the growth and branching of neurites in response to different combinations of gradient and absolute stiffness values based on the data in Chapter 5. With this model, a spatial arrangement of mechanical factors, i.e. combination of gradient/absolute stiffness, is proposed to design a new NGC and direct future experimentation.

6.2 Methods

Experimentally, neuronal cells were observed to respond to stiffness gradients by modifying their branching behaviour and orientation. Neurites grew toward softer or stiffer substrate regions, depending on the gradient and absolute stiffness associated with their environment. This valuable data set was used as a basis to develop the mathematical model, described in Section 6.2.1. The mathematical model was build using Matlab software (Release 2108a, The MathWorks, Inc., Natick, Massachusetts, United States). Seeking to capture the biological behaviour observed (orientation and branching pattern), the model was built based on previous work and optimised to fit the experimental data set. Sections 6.2.2 ,6.2.3 describe the tools used to build the model, respectively for the orientation and the branching pattern and Section 6.2.4 describes the tool used to optimise the model.

6.2.1 Experimental data set

In order to capture the specific behaviour of the neurites in response to gradients, the data collected from the experimental work on NG108-15 cell line, described in Chapter 5, were exploited. Specifically two sets of data were used, the first set of data quantified the neurite orientation obtained after 48 hours of culture *in vitro*, as shown in Figure 6.2. This histogram presents the distribution of the angles measured for each gradient/absolute stiffness condition (Control, Lower I-II-III and Higher I-II-III) (see in Section 4.4 Table 4.3 for details of each condition).

The second set of data was the distribution of branches given for each condition (Control, Lower I-II-III and Higher I-II-III) represented by a probability density function, as seen in Figure 6.3. For the model, the neurite growth rate was kept constant

and was taken from experimental measures to be 2 μm.h^{-1} (see Chapter 5).

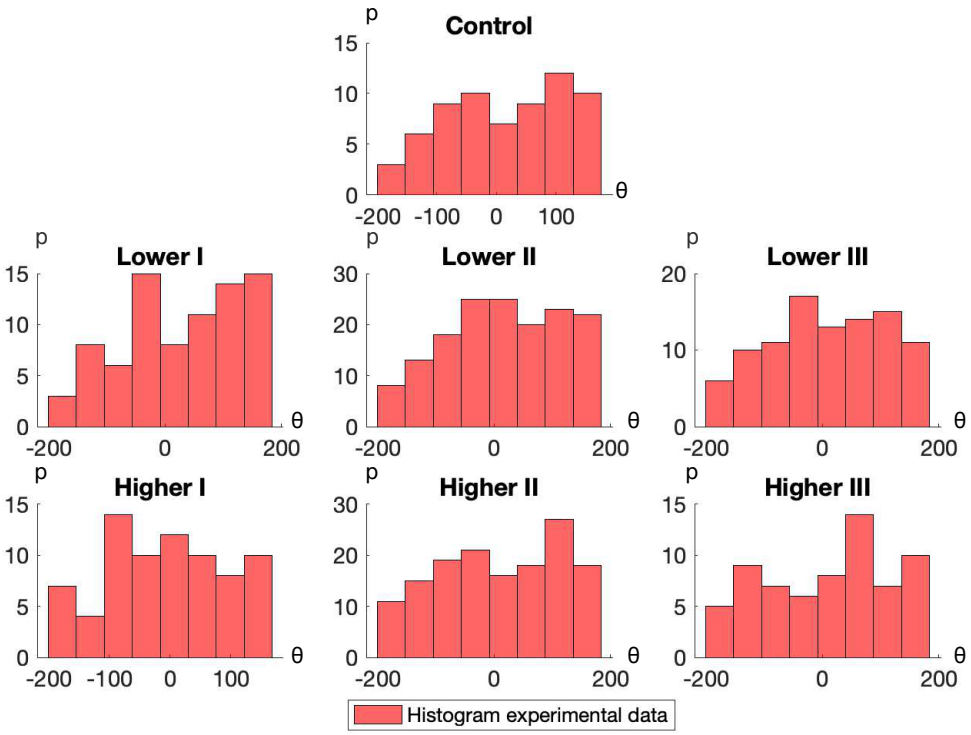

Figure 6.2: Distribution of the neurite orientation ($\theta \in$ [-180,180]°) measured experimentally for each condition (Control, Lower I-II-III and Higher I-II-III). Data collection detailed in Section 5.2.3.

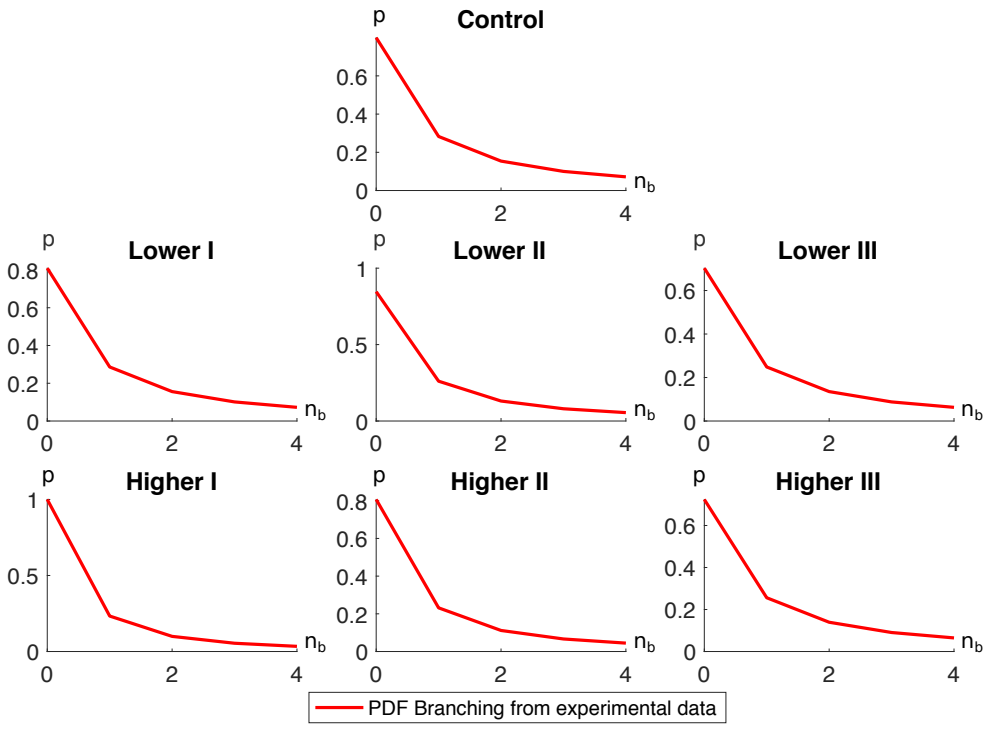

Figure 6.3: Probability distribution of number of branches (n_b) based on experimental data for each condition (Control, Lower I-II-III and Higher I-II-III). Data collection detailed in Section 5.2.3 Figure 5.2).

6.2.2 Model formulation

Brownian motion, first observed by Robert Brown in 1828, describes the random movement of particles in a fluid (Karatzas and Shreve, 1998). Previous studies have shown that in the absence of external guidance cues, cell locomotion on a substrate can be assimilated to the Brownian motion of particles. Even though fundamental mechanisms are not the same, the similarities in trajectories between cells and Brownian particles suggest that a mathematical relationship that links the two could be appropriate (Dunn and Brown, 1987; Stokes and Lauffenburger, 1991; Stefanoni et al., 2011). Langevin (1908) applied Newtonian dynamics to introduce the concept of the equation of motion of a random variable (in this case the position of a Brownian particle), and so, the Langevin equation, an analytical approach to random processes was introduced. This is useful to this day to describe cell migration (Dunn and Brown, 1987; Stokes et al., 1991; Stefanoni et al., 2011). This equation (Coffey W. T., 1985; Langevin, 1908) can be written down using Newton's second law, assuming that the cell experiences two forces, namely: (a) the drag force, $-\zeta\dot{x}(t)$, representing a dynamical friction experienced by the cell to slow its movement, with ζ being the drag coefficient and $\dot{x}(t)$ the velocity, and (b) $F(t)$, the sum of all the stochastic processes acting on the cell. $F(t)$ is commonly described as white noise following a Gaussian distribution with zero mean (Coffey W. T., 1985; Zwanzig, 2001). Langevin's stochastic differential equation of motion can be summarised as follows

$$m\ddot{x}(t) = -\zeta\dot{x}(t) + F(t), \tag{6.1}$$

for a cell of mass m. For neurons in a tissue, the ratio between inertial and viscous forces is low (Reynold's number of $\sim 10^{-7}$ for a growth cone) (Zubler and Douglas,

2009) allowing the assumption that $m\ddot{x}(t) = 0$. Thus, Eq. (6.1) becomes

$$\dot{x}(t) = \frac{1}{\zeta}F(t). \tag{6.2}$$

Then, by integrating Eq.(6.2) using Euler's method, the position of the neurite at each iteration, x_t, can be calculated in terms of its previous position, x_{t-1}, (Segev and Ben-Jacob, 1998; Zubler and Douglas, 2009) and can be described as:

$$x_t = x_{t-1} + \frac{1}{\zeta}F(t)\Delta t, \tag{6.3}$$

where Δt is the time step (see Table 6.1).

For the durotaxis model reported by Stefanoni et al. (2011), the direction of $F(t)$ is adapted to be biased towards higher values of stiffness. Based on the data set presented in Section 6.2.1, where neurite orientation was dependent on the combination of gradient and absolute stiffness values, the motion due to the stochastic force (durotaxis) in Eq.(6.3) had to be adapted, therefore its direction follows a probability density function taken from the experimental data.

To avoid generating an irregular neurite shape, not in agreement with the experimental observations, the following assumptions were made: the first step of each neurite was made initially at an angle θ, taken from the measured probability distribution function depending on the local measurement of the stiffness, shown in Figure 6.2. Additionally, following the work of Katz (1985), axonal growth was assumed to follow fairly straight paths due to the axon mechanical resistance. Therefore, a new distribution of angles, ϕ, was defined to mimic this behaviour. The parameter ϕ follows a normal distribution ϕ ($\mu = 0$, σ), with ϕ boundaries $\in$ [-60;60]° (see Figure 6.4 and Table 6.1). The parameters of this distribution were fitted for each stiffness condition (see Section 6.2.4.2).

In order to be able to compare the simulation of the model to the data set collected,

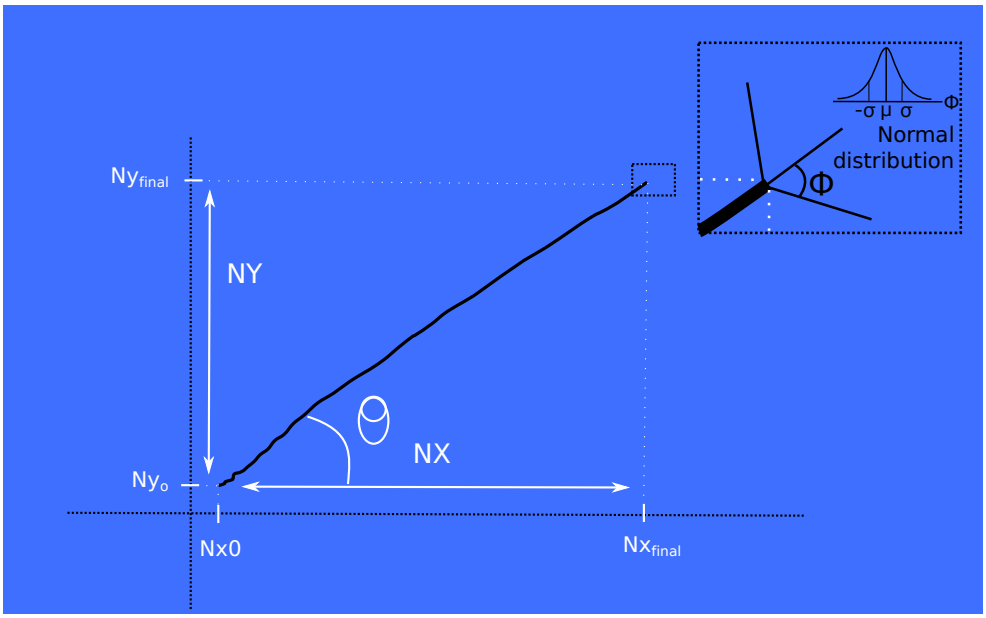

Figure 6.4: The measurement of simulated neurite orientation was establish following the experimental method. The orientation θ was measured for the full neurite outgrowth using Eq.(6.4). NX is the adjacent side and NY the opposite side used to calculate the angle θ, for each neurite, (NX, NY) are calculated using the initial position of the neurite (N_{x0}, N_{y0}) and the final position (Nx_{final}, Ny_{final}). The angle parameter ϕ added a more realistic walk to the model and was chosen to follow a normal distribution ϕ ($\mu = 0$, σ).

the neurite orientation θ of each neurite was calculated, at the end of each simulation, following the experimental procedure described in Section 5.2.3, as :

$$\theta = \cos^{-1}\left(\frac{NX}{\sqrt{(NX^2 + NY^2)}}\right), \tag{6.4}$$

where NX and NY are the displacement in the x and y axis respectively. The initial neurite positions (N_{x0},N_{y0}) were randomly distributed or mentioned otherwise.This is summarised in Figure 6.4.

Parameter	Symbol	Value	Units	Reference
Growth rate	G	0.002	mm.h^{-1}	Section 5.2.3 (2019)
Time step	Δ t	1	hour	-
Neurite position (X axis)	N_x	-	mm	-
Neurite position (Y axis)	N_y	-	mm	-
Neurite orientation	θ	[-180;180]	degree	Section 5.2.3 (2019)
Straightness bias	ϕ	[-60;60]	degree	Katz (1985)
Branching probability	P_i	-	-	Van Pelt et al. (1997)
Number or branches	n_b	[1;5]	-	Section 5.2.3 (2019)

Table 6.1: Parameters.

6.2.3 Branching model

Van Pelt and Verwer (1983) have studied probabilistic branching models of dendrite formation and have proposed mathematical equations describing the neurite branching process (Van Pelt and Verwer, 1983; Van Pelt et al., 1992, 1997). They proposed three branching models, with increasing levels of complexity, where the branching is assumed to occur exclusively at terminal segments (Van Pelt et al., 1992; Dityatev et al., 1995; Van Pelt et al., 1997) (see Figure 6.5). Their first model is called the B-model, where the branching probability (P_i) remains constant during the growth process and is expressed as follow

$$P_i = \frac{B}{T_b}, \tag{6.5}$$

where B is the expected number of branching events. The simulation is run over a period divided into T_b short periods called time bins. As mentioned by Van Pelt et al. (1997), the number T_b has to be orders of magnitude larger than B, in order for the branching probability $P_i << 1$, hence reducing the possibility of a segment to branch more than once per time bin. However, this simple model assumes a constant branching probability, and gives unrealistic results (see Figure 6.6) with rapid proliferation of the terminal segment and a clear increase in growth rate (Figure

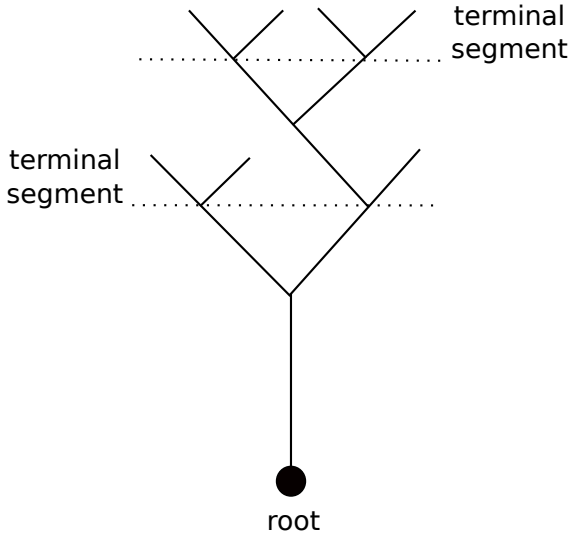

Figure 6.5: Branching tree showing the terminal segments. Adapted from Van Pelt and Verwer (1983).

6.6B).

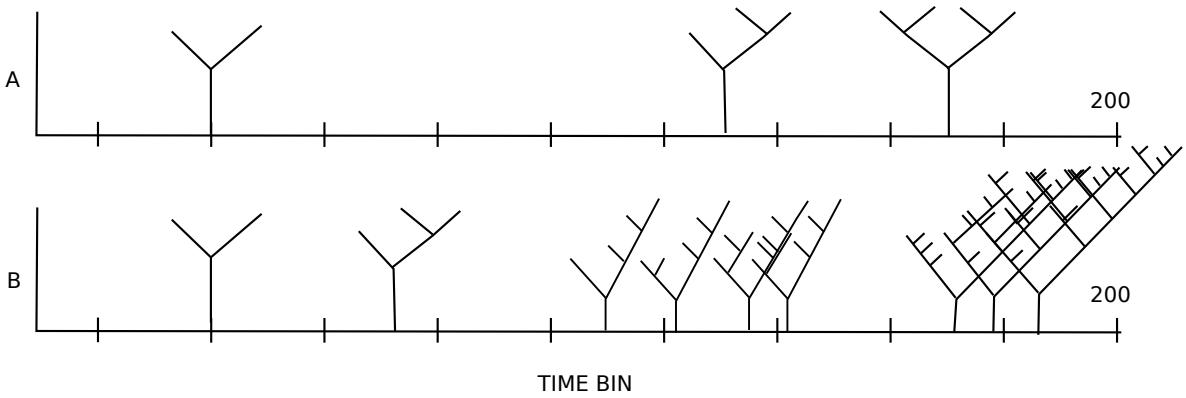

Figure 6.6: Branching pattern versus time bin based on B-model, constant branching probability. (A) Shows a few branching events and (B) shows a sequence with high proliferation of the branching pattern. Adapted from Van Pelt et al. (1997)

In order to reduce the growth accelerating effect, the authors extended the B-model to the BE-model, where the probability of each terminal segment branching, P_i, is now dependent on n, the number of occurring branching events. The probability

of branching is then expressed as

$$P_i = \frac{B}{(T_b)n^E}, \tag{6.6}$$

where B is the expected number of branching events of a single path during the entire simulation (T_b) and E is a constraining factor. The parameter E has been chosen to be larger than 0, so each additional branching event will reduce the probability of branching, therefore if a neurite has branched already it is less likely to branch again. The parameter E modulated the strength of the degree dependency. Van Pelt et al. (1997) described how varying both E and B can result in a variety of P_i distributions.Therefore, these parameters were fitted to match the branching distribution measured experimentally following the procedure described in Section 6.2.4.3.

6.2.4 Model parameterisation

6.2.4.1 The Particle Swarm method

A particle swarm algorithm was used to optimise the orientation and branching models. The particle swarm method (PSwarm method), is a stochastic optimisation, based on a population (swarm) of particles developed by Kennedy et al. (1995). This iterative algorithm is commonly used for variables that have specific, well-defined lower and upper bounds (Vaz and Vicente, 2007, 2009). The underlying algorithm is comprised of two steps: (a) the poll step, which applies a pattern search method (coordinate search method), and (b) the search step, which generates points in the feasible region using particle swarming, to find a global minimum.

The PSwarm method is used to uniformly sample the parameter space and to ensure that the solution is not a local minima. Generating a population in the second step allows the algorithm to poll around the best particle, improving the overall robustness of the algorithm (Vaz and Vicente, 2009).

6.2.4.2 Parameterisation of the orientation model

Katz (1985) have shown that axons do not grow randomly and tend to maintain the same orientation throughout their growth. They have measured the bend of embryonic chick and frog axons *in vitro* on acid-rinsed glass surfaces from the straight of growth. For chick and frog axons elongation, they observed respectively less than 70° and less than 50° deviation from straight lines. Thus, in order to build a more realistic model, the following assumption was made: after picking the initial orientation angle θ from the experimental data set, neurites would elongate following an angle distribution θ that is biased towards the initial orientation angle.

Following the first step, the angle ϕ for each step, is taken from the normal distribution $\phi(\mu, \sigma)$, with $\mu = 0$. For each substrate condition (Control, Lower I-II-III and Higher I-II-III), the parameters ϕ and σ have been optimised using PSwarm algorithm and based on Katz (1985) work, given the ranges presented in Table 6.2.

A summary of the obtained values for each parameter and for each condition is given in Table 6.3.

6.2.4.3 Parameterisation of the branching model

Once again, the particle swarm optimisation method was used, this time to fit the parameters B, E and T_b, in order to define the branching probability function for each stiffness condition. The upper and lower bounds were based on previously investigated values by Van Pelt et al. (1992, 1997), and the ranges were modified to adapt it to the data set presented in Section 6.2.1, and are given Table 6.2.

However, due to the computation cost of the particle swarm algorithm, it was decided not to increase the number of iterations, and, instead, via an ad hoc process, ranges of the parameters (E, B and T_b) were refined to arrive at branching probability

density functions that better suited the experimental data sets. A summary of the obtained values for each parameter and for each condition after optimisation is given Table 6.3.

Parameter	Lower bound	Upper bound
σ (deg)	-60	60
ϕ (deg)	-60	60
E (1)	0	5
B (1)	0	5
$T_b(1)$	100	900

Table 6.2: Summary of the upper and lower bounds for each parameter fitted.

6.2.5 Statistical analysis

Statistical analysis of the simulations was done by using JMP Pro 13 software (JMP SAS Institute, Marlow, Buckinghamshire, UK). A non parametric comparison for each pair using the Wilcoxon method was used to assess the difference between the conditions and the control, as the populations were not normally distributed. Specific P values will be mentioned in each Figure caption.

	Control	Lower-I	Lower-II	Lower-III	Higher-I	Higher-II	Higher-III
E (kPa)	1.0	1.7	1.9	2.0	1.5	4.1	7.1
Slope (kPa.mm^{-1})	0	0.85	0.85	0.85	7.96	7.96	7.96
σ (rad)	37.7	2.0	45	3.5	19.8	26.8	12.8
ϕ (rad)	5.7	15.8	3.9	3.2	40.0	0.26	4.8
E (1)	1.5	1.5	1.7	1.5	2.1	1.8	1.5
B (1)	5	3	3	5	2	2	4
T_b(1)	600	400	400	700	200	300	600

Table 6.3: Summary of the stiffness characteristics of the collagen gel substrates and the parameter values obtained for the control and the gradient gels (lower and higher) after optimisation using the particle swarm algorithm.

6.3 Results

The orientation and the branching pattern were the two biological behaviours to model as a function of the mechanical gradients created in Chapter 4. Due to the specific data set obtained in Chapter 5, this work was based on models developed by Stefanoni et al. (2011) for the durotaxis (orientation) and Van Pelt et al., for the branching pattern and optimised to fully capture the desired behaviour. The branching and orientation predictions of the model were validated against experimental data and this is shown in Section 6.3.1. After validation, the model was used to simulate *in silico* neurite growth for seven different stiffness gradient conditions (see Table 6.3), for a short period of time, to identify the best stiffness candidate to use for a more extensive and computationally expensive step, and this is described in Section 6.3.2. Then, Section 6.3.3 presents the *in vivo* prediction, where the initial hypothesis was tested to see if the previously selected candidate will allow a better growth in a conduit than the control when placed within a NGC.

6.3.1 Model parameterisation

The model parameterisation was performed using the PS swarm algorithm. In order to be satisfied by the choice of parameters, the error function between the experimental distribution and the simulations needed to be minimised. The experimental data were collected after a period of time of 48 hours. Hence, the theoretical data set was built on a large number of simulations (100) for 48 steps (equivalent to 48 hours) unless mentioned otherwise. These data were then compared to the experimental data set for both the orientation and the branching pattern to establish the reliability of the model.

6.3.1.1 Parameterisation of the orientation model

In order to justify the number of neurites to use for each simulation to obtain realistic data and to avoid prohibitive simulation time, a sensitivity analysis was conducted, where 100 simulations were run for 10, 50, 100 and 1000 neurites for 48 hours and the percentage error obtained between the angle distribution of the simulation and the experimental data set calculated. As expected, increasing the number of neurites reduced the percentage error. Figure 6.7 shows the percentage of the total error between the simulated and the experimental data set for each condition (Control, Lower I-II-III and Higher I-II-III) for 10, 50, 100 and 1000 neurites.

Larger numbers of neurites simulated resulted in larger simulation time, e.g. less than an hour for 100 neurites versus more than 15 hours for 1000 neurites. Therefore, a fine balance between quantitative and qualitative results needed to be found. The best results were obtained for 1000 neurites, however, a large number of simulations for such a large number of neurites was highly computationally-expensive. A 40% difference was calculated between the results obtained with 50 versus 1000 neurites. Only a 20% difference was calculated between the results obtained with 100 versus 1000 neurites. Furthermore, 100 simulations of 100 neurites was less time and memory consuming than 1000 neurites and gave more satisfactory results than 10 and 50 neurites, making this parameter the best option for the simulation. Hence, 100 neurites was used for the simulations.

For 100 neurites, a percentage error between 10 and 15% ±SD was obtained for all the seven cases after the optimisation. The largest standard deviation was observed for the condition Higher-I and the percentage error was never higher than 35%. This was found to be satisfactory, as demonstrated in Figure 6.8, where on average less than 10% variation was visible between the experimental and theoretical angle distribution (1 simulation of 100 neurites for 48 hours).

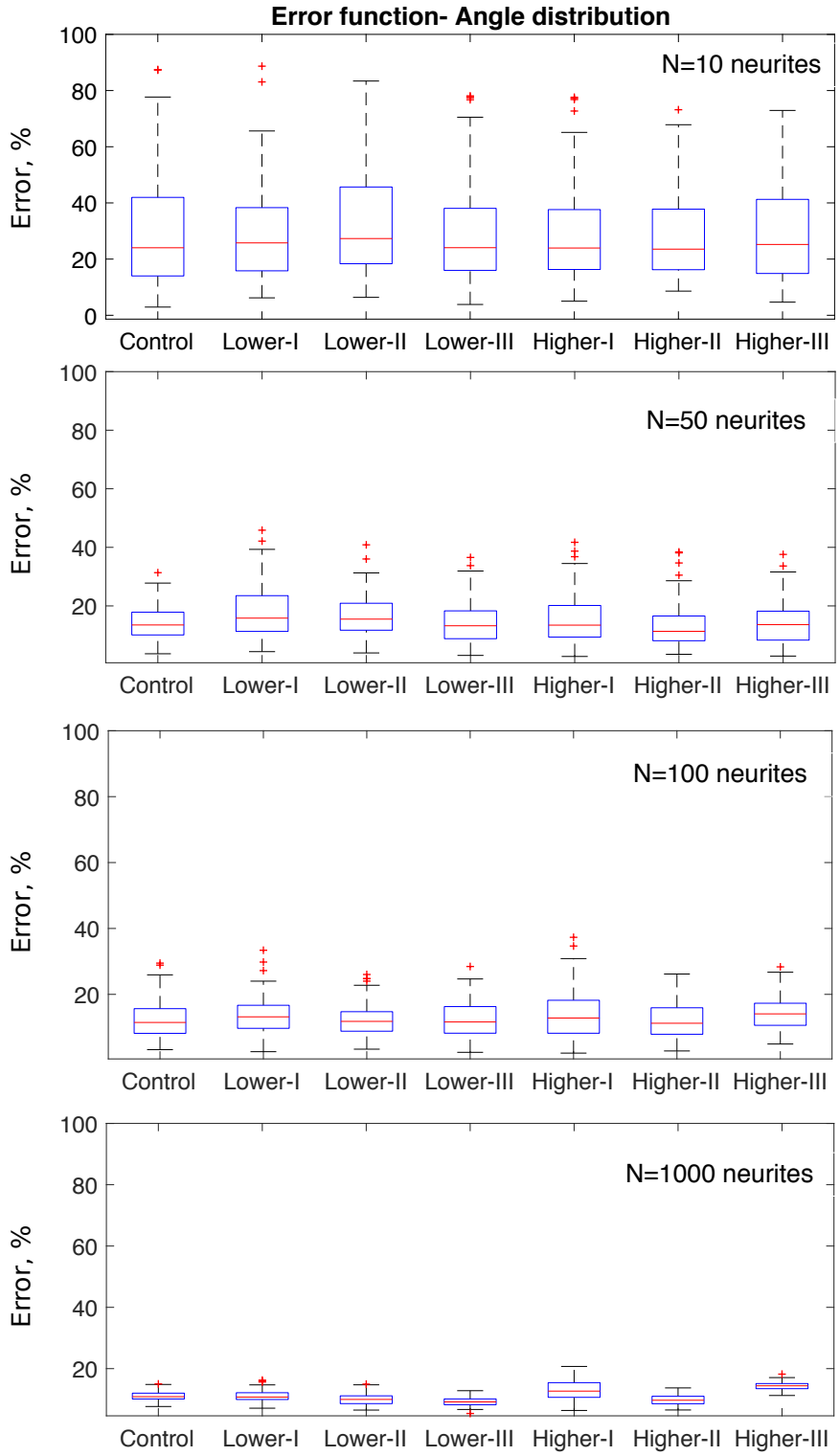

Figure 6.7: Sensitivity of the angle distribution model to neurite number. The graphs show the percentage error comparing the simulated orientation and the experimental data sets for 100 simulations for each conditions (Control, Lower I-II-III and Higher I-II-III) for 48 hours (48 steps). Four different numbers of neurites were tested to evaluate the sensitivity of the model (N=10, 50, 100, and 1000).

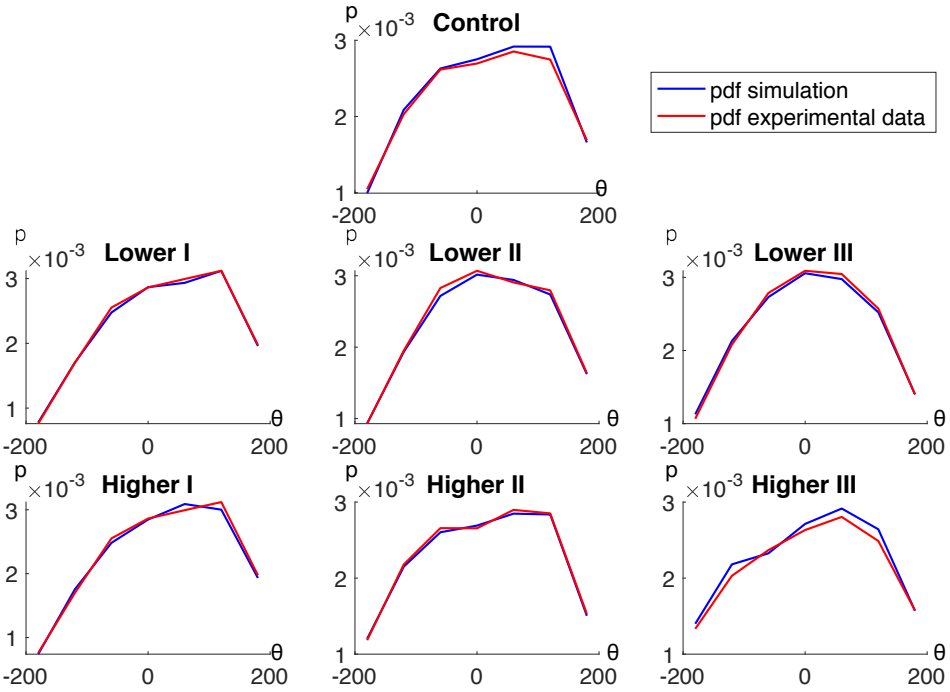

Figure 6.8: Example showing a plot of the probability density function (pdf) of the simulated neurite orientation θ for each condition (Control, Lower I-II-III and Higher I-II-III) for 100 neurites after 48 hours versus the pdf of the experimental data set.

6.3.1.2 Parameterisation of the branching model

Similarly to Section 6.3.1.1, 100 neurites were simulated 100 times for 48 hours, however, here the simulated branching pattern was compared to the data collected experimentally. Figure 6.9 shows the total percentage error between the theoretical and the experimental branching distributions for each of the seven conditions (Control, Lower I-II-III and Higher I-II-III). For Control, Lower I-II-III and Higher-III, the mean error is between 10 and 20%, and for the conditions Higher-I and Higher-II the mean error is between 30 and 40%.

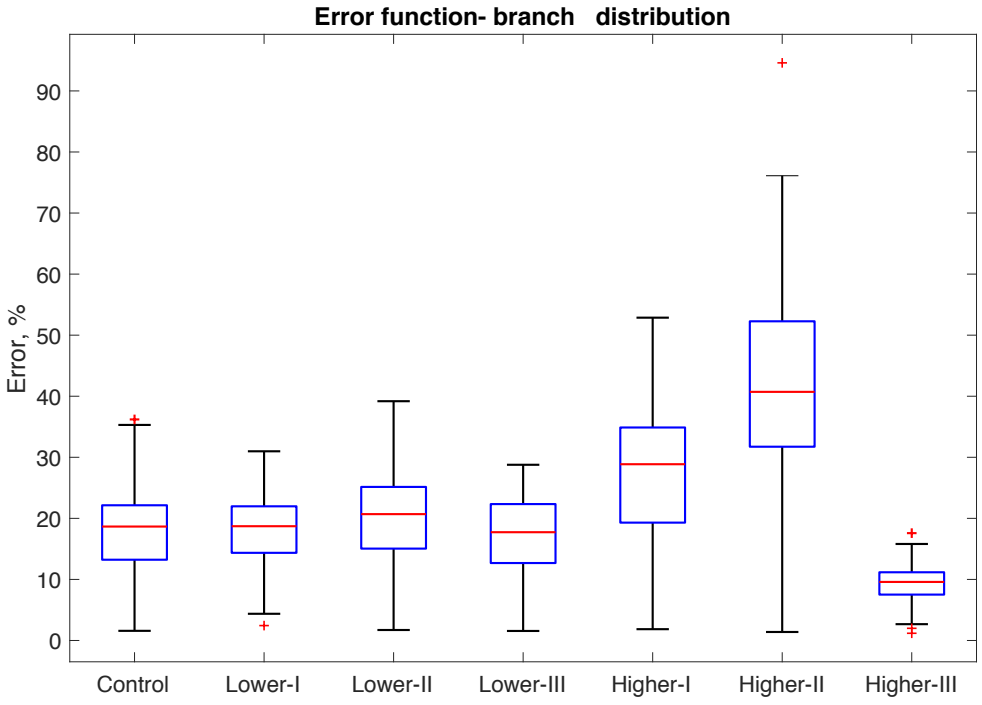

Figure 6.9: Percentage error comparing the simulated branching pattern to the experimental branching distribution for 100 simulations for each conditions(Control, Lower I-II-III and Higher I-II-III). 100 neurites where simulated for 48 hours.

6.3.2 *In vitro*-like simulations

In vitro neurite growth was simulated on a square piece of gel for each condition to identify the one that will allow the largest longitudinal neurite growth. Figure 6.10 shows for each condition, an example for one simulation of the pattern observed for 100 neurites after 120 hours (5 days), a time point chosen arbitrarily because it could be reproduced easily experimentally. The small red square represents the initial position of the neurites ($0.1\times$ 0.1mm^2). The neurites are spread randomly as they are when cells are pipetted onto a gel during an *in vitro* experiment. The bigger red square represents the maximum distance reachable by the neurites after a period of 120 hours at a growth rate of $2\mu m.h^{-1}$. A difference in straightness is observed depending on the substrate conditions as a result of the model optimisation. The branching pattern modelled is gradient/absolute stiffness value dependent, as observed experimentally.

In order to define the best stiffness candidate to use for more extensive *in vivo*-like simulations, each of the seven stiffness conditions were simulated 100 times (100 neurites for 120 hours) and the absolute longitudinal displacement was analysed (in mm). Figure 6.11 shows the mean of this absolute longitudinal displacement for each condition. The Higher-I condition showed the lowest longitudinal growth with an average displacement of 0.07 mm after 5 days. Overall, Lower I-II ($p < 0.001$) and Lower-III ($p < 0.0001$) gels appear to be better than the control and even though there is a small effect, it is highly significant. The condition Lower-III showed the longest longitudinal growth ($p < 0.0001$). Due to the high number of simulations (100) we can be confident in the statistical differences obtained regardless of the small length variation.

This model has identified the optimal condition for supporting neurite extension *in vitro* compared to the control, and Lower-III will be the candidate to be used for the *in vivo* predictions in the following Section.

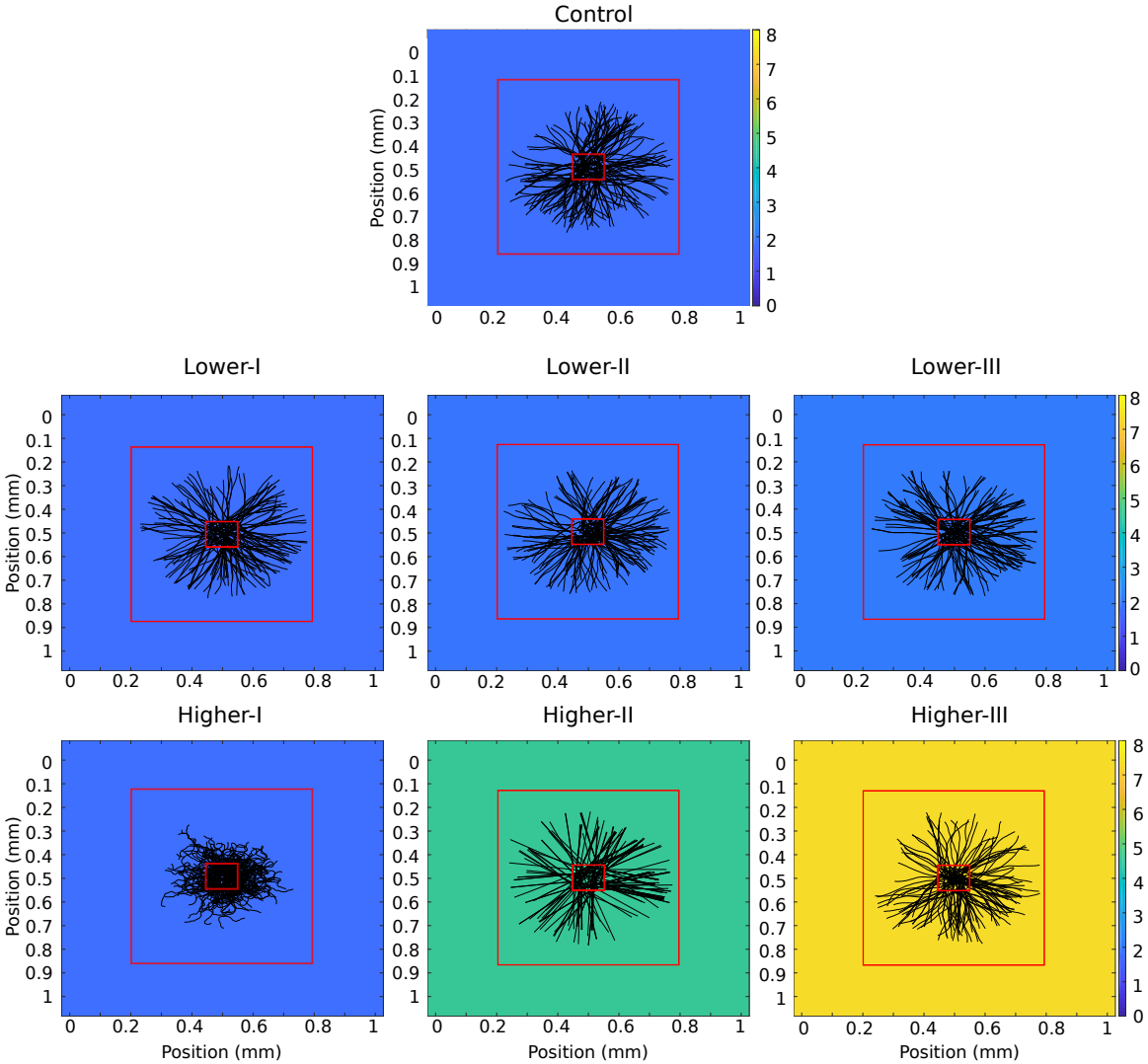

Figure 6.10: Example of the simulation of 100 neurites elongating for 120 hours *in vitro* after model optimisation. The small red square represents the initial random distribution of neurites to simulate cell seeding on a gel. The outer square represent the maximum length reachable aver a period of 120 hours at a growth rate of 0.002 $mm.h^{-1}$. Colorbar in kPa.

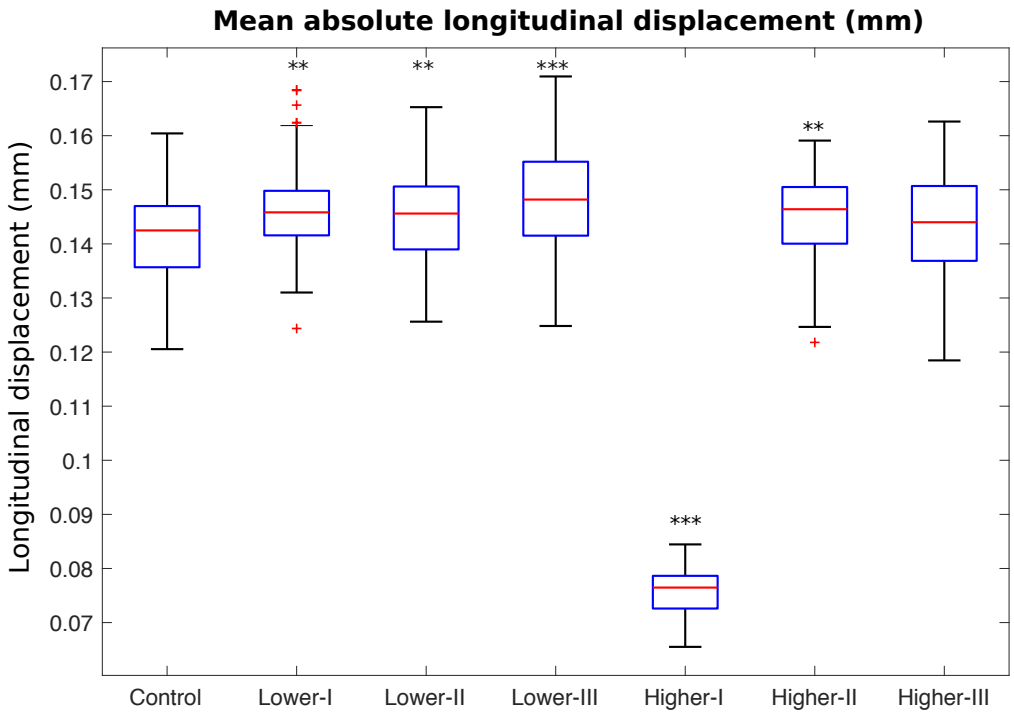

Figure 6.11: Mean absolute longitudinal displacement for each condition (Control, Lower I-II-III and Higher I-II-III). Results are shown for 100 simulations for 100 neurites after 5 days (120 hours). Data set for each condition is compared to the control. $^{**}p < 0.001$; $^{***}p < 0.0001$.

6.3.3 *In vivo* predictions

Following Section 6.3.2, Lower-III gels provide the best gradient/absolute stiffness combination to ensure the longest neurite longitudinal displacement. The condition selected is now used to test the more computationally expensive *in vivo* hypothesis that placing a stiffness gradient gel within a NGC might provide more adapted mechanical cues to neurites, and improve the therapeutic potential of the nerve repair solution. Initially neurites (100) were placed at equal distances (0.01 mm) on the $y - axis$ at the entrance of the conduit ($x = 0$).

Experimentally, each gels (Lower I-II-III and Higher I-II-III) tested *in vitro* had the dimensions of 1 mm $\times$ 0.8 mm, for this reason, after growing beyond 0.8 mm longitudinally, the *in silico* neurite behaviour is not necessarily predictive. Here, the focus is on the percentage of neurites reaching 0.8 mm for varying spatial arrangement of the mechanical properties at the entrance of a nerve conduit after 672 hours (representing 4 weeks, time based on experimental *in vivo* studies (Georgiou et al., 2013)). Figure 6.12 shows the difference in percentage of neurites reaching 0.8 mm for the control and the Lower-III condition. The results are shown for only 10 simulations as these simulations are computationally-expensive, hence, the results are representative. Experimentally, the focus is given to the longer neurites. This predictive model gives us the opportunity to analyse both the percentage of neurites including the developed branches and the percentage of original neurites only, and so isolate and explore the two different behaviours. The Lower-III condition at the entrance of a NGC seemed to be a better environment as $\sim$60% of the neurites reached 0.8 mm, compared to $\sim$40% for the control ($p<0.001$). The behaviour of the neurites on these two different types of spatial arrangement of the mechanical properties within a NGC is shown for one simulation in Figure 6.13.

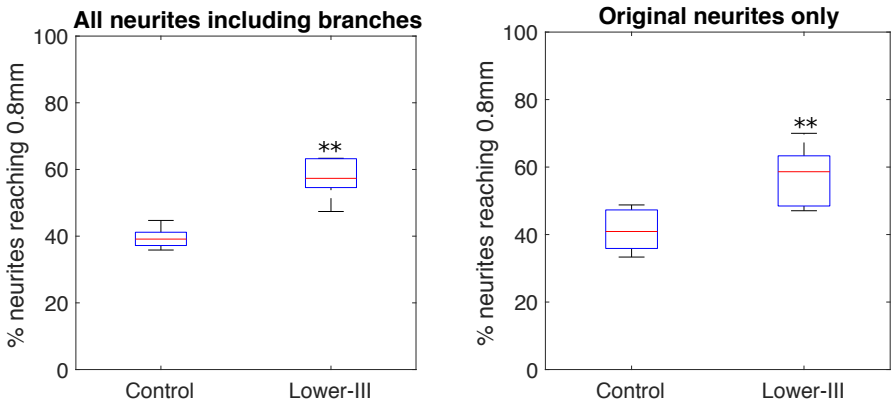

Figure 6.12: Graph showing the percentage of neurite reaching 0.8mm for Lower-III and the control placed at the entrance of a NGC. Results are shown for 10 simulations (100 neurites over 672 hours for each simulation at a growth rate of 0.002 $mm.h^{-1}$). Results shows that neurites are more likely to reach a longer distance when a stiffness gradient is placed at the entrance of a NGC.$^{**}p < 0.001$

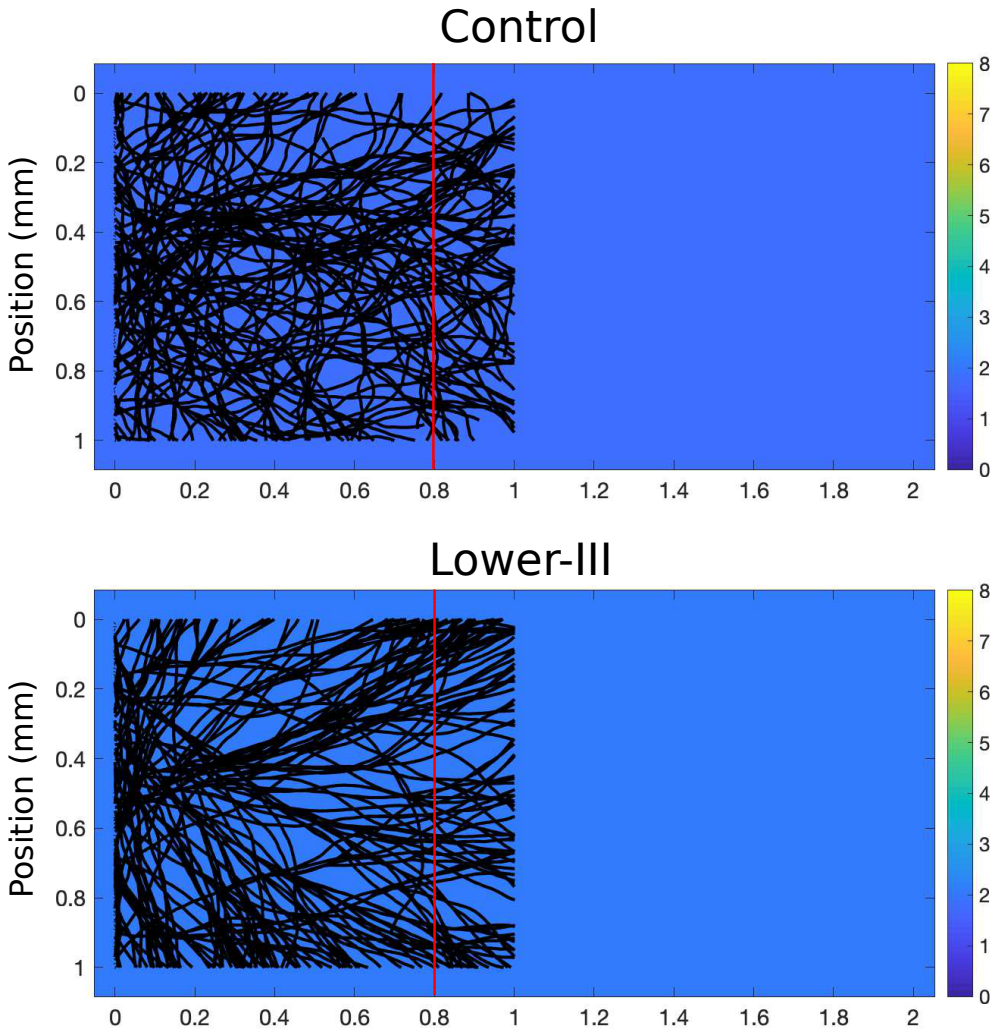

Figure 6.13: Example of a prediction given by the model for 100 neurites elongating for 672 hours (4 weeks) after model optimisation for Lower-III and Control stiffness condition placed at the entrance of a NGC (growth rate of 2 $\mu m.h^{-1}$). Neurite growth into the conduit was considered successful if 0.8 mm was reached (represented by the red line). The behaviour after this distance is not necessarily predictable.

6.4 Discussion

Although computational modelling provides its own challenges, such as initial mathematical model choice, the need for a sufficiently qualitative and quantitative data set to allow robust parameterisation, and the requirement of having the theoretical results experimentally validated (Coy et al., 2017), it offers a powerful tool to direct and refine experimental work, minimising the need for laborious and expensive experiments. This Chapter introduced a 2D discrete model able to predict neurite behaviour in response to various mechanical properties of a substrate, i.e. different gradient/absolute stiffness conditions.

In this Section, the choice of the models and assumptions made to build the aforementioned 2D model is described in Section 6.4.1, and is discussed for the orientation model, Section 6.4.1.1, and for the branching model, Section 6.4.1.2. Then, using the optimised model, the best arrangement of gradient/absolute stiffness condition was selected using *in vitro*-like simulations, the results of which will be discussed in Section 6.4.2. These results were used to test the initial *in vivo* hypothesis stating that adapting the spatial arrangement of gradient/absolute stiffness within a NGC could improve neurite growth. Section 6.4.3 will present and discuss the *in vivo* predictions.

6.4.1 Model

To the author's knowledge, Stefanoni et al. (2011) developed the only discrete mathematical model of cell motility in response to durotaxis presented in the literature. This Section will discuss why the Stefanoni et al. (2011) model was inappropriate to use as it is and how it has been adapted.

Stefanoni et al. (2011) developed the first 2D discrete model for durotaxis, to simulate cell movement influenced by the mechanical properties of the substrate. They parameterised their model using experimental data, showing cells moving towards the stiffer region of a defined domain (Lo et al., 2000). Based on similar migration mechanisms, where cells sense mechanical properties of the local environment, the experimental data set, obtained in Chapter 5, captured a different behaviour. Neurites behaviour was dependent on the combination of gradient/absolute stiffness, and elongated toward softer or stiffer substrate regions depending on the condition. Hence, for this study, a novel 2D discrete model has been developed and optimised based on this specific data set of experimental work. Further extension to the model can be made using experimental data as it becomes available in the future.

The model presented in this piece of work is based on the Langevin equation, widely used in the literature for modelling cell migration in response to the stiffness of the substrate (Dunn and Brown, 1987; Schienbein and Gruler, 1993; Buettner et al., 1994; Stefanoni et al., 2011). Although other bias such as chemotactic cues can be added to the Langevin equation, for the development of the model no external guidance cues were taken into account. Therefore, since such cues would potentially influence growth rate, preliminary results show the lowest estimate of the effect due to the mechanical properties. By only considering the mechanical cues, changes in behaviour are observed as a result of the variation of material stiffness, which facilitates a better understanding of the impact of stiffness gradients on neurite elongation. Additionally, it simplifies the model, and thus reduces the computing time required for simulations. In the future, the consideration of chemotactic cues, such as those present in a NGC that are secreted by the distal stump, would be useful to obtain better prediction of real life scenarios.

6.4.1.1 Orientation

One of the major assumption made was that neurites elongate in a straight manner and are unlikely to go backward at any given time point (Katz, 1985). Also, in previous studies it has been assumed that neurites perform persistent random walk (Segev and Ben-Jacob, 1998). For this reason, an angle distribution (ϕ) was defined with a straightness bias to the direction of $\pm 60°$. With time, and seeking to retain some elements of randomness that characterise neurite elongation, the distribution defined and optimised for ϕ did allow neurites to grow smoothly toward a preferential direction different from the initial growth orientation. The majority of the neurites performed persistent random walk and the overall neurite orientation appropriately represented the orientation observed and measured experimentally.

6.4.1.2 Branching pattern

Following Van Pelt et al. (1997), the degree-dependent branching probability BE-model was used to reproduce the branching pattern observed experimentally. It offers a degree of complexity with a reduced number of parameters required to fit the experimental data. The fitting error for some conditions could be improved by increasing the complexity of the model.

> *" With four parameters I can fit an elephant, and with five I can make him wiggle his trunk."* -John von Neumann.

Some stiffness conditions could be better optimised but overall, the BE-model was a satisfactory choice. Van Pelt et al. (1997), developed a more complex model called the BES-model which gives a degree dependent and order dependent branching probabilities. This last model introduces two new parameters, the centrifugal order of the terminal segment (γ) and C a normalisation constant and so increases the number of uncertainties. It could be investigated in the future to see if adding an extra degree of

complexity could trigger some branching pattern and help to reduce the error between the experimental and theoretical data set.

Overall, after optimisation of the parameters, the model gives results in agreement with the data set collected previously from the *in vitro* experiments. Both the orientation and branching pattern were satisfying, thus, the model was used to simulate the best stiffness conditions to be investigated further.

6.4.2 *In vitro*-like simulations

Here, it was assumed that after 48 hours, the neurites would continue to follow the same behaviour. After validation of the model presented in the previous Sections, neurites were simulated to grow for 5 days (120 hours). The best candidate was the Lower-III gel (2 kPa - 2.5% gradient slope), which displayed a longitudinal elongation significantly higher ($p < 0.0001$) than the control (1.7kPa - 0% gradient slope). Neurites longitudinal growth was better on a compliant substrate with a slight stiffness gradient (2.5%, 0.85 kPa.mm^{-1}). This observation is in agreement with previous studies showing neurons *in vitro* prefer to grow on compliant substrates (Flanagan et al., 2002; Franze and Guck, 2010). However, due to the assumptions, the observations made can not be compared directly to experimental data for the moment. In the future, the predicted best candidate can be tested experimentally against the control for a period of 5 days to validate the model. Combining experimental and computational work has allowed to refine the *in vitro* design of the next experiment for validation of the model, thus, reducing time and financial costs, as expected by Coy et al. (2017).

6.4.3 *In vivo* predictions

Although for an *in vitro* experimental set up, the conduit would be three-dimensional, it is assumed that the gradient gels can be made as a sheet of collagen and rolled up, as shown Figure 6.14. This design then allows an assumption that the neurites would elongate on a 2D surface even if in a 3D context, and the model could be used to test the initial hypothesis and give interesting *in vivo* predictions.

From Section 6.3.2, it was found that the Lower-III gels provided the best gradient/absolute stiffness condition for longitudinal growth, hence, they were chosen to perform the *in vivo*-like simulations. In addition, once again, it was assumed that after 48 hours, the neurites would continue to follow the same behaviour (see Section 6.4.2), allowing the simulation of neurite growth for a period a 4 weeks based on previous experimental *in vivo* time protocols (Georgiou et al., 2013).

The stiffness gradient condition, Lower-III, is showing encouraging results compared to the control. The predictions have shown that significantly more neurites were reaching a longer distance when growing on a stiffness gradient than on a mechanically homogeneous control gel after 4 weeks.

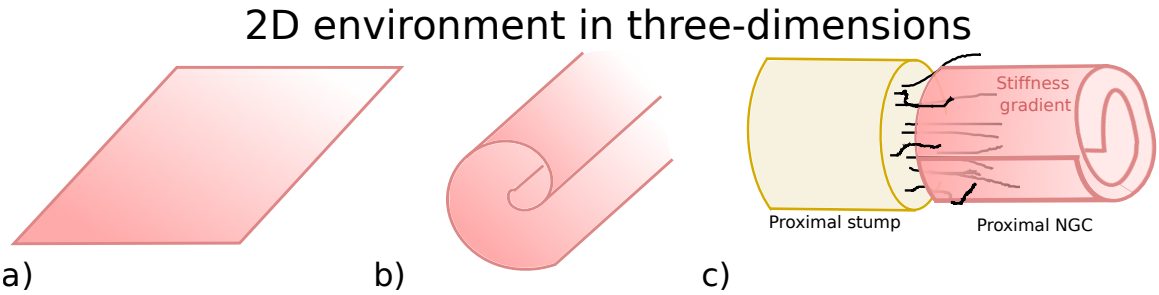

Figure 6.14: Experimental set up that supports the assumption that neurites will elongate on a 2D environment. As in Georgiou et al. (2013), conduits are fabricated following these three steps: a) a collagen gradient sheet is fabricated, b) the collagen sheet is rolled to obtain a tubular structure, an c) for this 3D model, neurites (in red) will elongate on the material following the 2D set up investigated computationally and *in vitro*.

6.4.4 Conclusion and future work

The 2D discrete model presented demonstrated the advantages of being able to quickly simulate and compare the neurite distributions achieved when confronted with various stiffness designs. The use of such a model to identify the most likely design of mechanical cues for successful growth in an NGC would give a much needed sense of the direction to take to subsequent experimental studies. This 2D model is an overestimation of the reality, however, results are promising and should be investigated further. The predictions gave valuable information allowing progression toward the next stage of the experimental-theoretical feedback loop shown in Figure 6.1. *In vitro* experiments can be conducted on the Lower-III stiffness condition to allow model validation and to refine it. This targeted experimental validation step is then less time consuming and cost-effective compared to a purely experimental approach. The *in vivo* predictions could then be validated further with experiments *in vivo*, for 4 weeks, using the Lower-III gradient gel and control collagen sheets, following the set up proposed in Figure 6.14. A 3D model of the neurite response to stiffness gradients could also be implemented in the future and other external guidance could be considered in the model. The results will then be compared against the experimental data and will allow validation and refinement of the model; this cycle will go on until a nerve guidance conduit is proposed for clinical use.

This theoretical-experimental feedback loop provides crucial informations to help tissue engineers to make faster progress in the development of nerve guidance conduit.

Chapter 7

General conclusion

7.1 Overview

Peripheral nerve injury, causing loss of sensory and motor function, and chronic pain, can be devastating for the patients. It impacts their lifetime productivity, therefore comes with societal costs as well as healthcare and rehabilitation costs. The peripheral nervous system has shown the potential to regenerate following surgical repair.

Although the first attempt to repair severed peripheral nerves was reported thousands of years ago, the current clinical solution for transected peripheral nerves, nerve grafting, first reported in the 19^{th} century, still remains the gold standard. Over the past decades, the use of nerve conduits for repair of transected nerve has become increasingly popular. Despite their ability to address some of the nerve graft limitations, e.g. donor site morbidity, double surgery, and a limited amount of nerve supply, functional nerve recovery is in most cases partial and unsatisfactory for the patient. To improve on this, researchers have focused on the development of new growth factor and supporting cell delivery systems, as well as new materials. Currently, knowledge on how the mechanical environment influences nerve regeneration remains incomplete and would benefit from a better understanding to help in the development of new

nerve repair solutions.

The goal of this thesis was to investigate the effect of mechanical cues on neuronal behaviour and propose a new design rationale for peripheral nerve tissue engineering applications. This work was a multidisciplinary project that brought together tissue engineering, biomaterials, cell culture and mathematical modelling. The experimental-theoretical feedback loop described by Coy et al. (2017), describing the need to combine experimental and mathematical approaches together to make faster progress in nerve tissue engineering, was exploited.

Here, the results presented can contribute to the improvement of nerve guidance conduits by providing novel information about the neuronal response to mechanical stimuli, i.e. the combination of gradient and absolute stiffness value. The first objective of the experimental work was to investigate the mechanical properties of rat peripheral nerve tissue and RAFT-stabilised collagen gel, a material found to display properties similar to nerve tissue. The second objective was focused on the development, design and optimisation of a new technique to obtain consistently reproducible and well-characterised stiffness gradients using RAFT-stabilised collagen gels to be used in studies investigating cell-substrate interaction. Accordingly, following creation of stiffness gradients, neuronal cell mechanosensitivity was tested in response to these specific substrates. The data set obtained was used to inform a mathematical model, built to aid the design of novel tissue engineering conduits for nerve repair, i.e. to inform the optimal spatial arrangement of mechanical properties for nerve guidance conduits.

The determination of the viscoelastic properties of the host tissue, nerve, is crucial for the development of nerve guidance conduits. Because of the variability encountered when investigating physiological tissues, e.g. species, tissue location, specimen shape, and preservation techniques, as well as the inconsistency across the mechanical testing, soft tissue characterisation still remains a challenge. Chapter 2 assessed

the frequency-dependent viscoelastic properties of fresh rat sciatic nerve under dynamic mechanical forces. Known to be a viscoelastic tissue, fresh rat sciatic nerve exhibited predominantly elastic behaviour under tensile DMA testing. This piece of work gives general information on the viscoelastic properties of fresh nerve and the order of magnitude of the results is consistent with previously reported values (Ju et al., 2004, 2006, 2017), and (Rosso et al., 2017b). Previous studies have tended to rely on ramp loading for nerve stiffness measurement, using a single strain rate, which does not allow characterisation of the frequency-dependant viscoelastic properties that nerve tissues exhibits. Therefore, this work has helped to establish a protocol for dynamic mechanical characterisation that can be applied to fresh nerve tissue and also to candidate biomaterials, facilitating the subsequent development of both mechanically-tuned repair conduits and physiologically-relevant substrates for studying neuronal behaviour.

Chapter 3 reported a thorough comprehensive characterisation which uses a variety of different techniques to understand fully the key fundamental mechanical behaviour of RAFT-stabilised collagen gels. It has been demonstrated that stabilisation of collagen hydrogels, viscoelastic material, using the RAFT-stabilisation technique (Levis et al., 2015) produces reproducible dense material with properties similar to the host-tissue. It was found that the fully-hydrated starting gel geometry affects the final collagen matrix properties (fluid loss and collagen density). A comprehensive set of mechanical tests have shown that this material exhibits different tensile, compressive and rheological viscoelastic properties and that varying the initial volume of collagen solution does not significantly impact these properties for a given geometry. It exhibited viscoelastic behaviour under compressive and shear stress and a predominantly elastic behaviour under tensile stress. In addition, the data suggested that irreversible structural changes may occur at frequencies higher than 15 Hz. Moreover, the experimental data obtained for each mechanical test was correlated with a

frequency sweep through the identification of an empirical relationship. These results can be used for numerous applications in the area of tissue engineering, for example, to correlate cell behaviour with matrix properties and to understand the fundamentals of material-tissue interactions in regenerative medicine.

Chapter 4 described the development, design and optimisation of a new technique to make gels with controlled and defined physical (density) and mechanical (surface stiffness) gradients. RAFT-stabilised collagen gels characterised in Chapter 3, were used and tissue engineering technology was adapted for generating stiffness gradients based on Levis et al. (2015) and Cheema and Brown (2013) work. This new protocol has shown to not damage the collagen fibril structure and did not require the addition of potential signalling cues, e.g. enzymes. Based on a trial-and-error design process, a protocol to fabricate two different stiffness gradient materials (lower and higher) has been presented, using CAD designed and 3D printed moulds. These defined stiffness gradient gels offer a valuable culture model, and can be used as a platform to study cell-substrate interactions.

Chapter 5 investigated the interaction between neuronal cells, NG108-15, with the gradients created in Chapter 4, and showed that neuronal cells were mechanosensitive to the surface stiffness gradients produced. Neuronal cells responded to these gradients by modifying their branching behaviour and orientation. This study provided novel insights into neuronal cell durotaxis. It demonstrated variation on neurite orientation in response to the presence of a stiffness gradient, dependant on the combination of the gradient slope and the absolute stiffness value. Reported for the first time, neurites were growing both toward stiffer or softer substrate regions, depending on the gradient/absolute stiffness combination, which emphasises the importance of how both these cues combine to induce a controlled orientation. This work presents a promising strategy to be investigated further for neural tissue engineering.

Seeking to apply previous findings to a specific clinical challenge and to accelerate

the design process by reducing experimental costs, Chapter 6 proposed a mathematical model to test the following hypothesis: "a stiffness gradient within nerve guidance conduit could guide neurite growth and improve the performance of the device", to aid the design of translational tissue-engineered constructs. A 2D discrete model was built based on experimental data collected in Chapter 5. The model was build based on the Stefanoni et al. (2011) model to mimic the orientation behaviour and the Van Pelt and Verwer (1983) branching pattern model. After validation against experimental data, the model was used to identify the best arrangement of mechanical cues for successful growth within a nerve guidance conduit, based on the materials described in Chapter 4. These results gave valuable information to assist in refining future experiments further.

7.2 Conclusion

In conclusion, the investigation of the mechanical properties of fresh rat sciatic nerve tissue and RAFT-stabilised collagen gels led to the development of a new protocol to fabricate two defined and reproducible collagen stiffness gradient substrates within a physiologically relevant stiffness range. Used as a platform to study cell-substrate interaction, neuronal cells were cultured on these substrates to explore the influence of stiffness gradient and magnitude on neuronal regeneration. The results of this work suggest that the choice of the mechanical parameters affects neuronal morphology, specifically the orientation and branching, thus may be a key parameter integrated by neurons when making critical pathfinding decisions. Last but not least, a mathematical model, informed by the experimental results, was built to refine future experimental design, therefore proposing a new design rationale with controlled mechanical factors for nerve tissue engineering application. This model can be seen as a starting point for coupling theoretical and experimental techniques to investigate

the incorporation of mechanical cues in biomaterial designs for nerve repair solutions.

> *One never notices what has been done; one can only see what remains to be done.*- Marie Curie

7.3 Future directions

Mechanical properties of fresh human nerve still remain to be assessed. Barberio et al. (2018) investigated the frequency-dependant viscoelastic properties of embalmed human nerves. Indeed, using fresh human nerve is ethically challenging, and when this challenge can be addressed, researchers are then confronted with the limited amount of supply. Furthermore, soft tissues like nerve will stiffen *in vivo* after the time of death, related to the absence of blood supply. For instance, Weickenmeier et al. (2018) have shown high stiffness variations (increase) happening within minutes for brain tissues and Matthews and Ellis (1968) have observed for tendons an increasing pattern within hours *post-mortem*. Therefore, a detailed investigation of mechanical behaviours of tissue *ex vivo* can become questionable. As to date, to the author's knowledge, there is no studies which reports frequency-dependent viscoelastic properties of the living peripheral nerves, some preliminary experiments have been conducted to investigate the evolution of fresh rat nerve stiffness for three different time points (see Chapter 2). Results showed that after a three hour time window from time of death, mechanical properties were not significantly different. This investigation offers the possibility to support future work on freshly harvested human nerves. This work has not been conducted yet for ethical reasons, but plans are in place to do so based on the results of this study. This preliminary rat nerve mechanics experiment supports the possibility of testing human nerve tissues from an amputated upper limb within a time window of 2-3 hours (for the tissue to be transported from the theatre to the laboratory and prepared for testing). This experiment could provide insights into the differences

in stiffness between joint regions and non joint regions, highlighted by Mason and Phillips (2011) for rat median and sciatic nerves. Microscopic examination of the human nerves will also be conducted to analyse collagen fibrils and correlate collagen fibril diameter and joint location.

The moulds used to fabricate collagen gradient gels were CAD-designed and 3D printed moulds, providing an adaptable approach to support future studies. The stiffness range and steepness of the gradient can be easily modified, e.g. by modifying the shape of the mould. It could be of use to test different scenarios, and ensure a high degree of freedom. Indeed, as seen previously, the experimental work is refined by a mathematical model, assuming that the complexity of the model will allow prediction of neuronal response to local mechanical cues, this protocol will have the potential to adapt and offer a design to test experimentally the model's prediction. Furthermore, as numerous physiological tissues are heterogeneous, the influence of the mechanical environment on cell behaviour still remains largely understudied. This platform could offer an opportunity to investigate a multitude of scenarios, e.g. using different hydrogels or adapting the shape of the gradient, to study the behaviour a large variety of cell types, and therefore be of more general use in the tissue engineering research community.

Mechanosensitivity of neuronal cells to defined stiffness gradients has been observed. However, a more in-depth understanding of the underlying mechanism behind the cell behaviour, depicted here, would be of great use for peripheral nerve engineers. In addition, in this thesis, as the main focus was on the mechanical factors, the impact of the other guidance cues, e.g. chemical factors, has been neglected. Ideally, this work provides a "stepping stone" for further investigation where both mechanical and chemical factors would be combined to design the optimal nerve guidance conduits. In the longer term, the complexity of this experimental model can be improved and more external parameters could be introduced to develop a therapeutic strategy that

could surpass current nerve graft approaches.

Following the mathematical predictions, a stiffness gradient candidate has shown potential to induce better growth within a nerve guidance conduit, and as a result of this work, is proposed as a new design rationale for nerve tissue engineering. In the future, this predicted best candidate could be tested experimentally against a control to evaluate the potential of the predictions. Studies will be required to evaluate the induced neurite orientation and the ability to control it *in vivo* through implanting gradient engineered nerve guidance conduits. Results will then be used to refine and validate the computational model. This experimental-theoretical cycle could then lead, in the near future, to the fabrication of experimental constructs that could potentially be translated to the clinic.

Appendix A

Matlab code

Here, the matlab code used for the simulations presented in Chapter 6 is detailed.

A.1 Main file

```
%Main file to compile the code
clear all
close all
%load data
load('optimization.mat')
%load('invivo.mat')
load('invivobis.mat')
%load('invivo2.mat')
%load('invivo3.mat')
%load('invivo4.mat')
load('Orientation.mat')
load('probability2.mat','X1','X2','X3','X4','X5','X6','X7','X_fit'...
    )
%%%probability density function
load('angle45.mat')
load('branches.mat','ControlB','Higher1B','Higher2B','Higher3B','...
    Lower1B','Lower2B','Lower3B')
% load('grad_opt.mat')
% load('gradient.mat')

fit=X_fit;
%%%COntrol
Model=Control;
Gradt=Grad1;
%%%lower1
```

```
Model3=Control;
Gradt3=Grad2;
%%%lower2
Model2=lower2;
Gradt2=Grad2;
%%%lower3
Model1=lower3;
Gradt1=Grad2;
%%%higher1
Model6=Control;
Gradt6=Grad3;
%%%higher2
Model5=higher2;
Gradt5=Grad3;
%%%higher3
Model4=higher3;
Gradt4=Grad3;


%

 %evenly space grid
GradX = linspace(0,2,length(Model(1,:)));
GradY = linspace(0,1,length(Model(:,1)));
G=0.002;%growth rate um/h
N=100;%number of neurites
n=672;%number of steps

bins=7;
%%%%%OPTIMISATION ANGLES
nVars=2;%number of decision variables (unknown)
% x=zeros(1,nVars);
%%% Matrix size of decision variable
lb=-60*ones(1,nVars);   %lower bound of decision variable
ub=-lb;     %upperbound of decision variable


%%%OPTIMISATION NEURITES BRANCHING
X_fitb=0:4;
NVARS2=3;%%%B E EN
lb2=[0,0.25,100];
ub2=[5,2,900];
%
%

%[NEURITE_ANGLE6,Degree_Branches6,NX6,NY6,NeuriteX6,NeuriteY6]=...
    simulationopt(Model5,Gradt5,n,N,G,GradX,GradY);%higher-medium
%[NEURITE_ANGLE1,Degree_Branches1,NX1,NY1,NeuriteX1,NeuriteY1]=...
    simulationopt(Model,Gradt,n,N,G,GradX,GradY);%control
%[NEURITE_ANGLE7,Degree_Branches7,NX7,NY7,NeuriteX7,NeuriteY7]=...
    simulationopt(Model6,Gradt6,n,N,G,GradX,GradY);%higher-low
% % [NEURITE_ANGLE1]=simulation(Model,Gradt,n,N,G,GradX,GradY);%...
    control
```

```
73 % % [NEURITE_ANGLE2]=simulation(Model1,Gradt1,n,N,G,GradX,GradY);%...
       lower-high
74 % % [NEURITE_ANGLE3]=simulation(Model2,Gradt2,n,N,G,GradX,GradY);%...
       lower-medium
75 % % [NEURITE_ANGLE4]=simulation(Model3,Gradt3,n,N,G,GradX,GradY);%...
       lower-low
76 % % [NEURITE_ANGLE5]=simulation(Model4,Gradt4,n,N,G,GradX,GradY);%...
       higher-high
77 % % [NEURITE_ANGLE6]=simulation(Model5,Gradt5,n,N,G,GradX,GradY);%...
       higher-medium
78 % % [NEURITE_ANGLE7]=simulation(Model6,Gradt6,n,N,G,GradX,GradY);%...
       higher-low
79
80 %
81 d=10;
82 Angle_control=cell(1,d);
83 % Angle_LowerI=cell(1,d);
84 % Angle_LowerII=cell(1,d);
85 Angle_LowerIII=cell(1,d);
86 % Angle_higher_I=cell(1,d);
87 % Angle_higher_II=cell(1,d);
88 % Angle_higher_III=cell(1,d);
89 %
90 increment1=zeros(1,d);
91 increment2=zeros(1,d);
92 % increment3=zeros(1,d);
93 %increment4=zeros(1,d);
94 % increment5=zeros(1,d);
95 % increment6=zeros(1,d);
96 % increment7=zeros(1,d);
97
98
99 branche_control=cell(1,d);
100 % branche_LowerI=cell(1,d);
101 % branche_LowerII=cell(1,d);
102 branche_LowerIII=cell(1,d);
103 % branche_higher_I=cell(1,d);
104 % branche_higher_II=cell(1,d);
105 % branche_higher_III=cell(1,d);
106 %
107 NX_control=cell(1,d);
108 % NX_LowerI=cell(1,d);
109 % NX_LowerII=cell(1,d);
110 NX_LowerIII=cell(1,d);
111 % NX_higher_I=cell(1,d);
112 % NX_higher_II=cell(1,d);
113 % NX_higher_III=cell(1,d);
114
115 NeuriteX_control=cell(1,d);
116 % NeuriteX_LowerI=cell(1,d);
117 % NeuriteX_LowerII=cell(1,d);
118 NeuriteX_LowerIII=cell(1,d);
119 %NeuriteX_higher_I=cell(1,d);
120 % NeuriteX_higher_II=cell(1,d);
```

```
121 % NeuriteX_higher_III=cell(1,d);
122
123 NeuriteY_control=cell(1,d);
124 % NeuriteY_LowerI=cell(1,d);
125 % NeuriteY_LowerII=cell(1,d);
126 NeuriteY_LowerIII=cell(1,d);
127 % NeuriteY_higher_I=cell(1,d);
128 % NeuriteY_higher_II=cell(1,d);
129 % NeuriteY_higher_III=cell(1,d);
130
131
132 for i=1:d
133 [NEURITE_ANGLE1,Degree_Branches1,NX1,NY1,NeuriteX1,NeuriteY1,...
       increment_1]=simulationopt(Model,Gradt,n,N,G,GradX,GradY);%...
       control
134 [NEURITE_ANGLE2,Degree_Branches2,NX2,NY2,NeuriteX2,NeuriteY2,...
       increment_2]=simulationopt(Model1,Gradt1,n,N,G,GradX,GradY);%...
       lower-high
135 % [NEURITE_ANGLE3,Degree_Branches3,NX3,NY3,NeuriteX3,NeuriteY3,...
       increment_3]=simulationopt(Model2,Gradt2,n,N,G,GradX,GradY);%...
       lower-medium
136 % [NEURITE_ANGLE4,Degree_Branches4,NX4,NY4,NeuriteX4,NeuriteY4,...
       increment_4]=simulationopt(Model3,Gradt3,n,N,G,GradX,GradY);%...
       lower-low
137 % [NEURITE_ANGLE5,Degree_Branches5,NX5,NY5,NeuriteX5,NeuriteY5,...
       increment_5]=simulationopt(Model4,Gradt4,n,N,G,GradX,GradY);%...
       higher-high
138 % [NEURITE_ANGLE6,Degree_Branches6,NX6,NY6,NeuriteX6,NeuriteY6,...
       increment_6]=simulationopt(Model5,Gradt5,n,N,G,GradX,GradY);%...
       higher-medium
139 % [NEURITE_ANGLE7,Degree_Branches7,NX7,NY7,NeuriteX7,NeuriteY7,...
       increment_7]=simulationopt(Model6,Gradt6,n,N,G,GradX,GradY);%...
       higher-low
140
141     NeuriteX_control{i}=NeuriteX1;
142 %     NeuriteX_LowerI{i}=NeuriteX4;
143 %     NeuriteX_LowerII{i}=NeuriteX3;
144     NeuriteX_LowerIII{i}=NeuriteX2;
145 %     NeuriteX_higher_I{i}=NeuriteX7;
146 %     NeuriteX_higher_II{i}=NeuriteX6;
147 %     NeuriteX_higher_III{i}=NeuriteX5;
148 %
149
150     NeuriteY_control{i}=NeuriteY1;
151 %     NeuriteY_LowerI{i}=NeuriteY4;
152 %     NeuriteY_LowerII{i}=NeuriteY3;
153     NeuriteY_LowerIII{i}=NeuriteY2;
154 %     NeuriteY_higher_I{i}=NeuriteY7;
155 %     NeuriteY_higher_II{i}=NeuriteY6;
156 %     NeuriteY_higher_III{i}=NeuriteY5;
157 %
158
159     NX_control{i}=NX1;
160 %     NX_LowerI{i}=NX4;
```

```
%     NX_LowerII{i}=NX3;
    NX_LowerIII{i}=NX2;
%     NX_higher_I{i}=NX7;
%     NX_higher_II{i}=NX6;
%     NX_higher_III{i}=NX5;

    branche_control{i}=Degree_Branches1;
%     branche_LowerI{i}=Degree_Branches4;
%     branche_LowerII{i}=Degree_Branches3;
    branche_LowerIII{i}=Degree_Branches2;
%     branche_higher_I{i}=Degree_Branches7;
%     branche_higher_II{i}=Degree_Branches6;
%     branche_higher_III{i}=Degree_Branches5;
%
    Angle_control{i}=NEURITE_ANGLE1;
%     Angle_LowerI{i}=NEURITE_ANGLE4;
%     Angle_LowerII{i}=NEURITE_ANGLE3;
    Angle_LowerIII{i}=NEURITE_ANGLE2;
%     Angle_higher_I{i}=NEURITE_ANGLE7;
%     Angle_higher_II{i}=NEURITE_ANGLE6;
%     Angle_higher_III{i}=NEURITE_ANGLE5;

    increment1(1,i)=increment_1;
    increment2(1,i)=increment_2;
%     increment3(1,i)=increment_3;
%     increment4(1,i)=increment_4;
%     increment5(1,i)=increment_5;
%     increment6(1,i)=increment_6;
%     increment7(1,i)=increment_7;
end
 save('nointerface2.mat')



% % % %[NEURITE_ANGLE1,Degree_Branches1]=simulation2bis(Control,...
    Grad_zero,n,N,G,GradX,GradY);%control
% % % %[NEURITE_ANGLE2,Degree_Branches2]=simulation2bis(Lower,...
    grad_two,n,N,G,GradX,GradY);%lower
% % % %gradient
% % % %[NEURITE_ANGLE3,Degree_Branches3]=simulation2bis(Trial4,...
    Gradient_Trial4,n,N,G,GradX,GradY);%higher
% % % %gradient

% %%%probability for the angles
 %probabilityplot(X1,X2,X3,X4,X5,X6,X7,NEURITE_ANGLE1,...
     NEURITE_ANGLE2,NEURITE_ANGLE3,NEURITE_ANGLE4,NEURITE_ANGLE5,...
     NEURITE_ANGLE6,NEURITE_ANGLE7,bins,X_fit)
% % %error_function2(X1,X2,X3,X4,X5,X6,X7,NEURITE_ANGLE1,...
    NEURITE_ANGLE2,NEURITE_ANGLE3,NEURITE_ANGLE4,NEURITE_ANGLE5,...
    NEURITE_ANGLE6,NEURITE_ANGLE7,bins)
%
%
% %%%%priobability for the branching
```

```
207 %probabilityplot_branch(ControlB,Lower3B,Lower2B,Lower1B,Higher3B,...
       Higher2B,Higher1B,Degree_Branches1,Degree_Branches2,...
       Degree_Branches3,Degree_Branches4,Degree_Branches5,...
       Degree_Branches6,Degree_Branches7,X_fitb)
208 % %%error_branch2(ControlB,Lower3B,Lower2B,Lower1B,Higher3B,...
       Higher2B,Higher1B,Degree_Branches1,Degree_Branches2,...
       Degree_Branches3,Degree_Branches4,Degree_Branches5,...
       Degree_Branches6,Degree_Branches7,X_fitb)
209
210
211
212
213 %%%%inverse the error
214 % NX1=-NX1;
215 % NX2=-NX2;
216 % NX3=-NX3;
217 % NX4=-NX4;
218 % NX5=-NX5;
219 % NX6=-NX6;
220 % NX7=-NX7;
221 %
222 %
223 % NY1=-NY1;
224 % NY2=-NY2;
225 % NY3=-NY3;
226 % NY4=-NY4;
227 % NY5=-NY5;
228 % NY6=-NY6;
229 % NY7=-NY7;
230 %
231 %
232 %
233 %
234 % figure
235 % subplot(3,3,2);
236 % hold on
237 % histogram(NX1,5)
238 % title('Control')
239 % legend('Nx')
240 % hold off
241 %
242 %
243 % subplot(3,3,6);
244 % hold on
245 % histogram(NX2,5)
246 % title('Lower III')
247 % hold off
248 %
249 % subplot(3,3,5);
250 % hold on
251 % histogram(NX3,5)
252 % title('Lower II')
253 % hold off
254 %
```

```
% subplot(3,3,4);
% hold on
% histogram(NX4,5)
% title('Lower I')
% hold off
%
% subplot(3,3,9);
% hold on
% histogram(NX5,5)
% title('Higher III')
% hold off
%
% subplot(3,3,8);
% hold on
% histogram(NX6,5)
% title('Higher II')
% hold off
%
% subplot(3,3,7);
% hold on
% histogram(NX7,5)
% title('Higher I')
% hold off
%
%
%
%
% figure
% subplot(3,3,2);
% hold on
% histogram(NY1,5)
% title('Control')
% legend('NY')
% hold off
%
%
% subplot(3,3,6);
% hold on
% histogram(NY2,5)
% title('Lower III')
%
% hold off
% subplot(3,3,5);
% hold on
% histogram(NY3,5)
% title('Lower II')
% hold off
%
% subplot(3,3,4);
% hold on
% histogram(NY4,5)
% title('Lower I')
% hold off
%
```

```
% subplot(3,3,9);
% hold on
% histogram(NY5,5)
% title('Higher III')
% hold off
% subplot(3,3,8);
% hold on
% histogram(NY6,5)
% title('Higher II')
% hold off
%
% subplot(3,3,7);
% hold on
% histogram(NY7,5)
% title('Higher I')
% hold off
% %



% figure
% hold on
% histogram(NY1)
% hold off

%histogram(X1,7) %control
%histogram(X2,7) %Lower_III
% histogram(X3,7) %Lower-II
% histogram(X4,7) %Lower-I
% histogram(X5,7) %Higher-III
% histogram(X6,7) %higher-II
% histogram(X7,7) %Higher-I
```

A.2 Optimisation

A.2.1 Optimisation of the angle distribution

```
%%%OPTIMISATION NEURITES BRANCHING
X_fitb=0:4;
NVARS2=3;%%%B E EN
lb2=[0,0.25,100];
ub2=[5,2,900];
%
%%%%optimisation for angle distribution
options = optimoptions('particleswarm', 'Display', 'iter','...
    SwarmSize',50);
```

```
%%f=@(x)error_function(X1,bins,Model,Gradt,n,N,G,GradX,GradY,x,...
    X_fit);
 %f=@(x)error_function(X2,bins,Model1,Gradt1,n,N,G,GradX,GradY,x,...
     X_fit);%%Lower3
%f=@(x)error_function(X3,bins,Model2,Gradt2,n,N,G,GradX,GradY,x,...
    X_fit);%Lower2
%f=@(x)error_function(X4,bins,Model3,Gradt3,n,N,G,GradX,GradY,x,...
    X_fit);%%Lower1
%f=@(x)error_function(X5,bins,Model4,Gradt4,n,N,G,GradX,GradY,x,...
    X_fit);%Higher3
% %f=@(x)error_function(X6,bins,Model5,Gradt5,n,N,G,GradX,GradY,x,...
    X_fit);%higher2
f=@(x)error_function(X7,bins,Model6,Gradt6,n,N,G,GradX,GradY,x,...
    X_fit);%higher1
% % % %
[x,fval,exitflag] = particleswarm(f,nVars,lb,ub,options);
% %
```

A.2.2 Optimisation of the branching pattern

```

%%%optimisation for branching
options = optimoptions('particleswarm', 'Display', 'iter','...
    SwarmSize',50);
%fb=@(x)error_branching(ControlB,Model,Gradt,n,N,G,GradX,GradY,x,...
    X_fitb);
%fb=@(x)error_branching(Lower3B,Model1,Gradt1,n,N,G,GradX,GradY,x,...
    X_fitb);%%Lower3
%fb=@(x)error_branching(Lower2B,Model2,Gradt2,n,N,G,GradX,GradY,x,...
    X_fitb);%Lower2
%fb=@(x)error_branching(Lower1B,Model3,Gradt3,n,N,G,GradX,GradY,x,...
    X_fitb);%%Lower1
%fb=@(x)error_branching(Higher3B,Model4,Gradt4,n,N,G,GradX,GradY,x...
    ,X_fitb);%Higher3
 %fb=@(x)error_branching(Higher2B,Model5,Gradt5,n,N,G,GradX,GradY,...
     x,X_fitb);%higher2
fb=@(x)error_branching(Higher1B,Model6,Gradt6,n,N,G,GradX,GradY,x,...
    X_fitb);%higher1
[x,fval,exitflag] = particleswarm(fb,NVARS2,lb2,ub2,options);
```

A.3 Error function

A.3.1 Angle distribution

```
1
2  function [erf]=error_function(exp_data,bins,Model,Gradt,n,N,G,...
       GradX,GradY,x,X_fit)
3  theta=x(1);
4  mean=0;
5  sigma=x(2);
6  [NEURITE_ANGLE]=simulation(Model,Gradt,n,N,G,GradX,GradY,theta,...
       mean,sigma);%control
7
8
9  Prob_Theta=fitdist(exp_data,'Kernel');
10 Prob_Thetabis=fitdist(transpose(NEURITE_ANGLE),'Kernel');
11
12
13 Y = pdf(Prob_Theta,X_fit);
14 Ybis=pdf(Prob_Thetabis,X_fit);
15 meanYY=abs(Ybis-Y)./Y.*100;
16 erf=sum(meanYY)/length(meanYY);
```

A.3.2 Branching pattern

```
1  function [erfb]=error_branching(exp_data,Model,Gradt,n,N,G,GradX,...
       GradY,x,X_fitb)
2  B=x(1);
3
4  E=x(2);
5  EN=x(3);
6  [NEURITE_ANGLE,Degree_Branches]=simulation2(Model,Gradt,n,N,G,...
       GradX,GradY,B,E,EN);%control
7
8
9
10 prob_branch=fitdist(exp_data,'HalfNormal');
11 prob_branchbis=fitdist(transpose(Degree_Branches),'HalfNormal');
12
13
14 Y = pdf(prob_branch,X_fitb);
15 Ybis=pdf(prob_branchbis,X_fitb);
16 meanYY=abs(Ybis-Y)./Y.*100;
17 erfb=sum(meanYY)/length(meanYY);
```

A.3.3 Neurite elongation simulation

```
1
2
3  %Neurite behaviour on the top of the different gradient conditions
4  function [NEURITE_ANGLE,Degree_Branches,NX,NY,NeuriteX,NeuriteY,...
       increment]=simulationopt(Model,Gradt,n,N,G,GradX,GradY)
5  load('branches.mat','B1','B2','B3','B4','B5','B6','B7','X_branche'...
       )
6  load('pdf.mat','Y1','Y2','Y3','Y4','Y5','Y6','Y7','X_fit')
7
8
9  %%%neurites positions x and y
10
11 NeuriteX=zeros(n,N*n);
12 NeuriteY=zeros(n,N*n);
13 increment=N;
14 Value_branching=1:1:N;
15 %%%%random starting point for each neurite on the gradient
16 % xmin=0.45;
17 % xmax=0.55;
18 xmin=0;
19 xmax=0;
20 randN=N;
21 Nx=xmin+rand(1,randN)*(xmax-xmin);
22 % ymin=0.45;
23 % ymax=0.55;
24 ymin=0;
25 ymax=1;
26 % Ny=ymin+rand(1,randN)*(ymax-ymin);
27 Ny=0.01:1/N:ymax;
28 %%%initial condition for the position
29 NeuriteX(1,1:N)=Nx;
30 NeuriteY(1,1:N)=Ny;
31 angle=zeros(n,N*n);
32 rotationangle=zeros(n,N*n);
33 NEURITE_ANGLE=zeros(1,N);
34 phi=X_fit;
35 tet=-3.14:0.34:3.14;
36 prob_tet=0.1.*ones(1,19);
37 %%%%original number of neurite per branches
38 y=ones(1,N);
39 Probbranch=ones(1,N);
40 Degree_Branches=ones(1,N);
41 [X,Y] = meshgrid(GradX,GradY);
42
43 %set size of the figure
44 x0=10;
45 y0=10;
46 width=1400;
47 height=1400;
```

```
48 %%%%Branchinng probability parameters (obtained after optimisation...
       )
49 B1=4.8;
50 B2=4.9198;     %%IIIlow
51 B3=3.3854;     %%IIlow
52 B4=3.2386;    %%Ilow
53 B5=4.3441;     %%%IIIhigh
54 B6=2.4204;%%%IIhigh
55 B7=2;    %%%Ihigh
56 E1=1.5;
57 E2=1.5;
58 E3=1.7;
59 E4=1.5;
60 E5=1.5;
61 E6=1.8;
62 E7=2.1;
63 EN1=600;
64 EN2=700;
65 EN3=400;
66 EN4=400;
67 EN5=600;
68 EN6=300;
69 EN7=200;
70 % B=B;%parameter to be optimised
71 % E=E;%parameter to be optimised
72 % h=0;%%%initialisation of the value
73 % EN=EN;
74 %  vidObj = VideoWriter('Contril-long.avi');
75 %  open(vidObj);
76 r=ones(n,N*n);
77 q=ones(n,N*n);
78
79
80 for j=2:n %%%for each position step
81
82 %%interpolate the neurite position and the stiffness value
83 %%%value of the stiffness for each position of each neurites
84 Stiff=interp2(X,Y,Model,NeuriteX(1:j,1:increment),NeuriteY(1:j,1:...
       increment),'nearest');
85 Stiff(isnan(Stiff))=0;%%%set all NaN to zero
86 Gradient=interp2(X,Y,Gradt, NeuriteX,NeuriteY);
87 Gradient(isnan(Gradient))=0;
88 %%%Probability to reach pick a point
89 %%stiffness around each point%
90 %%%play around with probability function
91 %%%Probability to reach pick a point
92 %%stiffness around each point%
93 %%%play around with probability function
94 %%use incrementation for added neurites due to branching
95 for m=1:increment
96   %%%define stiffness conditions
97   if Stiff(j-1,m)==0
98       Probbranch(1,m)=B1/(EN1*(transpose(y(1,m)^E1)));
99         if j==2
```

```
100         rotationangle(j,m)=0;
101         Probpoint=prob_tet;%probability to pick a point within the...
                experimental pdf (-pi:pi)
102         SUMM=cumsum(Probpoint);
103         MAX_SUMM=max(SUMM);
104         Random_Number=rand*MAX_SUMM;
105         CHOICE=SUMM-Random_Number;
106         k=CHOICE<0;%check all the negative values
107         k=sum(k,2);%%summ all the 1 values
108         k=k+1;%% obtain the index of the first non negative value
109
110         %%%Final value of the angle picked
111         angle(j,m)=tet(1,k);
112
113         else
114             %%%angle variation from optimisation
115         [cont_dist,cont_angle]=ang_dist(45,0,20);
116
117         Probpoint=cont_dist;%probability to pick a point
118         SUMM=cumsum(Probpoint);
119         MAX_SUMM=max(SUMM);
120         Random_Number=rand*MAX_SUMM;
121         CHOICE=SUMM-Random_Number;
122         k=CHOICE<0;%check all the negative values
123         k=sum(k,2);%%summ all the 1 values
124         k=k+1;%% obtain the index of the first non negative value
125
126         %%%Final value of the angle picked
127         angle(j,m)=cont_angle(1,k);
128         A=NeuriteY(j-2,m)-NeuriteY(j-1,m);
129         if A<0
130         rotationangle(j,m)=acos((NeuriteX(j-1,m)-NeuriteX(j-2,m))/...
                sqrt((NeuriteX(j-1,m)-NeuriteX(j-2,m)).^2+(NeuriteY(j...
                -1,m)-NeuriteY(j-2,m)).^2));
131         else
132             rotationangle(j,m)=-acos((NeuriteX(j-1,m)-NeuriteX(j...
                    -2,m))/sqrt((NeuriteX(j-1,m)-NeuriteX(j-2,m)).^2+(...
                    NeuriteY(j-1,m)-NeuriteY(j-2,m)).^2));
133         end
134         end
135   end
136
137
138
139   if Stiff(j-1,m)==1.77
140         %%%Control
141     if Gradient(j,m)==0
142          Probbranch(1,m)=B1/(EN1*(transpose(y(1,m)^E1)));
143         if j==2
144         rotationangle(j,m)=0;
145         Probpoint=Y1;%probability to pick a point within the ...
                experimental pdf (-180:180)
146         SUMM=cumsum(Probpoint);
147         MAX_SUMM=max(SUMM);
```

```
148         Random_Number=rand*MAX_SUMM;
149         CHOICE=SUMM-Random_Number;
150         k=CHOICE<0;%check all the negative values
151         k=sum(k,2);%%summ all the 1 values
152         k=k+1;%% obtain the index of the first non negative value
153
154         %%%Final value of the angle picked
155         angle(j,m)=phi(1,k);
156
157         else
158             %%%angle variation from optimisation
159         [cont_dist,cont_angle]=ang_dist(5.7155,0,37.6507);
160
161         Probpoint=cont_dist;%probability to pick a point
162         SUMM=cumsum(Probpoint);
163         MAX_SUMM=max(SUMM);
164         Random_Number=rand*MAX_SUMM;
165         CHOICE=SUMM-Random_Number;
166         k=CHOICE<0;%check all the negative values
167         k=sum(k,2);%%summ all the 1 values
168         k=k+1;%% obtain the index of the first non negative value
169
170         %%%Final value of the angle picked
171         angle(j,m)=cont_angle(1,k);
172         A=NeuriteY(j-2,m)-NeuriteY(j-1,m);
173         if A<0
174         rotationangle(j,m)=acos((NeuriteX(j-1,m)-NeuriteX(j-2,m))/...
                sqrt((NeuriteX(j-1,m)-NeuriteX(j-2,m)).^2+(NeuriteY(j...
                -1,m)-NeuriteY(j-2,m)).^2));
175         else
176             rotationangle(j,m)=-acos((NeuriteX(j-1,m)-NeuriteX(j...
                    -2,m))/sqrt((NeuriteX(j-1,m)-NeuriteX(j-2,m)).^2+(...
                    NeuriteY(j-1,m)-NeuriteY(j-2,m)).^2));
177         end
178         end
179         %%%if lower gradient
180     elseif Gradient(j,m)==2.5
181          Probbranch(1,m)=B4/(EN4*(transpose(y(1,m)^E4)));
182         if j==2
183         rotationangle(j,m)=0;
184         Probpoint=Y4;%probability to pick a point from pdf lower ...
                gradient (-180:180)
185         SUMM=cumsum(Probpoint);
186         MAX_SUMM=max(SUMM);
187         Random_Number=rand*MAX_SUMM;
188         CHOICE=SUMM-Random_Number;
189         k=CHOICE<0;%check all the negative values
190         k=sum(k,2);%%summ all the 1 values
191         k=k+1;%% obtain the index of the first non negative value
192
193         %%%Final value of the angle picked
194         angle(j,m)=phi(1,k);
195         else
196             %%%angle value from optimisation
```

```
197         [Low_I_dist,Low_I_angle]=ang_dist(15.8141,0,2.0116);
198
199         Probpoint=Low_I_dist;%probability to pick a point
200         SUMM=cumsum(Probpoint);
201         MAX_SUMM=max(SUMM);
202         Random_Number=rand*MAX_SUMM;
203         CHOICE=SUMM-Random_Number;
204         k=CHOICE<0;%check all the negative values
205         k=sum(k,2);%%summ all the 1 values
206         k=k+1;%% obtain the index of the first non negative value
207
208         %%%Final value of the angle picked
209         angle(j,m)=Low_I_angle(1,k);
210        A=NeuriteY(j-2,m)-NeuriteY(j-1,m);
211         if A<0
212         rotationangle(j,m)=acos((NeuriteX(j-1,m)-NeuriteX(j-2,m))/...
               sqrt((NeuriteX(j-1,m)-NeuriteX(j-2,m)).^2+(NeuriteY(j...
               -1,m)-NeuriteY(j-2,m)).^2));
213         else
214             rotationangle(j,m)=-acos((NeuriteX(j-1,m)-NeuriteX(j...
                   -2,m))/sqrt((NeuriteX(j-1,m)-NeuriteX(j-2,m)).^2+(...
                   NeuriteY(j-1,m)-NeuriteY(j-2,m)).^2));
215         end
216         end
217
218         %%%if higher gradient
219     elseif Gradient(j,m)==45
220         Probbranch(1,m)=B7/(EN7*(transpose(y(1,m)^E7)));
221         if j==2
222         rotationangle(j,m)=0;
223         Probpoint=Y7;%probability to pick a point (-180:180)
224         SUMM=cumsum(Probpoint);
225         MAX_SUMM=max(SUMM);
226         Random_Number=rand*MAX_SUMM;
227         CHOICE=SUMM-Random_Number;
228         k=CHOICE<0;%check all the negative values
229         k=sum(k,2);%%summ all the 1 values
230         k=k+1;%% obtain the index of the first non negative value
231
232         %%%Final value of the angle picked
233         angle(j,m)=phi(1,k);
234         else
235         [High_I_dist,High_I_angle]=ang_dist(40,0,19.8740);
236
237         Probpoint=High_I_dist;%probability to pick a point
238         SUMM=cumsum(Probpoint);
239         MAX_SUMM=max(SUMM);
240         Random_Number=rand*MAX_SUMM;
241         CHOICE=SUMM-Random_Number;
242         k=CHOICE<0;%check all the negative values
243         k=sum(k,2);%%summ all the 1 values
244         k=k+1;%% obtain the index of the first non negative value
245
246         %%%Final value of the angle picked
```

```
247          angle(j,m)=High_I_angle(1,k);
248          A=NeuriteY(j-2,m)-NeuriteY(j-1,m);
249          if A<0
250          rotationangle(j,m)=acos((NeuriteX(j-1,m)-NeuriteX(j-2,m))/...
                 sqrt((NeuriteX(j-1,m)-NeuriteX(j-2,m)).^2+(NeuriteY(j...
                 -1,m)-NeuriteY(j-2,m)).^2));
251          else
252              rotationangle(j,m)=-acos((NeuriteX(j-1,m)-NeuriteX(j...
                     -2,m))/sqrt((NeuriteX(j-1,m)-NeuriteX(j-2,m)).^2+(...
                     NeuriteY(j-1,m)-NeuriteY(j-2,m)).^2));
253          end
254          end
255
256      end
257      %%%%%if II-lower
258  elseif Stiff(j-1,m)==1.90
259      Probbranch(1,m)=B3/(EN3*(transpose(y(1,m)^E3)));
260          if j==2
261          rotationangle(j,m)=0;
262          Probpoint=Y3;%probability to pick a point (-180:180)
263          SUMM=cumsum(Probpoint);
264          MAX_SUMM=max(SUMM);
265          Random_Number=rand*MAX_SUMM;
266          CHOICE=SUMM-Random_Number;
267          k=CHOICE<0;%check all the negative values
268          k=sum(k,2);%%summ all the 1 values
269          k=k+1;%% obtain the index of the first non negative value
270
271          %%%Final value of the angle picked
272          angle(j,m)=phi(1,k);
273          else
274          [Low_II_dist,Low_II_angle]=ang_dist(-3.9395,0,45);
275
276          Probpoint=Low_II_dist;%probability to pick a point
277          SUMM=cumsum(Probpoint);
278          MAX_SUMM=max(SUMM);
279          Random_Number=rand*MAX_SUMM;
280          CHOICE=SUMM-Random_Number;
281          k=CHOICE<0;%check all the negative values
282          k=sum(k,2);%%summ all the 1 values
283          k=k+1;%% obtain the index of the first non negative value
284
285          %%%Final value of the angle picked
286          angle(j,m)=Low_II_angle(1,k);
287          A=NeuriteY(j-2,m)-NeuriteY(j-1,m);
288          if A<0
289          rotationangle(j,m)=acos((NeuriteX(j-1,m)-NeuriteX(j-2,m))/...
                 sqrt((NeuriteX(j-1,m)-NeuriteX(j-2,m)).^2+(NeuriteY(j...
                 -1,m)-NeuriteY(j-2,m)).^2));
290          else
291              rotationangle(j,m)=-acos((NeuriteX(j-1,m)-NeuriteX(j...
                     -2,m))/sqrt((NeuriteX(j-1,m)-NeuriteX(j-2,m)).^2+(...
                     NeuriteY(j-1,m)-NeuriteY(j-2,m)).^2));
292          end
```

```
293         end
294
295
296         %%%%if III-lower
297 elseif Stiff(j-1,m)==2
298     Probbranch(1,m)=B2/(EN2*(transpose(y(1,m)^E2)));
299         if j==2
300         rotationangle(j,m)=0;
301         Probpoint=Y2;%probability to pick a point (-180:180)
302         SUMM=cumsum(Probpoint);
303         MAX_SUMM=max(SUMM);
304         Random_Number=rand*MAX_SUMM;
305         CHOICE=SUMM-Random_Number;
306         k=CHOICE<0;%check all the negative values
307         k=sum(k,2);%%summ all the 1 values
308         k=k+1;%% obtain the index of the first non negative value
309
310         %%%Final value of the angle picked
311         angle(j,m)=phi(1,k);
312         else
313         [Low_III_dist,Low_III_angle]=ang_dist(-3.1827,0,3.4898);
314
315         Probpoint=Low_III_dist;%probability to pick a point
316         SUMM=cumsum(Probpoint);
317         MAX_SUMM=max(SUMM);
318         Random_Number=rand*MAX_SUMM;
319         CHOICE=SUMM-Random_Number;
320         k=CHOICE<0;%check all the negative values
321         k=sum(k,2);%%summ all the 1 values
322         k=k+1;%% obtain the index of the first non negative value
323
324         %%%Final value of the angle picked
325         angle(j,m)=Low_III_angle(1,k);
326         A=NeuriteY(j-2,m)-NeuriteY(j-1,m);
327         if A<0
328         rotationangle(j,m)=acos((NeuriteX(j-1,m)-NeuriteX(j-2,m))/...
               sqrt((NeuriteX(j-1,m)-NeuriteX(j-2,m)).^2+(NeuriteY(j...
               -1,m)-NeuriteY(j-2,m)).^2));
329         else
330             rotationangle(j,m)=-acos((NeuriteX(j-1,m)-NeuriteX(j...
                   -2,m))/sqrt((NeuriteX(j-1,m)-NeuriteX(j-2,m)).^2+(...
                   NeuriteY(j-1,m)-NeuriteY(j-2,m)).^2));
331         end
332         end
333
334
335         %%%%if II-higher
336 elseif Stiff(j-1,m)==4.5
337     Probbranch(1,m)=B6/(EN6*(transpose(y(1,m)^E6)));
338         if j==2
339         rotationangle(j,m)=0;
340         Probpoint=Y6;%probability to pick a point (-180:180)
341         SUMM=cumsum(Probpoint);
342         MAX_SUMM=max(SUMM);
```

```
343         Random_Number=rand*MAX_SUMM;
344         CHOICE=SUMM-Random_Number;
345         k=CHOICE<0;%check all the negative values
346         k=sum(k,2);%%summ all the 1 values
347         k=k+1;%% obtain the index of the first non negative value
348 
349         %%%Final value of the angle picked
350         angle(j,m)=phi(1,k);
351         else
352         [High_II_dist,High_II_angle]=ang_dist(0.2621,0,26.8327);
353 
354         Probpoint=High_II_dist;%probability to pick a point
355         SUMM=cumsum(Probpoint);
356         MAX_SUMM=max(SUMM);
357         Random_Number=rand*MAX_SUMM;
358         CHOICE=SUMM-Random_Number;
359         k=CHOICE<0;%check all the negative values
360         k=sum(k,2);%%summ all the 1 values
361         k=k+1;%% obtain the index of the first non negative value
362 
363         %%%Final value of the angle picked
364         angle(j,m)=High_II_angle(1,k);
365         A=NeuriteY(j-2,m)-NeuriteY(j-1,m);
366         if A<0
367         rotationangle(j,m)=acos((NeuriteX(j-1,m)-NeuriteX(j-2,m))/...
                sqrt((NeuriteX(j-1,m)-NeuriteX(j-2,m)).^2+(NeuriteY(j...
                -1,m)-NeuriteY(j-2,m)).^2));
368         else
369             rotationangle(j,m)=-acos((NeuriteX(j-1,m)-NeuriteX(j...
                    -2,m))/sqrt((NeuriteX(j-1,m)-NeuriteX(j-2,m)).^2+(...
                    NeuriteY(j-1,m)-NeuriteY(j-2,m)).^2));
370         end
371         end
372 
373 
374         %%%if III-higher
375 elseif Stiff(j-1,m)==7.3
376     Probbranch(1,m)=B5/(EN5*(transpose(y(1,m)^E5)));
377         if j==2
378         rotationangle(j,m)=0;
379         Probpoint=Y5;%probability to pick a point (-180:180)
380         SUMM=cumsum(Probpoint);
381         MAX_SUMM=max(SUMM);
382         Random_Number=rand*MAX_SUMM;
383         CHOICE=SUMM-Random_Number;
384         k=CHOICE<0;%check all the negative values
385         k=sum(k,2);%%summ all the 1 values
386         k=k+1;%% obtain the index of the first non negative value
387 
388         %%%Final value of the angle picked
389         angle(j,m)=phi(1,k);
390         else
391         [High_III_dist,High_III_angle]=ang_dist(-4.8693,0,12.8057)...
                ;
```

```
392
393         Probpoint=High_III_dist;%probability to pick a point
394         SUMM=cumsum(Probpoint);
395         MAX_SUMM=max(SUMM);
396         Random_Number=rand*MAX_SUMM;
397         CHOICE=SUMM-Random_Number;
398         k=CHOICE<0;%check all the negative values
399         k=sum(k,2);%%summ all the 1 values
400         k=k+1;%% obtain the index of the first non negative value
401
402         %%%Final value of the angle picked
403         angle(j,m)=High_III_angle(1,k);
404        A=NeuriteY(j-2,m)-NeuriteY(j-1,m);
405         if A<0
406         rotationangle(j,m)=acos((NeuriteX(j-1,m)-NeuriteX(j-2,m))/...
               sqrt((NeuriteX(j-1,m)-NeuriteX(j-2,m)).^2+(NeuriteY(j...
               -1,m)-NeuriteY(j-2,m)).^2));
407         else
408             rotationangle(j,m)=-acos((NeuriteX(j-1,m)-NeuriteX(j...
                   -2,m))/sqrt((NeuriteX(j-1,m)-NeuriteX(j-2,m)).^2+(...
                   NeuriteY(j-1,m)-NeuriteY(j-2,m)).^2));
409         end
410         end
411
412
413   end
414
415   if NeuriteX(j-1,m)<0 || NeuriteX(j-1,m)>1
416       r(j,m)=0;
417   end
418   if NeuriteY(j-1,m)<0 || NeuriteY(j-1,m)>1
419       q(j,m)=0;
420   end
421 end
422
423
424
425
426
427 % %
428 %
429 %%%%%for each step give the angle and position
430 angle(j,:)=deg2rad(angle(j,:))+rotationangle(j,:);
431 NeuriteX(j,:)=NeuriteX(j-1,:)+G*cos(angle(j,:)).*r(j,:).*q(j,:);
432 NeuriteY(j,:)=NeuriteY(j-1,:)+G*sin(angle(j,:)).*q(j,:).*r(j,:);
433
434  %probability to pick to branche
435
436         Random_Number=rand(numel(y),1);
437
438         k_branch=Random_Number>Probbranch;%check all the negative ...
               values (index of firsst non negative value )
439         %k_branch=k_branch+1;%% obtain the index of the first non ...
               negative value
```

```
440
441         L=find(k_branch(1:numel(y))==0);
442         if L>0 %%if there is branching
443         h=numel(L);
444         %%%create a new culomn with the original neurite info
445         NeuriteX(:,increment+1:increment+h)=NeuriteX(:,L);%L(1):L(...
                h));
446         NeuriteY(:,increment+1:increment+h)=NeuriteY(:,L);%L(1):L(...
                h));
447         angle(:,increment+1:increment+h)=angle(:,L);%L(1):L(h));
448         rotationangle(:,increment+1:increment+h)=rotationangle(:,L...
                );%L(1):L(h));
449         %%%%%Give a number to each original neurite and same to ...
                its
450         %%%%%generated branches
451         Value_branching(1,increment+1:increment+h)=Value_branching...
                (1,L);
452         else
453             h=0;
454         end
455         increment=increment+h;
456         %%%modify the number of neurites (increse due tu branching...
                )
457
458         %%%count the number of branches per original neurites
459         %Degree of branching
460
461         %%%%Number of terminal segments
462         y=sum(Value_branching==Value_branching');
463         %%%DNumber of branches
464         Degree_Branches=y-1;
465
466
467
468
469
470 %
471 % %%%%plot the neurites position for each step (pause time ...
      consumming)
472 % imagesc(GradX,GradY,Model)
473 %
474 % hold on
475 % %%%%plot(trueNeuriteX(1:j,:),trueNeuriteY(1:j,:),'Color','k','...
      Linewidth',2);
476 % plot(NeuriteX(1:j,1:increment),NeuriteY(1:j,1:increment),'Color...
      ','k','Linewidth',2);
477 % colorbar
478 % caxis([0 8]);
479 % set(gcf,'position',[x0,y0,width,height])
480 % % drawnow
481 % % F=getframe(gcf);
482 % % writeVideo(vidObj,F);
483 % pause(0.001)
484
```

```
485
486 NX=-(NeuriteX(1,1:increment)-NeuriteX(j,1:increment));
487 NY=-(NeuriteX(1,1:increment)-NeuriteY(j,1:increment));
488 end
489 %
490 % figure
491 % imagesc(GradX,GradY,Model)
492 % hold on
493 % plot(NeuriteX(:,1:increment),NeuriteY(:,1:increment),'Color','k...
      ','Linewidth',2);
494 % colorbar
495 % caxis([0 8]);
496 % set(gcf,'position',[x0,y0,width,height])
497
498
499 %
500
501
502
503
504 %close(vidObj);
505
506 % video=VideoWriter('Control.avi','Uncompressed AVI');
507 % open(video)
508 % writeVideo(video,F)
509 % close(video)
510 %%%%%final neurite angle distribution
511 for m=1:N
512   A= NeuriteY(1,m)-NeuriteY(n,m);
513   if A<0
514   NEURITE_ANGLE(1,m)=acos((NeuriteX(n,m)-NeuriteX(1,m))/sqrt((...
        NeuriteX(n,m)-NeuriteX(1,m)).^2+(NeuriteY(n,m)-NeuriteY(1,m))...
        .^2));
515   else
516   NEURITE_ANGLE(1,m)=-acos((NeuriteX(n,m)-NeuriteX(1,m))/sqrt((...
        NeuriteX(n,m)-NeuriteX(1,m)).^2+(NeuriteY(n,m)-NeuriteY(1,m))...
        .^2));
517   end
518   NEURITE_ANGLE(1,m)=rad2deg(NEURITE_ANGLE(1,m));
519 end
```

A.3.3.1 gradient figure file

```
1
2
3 load('simulation100_100_120bis.mat')
4
5 %set size of the figure
6 x0=10;
```

```
y0=10;
width=1000;
height=1000;
i=1;
figure
imagesc(GradX,GradY,Model)
hold on
%%%ONLY 3 BRANCHES TO FOR THE ANGLE FIGURE
%plot(NeuriteX_control{1}(:,1:3),NeuriteY_control{1}(:,1:3),'Color...
    ','k','Linewidth',2);
%%%ALL THE NEURITES AND THEIR BRANCHES
plot(NeuriteX_control{1}(:,1:increment1(1,i)),NeuriteY_control...
    {1}(:,1:increment1(1,i)),'Color','k','Linewidth',2);
colorbar
caxis([0 8]);
set(gcf,'position',[x0,y0,width,height])
title('Control')
hold off

figure
imagesc(GradX,GradY,Model1)
hold on
plot(NeuriteX_LowerIII{1}(:,1:increment2(1,i)),NeuriteY_LowerIII...
    {1}(:,1:increment2(1,i)),'Color','k','Linewidth',2);
colorbar
caxis([0 8]);
set(gcf,'position',[x0,y0,width,height])
title('Lower-III')
hold off

figure
imagesc(GradX,GradY,Model2)
hold on
plot(NeuriteX_LowerII{1}(:,1:increment3(1,i)),NeuriteY_LowerII...
    {1}(:,1:increment3(1,i)),'Color','k','Linewidth',2);
colorbar
caxis([0 8]);
set(gcf,'position',[x0,y0,width,height])
title('Lower-II')
hold off

figure
imagesc(GradX,GradY,Model3)
hold on
plot(NeuriteX_LowerI{1}(:,1:increment4(1,i)),NeuriteY_LowerI...
    {1}(:,1:increment4(1,i)),'Color','k','Linewidth',2);
colorbar
caxis([0 8]);
set(gcf,'position',[x0,y0,width,height])
title('Lower-I')
hold off

figure
imagesc(GradX,GradY,Model4)
```

```
hold on
plot(NeuriteX_higher_III{1}(:,1:increment5(1,i)),...
    NeuriteY_higher_III{1}(:,1:increment5(1,i)),'Color','k','...
    Linewidth',2);
colorbar
caxis([0 8]);
set(gcf,'position',[x0,y0,width,height])
title('HIgher-III')
hold off


figure
imagesc(GradX,GradY,Model5)
hold on
plot(NeuriteX_higher_II{1}(:,1:increment6(1,i)),NeuriteY_higher_II...
    {1}(:,1:increment6(1,i)),'Color','k','Linewidth',2);
colorbar
caxis([0 8]);
set(gcf,'position',[x0,y0,width,height])
title('Higher-II')
hold off

figure
imagesc(GradX,GradY,Model6)
hold on
plot(NeuriteX_higher_I{1}(:,1:increment7(1,i)),NeuriteY_higher_I...
    {1}(:,1:increment7(1,i)),'Color','k','Linewidth',2);
colorbar
caxis([0 8]);
set(gcf,'position',[x0,y0,width,height])
title('Higher-I')
hold off
```

A.3.4 in-vivo like simulation file

```


%load('simulation4_01_100_672.mat')
% load('simulation4_02_100_672.mat')
% load('simulation4_03_100_672.mat')
% load('simulation4_04_100_672.mat')
%load('invivo04figure.mat')
%load('invivobis.mat')
% load('nointerface2.mat')
% load('invivo02figure.mat')
% load('invivo03figure.mat')
% load('invivo04figure.mat')
% GradX = linspace(0,2,length(Model(1,:)));
% GradY = linspace(0,1,length(Model(:,1)));
```

```
15 %  d=5;
16 % % % %
17 %
18 % count=cell(1,d);
19 % countzero=cell(1,d);
20 % sum_count=cell(1,d);
21 % sum_countzero=cell(1,d);
22 % PercentX=zeros(1,d);
23 % counta=cell(1,d);
24 % countazero=cell(1,d);
25 % sum_counta=cell(1,d);
26 % sum_countazero=cell(1,d);
27 % PercentXa=zeros(1,d);
28 %
29 % count2=cell(1,d);
30 % count2zero=cell(1,d);
31 % sum_count2=cell(1,d);
32 % sum_count2zero=cell(1,d);
33 % PercentX2=zeros(1,d);
34 %
35 % count2a=cell(1,d);
36 % count2azero=cell(1,d);
37 % sum_count2a=cell(1,d);
38 % sum_count2azero=cell(1,d);
39 % PercentX2a=zeros(1,d);
40 %
41 % for i=1:d
42 %
43 %     %%%%taking into account all neurites, branches included
44 %
45 %    %%%count the neuriteX>0.8mm after 672hours on the control
46 %    count{i}= NeuriteX_control{i}(:,1:increment1(1,i))>0.8;
47 %    countzero{i}= NeuriteX_control{i}(:,1:increment1(1,i))>0.15;
48 %    count{i}=sum(count{i});
49 %    countzero{i}=sum(countzero{i});
50 %    count{i}=count{i}>0;
51 %    countzero{i}=countzero{i}>0;
52 %    sum_count{i}=sum(count{i},2);
53 %    sum_countzero{i}=sum(countzero{i},2);
54 %    %%%count the neuriteX>0.8mm after 672hours on the lowerIII
55 %    count2{i}= NeuriteX_LowerIII{i}(:,1:increment2(1,i))>0.8;
56 %    count2zero{i}= NeuriteX_LowerIII{i}(:,1:increment2(1,i))>0.15...
     ;
57 %    count2{i}=sum(count2{i});
58 %    count2zero{i}=sum(count2zero{i});
59 %    count2{i}=count2{i}>0;
60 %    count2zero{i}=count2zero{i}>0;
61 %    sum_count2{i}=sum(count2{i},2);
62 %    sum_count2zero{i}=sum(count2zero{i},2);
63 %
64 %    %%%put results in Percentage
65 %     %%%5for the control
66 %     PercentX(1,i)=sum_count{i}./sum_countzero{i}.*100;
67 %     %%%for lowerIII
```

```
%     PercentX2(1,i)=sum_count2{i}./sum_count2zero{i}.*100;
%
%        %%%taking into account only original neurites
%      %%%count the neuriteX>0.8mm after 672hours on the control
%    counta{i}= NeuriteX_control{i}(:,1:100)>0.8;
%    countazero{i}= NeuriteX_control{i}(:,1:100)>0.15;
%    counta{i}=sum(counta{i});
%    countazero{i}=sum(countazero{i});
%    counta{i}=counta{i}>0;
%    countazero{i}=countazero{i}>0;
%    sum_counta{i}=sum(counta{i},2);
%    sum_countazero{i}=sum(countazero{i},2);
%    %%%count the neuriteX>0.8mm after 672hours on the lowerIII
%    count2a{i}= NeuriteX_LowerIII{i}(:,1:100)>0.8;
%     count2azero{i}= NeuriteX_LowerIII{i}(:,1:100)>0.15;
%    count2a{i}=sum(count2a{i});
%    count2azero{i}=sum(count2azero{i});
%    count2a{i}=count2a{i}>0;
%    count2azero{i}=count2azero{i}>0;
%    sum_count2a{i}=sum(count2a{i},2);
%    sum_count2azero{i}=sum(count2azero{i},2);
%
%    %%%put results in Percentage
%     %%%5for the control
%     PercentXa(1,i)=sum_counta{i}./sum_countazero{i}.*100;
%     %%%for lowerIII
%     PercentX2a(1,i)=sum_count2a{i}./sum_count2azero{i}.*100;
%
% end
%
PercentX=transpose(PercentX);
PercentX2=transpose(PercentX2);
PercentXa=transpose(PercentXa);
PercentX2a=transpose(PercentX2a);
figure
subplot(1,2,1);
hold on
boxplot([PercentX,PercentX2],'Labels',{'Control','Lower-III'})
ylabel('% neurites reaching 0.8mm')
%xlabel('Space at the interface : 0.1mm')
%xlabel('Space at the interface : 0.2mm')
%xlabel('Space at the interface : 0.3mm')
%xlabel('Space at the interface : 0.4mm')
title('All neurites including branches')
hold off

subplot(1,2,2);
hold on
boxplot([PercentXa,PercentX2a], 'Labels', {'Control', 'Lower-III'...
    })
ylabel('% neurites reaching 0.8mm')
%xlabel('Space at the interface : 0.1mm')
%xlabel('Space at the interface : 0.2mm')
 %xlabel('Space at the interface : 0.3mm')
```

```
121 %xlabel('Space at the interface : 0.4mm')
122 title('Original neurites only')
123 hold off
124 % %
125 %%%%%figure of one simulation
126 % %set size of the figure
127 % x0=10;
128 % y0=10;
129 % width=1000;
130 % height=500;
131 % i=1;
132 % j=1;
133 % figure
134 % imagesc(GradX,GradY,Model)
135 % hold on
136 % plot(NeuriteX_control{i}(:,1:increment1(1,i)),NeuriteY_control{i...
      }(:,1:increment1(1,i)),'Color','k','Linewidth',2);
137 % colorbar
138 % caxis([0 8]);
139 % set(gcf,'position',[x0,y0,width,height])
140 % title('Control')
141 % hold off
142 %
143 % figure
144 % imagesc(GradX,GradY,Model1)
145 % hold on
146 % plot(NeuriteX_LowerIII{j}(:,1:increment2(1,j)),NeuriteY_LowerIII...
      {j}(:,1:increment2(1,j)),'Color','k','Linewidth',2);
147 % colorbar
148 % caxis([0 8]);
149 % set(gcf,'position',[x0,y0,width,height])
150 % title('Lower-III')
151 % hold off
```

Bibliography

Abramoff, M., Magalhães, P. J., and Ram, S. J. (2004). *Image processing with ImageJ*, volume 11. Laurin Pub. Co.

Ahearne, M., Yang, Y., El Haj, A. J., Then, K. Y., and Liu, K.-K. (2005). Characterizing the viscoelastic properties of thin hydrogel-based constructs for tissue engineering applications. *J. R. Soc. Interface*, 2(5):455–63.

Allen, S. J., Dawbarn, D., j Allen, S., Dawbarn, D., Allen, S. J., and Dawbarn, D. (2006). Clinical relevance of the neurotrophins and their receptors. *Clin. Sci.*, 110(2):175–191.

Aloe, L. (2004). Rita Levi-Montalcini: the discovery of nerve growth factor and modern neurobiology. *Trends Cell Biol.*, 14(7):395–399.

Aloe, L. (2011). Rita Levi-Montalcini and the discovery of NGF, the first nerve cell growth factor. *Arch. Ital. Biol.*, 149(2):175–181.

Alt, W. (1980). Biased random walk models for chemotaxis and related diffusion approximations. *J. Math. Biol*, 9:147–177.

Ansselin, A. D., Fink, T., and Davey, D. F. (1997). Peripheral nerve regeneration through nerve guides seeded with adult Schwann cells. *Neuropathol. Appl. Neurobiol.*, 23(5):387–398.

Arslantunali, D., Dursun, T., Yucel, D., Hasirci, N., and Hasirci, V. (2014). Peripheral nerve conduits: Technology update. *Med. Devices Evid. Res.*, 7:405–424.

Bąk, M., Gutkowska, O. N., Wagner, E., and Gosk, J. (2017). The role of chitin and chitosan in peripheral nerve reconstruction. *Polym. Med.*, 47(1):43–47.

Balgude, A. P., Yu, X., Szymanski, A., and Bellamkonda, R. V. (2001). Agarose gel stiffness determines rate of DRG neurite extension in 3D cultures. *Biomaterials*, 22(10):1077–1084.

Banse, X., Sims, T. J., and Bailey, A. J. (2002). Mechanical Properties of Adult Vertebral Cancellous Bone: Correlation With Collagen Intermolecular Cross-Links. *J. Bone Miner. Res.*, 17(9):1621–1628.

Baranauskas, V., Vidal, B. C., and Parizotto, N. a. (1998). Observation of geometric structure of collagen molecules by atomic force microscopy. *Appl. Biochem. Biotechnol.*, 69(2):91–97.

Barbarisi, M., Marino, G., Armenia, E., Vincenzo, Q., Rosso, F., Porcelli, M., and Barbarisi, A. (2015). Use of polycaprolactone (PCL) as scaffolds for the regeneration of nerve tissue. *J. Biomed. Mater. Res. Part A*, 103(5):1755–1760.

Barberio, C., Chaudhry, T., Power, D., Lawless, B., Espino, D., Tan, S., and Wilton, J. (2019). The effect of shoulder abduction and medial epicondylectomy on ulnar nerve strain: A preliminary study. *J. Musculoskelet. Surg. Res.*, 3(1):134.

Barberio, C. G., Chaudhry, T., Power, D. M., Tan, S., Lawless, B. M., Espino, D. M., and Wilton, J. C. (2018). Towards viscoelastic characterisation of the human ulnar nerve: An early assessment using embalmed cadavers. *Med. Eng. Phys.*

Barnes, J. M., Przybyla, L., and Weaver, V. M. (2017). Tissue mechanics regulate brain development, homeostasis and disease. *Co. Biol.*

Barnes, S. C., Lawless, B. M., Shepherd, D. E. T., Espino, D. M., Bicknell, G. R., and Bryan, R. T. (2016). Viscoelastic properties of human bladder tumours. *J. Mech. Behav. Biomed. Mater.*, 61:250–257.

Barnes, S. C., Shepherd, D. E. T., Espino, D. M., and Bryan, R. T. (2015). Frequency dependent viscoelastic properties of porcine bladder. *J. Mech. Behav. Biomed. Mater.*

Behar, T. N., Schaffner, a. E., Colton, C. a., Somogyi, R., Olah, Z., Lehel, C., and Barker, J. L. (1994). GABA-induced chemokinesis and NGF-induced chemotaxis of embryonic spinal cord neurons. *J. Neurosci.*, 14(1):29–38.

Bellamkonda, R. V. (2006). Peripheral nerve regeneration: An opinion on channels, scaffolds and anisotropy. *Biomaterials*, 27:3515–3518.

Besseau, L., Coulomb, B., Lebreton-Decoster, C., and Giraud-Guille, M. M. (2002). Production of ordered collagen matrices for three-dimensional cell culture. *Biomaterials*, 23(1):27–36.

Binnig, G., Quate, C. F., and Gerber, C. (1986). Atomic Force Microscope. *Phys. Rev. Lett.*, 56(9).

Bitar, M., Salih, V., Brown, R. A., and Nazhat, S. N. (2007). Effect of multiple unconfined compression on cellular dense collagen scaffolds for bone tissue engineering. *J. Mater. Sci. Mater. Med.*, 18(2):237–244.

Black, J. (2018). *Natural and Living Biomaterials*.

Borschel, G. H., Kia, K. F., Kuzon, W. M., and Dennis, R. G. (2003). Mechanical Properties of Acellular Peripheral Nerve. *J. Surg. Res.*, 114:133–139.

Bozkurt, A., Deumens, R., Beckmann, C., Damink, L. O., Schügner, F., Heschel, I., Sellhaus, B., Weis, J., Jahnen-Dechent, W., Brook, G. A., and Others (2009). In

vitro cell alignment obtained with a Schwann cell enriched microstructured nerve guide with longitudinal guidance channels. *Biomaterials*, 30(2):169–179.

Bracaglia, L. G., Smith, B. T., Watson, E., Arumugasaamy, N., Mikos, A. G., and Fisher, J. P. (2017). 3D printing for the design and fabrication of polymer-based gradient scaffolds. *Acta Biomater.*, 56:3–13.

Braun, S., Croizat, B., Lagrange, M.-C., Warter, J.-M., and Poindron, P. (1996). Neurotrophins increase motoneurons' ability to innervate skeletal muscle fibers in rat spinal cord-human muscle cocultures. *J. Neurol. Sci.*, 136(1):17–23.

Brown, R. A., Wiseman, M., Chuo, C.-B., Cheema, U., and Nazhat, S. N. (2005). Ultrarapid engineering of biomimetic materials and tissues: Fabrication of nano- and microstructures by plastic compression. *Adv. Funct. Mater.*, 15(11):1762–1770.

Buehler, M. J. (2008). Nanomechanics of collagen fibrils under varying cross-link densities: Atomistic and continuum studies. *J. Mech. Behav. Biomed. Mater.*, pages 59–67.

Buettner, H. M., Pittman, R. N., and Ivins, J. K. (1994). A model of neurite extension across regions of nonpermissive substrate: simulations based on experimental measurement of growth cone motility and filopodial dynamics. *Dev. Biol.*, 163:407–422.

Buffinton, C. M., Tong, K. J., Blaho, R. A., Buffinton, E. M., and Ebenstein, D. M. (2015). Comparison of mechanical testing methods for biomaterials: Pipette aspiration, nanoindentation, and macroscale testing. *J. Mech. Behav. Biomed. Mater.*, 51:367–379.

Burdick, J. A., Khademhosseini, A., and Langer, R. (2004). Fabrication of Gradient Hydrogels Using a Microfluidics/ Photopolymerization Process. *Langmuir*, 20(13).

Burton, H. E., Freij, J. M., and Espino, D. M. (2017). Dynamic Viscoelasticity and Surface Properties of Porcine Left Anterior Descending Coronary Arteries. *Cardiovasc. Eng. Technol.*, 8(1):41–56.

Campbell, W. W. (2008). Evaluation and management of peripheral nerve injury. *Clin. Neurophysiol.*, 119(9):1951–1965.

Cao, X. and Shoichet, M. S. (2001). Defining the concentration gradient of nerve growth factor for guided neurite outgrowth. *Neuroscience*, 103(3):831–840.

Carballo-Molina, O. A. and Velasco, I. (2015). Hydrogels as scaffolds and delivery systems to enhance axonal regeneration after injuries. *Front. Cell. Neurosci.*, 9(13).

Castro, A. P., Laity, P., Shariatzadeh, M., Wittkowske, C., Holland, C., and Lacroix, D. (2016). Combined numerical and experimental biomechanical characterization of soft collagen hydrogel substrate. *J. Mater. Sci. Mater. Med.*, 27(4):1–9.

Chang, W., Shah, M. B., Lee, P., and Yu, X. (2018). Tissue-engineered spiral nerve guidance conduit for peripheral nerve regeneration. *Acta Biomater.*, 73:302–311.

Chao, P.-H. G., Sheng, S.-C., and Chang, W.-R. (2014). Micro-composite substrates for the study of cell-matrix mechanical interactions. *J. Mech. Behav. Biomed. Mater.*, 38:232–241.

Charriere, G., Bejot, M., Schnitzler, L., Ville, G., and Hartmann, D. J. (1989). Reactions to a bovine collagen implant: Clinical and immunologic study in 705 patients. *J. Am. Acad. Dermatol.*, 21(6):1203–1208.

Cheema, U. and Brown, R. A. (2013). Rapid Fabrication of Living Tissue Models by Collagen Plastic Compression: Understanding Three-Dimensional Cell Matrix Repair In Vitro. *Adv. wound care*, 2(4):176–184.

Chen, E. J., Novakofski, J., Jenkins, W. K., and Brien, W. D. O. (1996). Young's Modulus Measurements of Soft Tissues with Application to Elasticity Imaging. *IEEE*, 43(1):191–194.

Chen, R.-J., Lin, C.-C. K., and Ju, M.-S. (2010a). In situ biomechanical properties of normal and diabetic nerves: An efficient quasi-linear viscoelastic approach. *J. Biomech.*, 43.

Chen, R.-J., Lin, C.-C. K., and Ju, M.-S. (2010b). In situ transverse elasticity and blood perfusion change of sciatic nerves in normal and diabetic rats. *Clin. Biomech.*, 25:409–414.

Cheung, Y. K., Azeloglu, E. U., Shiovitz, D. A., Costa, K. D., Seliktar, D., and Sia, S. K. (2009). Microscale control of stiffness in a cell-adhesive substrate using microfluidics-based lithography. *Angew. Chemie - Int. Ed.*, 48(39):7188–7192.

Cho, S.-H., Noh, J.-R., Cho, M. Y., Go, M.-J., Kim, Y.-H., Kang, E. S., Kim, Y. H., Lee, C.-H., and Lim, Y. T. (2017). An injectable collagen/poly(γ-glutamic acid) hydrogel as a scaffold of stem cells and α-lipoic acid for enhanced protection against renal dysfunction. *Biomater. Sci.*, 5(2):285–294.

Ciaramitaro, P., Mondelli, M., Logullo, F., Grimaldi, S., Battiston, B., Sard, A., Scarinzi, C., Migliaretti, G., Faccani, G., and Cocito, D. (2010). Traumatic peripheral nerve injuries: epidemiological findings, neuropathic pain and quality of life in 158 patients. *J. Peripher. Nerv. Syst.*, 15(2):120–127.

Coffey W. T. (1985). Development and application of the theory of Brownian notion. *Phys. Rev.*, 36:823–841.

Cohen-Cory, S. and Fraser, S. E. (1995). Effects of brain-derived neurotrophic factor on optic axon branching and remodelling in vivo. *Nature*, 378(6553):192.

Coy, R. H., Evans, O. R., Phillips, J. B., and Shipley, R. J. (2017). An integrated theoretical-experimental approach to accelerate translational tissue engineering. *J. Tissue Eng. Regen. Med.*

Davidenko, N., Schuster, C. F., Bax, D. V., Raynal, N., Farndale, R. W., Best, S. M., and Cameron, R. E. (2015). Control of crosslinking for tailoring collagen-based scaffolds stability and mechanics. *Acta Biomater.*, 25:131–142.

Davies, A. M., Horton, A., Burton, L. E., Schmelzer, C., Vandlen, R., and Rosenthal, A. (1993). Neurotrophin-4/5 is a mammalian-specific survival factor for distinct populations of sensory neurons. *J. Neurosci.*, 13(11):4961–4967.

Davis, H. (1926). The conduction of the nerve impulse. *Physiol. Rev.*, 6(4):547–595.

Deumens, R., Bozkurt, A., Meek, M. F., Marcus, M. A. E., Joosten, E. A. J., Weis, J., and Brook, G. A. (2010). Repairing injured peripheral nerves: Bridging the gap. *Prog. Neurobiol.*, 92(3):245–276.

Dickinson, R. B. and Tranquillo, R. T. (1993). Mathematical Biology A stochastic model for adhesion-mediated cell random motility and haptotaxis. *J. Math. Biol*, 31:563–600.

Diederich, V. E., Studer, P., Kern, A., Lattuada, M., Storti, G., Sharma, R. I., Snedeker, J. G., and Morbidelli, M. (2013). Bioactive polyacrylamide hydrogels with gradients in mechanical stiffness. *Biotechnol. Bioeng.*, 110(5):1508–1519.

Discher, D. E., Janmey, P., and Wang, Y.-L. (2005). Tissue cells feel and respond to the stiffness of their substrate. *Science*, 310(5751):1139–43.

Dityatev, A. E., Chmykhova, N. M., Studer, L., Karamian, O. A., Kozhanov, V. M., and Clamann, H. P. (1995). Comparison of the topology and growth rules of motoneuronal dendrites. *J. Comp. Neurol.*, 363(3):505–516.

Dodla, M. C., Alvarado-Velez, M., Mukhatyar, V. J., and Bellamkonda, R. V. (2019). Peripheral Nerve Regeneration. *Princ. Regen. Med.*, 3:1223–1236.

Drobnič, M., Radosavljevič, D., Ravnik, D., Pavlovčič, V., and Hribernik, M. (2006). Comparison of four techniques for the fixation of a collagen scaffold in the human cadaveric knee. *Osteoarthr. Cartil.*

Du, J., Chen, H., Qing, L., Yang, X., and Jia, X. (2018). Biomimetic neural scaffolds: a crucial step towards optimal peripheral nerve regeneration. *Biomater. Sci.*, 6(6):1299–1311.

Du, Y., Hancock, M. J., He, J., Villa-Uribe, J. L., Wang, B., Cropek, D. M., and Khademhosseini, A. (2009). Convection-driven generation of long-range material gradients. *Biomaterials*, 31:2686–2694.

Dunn, G. A. and Brown, A. F. (1987). A unified approach to analysing cell motility. *J. Cell Sci.*, 8:81–102.

Efremov, Y. M., Wang, W.-H., Hardy, S. D., Geahlen, R. L., and Raman, A. (2017). Measuring nanoscale viscoelastic parameters of cells directly from AFM force-displacement curves. *Sci. Rep.*, 7(1):1541.

E.Hadjizadeh, V. Mudera, R. B. (2009). Close dependence of fibroblast proliferation on collagen scaffold matrix stiffness. *J. Tissue Eng. Regen. Med.*, 4(7):524–531.

Eric Huebner, S. A. and Strittmatter, S. M. (2010). Axon Regeneration in the Peripheral and Central Nervous. *Results Probl Cell Differ.*

Evans, E. B., Brady, S. W., Tripathi, A., and Hoffman-Kim, D. (2018). Schwann cell durotaxis can be guided by physiologically relevant stiffness gradients. *Biomater. Res.*, 22:14.

Evans, G. R., Brandt, K., Katz, S., Chauvin, P., Otto, L., Bogle, M., Wang, B., Meszlenyi, R. K., Lu, L., Mikos, A. G., and Patrick, C. W. (2002). Bioactive poly(l-lactic acid) conduits seeded with Schwann cells for peripheral nerve regeneration. *Biomaterials*, 23(3):841–848.

Fawcett, J. W., Keynes, R. J., Faweett, J. W., and Keynes, R. J. (1990). Peripheral nerve regeneration. *Annu. Rev. Neurosci.*, 13(1):43–60.

Ferreira, A. M., Gentile, P., Chiono, V., and Ciardelli, G. (2012). Collagen for bone tissue regeneration. *Acta Biomater.*, 8:3191–3200.

Fine, E. G., Decosterd, I., Papaloïzos, M., Zurn, A. D., and Aebischer, P. (2002). GDNF and NGF released by synthetic guidance channels support sciatic nerve regeneration across a long gap. *Eur. J. Neurosci.*, 15(4):589–601.

Flanagan, L. A., Ju, Y.-E., Marg, B., Osterfield, M., and Janmey, P. A. (2002). Neurite branching on deformable substrates. *Neuroreport*, 13(18):2411.

Franze, K. (2011). Atomic force microscopy and its contribution to understanding the development of the nervous system. *Curr. Opin. Genet. Dev.*, 21(5):530–537.

Franze, K. and Guck, J. (2010). The biophysics of neuronal growth. *Reports Prog. Phys.*, 73(9):94601.

Franze, K., Janmey, P. A., and Guck, J. (2013). Mechanics in Neuronal Development and Repair. *Annu. Rev. Biomed. Eng.*, pages 227–51.

García, S., Sunyer, R., Olivares, A., Noailly, J., Atencia, J., and Trepat, X. (2014). Generation of stable orthogonal gradients of chemical concentration and substrate stiffness in a microfluidic device. *Lab Chip*, 15:2606.

Gaudet, A. D., Popovich, P. G., and Ramer, M. S. (2011). Wallerian degeneration:

Gaining perspective on inflammatory events after peripheral nerve injury. *J. Neuroinflammation*.

Geerligs, M., Peters, G. W. M., Ackermans, P. A. J., Oomens, C. W. J., and Baaijens, F. P. T. (2008). Linear viscoelastic behavior of subcutaneous adipose tissue. *Biorheology*, 45:677–688.

Gentleman, E., Lay, A. N., Dickerson, D. A., Nauman, E. A., Livesay, G. A., and Dee, K. C. (2003). Mechanical characterization of collagen fibers and scaffolds for tissue engineering. *Biomaterials*, 24(21):3805–3813.

Georgeu, G. A., Walbeehm, E. T., Tillett, R., Afoke, A., Brown, R. A., and Phillips, J. B. (2005). Investigating the mechanical shear-plane between core and sheath elements of peripheral nerves. *Cell Tissue Res.*, 320(2):229–234.

Georgiou, M., Bunting, S. C. J., Davies, H. A., Loughlin, A. J., Golding, J. P., and Phillips, J. B. (2013). Engineered neural tissue for peripheral nerve repair. *Biomaterials*, 34(30):7335–7343.

Geuna, S., Raimondo, S., Ronchi, G., Di Scipio, F., Tos, P., Czaja, K., and Fornaro, M. (2009). Chapter 3 Histology of the Peripheral Nerve and Changes Occurring During Nerve Regeneration. *Int. Rev. Neurobiol.*, 87:27–46.

Ghahary, A., McPherson, P. S., and Cheng, K. W. (1989). A serum factor inducing neurite retraction of morphologically differentiated neuroblastoma x glioma NG108-15 cells. *J Cell Sci*, 92(Pt 2):251–6.

Ghosh, K., Pan, Z., Guan, E., Ge, S., Liu, Y., Nakamura, T., Ren, X.-D., Rafailovich, M., and Clark, R. A. F. (2007). Cell adaptation to a physiologically relevant ECM mimic with different viscoelastic properties. *Biomaterials*, 28:671–679.

Gordon, T. (2015). The Biology, Limits, and Promotion of Peripheral Nerve Regeneration in Rats and Humans. *Nerves Nerve Inj.*, 2:993–1019.

Gray, D. S., Tien, J., and Chen, C. S. (2003). Repositioning of cells by mechanotaxis on surfaces with micropatterned Young's modulus. *J. Biomed. Mater. Res.*, 45(150):51209–51212.

Grewal, R., Xu, J., Sotereanos, D. G., and Woo, S. L. (1996). Biomechanical properties of peripheral nerves. *Hand Clin.*, 12(2):195–204.

Griffin, M., Malahias, M., S, H., and Khan, W. S. (2013). Peripheral nerve injury: principles for repair and regeneration. *J. Bone Jt. Surg.*, 95(23):2144–2151.

Grinsell, D. and Keating, C. P. (2014). Peripheral nerve reconstruction after injury: a review of clinical and experimental therapies. *Biomed Res. Int.*

Gu, X., Ding, F., Yang, Y., and Liu, J. (2011). Construction of tissue engineered nerve grafts and their application in peripheral nerve regeneration. *Prog. Neurobiol.*, 93(2):204–230.

Guenard, V., Kleitman, N., Morrissey, T. K., Bunge, R. P., and Aebischer, P. (1992). Syngeneic Schwann cells derived from adult nerves seeded in semipermeable guidance channels enhance peripheral nerve regeneration. *J. Neurosci.*, 12(9):3310–3320.

Gutenkunst, R. N., Waterfall, J. J., Casey, F. P., Brown, K. S., Myers, C. R., and Sethna, J. P. (2007). Universally Sloppy Parameter Sensitivities in Systems Biology Models. *PLoS Comput. Biol.*, 3(10):1971–1978.

Hackley, V. A. and Ferraris, C. F. (2001). Guide to Rheological Nomenclature: Measurements in Ceramic Particulate Systems. *NIST Spec. Publ.*, 946.

Hadden, W. J., Young, J. L., Holle, A. W., Mcfetridge, M. L., Kim, D. Y., Wijesinghe, P., Taylor-Weiner, H., Wen, J. H., Lee, A. R., Bieback, K., Vo, B.-N., Sampson, D. D., Kennedy, B. F., Spatz, J. P., Engler, A. J., Choi, Y. S., and Weitz, D. A. (2017). Stem cell migration and mechanotransduction on linear stiffness gradient hydrogels. *Proc. Natl. Acad. Sci.*

Hadjipanayi, E., Mudera, V., and Brown, R. A. (2009). Guiding cell migration in 3D: A collagen matrix with graded directional stiffness. *Cell Motil. Cytoskeleton*, 66(3):121–128.

Haftek, J. (1970). Stretch Injury of Peripheral Nerve, Acute Effects of Stretching on Rabbit Nerve. *J. bone Jt. Surg.*, 52B(2):354–365.

Hagg, T. (2009). From neurotransmitters to neurotrophic factors to neurogenesis. *Neurosci.*, 15(1):20–27.

Harley, B. A., Leung, J. H., Silva, E. C. C. M., and Gibson, L. J. (2006). Mechanical characterization of collagen glycosaminoglycan scaffolds. *Acta Biomater.*, 3:463–474.

Hart, A. M., Terenghi, G., and Wiberg, M. (2008). Neuronal death after peripheral nerve injury and experimental strategies for neuroprotection. *Neurol. Res.*, 30:999–1011.

Hartman, C. D., Isenberg, B. C., Chua, S. G., and Wong, J. Y. (2016). Vascular smooth muscle cell durotaxis depends on extracellular matrix composition. *Proc. Natl. Acad. Sci.*, 113(40):11190–11195.

Hasan, S., Geissler, D., Wink, K., Hagen, A., Heiland, J. J., and Belder, D. (2018). Fluorescence lifetime-activated droplet sorting in microfluidic chip systems. *R. Soc. Chem.*

Hassanzadeh, P., Atyabi, F., and Dinarvand, R. (2018). Tissue engineering: Still facing a long way ahead. *J. Control. Release*, 279:181–197.

Heumann, R., Lindholm, D., Bandtlow, C., Meyer, M., Radeke, M. J., Misko, T. P., Shooter, E., and Thoenen, H. (1987). Differential regulation of mRNA encoding nerve growth factor and its receptor in rat sciatic nerve during development, degeneration, and regeneration: role of macrophages. *Proc. Natl. Acad. Sci.*, 84(23):8735–8739.

Hoffman-Kim, D., Mitchel, J. A., and Bellamkonda, R. V. (2010). Topography, cell response, and nerve regeneration. *Annu. Rev. Biomed. Eng.*, 12:203–31.

Hoke, A. (2006). Schwann Cells Express Motor and Sensory Phenotypes That Regulate Axon Regeneration. *J. Neurosci.*, 26(38):9646–9655.

Höke, A., Gordon, T., Zochodne, D. W., and Sulaiman, O. A. R. (2002). A decline in glial cell-line-derived neurotrophic factor expression is associated with impaired regeneration after long-term Schwann cell denervation. *Exp. Neurol.*, 173(1):77–85.

Hollister, S. J. (2005). Porous scaffold design for tissue engineering. *Nat. Mater.*, 4(7):518–524.

Holmes, T. C. (2002). Novel peptide-based biomaterial scaffolds for tissue engineering. *Trends Biotechnol.*, 20(1):16–21.

Houschyar, K. S., Momeni, A., Pyles, M. N., Cha, J. Y., Maan, Z. N., Duscher, D., Jew, O. S., Siemers, F., and van Schoonhoven, J. (2016). The role of current techniques and concepts in peripheral nerve repair. *Plast. Surg. Int.*

Hu, Y., Wu, Y., Gou, Z., Tao, J., Zhang, J., Liu, Q., Kang, T., Jiang, S., Huang, S., He, J., Chen, S., and Du, Y. (2016). 3D-engineering of Cellularized Conduits for Peripheral Nerve Regeneration. *Sci. Rep.*, 6:32184.

Instrument, J. (2008). Determining the elastic modulus of biological samples using atomic force microscopy. *JPK Instruments Appl. Rep.*, pages 1–9.

Isenberg, B. C., DiMilla, P. A., Walker, M., Kim, S., and Wong, J. Y. (2009). Vascular Smooth Muscle Cell Durotaxis Depends on Substrate Stiffness Gradient Strength. *Biophys. J.*, 97(5):1313–1322.

Jabbarzadeh, E. and Abrams, C. F. (2005). Chemotaxis and random motility in unsteady chemoattractant fields: a computational study. *J. Theor. Biol.*, 235(2):221–232.

Jia, Y., Yang, W., Zhang, K., Qiu, S., Xu, J., Wang, C., and Chai, Y. (2019). Nanofiber arrangement regulates peripheral nerve regeneration through differential modulation of macrophage phenotypes. *Acta Biomater.*, 83:291–301.

Jiang, X., Lim, S. H., Mao, H.-Q., and Chew, S. Y. (2010). Current applications and future perspectives of artificial nerve conduits. *Exp. Neurol.*, 223(1):86–101.

Jianming Li, S. C., Shi, R., and Shi, R. (2010). Biomimetic Architectures for Tissue Engineering. *InTech*.

Johnson, P. M., Reynolds, T. B., Stansbury, J. W., and Bowman, C. N. (2005). High throughput kinetic analysis of photopolymer conversion using composition and exposure time gradients. *Polymer (Guildf).*

Ju, M. S., Lin, C. C. K., and Chang, C. T. (2017). Researches on biomechanical properties and models of peripheral nerves - A review.

Ju, M.-S., Lin, C.-C. K., Fan, J.-L., and Chen, R.-J. (2006). Transverse elasticity and blood perfusion of sciatic nerves under in situ circular compression. *J. Biomech.*, 39(1):97–102.

Ju, M.-S., Lin, C.-C. K., Lin, C.-W., Ju, M. S., and Lin, C. W. (2004). Transverse elasticity of rabbit sciatic nerves tested by in vitro compression. *J. Chinese Inst. Eng.*, 27(7):965–971.

Kaplan, A., Sanz, R., Ferraro, G. B., Alchini, R., and Fournier, A. E. (2014). Axon Growth and Regeneration. *Methods Mol. Biol.*, 1162(April 2016):43–56.

Kaplan, E. L., Salti, G. I., Roncella, M., Fulton, N., and Kadowaki, M. (2009a). History of the recurrent laryngeal nerve: from Galen to Lahey. *World J. Surg.*, 33(3):386–393.

Kaplan, S., Odaci, E., Unal, B., Sahin, B., and Fornaro, M. (2009b). Chapter 2 Development of the Peripheral Nerve. *Int. Rev. Neurobiol.*, 87:9–26.

Kapur, T. A. and Shoichet, M. S. (2004). Immobilized concentration gradients of nerve growth factor guide neurite outgrowth. *J. Biomed. Mater. Res.*, 68A(2):235–243.

Karatzas, I. and Shreve, S. E. (1998). *Brownian Motion*. Springer, New York, NY.

Katz, M. J. (1985). How Straight Do Axons Grow?'. *J. Neurosci.*, 5(3):589–595.

Kawano, T. and Kidoaki, S. (2011). Elasticity boundary conditions required for cell mechanotaxis on microelastically-patterned gels. *Biomaterials*.

Kayal, C., Shipley, R. J., and Phillips, J. B. (2019). Journal of the Mechanical Behavior of Biomedical Materials Physical and mechanical properties of RAFT-stabilised collagen gels for tissue engineering applications. *J. Mech. Behav. Biomed. Mater.*, 99(July):216–224.

Kehoe, S., Zhang, X., and Boyd, D. (2012). FDA approved guidance conduits and wraps for peripheral nerve injury: A review of materials and efficacy. *Injury*, 43(5):553–572.

Keller, E. and Segel, L. (1971). Model for chemotaxis. *J. Theor. Biol.*, 30:225–234.

Kennedy, J., Eberhart, R., and Gov, B. (1995). Particle Swarm Optimization. *IEEE*.

Khetan, S. and Burdick, J. A. (2010). Patterning network structure to spatially control cellular remodeling and stem cell fate within 3-dimensional hydrogels. *Biomaterials*, 31:8228–8234.

Kidoaki, S. and Matsuda, T. (2008). Microelastic gradient gelatinous gels to induce cellular mechanotaxis. *J. Biotechnol.*, 133:225–230.

Kidoaki, S. and Sakashita, H. (2013). Rectified Cell Migration on Saw-Like Micro-Elastically Patterned Hydrogels with Asymmetric Gradient Ratchet Teeth. *PLoS One*, 8(10):1–10.

Kim, S. M., Lee, M. S., Jeon, J., Lee, D. H., Yang, K., Cho, S., Han, I., and Yang, H. S. (2018). Biodegradable Nerve Guidance Conduit with Microporous and Micropatterned Poly(lactic-co-glycolic acid) Accelerated Sciatic Nerve Regeneration. *Macromol. Biosci.*, 18(12):1–14.

Kim, T. H., An, D. B., Oh, S. H., Kang, M. K., Song, H. H., and Lee, J. H. (2015). Creating stiffness gradient polyvinyl alcohol hydrogel using a simple gradual freezingthawing method to investigate stem cell differentiation behaviors. *Biomaterials*, 40:51–60.

Kloxin, A. M., Benton, J. A., and Anseth, K. S. (2009). In situ elasticity modulation with dynamic substrates to direct cell phenotype. *Biomaterials*, 31:1–8.

Kloxin, A. M., Tibbitt, M. W., Kasko, A. M., Fairbairn, J. A., and Anseth, K. S. (2010). Tunable hydrogels for external manipulation of cellular microenvironments through controlled photodegradation. *Adv. Mater.*, 22(1):61–66.

Koch, D., Rosoff, W. J., Jiang, J., Geller, H. M., and Urbach, J. S. (2012). Strength in the Periphery: Growth Cone Biomechanics and Substrate Rigidity Response in Peripheral and Central Nervous System Neurons. *Biophysj*, 102(3):452–460.

Koopmans, G., Hasse, B., and Sinis, N. (2009). The Role of Collagen in Peripheral Nerve Repair. In *Int. Rev. Neurobiol.*, volume 87, chapter 19, pages 363–379. Elsevier.

Koser, D. E., Thompson, A. J., Foster, S. K., Dwivedy, A., Pillai, E. K., Sheridan, G. K., Svoboda, H., Viana, M., Costa, L. D. F., Guck, J., Holt, C. E., and Franze, K. (2016). Mechanosensing is critical for axon growth in the developing brain. *Nat. Neurosci.*, 19(12):1592–1598.

Krieg, M., Flaschner, G., Alsteens, D., Gaub, B. M., Roos, W. H., Wuite, G. J., Gaub, H. E., Gerber, C., Dufrene, Y. F., and Muller, D. J. (2019). Atomic force microscopy-based mechanobiology. *Nat. Rev. Phys.*, pages 41–57.

Krishnan, L., Weiss, J. A., Wessman, M. D., and Hoying, J. B. (2004). Design and Application of a Test System for Viscoelastic Characterization of Collagen Gels. *Tissue Eng.*, 10.

Kuo, C.-H. R., Xian, J., Brenton, J. D., Franze, K., and Sivaniah, E. (2012). Complex Stiffness Gradient Substrates for Studying Mechanotactic Cell Migration. *Adv. Mater.*, 24(45):6059–6064.

Langevin, P. (1908). On the theory of Brownian Motion. *Am. J. Phys.*

Lawless, B. M., Barnes, S. C., Espino, D. M., and Shepherd, D. E. T. (2016). Viscoelastic properties of a spinal posterior dynamic stabilisation device. *J. Mech. Behav. Biomed. Mater.*, 59:519–526.

Leach, J. B., Brown, X. Q., Jacot, J. G., DiMilla, P. A., and Wong, J. Y. (2007). Neurite outgrowth and branching of PC12 cells on very soft substrates sharply decreases below a threshold of substrate rigidity. *J. Neural Eng.*, 4(2):26–34.

Lee, A. C., Vivian, M. Y., Lowe, J. B., Brenner, M. J., Hunter, D. A., Mackinnon, S. E., and Sakiyama-Elbert, S. E. (2003). Controlled release of nerve growth factor enhances sciatic nerve regeneration. *Exp. Neurol.*, 184(1):295–303.

Lee, D., Golden, &. K., Rahman, M., Moran, &. A., Gonzalez, &. B., and Ryu, &. S. (2018). Fabrication of Hydrogels with a Stiffness Gradient Using Limited Mixing in the Hele-Shaw Geometry. *Exp. Mech.*

Leipzig, N. D. and Shoichet, M. S. (2009). The effect of substrate stiffness on adult neural stem cell behavior. *Biomaterials*, 30(36):6867–6878.

Leite, F. L., Mattoso, L. H. C., Oliveira, O. N., and Herrmann, P. S. P. (2007). The Atomic Force Spectroscopy as a Tool to Investigate Surface Forces: Basic Principles and Applications. *Mod. Res. Educ. Top. Microsc.*

Lentz, S. I., Knudson, C. M., Korsmeyer, S. J., and Snider, W. D. (1999). Neurotrophins support the development of diverse sensory axon morphologies. *J. Neurosci.*, 19(3):1038–1048.

Levis, H. J., Brown, R. A., and Daniels, J. T. (2010). Plastic compressed collagen as a biomimetic substrate for human limbal epithelial cell culture. *Biomaterials*, 31:7726–7737.

Levis, H. J., Kureshi, A. K., Massie, I., Morgan, L., Vernon, A. J., and Daniels, J. T. (2015). Tissue Engineering the Cornea: The Evolution of RAFT. *J. Funct. Biomater.*, 6:50–65.

Li, C., Ouyang, L., Pence, I. J., Moore, A. C., Lin, Y., Winter, C. W., Armstrong, J. P. K., and Stevens, M. M. (2019). Buoyancy-Driven Gradients for Biomaterial Fabrication and Tissue Engineering. *Adv. Mater.*, 1900291:1–7.

Li, Z., Wang, W., Kratz, K., Küchler, J., Xu, X., Zou, J., Deng, Z., Sun, X., Gossen, M., Ma, N., and Lendlein, A. (2017). Influence of surface roughness on neural differentiation of human induced pluripotent stem cells. *Clin. Hemorheol. Microcirc.*, 64(3):355–366.

Lo, C.-M., Wang, H.-B., Dembo, M., and Wang, Y.-l. (2000). Cell movement is guided by the rigidity of the substrate. *Biophys. J.*, 79(1):144–152.

Ma, L., Gao, C., Mao, Z., Zhou, J., Shen, J., Hu, X., and Han, C. (2003). Collagen/chitosan porous scaffolds with improved biostability for skin tissue engineering. *Biomaterials*, 24(26):4833–4841.

Ma, Z., Hu, S., Tan, J. S., Myer, C., Njus, N. M., and Xia, Z. (2013). In vitro and in vivo mechanical properties of human ulnar and median nerves. *J. Biomed. Mater. Res. Part A*, 101A(9):2718–2725.

Madhavan, K., Belchenko, D., Motta, A., and Tan, W. (2009). Evaluation of composition and crosslinking effects on collagen-based composite constructs. *Acta Biomater.*, 6:1413–1422.

Magdeldin, T., López-Dávila, V., Pape, J., Cameron, G. W. W., Emberton, M., Loizidou, M., and Cheema, U. (2017). Engineering a vascularised 3D in vitro model of cancer progression. *Sci. Rep.*, 7(1):44045.

Maisonpierre, P., Belluscio, L., Squinto, S., IP, N., Furth, M., Lindsay, R., and Yancopoulos, G. (1990). Neurotrophin-3: a neurotrophic factor related to NGF and BDNF. *Science (80-.).*, 247:1446–1451.

Marklein, R. A. and Burdick, J. A. (2009). Spatially controlled hydrogel mechanics to modulate stem cell interactions. *Soft Matter*.

Martin, C., Dejardin, T., Hart, A., Riehle, M. O., and Cumming, D. R. S. (2014). Directed Nerve Regeneration Enabled by Wirelessly Powered Electrodes Printed on a Biodegradable Polymer. *Adv. Healthc. Mater.*, 3(7):1001–1006.

Martin, Y. H., Jubin, K., Smalley, S., Wong, J. P. F., Brown, R. A., and Metcalfe, A. D. (2017). A novel system for expansion and delivery of human keratinocytes for the treatment of severe cutaneous injuries using microcarriers and compressed collagen. *J. Tissue Eng. Regen. Med.*, 11(11):3124–3133.

Mason, S. and Phillips, J. B. (2011). An ultrastructural and biochemical analysis of collagen in rat peripheral nerves: The relationship between fibril diameter and mechanical properties. *J. Peripher. Nerv. Syst.*

Matthews, L. S. and Ellis, D. (1968). Viscoelastic properties of cat tendon: Effects of time after death and preservation by freezing. *J. Biomech.*, 1(2):65–71.

Mi, S., Chen, B., Wright, B., and Connon, C. J. (2010). Plastic compression of a collagen gel forms a much improved scaffold for ocular surface tissue engineering over conventional collagen gels. *J. Biomed. Mater. Res. Part A*, 95A(2):447–453.

Midha, R., Munro, C. A., Dalton, P. D., Tator, C. H., and Shoichet, M. S. (2003). Growth factor enhancement of peripheral nerve regeneration through a novel synthetic hydrogel tube. *J. Neurosurg.*, 99(3):555–565.

Mobini, S., Spearman, B. S., and Lacko, C. S. (2017). Recent advances in strategies for peripheral nerve tissue engineering. *Curr. Opin. Biomed. Eng.*, 4:134–142.

Moeendarbary, E., Weber, I. P., Sheridan, G. K., Koser, D. E., Soleman, S., Haenzi,

B., Bradbury, E. J., Fawcett, J., and Franze, K. (2017). The soft mechanical signature of glial scars in the central nervous system. *Nat. Commun.*, 8:14787.

Moore, A. M., MacEwan, M., Santosa, K. B., Chenard, K. E., Ray, W. Z., Hunter, D. A., Mackinnon, S. E., and Johnson, P. J. (2011). Acellular nerve allografts in peripheral nerve regeneration: a comparative study. *Muscle Nerve*, 44(2):221–234.

Moore, K., Macsween, M., and Shoichet, M. (2006). Immobilized Concentration Gradients of Neurotrophic Factors Guide Neurite Outgrowth of Primary Neurons in Macroporous Scaffolds. *Tissue Eng.*, 12(2):267–278.

Moreo, P., García-Aznar, J. M., and Doblaré, M. (2008). Modeling mechanosensing and its effect on the migration and proliferation of adherent cells. *Acta Biomater.*, 4(3):613–621.

Mosiewicz, K. A., Kolb, L., Van Der Vlies, A. J., and Lutolf, M. P. (2014). Microscale patterning of hydrogel stiffness through light-triggered uncaging of thiols. *Biomater. Sci.*, 2:1640.

Moskow, J., Ferrigno, B., Mistry, N., Jaiswal, D., Bulsara, K., Rudraiah, S., and Kumbar, S. G. (2018). Review: Bioengineering approach for the repair and regeneration of peripheral nerve. *Bioact. Mater.*

Muheremu, A. and Ao, Q. (2015). Past, Present, and Future of Nerve Conduits in the Treatment of Peripheral Nerve Injury. *Biomed Res. Int.*, 2015.

Nectow, A. R., Marra, K. G., and Kaplan, D. L. (2012). Biomaterials for the development of peripheral nerve guidance conduits. *Tissue Eng. Part B. Rev.*, 18(1):40–50.

Neel, E. A. A., Bozec, L., Knowles, J. C., Syed, O., Mudera, V., Day, R., and Hyun, J. K. (2013). Emerging collagen based therapies hit the patient. *Adv. Drug Deliv. Rev.*, 65:429–456.

Neel, E. A. A., Cheema, U., Knowles, J. C., Brown, R. A., and Nazhat, S. N. (2006). Use of multiple unconfined compression for control of collagen gel scaffold density and mechanical properties. *Soft Matter*, 2(11):986–992.

Nemir, S., Hayenga, H. N., and West, J. L. (2010). PEGDA hydrogels with patterned elasticity: Novel tools for the study of cell response to substrate rigidity. *Biotechnol. Bioeng.*, 105(3):636–644.

Ngo, P., Ramalingam, P., Phillips, J. A., and Furuta, G. T. (2006). Collagen gel contraction assay. *Cell-Cell Interact. Methods Protoc.*, 341:103–109.

Noback, C., Strominger, N., Demarest, R., and Ruggiero, D. (2005). *The human nervous system: structure and function*. Number 744. Springer Science & Business Media.

Ochi, K., Horiuchi, Y., Nakamura, T., Sato, K., Arino, H., and Koyanagi, T. (2013). Ulnar nerve strain at the elbow in patients with cubital tunnel syndrome: Effect of simple decompression. *J. Hand Surg. Eur. Vol.*

Orsi, G., Fagnano, M., De Maria, C., Montemurro, F., and Vozzi, G. (2017). A new 3D concentration gradient maker and its application in building hydrogels with a 3D stiffness gradient. *J. Tissue Eng. Regen. Med.*, 11(1):256–264.

Oyen, M. L. (2014). Mechanical characterisation of hydrogel materials. *Int. Mater. Rev.*, 59(1):44–59.

Painter, K. J. (2009). Continuous Models for Cell Migration in Tissues and Applications to Cell Sorting via Differential Chemotaxis. *Bull. Math. Biol.*, 71:1117–1147.

Parenteau-Bareil, R., Gauvin, R., and Berthod, F. (2010). Collagen-based biomaterials for tissue engineering applications. *Materials (Basel).*, 3(3):1863–1887.

Patlak, C. S. (1953). Random walk with persistence and external biais. *Bull. Math. Biophys.*, 15.

Pawelec, K., Koffler, J., D.Shahriari, D., Galvan, A., Tuszynski, M., and Sakamoto, J. (2018). Microstructure and in vivo characterization of multi-channel nerve guidance scaffolds. *Biomed. Mater.*, 13:1–10.

Pelham, R. J. and Wang, Y. L. (1998). Cell locomotion and focal adhesions are regulated by the mechanical properties of the substrate. *Biol. Bull.*, 194(3):348–350.

Peng, W., Li, C.-W., Chiu, I.-M., and Wang, J. (2017). Nerve guidance conduit with a hybrid structure of a PLGA microfibrous bundle wrapped in a micro/nanostructured membrane. *Int. J. Nanomedicine*, pages 12–421.

Pfister, B. J., Gordon, T., Loverde, J. R., Kochar, A. S., Mackinnon, S. E., and Cullen, D. K. (2011). Biomedical engineering strategies for peripheral nerve repair: surgical applications, state of the art, and future challenges. *Crit. Rev. Biomed. Eng.*, 39(2):81–124.

Pfister, L. A., Papalo\"\izos, M., Merkle, H. P., and Gander, B. (2007). Nerve conduits and growth factor delivery in peripheral nerve repair. *J. Peripher. Nerv. Syst.*, 12(2):65–82.

Phillips, J. B. (2014). Building stable anisotropic tissues using cellular collagen gels. *Organogenesis*.

Phillips, J. B., Bunting, S. C., Hall, S. M., and Brown, R. A. (2005). Neural Tissue Engineering: A Self-Organizing Collagen Guidance Conduit. *Tissue Eng.*, 11(9-10):1611–1617.

Phillips, J. B., Smit, X., De Zoysa, N., Afoke, A., and Brown, R. A. (2004). Peripheral nerves in the rat exhibit localized heterogeneity of tensile properties during limb movement. *J Physiol*, 557:879–887.

Popa, S., Boran, S., and Simulescu, V. (2017). Collagen Films Obtained from Collagen Solutions Characterized by Rheology. *Mater. Plast.*, 54(2):359–361.

Rajangam, T. and An, S. S. A. (2013). Fibrinogen and fibrin based micro and nano scaffolds incorporated with drugs, proteins, cells and genes for therapeutic biomedical applications. *Int. J. Nanomedicine*, 8:3641–3662.

Rammensee, S., Kang, M. S., Georgiou, K., Kumar, S., and Schaffer, D. V. (2017). Dynamics of Mechanosensitive Neural Stem Cell Differentiation. *Stem Cells*, 35(2):497–506.

Ratner, B. D., Hoffman, A. S., Schoen, F. J., and Lemons, J. E. (2004). *An introduction to materials in medicine*. Academic press, biomateria edition.

Ray, W. Z. and Mackinnon, S. E. (2010). Management of nerve gaps: autografts, allografts, nerve transfers, and end-to-side neurorrhaphy. *Exp. Neurol.*, 223(1):77–85.

Rickett, T., Connell, S., Bastijanic, J., Hegde, S., and Shi, R. (2011). Functional and Mechanical Evaluation of Nerve Stretch Injury. *J. Med. Syst.*, 35(5):787–793.

Roca-Cusachs, P., Sunyer, R., and Trepat, X. (2013). Mechanical guidance of cell migration: lessons from chemotaxis. *Curr. Opin. Cell Biol.*, 25:543–549.

Rosner, B. I., Siegel, R. A., Grosberg, A., and Tranquillo, R. T. (2003). Rational design of contact guiding, neurotrophic matrices for peripheral nerve regeneration. *Ann. Biomed. Eng.*, 31(11):1383–1401.

Rosoff, W. J., Urbach, J. S., Esrick, M. A., McAllister, R. G., Richards, L. J., and Goodhill, G. J. (2004). A new chemotaxis assay shows the extreme sensitivity of axons to molecular gradients. *Nat. Neurosci.*, 7(6):678–682.

Rosso, F., Giordano, A., Barbarisi, M., and Barbarisi, A. (2004). From Cell-ECM Interactions to Tissue Engineering. *J. Cell. Physiol.*, 199(2):174–180.

Rosso, G., Liashkovich, I., Gess, B., Young, P., Kun, A., and Shahin, V. (2014). Unravelling crucial biomechanical resilience of myelinated peripheral nerve fibres provided by the Schwann cell basal lamina and PMP22. *Sci. Rep.*

Rosso, G., Liashkovich, I., Young, P., Röhr, D., and Shahin, V. (2017a). Schwann cells and neurite outgrowth from embryonic dorsal root ganglions are highly mechanosensitive. *Nanomedicine Nanotechnology, Biol. Med.*, 13(2):493–501.

Rosso, G., Liashkovich, I., Young, P., Shahin, V., Parkinson, D. B., and Shahin, V. (2017b). Nano-scale Biophysical and Structural Investigations on Intact and Neuropathic Nerve Fibers by Simultaneous Combination of Atomic Force and Confocal Microscopy. *Front. Mol. Neurosci.*, 10.

Rosso, G., Young, P., and Shahin, V. (2017c). Implications of Schwann Cells Biomechanics and Mechanosensitivity for Peripheral Nervous System Physiology and Pathophysiology. *Front. Mol. Neurosci.*, 10:345.

Rosso, G., Young, P., and Shahin, V. (2017d). Mechanosensitivity of Embryonic Neurites Promotes Their Directional Extension and Schwann Cells Progenitors Migration. *Cell. Physiol. Biochem.*, 44(4):1263–1270.

Ryan, A. J., Lackington, W. A., Hibbitts, A. J., Matheson, A., Alekseeva, T., Stejskalova, A., Roche, P., and O'Brien, F. J. (2017). A Physicochemically Optimized and Neuroconductive Biphasic Nerve Guidance Conduit for Peripheral Nerve Repair. *Adv. Healthc. Mater.*, 6(24):1700954.

Sachot, N., Engel, E., and Castano, O. (2014). Hybrid Organic-Inorganic Scaffolding Biomaterials for Regenerative Therapies. *Curr. Org. Chem.*, 18(18):2299–2314.

Sadeghi, H., Espino, D. M., and Shepherd, D. E. T. (2015). Variation in viscoelastic properties of bovine articular cartilage below, up to and above healthy gait-relevant loading frequencies. *Proc. Inst. Mech. Eng. H.*, 229(2):115–23.

Saha, K., Keung, A. J., Irwin, E. F., Li, Y., Little, L., Schaffer, D. V., and Healy, K. E. (2008). Substrate Modulus Directs Neural Stem Cell Behavior. *Biophys. J.*, 95:4426–4438.

Sakane, T. and Pardridge, W. M. (1997). Carboxyl-directed pegylation of brain-derived neurotrophic factor markedly reduces systemic clearance with minimal loss of biologic activity. *Pharm. Res.*, 14(8):1085–1091.

Sant, S., Hancock, M. J., Donnelly, J. P., Iyer, D., and Khademhosseini, A. (2010). Biomimetic gradient hydrogels for tissue engineering. *Can. J. Chem. Eng.*, 88(6):899–911.

Saraf, H., Ramesh, K. T., Lennon, A. M., Merkle, A. C., and Roberts, J. C. (2007). Mechanical properties of soft human tissues under dynamic loading. *J. Biomech.*, 40:1960–1967.

Sarker, M., Naghieh, S., McInnes, A. D., Schreyer, D. J., and Chen, X. (2018). Strategic Design and Fabrication of Nerve Guidance Conduits for Peripheral Nerve Regeneration. *Biotechnol. J.*, 13(7):1–16.

Schienbein, M. and Gruler, H. (1993). Langevin equation, Fokker-Planck equation and cell migration. *Artic. Bull. Math. Biol.*, 55(3):585–608.

Schmidt, G. (1993). Eduard Albert and the beginning of humann nnerve grafting. Technical report, University vienna.

Schroyen, B., Swan, J. W., Van Puyvelde, P., and Vermant, J. (2017). Quantifying the dispersion quality of partially aggregated colloidal dispersions by high frequency rheology. *Soft Matter*.

Schuh, C. M., Day, A. G., Redl, H., and Phillips, J. (2018). An Optimized Collagen-Fibrin Blend Engineered Neural Tissue Promotes Peripheral Nerve Repair. *Tissue Eng. Part A*, 24(17-18):1332–1340.

Seddon, H. J. (1943). Three types of nerve injury. *Brain*, 66(4):237–288.

Segev, R. and Ben-Jacob, E. (1998). Generic Modeling of Chemotactic Based Self-Wiring of Neural Networks. *Condens. Matter*.

Seidi, A., Ramalingam, M., Elloumi-Hannachi, I., Ostrovidov, S., and Khademhosseini, A. (2011). Gradient biomaterials for soft-to-hard interface tissue engineering. *Acta Biomater.*, 7(4):1441–1451.

Seifert, J., Hammer, C. M., Rheinlaender, J., Sel, S., Scholz, M., Paulsen, F., and Schäffer, T. E. (2014). Distribution of Young's Modulus in Porcine Corneas after Riboflavin/UVA-Induced Collagen Cross-Linking as Measured by Atomic Force Microscopy. *PLoS One*, 9(1).

Sendtner, M., Holtmann, B., Kolbeckt, R., Thoenen, H., and Bardet, Y.-A. (1992). Brain-derived neurotrpphic factor prevents the death of motoneurons in newborn rats after nerve section. *Nature*.

Senger, J., Verge, V., Macandili, H., Olson, J., Chan, K., and Webber, C. (2018). Electrical stimulation as a conditioning strategy for promoting and accelerating peripheral nerve regeneration. *Exp. Neurol.*, 302:75–84.

Sensharma, P., Madhumathi, G., Jayant, R. D., and Jaiswal, A. K. (2017). Biomate-

rials and cells for neural tissue engineering: Current choices. *Mater. Sci. Eng. C*, 77:1302–1315.

Sexton, K. W., Pollins, A. C., Cardwell, N. L., Corral, G. A. D., Bittner, G. D., Shack, R. B., Nanney, L. B., and Thayer, W. P. (2012). Association for Academic Surgery Hydrophilic polymers enhance early functional outcomes after nerve autografting. *J. Surg. Res.*, 177:392–400.

Shah, S. B. (2017). Tissue Biomechanics: Whales Have Some Nerve. *Curr. Biol.*, 27:172–190.

Shivakumar, S. and Maffia, G. (2014). Rheology of Dispersions of Collagen Fibrils. *IJERT*, 3(11):798–802.

Shoulders, M. D. and Raines, R. T. (2009). Collagen structure and stability. *Annu. Rev. Biochem.*, 78:929–58.

Shu, Y., Chan, H. N., Guan, D., Wu, H., and Ma, L. (2017). A simple fabricated thickness-based stiffness gradient for cell studies. *Sci. Bull.*, 62(3):222–228.

Siemionow, M. and Brzezicki, G. (2009). Chapter 8 Current Techniques and Concepts in Peripheral Nerve Repair. *Int. Rev. Neurobiol.*, 87:141–172.

Smith, J. T., Tomfohr, J. K., Wells, M. C., Beebe, T. P., Kepler, T. B., and Reichert, W. M. (2004). Measurement of Cell Migration on Surface-Bound Fibronectin Gradients. *Langmuir*, pages 8279–8286.

Smith Callahan, L. A. (2018). Gradient Material Strategies for Hydrogel Optimization in Tissue Engineering Applications. *High-Throughput*, 7(1):1.

Son, Y. J. and Thompson, W. J. (1995). Schwann cell processes guide regeneration of peripheral axons. *Neuron*, 14(1):125–132.

Stang, F., Fansa, H., Wolf, G., and Keilhoff, G. (2005). Collagen nerve conduits–assessment of biocompatibility and axonal regeneration. *Biomed. Mater. Eng.*, 15(1, 2):3–12.

Stefanoni, F., Ventre, M., Mollica, F., and Netti, P. A. (2011). A numerical model for durotaxis. *J. Theor. Biol.*, 280(1):150–158.

Steffens, D., Braghirolli, D. I., Maurmann, N., and Pranke, P. (2018). Update on the main use of biomaterials and techniques associated with tissue engineering. *Drug Discov. Today*.

Sterne, G. D., Brown, R. A., Green, C. J., and Terenghi, G. (1997). Neurotrophin-3 delivered locally via fibronectin mats enhances peripheral nerve regeneration. *Eur. J. Neurosci.*, 9(7):1388–1396.

Stokes, C. L. and Lauffenburger, D. A. (1991). Analysis of the roles of microvessel endothelial cell random motility and chemotaxis in angiogenesis. *J. Theor. Biol.*, 152(3):377–403.

Stokes, C. L., Lauffenburger, D. A., and Williams, S. K. (1991). Migration of Individual Microvessel Endothelial Cells: Stochastic Model and Parameter Measurement. *J. Cell Sci.*, pages 419–430.

Stowers, R. S., Allen, S. C., and Suggs, L. J. (2015). Dynamic phototuning of 3D hydrogel stiffness. *Proc. Natl. Acad. Sci. U. S. A.*, 112(7):1953–1958.

Stylianou, A. (2017). Atomic force microscopy for collagen-based nanobiomaterials. *J. Nanomater.*, 2017.

Subramanian, A., Krishnan, U. M., and Sethuraman, S. (2009). Development of biomaterial scaffold for nerve tissue engineering: Biomaterial mediated neural regeneration. *J. Biomed. Sci.*, 16(1):108.

Sundararaghavan, H. G., Monteiro, G. A., Firestein, B. L., and Shreiber, D. I. (2009). Neurite growth in 3D collagen gels with gradients of mechanical properties. *Biotechnol. Bioeng.*, 102(2):632–643.

Sundararaghavan, H. G., Monteiro, G. A., Lapin, N. A., Chabal, Y. J., Miksan, J. R., and Shreiber, D. I. (2008). Genipin-induced changes in collagen gels: Correlation of mechanical properties to fluorescence. *J. Biomed. Mater. Res. Part A*, 87A(2):308–320.

Sunderland, S. (1951). The Function of Nerve Fibers whose structure has been disorganized. *Brain*, 3:113–119.

Sunderland, S. I. R. S., Microstructure, T. H. E., and Nerve, O. F. (1990). The Anatomy and Physiology of Nerve Injury. *Muscle Nerve*, 13(9):771–784.

Sunyer, R., Jin, A. J., Nossal, R., and Sackett, D. L. (2012). Fabrication of hydrogels with steep stiffness gradients for studying cell mechanical response. *PLoS One*, 7(10):e46107.

TA Instruments. Rheology Solutions: Determining the Linear Viscoelastic Region in Polymers. *Rs-23*.

Tabata, Y. (2003). Tissue regeneration based on growth factor release. *Tissue Eng.*, 9(4, Supplement 1):5–15.

Tai, T.-W., Su, F.-C., Chien, J.-T., Lee, J.-S., Huang, Y.-H., Lin, C.-L., and Jou, M. (2015). Basic Science Changes in excursion and strain in the rat sciatic nerve under cauda equina compression induced by epidural balloon inflation. *Spine J.*, 15:329–335.

Taniuchi, M., Clark, H. B., and Johnson, E. M. (1986). Induction of nerve growth

factor receptor in Schwann cells after axotomy. *Proc. Natl. Acad. Sci.*, 83(11):4094–4098.

Tao, J., Hu, Y., Wang, S., Zhang, J., Liu, X., Gou, Z., Cheng, H., Liu, Q., Zhang, Q., You, S., and Gou, M. (2017). A 3D-engineered porous conduit for peripheral nerve repair. *Sci. Rep.*, 7(1):46038.

Tayalia, P. and Mooney, D. J. (2009). Controlled growth factor delivery for tissue engineering. *Adv. Mater.*, 21(32-33):3269–3285.

Terenghi, G. (1999). Peripheral nerve regeneration and neurotrophic factors. *J. Anat.*, 194(1):1–14.

Terris, D. J., Toft, K. M., Moir, M., Lum, J., and Wang, M. (2001). Brain-derived neurotrophic factor–enriched collagen tubule as a substitute for autologous nerve grafts. *Arch. Otolaryngol. Head. Neck Surg.*, 127(3):294–298.

Thomson, S. E., Charalambous, C., Smith, C.-A., Tsimbouri, P. M., Déjardin, T., Kingham, P. J., Hart, A. M., and Riehle, M. O. (2017a). Microtopographical cues promote peripheral nerve regeneration via transient mTORC2 activation. *Acta Biomater.*, 60:220–231.

Thomson, S. E., Dahlin, L. B., Hart, A. M., Ng, N. Y., Wiberg, M., Riehle, M. O., and Kingham, P. J. (2017b). Bioengineered nerve conduits and wraps for peripheral nerve repair of the upper limb. *Cochrane Database Syst. Rev.*, (3).

Tierney, C. M., Haugh, M. G., Liedl, J., Mulcahy, F., Hayes, B., and O 'brien, F. J. (2009). The effects of collagen concentration and crosslink density on the biological, structural and mechanical properties of collagen-GAG scaffolds for bone tissue engineering. *J. Mech. Behav. Biomed. Mater.*, 2:202–209.

Tillett, R. L., Afoke, A., Hall, S. M., Brown, R. A., and Phillips, J. B. (2004). Investigating mechanical behaviour at a core-sheath interface in peripheral nerve. *J. Peripher. Nerv. Syst.*, 9(4):255–262.

Toby, E. B., Hanesworth, D., and City, K. (1998). Ulnar Nerve Strains at the Elbow. *J. Hand Surg. Am.*, pages 992–997.

Tong, X., Jiang, J., Zhu, D., and Yang, F. (2016). Hydrogels with Dual Gradients of Mechanical and Biochemical Cues for Deciphering Cell-Niche Interactions. *Biomater. Sience Eng.*

Topp, K. S. and Boyd, B. S. (2006). Structure and Biomechanics of Peripheral Nerves: Nerve Responses to Physical Stresses and Implications for Physical Therapist Practice. *Phys. Ther.*, 86(1):92–109.

Topp, K. S. and Boyd, B. S. (2012). Peripheral Nerve: From the Microscopic Functional Unit of the Axon to the Biomechanically Loaded Macroscopic Structure. *J. Hand Ther.*, 25(2):142–152.

Tranquillo, R. T. and Lauffenburger, D. A. (1987). Stochastic model of leukocyte chemosensory movement. *J. Math. Biol*, 25:229–262.

Tria, M. A., Fusco, M., Vantini, G., and Mariot, R. (1994). Pharmacokinetics of nerve growth factor (NGF) following different routes of administration to adult rats. *Exp. Neurol.*, 127(2):178–183.

Tse, J. R. and Engler, A. J. (2011). Stiffness gradients mimicking in vivo tissue variation regulate mesenchymal stem cell fate. *PLoS One*, 6(1).

Tse, T. H. Z., Chan, B. P., Chan, C. M., and Lam, J. (2007). Mathematical modeling of guided neurite extension in an engineered conduit with multiple concentration gradients of Nerve Growth Factor (NGF). *Ann. Biomed. Eng.*, 35(9):1561–1572.

Valtorta, D. and Mazza, E. (2005). Dynamic measurement of soft tissue viscoelastic properties with a torsional resonator device. *Med. Image Anal.*, 9.

Van Pelt, J., Dityatev, A. E., and Uylings, H. B. (1997). Natural variability in the number of dendritic segments: model-based inferences about branching during neurite outgrowth. *J. Comp. Neurol.*, 387(3):325–40.

Van Pelt, J., Uylings, H. B., Verwer, R. W., Pentney, R. J., and Woldenberg, M. J. (1992). Tree asymmetry–a sensitive and practical measure for binary topological trees. *Bull. Math. Biol.*, 54(5):759–84.

Van Pelt, J. and Verwer, R. W. H. (1983). The exact probabilities of branching patterns under terminal and segmental growth hypotheses. *Bull. Math. Biol.*, 45(2):269–285.

Vaz, A. I. F. and Vicente, L. N. (2007). A particle swarm pattern search method for bound constrained global optimization. *J. Glob. Optim.*, 39(2):197–219.

Vaz, A. I. F. and Vicente, L. N. (2009). PSwarm: A Hybrid Solver for Linearly Constrained Global Derivative-Free Optimization. *Optim. Methods Softw.*

Vincent, L. G., Choi, Y. S., Alonso-Latorre, B., del Álamo, J. C., and Engler, A. J. (2013). Mesenchymal stem cell durotaxis depends on substrate stiffness gradient strength. *Biotechnol. J.*, 8(4):472–484.

Wallace, D. G. and Rosenblatt, J. (2003). Collagen gel systems for sustained delivery and tissue engineering. *Adv. Drug Deliv. Rev.*, 55(12):1631–1649.

Walmod, P. S., Hartmann-Petersen, R., Berezin, A., Prag, S., Kiselyov, V. V., Berezin, V., and Bock, E. (2001). Evaluation of Individual-Cell Motility. In *Cytoskelet. Methods Protoc.*, chapter 6, pages 059–083. Humana Press, New Jersey.

Wang, H.-B., Dembo, M., Hanks, S. K., and Wang, Y.-L. (2001). Focal adhesion kinase is involved in mechanosensing during fibroblast migration. *Cell Biol.*, 98:11295–11300.

Wang, P.-Y., Tsai, W.-B., and Voelcker, N. H. (2012). Screening of rat mesenchymal stem cell behaviour on polydimethylsiloxane stiffness gradients. *Acta Biomater.*

Waxman, S. G. (1977). Conduction in myelinated, unmyelinated, and demyelinated fibers. *Arch. Neurol.*, 34(10):585–589.

Weickenmeier, J., Kurt, M., Ozkaya, E., de Rooij, R., Ovaert, T., Ehman, R., Butts Pauly, K., and Kuhl, E. (2018). Brain stiffens post mortem. *J. Mech. Behav. Biomed. Mater.*, 84:88–98.

Wells, R. G. (2008). The role of matrix stiffness in regulating cell behavior. *Hepatology*, 47(4):1394–1400.

Willits, R. K. and Skornia, S. L. (2004). Effect of collagen gel stiffness on neurite extension. *J. Biomater. Sci. Polym. Ed.*, 15(12):1521–1531.

Wong, J. Y., Velasco, A., Rajagopalan, P., and Pham, Q. (2003). Directed Movement of Vascular Smooth Muscle Cells on Gradient-Compliant Hydrogels. *Langmuir*, 19:1908–1913.

Wu, J., Mao, Z., Tan, H., Han, L., Ren, T., and Gao, C. (2012). Gradient biomaterials and their influences on cell migration. *Interface Focus*, page rsfs20110124.

Wu, T., Li, D., Wang, Y., Sun, B., Li, D., Morsi, Y., El-Hamshary, H., Al-Deyab, S. S., and Mo, X. (2017). Laminin-coated nerve guidance conduits based on poly(L-lactide-co-glycolide) fibers and yarns for promoting Schwann cells' proliferation and migration . *J. Mater. Chem. B*, 5:3186.

Xu, X., Yee, W.-C., Hwang, P. Y. K., Yu, H., Wan, A. C. A., Gao, S., Boon, K.-L., Mao, H.-Q., Leong, K. W., and Wang, S. (2003). Peripheral nerve regeneration with sustained release of poly (phosphoester) microencapsulated nerve growth factor within nerve guide conduits. *Biomaterials*, 24(13):2405–2412.

Xu, X., Yu, H., Gao, S., Mao, H.-Q., Leong, K. W., and Wang, S. (2002). Polyphosphoester microspheres for sustained release of biologically active nerve growth factor. *Biomaterials*, 23(17):3765–3772.

Yamazaki, C. M., Kadoya, Y., Hozumi, K., Okano-Kosugi, H., Asada, S., Kitagawa, K., Nomizu, M., and Koide, T. (2010). A collagen-mimetic triple helical supramolecule that evokes integrin-dependent cell responses. *Biomaterials*, 31(7):1925–1934.

Yanagawa, F., Mizutani, T., Sugiura, S., Takagi, T., Sumaru, K., and Kanamori, T. (2015). Partially photodegradable hybrid hydrogels with elasticity tunable by light irradiation. *Colloids Surfaces B Biointerfaces*, 126:575–579.

Yang, C., Hillas, P. J., Báez, J. A., Nokelainen, M., Balan, J., Tang, J., Spiro, R., and Polarek, J. W. (2004). The application of recombinant human collagen in tissue engineering. *BioDrugs*, 18(2):103–119.

Yao, L., de Ruiter, G. C. W., Wang, H., Knight, A. M., Spinner, R. J., Yaszemski, M. J., Windebank, A. J., and Pandit, A. (2010). Controlling dispersion of axonal regeneration using a multichannel collagen nerve conduit. *Biomaterials*, 31(22):5789–5797.

Yin, Q., Kemp, G. J., Yu, L.-G., Wagstaff, S. C., and Frostick, S. P. (2001). Neurotrophin-4 delivered by fibrin glue promotes peripheral nerve regeneration. *Muscle Nerve*, 24(3):345–351.

Zaari, N., Rajagopalan, P., Kim, S. K., Engler, A. J., and Wong, J. Y. (2004). Photopolymerization in Microfluidic Gradient Generators: Microscale Control of Substrate Compliance to Manipulate Cell Response. *Adv. Mater.*, 16(23-24):2133–2137.

Zaman, M. H., Kamm, R. D., Matsudaira, P., and Lauffenburger, D. A. (2005). Computational Model for Cell Migration in Three-Dimensional Matrices. *Biophys. J.*, 89(2):1389–1397.

Zhu, X., Wei, H., and Zhu, H. (2018). Nerve wrap after end-to-end and tension-free neurorrhaphy attenuates neuropathic pain: A prospective study based on cohorts of digit replantation. *Sci. Rep.*, 8(1):620.

Zubler, F. and Douglas, R. (2009). A framework for modeling the growth and development of neurons and networks. *Front. Comput. Neurosci.*, 3:1–16.

Zuidema, J. M., Rivet, C. J., Gilbert, R. J., and Morrison, F. A. (2014). A protocol for rheological characterization of hydrogels for tissue engineering strategies. *J. Biomed. Mater. Res. Part B Appl. Biomater.*, 102(5):1063–1073.

Zwanzig, R. (2001). *Nonequilibrium statistical mechanics*. Oxford University Press.